UNIVERSITAT DE BARCELONA

Preparation of high efficiency $Cu_2ZnSn(S,Se)_4$ solar cells based on a single-step sulfo-selenization process

Haibing Xie

UNIVERSITAT DE BARCELONA

Preparation of high efficiency $Cu_2ZnSn(S,Se)_4$ solar cells based on a single-step sulfo-selenization process

Doctoral thesis presented by

Haibing Xie

Thesis directors:

Prof. Dr. Alejandro Pérez-Rodríguez

Dr. Edgardo Saucedo

Thesis tutor:

Prof. Dr. Alejandro Pérez-Rodríguez

Programa de Doctorat: **Enginyeria i Tecnologies Avançades**

Thesis submitted in September, 2016

Universitat de Barcelona

Facultat de Física, Department d'Electrònica

Table of Contents

List of abbreviations

ALD: atomic layer deposition

AM 1.5G: Reference global spectrum at air mass 1.5

APT: atom probe tomography

ARC: anti-reflective coating

AZO: Al doped ZnO

BIPV: building integrated photovoltaics

CBD: chemical bath deposition

CBM: conduction band maximum

CBO: conduction band offset

CIGS: Cu (In,Ga)Se_2

CIGSS: Cu(In,Ga)$(S,Se)_2$

CIS: $CuInS_2$

CISe: $CuInSe_2$

CISS: CuIn$(S,Se)_2$

C-V: capacitance-voltage

CSP: concentrated solar power

CZTS: Cu_2ZnSnS_4

CZTSe: $Cu_2ZnSnSe_4$

CZTSSe: $Cu_2ZnSn(S_xSe_{1-x})_4$ $(0 < x < 1)$

DAP: donor-acceptor pair

DLTS: deep-level transient spectroscopy

DSSC: dye-sensitized solar cell

EELS: electron energy loss spectroscopy

E_g: band gap

EHP: electron-hole pair

EQE: external quantum efficiency

E_u: Urbach energy

FF: fill factor

FTO: fluorine-doped tin oxide

GB: grain boundary

GD-OES: glow discharge optical emission spectrometer

HRTEM: high resolution transmission electron microscopy

ICP: inductively coupled plasma spectrometry

IQE: internal quantum efficiency

ITO: indium tin oxide

i-ZnO: intrinsic ZnO

J_{sc}: short circuit current

J-V: current density-voltage

JV-T: temperature dependence of J-V

NMR: nuclear magnetic resonance

PCE or η: power conversion efficiency

PDT: post deposition treatment

PID: potential induced degradation

PL: Photoluminescence spectroscopy

P_{light}: incident light power density

PLTT: post low temperature treatment

P_m: maximum generated power density

PV: photovoltaic

PVD: physical vapor deposition

QDAP: quasi donor-acceptor pair

RTP: rapid thermal processing

SCR: space charge region

SEM: scanning electron microscopy

SLG: soda lime glass

SQ limit: Shockley-Queisser limit

STEM: scanning transmission electron microscopy

TCO: transparent conductive oxide

TOF-SIMS: time-off-flight secondary ion mass spectrometry

UV: ultraviolet

V_{bi}: built-in voltage

VBM: valence band maximum

V_{oc}: open circuit voltage

XANES: X-ray absorption near edge structure

XPS: X-ray photoelectron spectroscopy

XRD: x-ray diffraction

XRF: X-ray fluorescence spectroscopy

Preface: Publications and summary of the thesis

The work presented in this thesis was fully carried out at Catalonia Institute for Energy Research (IREC), Barcelona, Spain from 2012 to 2016, funded by "China Scholarship Council" fellowship (CSC Nº 201206340113). The main subject of the thesis is to develop high efficiency $Cu_2ZnSn(S_xSe_{1-x})_4$ ($0 < x < 1$) thin film solar cells based on a single-step sulfo-selenization methodology.

The following four papers published in high impact peer-reviewed journals contribute to the main part of the thesis, which are submitted in accord with the requirements for the Doctor of Philosophy in Engineering and Advanced Technologies at the University of Barcelona:

1. ***Haibing Xie****, *Mirjana Dimitrievska, Xavier Fontané, Yudania Sánchez, Simon López-Marino, Victor Izquierdo-Roca, Verónica Bermúdez, Alejandro Pérez-Rodríguez, Edgardo Saucedo, "Formation and impact of secondary phases in Cu-poor Zn-rich $Cu_2ZnSn(S_{1-y}Se_y)_4$ ($0 \leqslant y \leqslant 1$) based solar cells",* **Solar Energy Materials & Solar Cells** *140 (2015) 289 – 298.*

2. ***Haibing Xie,*** *Yudania Sánchez, Simón López-Marino, Moisés Espíndola-Rodríguez, Markus Neuschitzer, Diouldé Sylla, Andrew Fairbrother, Victor Izquierdo-Roca, Alejandro Pérez-Rodríguez, and Edgardo Saucedo*, *"Impact of Sn-(S,Se) secondary phases in $Cu_2ZnSn(S,Se)_4$ solar cells: a chemical route for their selective removal and absorber surface passivation",* **ACS Applied Materials & Interface** *6 (2014) 12744 – 12751.*

3. ***Haibing Xie****, *Simon López-Marino, Tetiana Olar, Yudania Sánchez, Markus Neuschitzer, Florian Oliva, Sergio Giraldo, Victor Izquierdo-Roca, Iver Lauermann, Alejandro Pérez-Rodríguez, Edgardo Saucedo, "Impact of Na dynamics at the $Cu_2ZnSn(S,Se)_4$/CdS interface during post low temperature treatment of absorbers",* **ACS Applied Materials & Interfaces** *8 (2016) 5017-5024.*

4. *Yudania Sánchez*, *Moisés Espíndola-Rodríguez,* ***Haibing Xie****, Simón López-Marino, Markus Neuschitzer, Sergio Giraldo, Mirjana Dimitrievska, Marcel Placidi, Victor Izquierdo-Roca, Fabián Andrés Pulgarín-Agudelo, Osvaldo Vigil-Galán and Edgardo Saucedo, "Ultra-thin CdS for highly performing chalcogenides thin film based solar cells",* ***Solar Energy Materials and Solar Cells*** *(2016) Doi:10.1016/j.solmat.2015.12.037.*

   In addition, the thesis also includes several works that are in preparation for publication or submitted to journals, which together with the published papers above help to summarize the work during my Ph.D. career and complete the thesis.

   The thesis is structured into 6 chapters.

   Chapter 1 describes the introduction of solar cells and objectives of the thesis, which is separated into three subsections. First a brief introduction of solar cells is presented, including the motivations and development history, as well as the fundamental physics and basic device measurements and analysis of solar cells. The second subsection is a general introduction of kesterite solar cells, which are the main actors of the thesis. The motivation and development history of kesterite solar cells are presented, following are the detailed

discussions of the configuration of kesterite solar cells. Various layers are introduced, with the highlight on the kesterite absorber layer. In addition, the comparison of CZTS, CZTSSe and CZTSe solar cells is presented, and emphasis is put on the CZTSSe type which has the optimal band gap approaching the SQ limit curve peak and thus it is chosen for deep investigations in this thesis. The fabrication methods are also reviewed and the single-step sulfo-selenization process is highlighted, because it is the core technology used in this thesis. To get insights into kesterite solar cells, the similarities and peculiarities of kesterite solar cells compared with CIGS solar cells are also discussed. The final part clarifies the objectives of the thesis.

Chapter 2 details the experimental and methodology part of the thesis. This includes the whole process of manufacturing CZTSSe solar cells in IREC, as well as the characterization methods.

Chapter 3 discusses how to prepare high quality CZTSSe absorbers through the fine tuning of thermal treatments as well as thermodynamic equilibrium during thermal processes. This chapter includes two subsections. The first subsection details the preparation of CZTSSe absorbers with optimal S/(S+Se) ratio, high crystal quality, and minimized secondary phases, especially Zn(S, Se) in the interfaces. This can be achieved by modifying the added S/(S+Se) ratio, system pressure, and thermal treatment profiles and by cautious control of materials loss. Besides, the impact of absorbers S/(S+Se) ratio on the optoelectronic properties of devices is studied. This work is included in the paper entitled "Formation and impact of secondary phases in Cu-poor Zn-rich $Cu_2ZnSn(S_{1-y}Se_y)_4$ ($0 \leqslant y \leqslant 1$) based solar cells", which can be found in the Appendix. Finally, the thermodynamic equilibrium during the single-step sulfo-selenization process is analyzed. Chemical equilibrium equation is established according to reasonable assumptions, based on which the final S/(S+Se) ratio of the thin films is assumed to be the result of chemical equilibrium between CZTSSe and S_2/Se_2 vapor during the crystal growth process. Basic equations of the added S/(S+Se) ratio, the annealing temperature, and the final S/(S+Se) ratio in the CZTSSe thin films in different cases are also presented, elucidating the direct and indirect impact of the first two parameters on the final absorber S/(S+Se) ratio in ideally sealed or partially opened real systems.

Chapter 4 discusses one of the biggest challenges of kesterite solar cells: secondary phases. First of all, the existence of secondary phases is somehow inevitable, due to the narrow single phase existence region in the phase diagrams, non-stoichiometry composition used for high efficiency devices, and non-equilibrium thermal treatment conditions applied during processes. Secondly, to identify secondary phases is found to be tough at the beginning, due to the similar crystalline structure of ZnS and Cu_2SnS_3 with kesterite phase, which are hard to be distinguished by the extensively used XRD measurement. Different inspection methods are reviewed with the highlight on the pre-resonant Raman spectra. Thirdly, the distribution of secondary phases is very important for further understanding and optimization of device properties. If the secondary phases present at the back Mo/CZTSSe interface, a barrier layer on top of Mo or search of new back contact materials could be an option to solve the problem. If the secondary phases are in the bulk, probably the only way to prevent them is the optimization of thermal treatment or precursor preparation. However, if the secondary phases are on the surface of CZTSSe absorbers, things will become easier because they could be removed by etchings. Finally, the

chemical etchings of $Cu_x(S,Se)$, Zn(S,Se) and Cu-Sn-Se related secondary phases have been well developed except for Sn-(S,Se) secondary phases. To address this issue, an innovative $(NH_4)_2S$ etching is developed to effectively and selectively remove Sn-(S,Se) secondary phases. In addition, the origins of Sn-(S,Se) and its impact on CZTSSe solar cells are also investigated, yielding the identification of a passivation effect on the absorbers surface. A surface passivation mechanism of $(NH_4)_2S$ etching is proposed to illustrate this phenomenon. The paper "Impact of Sn-(S,Se) secondary phases in $Cu_2ZnSn(S,Se)_4$ solar cells: a chemical route for their selective removal and absorber surface passivation" details these findings.

Chapter 5 focuses on the CZTSSe/CdS interface, which forms the p-n junction and is very critical for the high performance of CZTSSe solar cells. First, Na dynamics in the CZTSSe/CdS interface is investigated during post low temperature treatment (PLTT) of CZTSSe absorbers. The motivation is arising from the fact that the PLTT process is proved to be beneficial for high efficiency kesterite solar cells by several groups whereas Na diffusion and distribution involved in PLTT are not studied, though Na is accepted as crucial in the chalcopyrite and kesterite field. Surprisingly large variations of device properties of CZTSSe solar cells during PLTT process can be correlated with different Na concentration in the active CZTSSe/CdS p-n junction region. An innovative model of Na dynamics is developed, featuring two Na fluxes including Na diffusion from the SLG to the absorbers and Na loss from the surface to the atmosphere. Depending on the rate of these two fluxes at a given temperature, namely $V_{Na\ diffusion}$ and $V_{Na\ loss}$, different Na in-depth profiles could be obtained. This model is validated by theoretical calculations and further by specially designed experiments. Results show that appropriate content of Na doping especially in the active CZTSSe/CdS interface region of solar cells could be critical for device performance, and PLTT process can be a way to optimize Na in-depth profiles. This work is described in the paper "Impact of Na dynamics at the $Cu_2ZnSn(S,Se)_4$/CdS interface during post low temperature treatment of absorbers". Second, Cu-doped CdS is investigated to improve the CdS deposition quality with the aim of high quality interface. Results show that the thickness of CdS can be reduced substantially when appropriate Cu doping was introduced, while comparable performance of CIGS and CZTSe solar cells can be maintained. This could be related to the good coverage of the thin CdS layer with homogeneous and pinhole free nature and may offer new possibilities to address the environmental concerns of the extensively used CdS buffer layer. The paper "Ultra-thin CdS for highly performing chalcogenides thin film based solar cells" summarizes this work. Third, interface recombination has been extensively reported to be one of the potential reasons for the large V_{oc} deficit of kesterite solar cells especially CZTSSe solar cells. To address this issue, an innovative wet chemical treatment using group Ⅲ chlorides (Ⅲ =Al ,Ga) and thioacetamide (CH_3CSNH_2) solution is performed. Less V_{oc} deficit and higher efficiency can be achieved by this chemical treatment due to the improvement of V_{oc} and FF, which is mainly related to the reduced interface recombination, the increase of surface band gap and the reduction of shunt paths. A champion CZTSSe solar cell with efficiency of 9.1% and FF over 69% is reported after the optimization of $AlCl_3$ related chemical treatments. This work is in preparation for publication.

Chapter 6 is the summary of the thesis and the outlook of kesterite solar cells.

Finally, in addition to the four papers listed above, the following papers co-authored by Haibing Xie which are related to the thesis work are as follows:

1. *M. Dimitrievska, **H. Xie**, A. Fairbrother, X. Fontané, G. Gurieva, E. Saucedo, A. Pérez-Rodríguez, S. Schorr, V. Izquierdo-Roca, "Multiwavelength excitation Raman scattering of $Cu_2ZnSn(S_xSe_{1-x})_4$ $(0 \leq x \leq 1)$ polycrystalline thin films: vibrational properties of sulfoselenide solid solutions", **Applied Physics Letters** 105 (2014) 031913.*
2. *J. López-García, **H. Xie**, V. Izquierdo-Roca, D. Sylla, X. Fontané, M. Blanes-Guardia, F. Ramos, M. Espindola-Rodriguez, S. López-Marino, E. Saucedo, A. Pérez-Rodriguez, "Synthesis of $CuIn(S, Se)_2$ quaternary alloys by screen printing and selenization-sulfurization sequential steps: Development of composition graded absorbers for low cost photovoltaic devices", **Materials Chemistry and Physics** 160 (2015) 237–243.*
3. *M. Dimitrievska, **H. Xie**, A. J. Jackson, X. Fontane, M. Espindola-Rodriguez, E. Saucedo, A. Perez-Rodriguez, A. Walsh, V. Izquierdo-Roca, "Resonant raman scattering of ZnS_xSe_{1-x} solid solutions: the role of S and Se electronic states", **Physical Chemistry Chemical Physics** 18 (2016) 7632-7640.*
4. *M. Dimitrievska, **H. Xie**, G. Gurieva, X. Fontane, A. Fairbrother, R. Gunder, E. Saucedo, A. Perez-Rodriguez, S. Schorr, V. Izquierdo-Roca, "Vibrational and structural properties of $Cu_2ZnSn(S_xSe_{1-x})_4$ $(0 \leq x \leq 1)$ solid solutions", **IEEE 40th Photovoltaic Specialist Conference (PVSC)** (2014) 0033-0036.*
5. *M. Dimitrievska, G. Gurieva, **H. Xie**, A. Carrete, A. Cabot, E. Saucedo, A. Pérez-Rodríguez, S. Schorr, V. Izquierdo-Roca, "Raman scattering quantitative analysis of the anion chemical composition in kesterite $Cu_2ZnSn(S_xSe_{1-x})_4$ solid solutions", **Journal of Alloys and Compounds** 628 (2015) 464–470.*
6. *T. Olar, I. Lauermann, **H. Xie**, M. Neuschitzer, E. Saucedo, W. Calvet, A. Steigert, B. Ümsür, B. Chacko, V. Parvan, M. Gorgoi, B. Senkovskiy, M. Ch Lux-Steiner, "Assessment of chemical and electronic Surface properties of the $Cu_2ZnSn(S,Se)_4$ after different etching procedures by synchrotron-based spectroscopies", **Energy Procedia** 84 (2016) 8-16.*
7. *M. Neuschitzer, Y. Sanchez, S. López-Marino, **H. Xie**, A. Fairbrother, M. Placidi, V. Izquierdo-Roca, A. Perez-Rodriguez, E. Saucedo, "Optimization of CdS Buffer Layer for High Performance CZTSe Solar Cells and the Effects of Light Soaking: Elimination of Cross Over and Red Kink", **Progress in Photovoltaics: Research and Applications** 23(2015)1660 –1667.*
8. *S. Lugo, Y. Sánchez, M. Neuschitzer, **H. Xie**, C. Insignares-Cuello, V. Izquierdo-Roca, Y. Peña, E. Saucedo, "Chemical bath deposition route for the synthesis of ultra-thin $CuIn(S,Se)_2$ based solar cells", **Thin Solid Films** 582 (2015) 74–78.*
9. *M. Dimitrievska, A. Fairbrother, R. Gunder, G. Gurieva, **H. Xie**, E. Saucedo, A. Perez-Rodriguez, V. Izquierdo-Roca, S. Schorr, "Role of S and Se atoms on the microstructural properties of kesterite $Cu_2ZnSn(S_xSe_{1-x})_4$ thin film solar cells", **Physical Chemistry Chemical Physics** 18 (2016)8692-8700.*
10. *S. Lopez-Marino, Y. Sanchez, M. Espindola-Rodriguez, X. Alcobe, **H. Xie**, M. Neuschitzer, I. Becerril, S. Giraldo, M. Dimitrievska, M. Placidi, L. Fourdrinier, V. Izquierdo-Roca, A. Perez-Rodriguez, E. Saucedo, "Alkali doping strategies for flexible and light-weight $Cu_2ZnSnSe_4$ solar cells", **Journal of Materials Chemistry A** 4(2016)1895-1907.*

11. *S. Giraldo, M. Neuschitzer, T. Thersleff, S. López-Marino, Y. Sánchez, **H. Xie**, M. Colina, M. Placidi, P. Pistor, V. Izquierdo-Roca, K. Leifer, A. Pérez-Rodríguez, E. Saucedo, "Large efficiency improvement in $Cu_2ZnSnSe_4$ solar cells by introducing a superficial Ge nanolayer", **Advanced Energy Materials** 5(2015)1501070.*
12. *S. Lopez-Marino, M. Espíndola-Rodríguez, Y. Sánchez, X. Alcobé, F. Oliva, **H. Xie**, M. Neuschitzer, S. Giraldo, M. Placidi, R. Caballero, V. Izquierdo-Roca, A. Pérez-Rodríguez , E. Saucedo, "The importance of back contact modification in $Cu_2ZnSnSe_4$ solar cells: the role of a thin MoO_2 layer", **Nano Energy** (2016). Doi:10.1016/j.nanoen.2016.06.034.*
13. *M. Espindola-Rodriguez, Y. Sanchez, S. López-Marino, D. Sylla, M. Placidi, M. Neuschitzer, **H. Xie**, V. Izquierdo-Roca, O. Vigil-Galán, E. Saucedo, "Selenization of Cu_2ZnSnS_4 thin films obtained by pneumatic spray pyrolysis", **Journal of Analytical and Applied Pyrolysis** (2016) Doi:10.1016/j.jaap.2016.04.008.*
14. *M. Neuschitzer, Y. Sánchez , T. Olar, T. Thersleff, S. López-Marino, F. Oliva, M. Espindola-Rodriguez, **H. Xie,** M. Placidi, V. Izquierdo-Roca, I. Lauermann, K. Leifer, A. Perez-Rodriguez, E. Saucedo, "The complex surface chemistry of kesterites: Cu/Zn re-ordering after low temperature post deposition annealing and its role in high performance devices", **Chemistry of Materials** 27(2015)5279-5287.*
15. *R. Kondrotas, R. Juškėnas, A. Naujokaitis, A. Selskis, R. Giraitis, Z. Mockus, S. Kanapeckaitė, G. Niaura, **H. Xie**, Y. Sánchez, E. Saucedo, "Characterization of $Cu_2ZnSnSe_4$ solar cells prepared from electrochemically co-deposited Cu–Zn–Sn alloy", **Solar Energy Materials & Solar Cells** 132 (2015) 21–28.*
16. *A.U. Sheleg, V.G. Hurtavy, A.V. Mudryi, V.D. Zhivulko, M. Ya Valakh, V.A. Yuhimchuk, I.S. Babichuk, **H. Xie**, E. Saucedo, "Crystallographic and optical characteristics of thin films of $Cu_2ZnSn(S_xSe_{1-x})_4$ solid solutions", **Journal of Applied Spectroscopy** 81(2014)776 –781.*

Contribution of the author to publications in the thesis

The author of the thesis, Haibing Xie, is responsible for the design and performing of the experiments, coordination of characterizations and interpretation of experimental results. He has directly participated in the development of the single-step sulfo-selenization process to prepare high efficiency CZTSSe solar cells, which includes the sputtering of metallic precursors, thermal treatment to form CZTSSe absorbers, etchings to remove secondary phases, post low temperature treatment of absorbers or devices to optimize the Na spatial distribution, surface engineering by chemical treatments, and sputtering of i-ZnO/ITO window layer. In addition, he has coordinated the CBD process of CdS buffer layer for the devices. Finally, the author has also performed XRD, SEM, EQE and I-V measurements and coordinated other characterizations when it is needed to understand the process and to interpret the experimental results.

Chapter 3:

Haibing Xie, Mirjana Dimitrievska, Xavier Fontané, Yudania Sánchez, Simon López-Marino, Victor Izquierdo-Roca, Verónica Bermúdez, Alejandro Pérez-Rodríguez,*

Edgardo Saucedo, "Formation and impact of secondary phases in Cu-poor Zn-rich $Cu_2ZnSn(S_{1-y}Se_y)_4$ ($0 \leqslant y \leqslant 1$) based solar cells", ***Solar Energy Materials & Solar Cells*** *140 (2015) 289 – 298.*

Impact Factor (IF): 4.7

1st quartile in areas: Electronic, Optical and Magnetic Materials; Renewable Energy

This article is about the optimization of thermal treatments to achieve high quality CZTSSe absorbers with appropriate S/(S+Se) ratio and less secondary phases in the interfaces. In addition, the impact of S/(S+Se) ratio in the absorbers on the optoelectronic properties of devices was also investigated. In this work, Haibing Xie has designed and carried out all the experiments to synthesize the CZTSSe absorbers and has coordinated the fabrication of the CZTSSe solar cells. He has also performed XRD, EQE and I-V measurements as well as the coordination of other characterizations. In addition, he is responsible for the interpretation of experimental results and in charge of the writing of the manuscript.

Chapter 4:

Haibing Xie, *Yudania Sánchez, Simón López-Marino, Moisés Espíndola-Rodríguez, Markus Neuschitzer, Diouldé Sylla, Andrew Fairbrother, Victor Izquierdo-Roca, Alejandro Pérez-Rodríguez, and Edgardo Saucedo*. "Impact of Sn-(S,Se) secondary phases in $Cu_2ZnSn(S,Se)_4$ solar cells: a chemical route for their selective removal and absorber surface passivation",* ***ACS Applied Materials & Interface*** *6 (2014) 12744 – 12751.*

Impact Factor: 7.1

1st quartile in areas: Nanoscience and Nanotechnology; Materials Science; Multidisciplinary

This article is mainly about the removal of Sn-(S,Se) secondary phases from the surface of CZTSSe absorbers by 22% w/w yellow $(NH_4)_2S$ solution. In addition, the impact of $(NH_4)_2S$ etching on the device properties was investigated and a passivation mechanism was proposed. In this work, Haibing Xie has designed and carried out all the experiments except for the CBD process. He is also responsible for the interpretation of the experimental results and has prepared the first draft of the manuscript. In addition, he has carried out all the characterizations of this work.

Chapter 5:

1. ***Haibing Xie****, *Simon López-Marino, Tetiana Olar, Yudania Sánchez, Markus Neuschitzer, Florian Oliva, Sergio Giraldo, Victor Izquierdo-Roca, Iver Lauermann, Alejandro Pérez-Rodríguez, Edgardo Saucedo,"Impact of Na dynamics at the $Cu_2ZnSn(S,Se)_4$/CdS interface during post low temperature treatment of absorbers",* ***ACS Applied Materials & Interfaces*** *8 (2016) 5017-5024.*

Impact Factor: 7.1

1st quartile in areas: Nanoscience and Nanotechnology; Materials Science; Multidisciplinary

In this article, the impact of Na dynamics during post low temperature treatment of CZTSSe absorbers is studied. Large performance variations can be related to the Na spatial distribution in the CZTSSe/CdS interface region. An innovative model is proposed to explain the behavior, which is further supported by theoretical calculations and specially designed experiments. After optimization of the PLTT process, CZTSSe devices with 7.1% and 8.3% are reported. In this work, Haibing Xie has designed and carried out all the experiments except for the CBD process. He has also carried out XRD, SEM, XRF, EQE and I-V measurements and coordinated XPS, Raman, SIMS, and C-V measurements. In addition, he is in charge of the interpretation of the experimental results and the writing of the manuscript.

2. *Yudania Sánchez*, Moisés Espíndola-Rodríguez,* ***Haibing Xie****, Simón López-Marino, Markus Neuschitzer, Sergio Giraldo, Mirjana Dimitrievska, Marcel Placidi, Victor Izquierdo-Roca, Fabián Andrés Pulgarín-Agudelo, Osvaldo Vigil-Galán and Edgardo Saucedo, "Ultra-thin CdS for highly performing chalcogenides thin film based solar cells",* ***Solar Energy Materials and Solar Cells*** *(2016) Doi:10.1016/j.solmat.2015.12.037.*

Impact Factor (IF): 4.7

1st quartile in areas: Electronic, Optical and Magnetic Materials; Renewable Energy

In this article, Cu-doped CdS is investigated. Results show that the thickness of CdS can be reduced substantially when appropriate Cu doping was introduced, while comparable performance of CIGS and CZTSe solar cells can be maintained. In this work, Haibing Xie has contributed to the preparation of the absorbers, the fabrication and characterization of the solar cells, and to the preparation of the manuscript and the experimental results explanations.

None of these articles have been used by other co-authors for their doctoral thesis.

Barcelona, 9th August, 2016

Prof. Alejandro Pérez Rodríguez Dr. Edgardo Saucedo

Prefacio: Publicaciones y resumen de la tesis

El trabajo presentado en esta tesis se ha desarrollado íntegramente en el Institut de Recerca en Energia de Catalunya" (IREC), en Barcelona, entre los años 2012 y 2016 y ha sido financiado mediante una beca del Consejo de Becas de China (CSC Nº 201206340113). El objetivo principal de la tesis se centra en el desarrollo de células solares de película delgada (thin-film) de $Cu_2ZnSn(S_xSe_{1-x})_4$ ($0 < x < 1$) mediante un proceso de sulfo-selenización de un solo paso.

Los siguientes cuatro artículos han sido publicados en revistas de revisión por pares (peer-reviewed) de alto impacto y conforman la parte principal de esta tesis, de acuerdo con los criterios establecidos por la Universidad de Barcelona para optar al título de Doctor en Ingeniería y Tecnologías Avanzadas:

1. ***Haibing Xie****, *Mirjana Dimitrievska, Xavier Fontané, Yudania Sánchez, Simon López-Marino, Victor Izquierdo-Roca, Verónica Bermúdez, Alejandro Pérez-Rodríguez, Edgardo Saucedo, "Formation and impact of secondary phases in Cu-poor Zn-rich $Cu_2ZnSn(S_{1-y}Se_y)_4$ ($0 \leq y \leq 1$) based solar cells", **Solar Energy Materials & Solar Cells** 140 (2015) 289 – 298.*

2. ***Haibing Xie,*** *Yudania Sánchez, Simón López-Marino, Moisés Espíndola-Rodríguez, Markus Neuschitzer, Diouldé Sylla, Andrew Fairbrother, Victor Izquierdo-Roca, Alejandro Pérez-Rodríguez, and Edgardo Saucedo*, "Impact of Sn-(S,Se) secondary phases in $Cu_2ZnSn(S,Se)_4$ solar cells: a chemical route for their selective removal and absorber surface passivation", **ACS Applied Materials & Interface** 6 (2014) 12744 – 12751.*

3. ***Haibing Xie****, *Simon López-Marino, Tetiana Olar, Yudania Sánchez, Markus Neuschitzer, Florian Oliva, Sergio Giraldo, Victor Izquierdo-Roca, Iver Lauermann, Alejandro Pérez-Rodríguez, Edgardo Saucedo, "Impact of Na dynamics at the $Cu_2ZnSn(S,Se)_4$/CdS interface during post low temperature treatment of absorbers", **ACS Applied Materials & Interfaces** 8 (2016) 5017-5024.*

4. *Yudania Sánchez*, Moisés Espíndola-Rodríguez, **Haibing Xie**, Simón López-Marino, Markus Neuschitzer, Sergio Giraldo, Mirjana Dimitrievska, Marcel Placidi, Victor Izquierdo-Roca, Fabián Andrés Pulgarín-Agudelo, Osvaldo Vigil-Galán and Edgardo Saucedo, "Ultra-thin CdS for highly performing chalcogenides thin film based solar cells", **Solar Energy Materials and Solar Cells** (2016) Doi:10.1016/j.solmat.2015.12.037.*

Asimismo, la tesis también incluye trabajos que no han sido publicados todavía pero los cuales están siendo preparados para su futura publicación en revistas científicas. Éstos, junto con los artículos enumerados arriba, resumen el trabajo realizado durante el doctorado y completan el contenido de esta tesis.

La tesis está estructurada en seis capítulos que se detallan a continuación:

En el primer capítulo se describen los aspectos fundamentales de la tecnología fotovoltaica y se establecen los objetivos de la tesis. El capítulo se divide en tres subsecciones. En primer lugar se realiza una introducción general sobre las células solares fotovoltaicas en la cual se exponen la motivación y el desarrollo histórico de esta tecnología así como los fundamentos físicos de su

funcionamiento y las medidas y análisis básicos necesarios para su caracterización. En la segunda sección se introducen las células solares de Kesterita, las cuales son el objeto de estudio principal de esta tesis. Se examinan la motivación y el desarrollo histórico de este material y, seguidamente, se profundiza en la configuración de las células solares basadas en el mismo. Se analizan las distintas capas que componen estas células solares haciendo hincapié en la capa absorbedora de Kesterita. Además, se realiza una comparación entre las células solares de los compuestos CZTS, CZTSSe y CZTSe poniendo especial énfasis en las de CZTSSe ya que presentan un band gap óptimo próximo al máximo de la curva del límite de Shockley-Queisser. Esta característica ha motivado la elección de las células solares de CZTSSe para su análisis en profundidad a lo largo de esta tesis. Posteriormente, se investigan los distintos métodos de fabricación del material resaltando la sulfo-selenización de un solo paso, el método principal empleado en esta tesis. Para una mejor comprensión de las células solares de Kesterita, se analizan sus similitudes y peculiaridades con respecto a las células solares de CIGS. Finalmente, el capítulo concluye con la presentación los objetivos de la tesis.

El segundo capítulo detalla la parte experimental de la tesis y la metodología empleada. En este capítulo se recoge el proceso completo de fabricación de las células solares de CZTSSe llevado a cabo en IREC así como los métodos empleados para su caracterización.

El tercer capítulo investiga cómo preparar absorbedores CZTSSe de alta calidad a través del ajuste preciso de los tratamientos térmicos y el equilibrio termodinámico. Este capítulo se compone de dos subsecciones. En la primera se explica la preparación de los absorbedores CZTSSe con una ratio S/(S+Se) óptima, alta calidad cristalina y un mínimo de fases secundarias, en particular de la fase Zn(S, Se) en las interfaces. Esto se consigue modificando la proporción S/(S+Se) añadida al sistema, la presión, el perfil térmico del tratamiento térmico y controlando minuciosamente la pérdida de material. Asimismo, se estudia el impacto que tiene la ratio S/(S+Se) de los absorbedores en las propiedades optoelectrónicas de los dispositivos fotovoltaicos. Este trabajo está recogido en el artículo titulado "Formation and impact of secondary phases in Cu-poor Zn-rich $Cu_2ZnSn(S_{1-y}Se_y)_4$ ($0 \leq y \leq 1$) based solar cells" que puede encontrarse en el apéndice de esta tesis. Finalmente, se presenta un análisis del equilibrio termodinámico durante el proceso de sulfo-selenización de un solo paso. La ecuación de equilibrio termodinámico es formulada en base a una serie de suposiciones que se fundamentan en la hipótesis de que la ratio final S/(S+Se) de las películas delgadas es el resultado del equilibrio químico entre el compuesto CZTSSe y el vapor de S_2/Se_2 durante el proceso de crecimiento cristalino. Se presentan ecuaciones basadas en la ratio S/(S+Se) añadida, la temperatura de recocido y el ratio S/(S+Se) final en la película de CZTSSe para distintos casos de estudio. Estas ecuaciones permiten esclarecer el impacto directo e indirecto de los dos primeros parámetros en la ratio S/(S+Se) final del absorbedor tanto en sistemas ideales estancos como en sistemas reales parcialmente abiertos.

El cuarto capítulo se centra en uno de los mayores desafíos de las células solares de kesterita: las fases secundarias. Esto es así por varias razones. Primeramente, la presencia de fases secundarias es prácticamente inevitable debido a que la región de una sola fase del diagrama de fases de la Kesterita es muy pequeña. Además, para la obtención de dispositivos de alta eficiencia se utilizan composiciones no estequiométricas y condiciones fuera del equilibrio en los tratamientos térmicos. En segundo lugar, la identificación de las fases secundarias puede resultar complicada a priori ya que el ZnS y Cu_2SnSe_3 tienen estructuras cristalinas muy similares a las de la fase Kesterita y, por tanto, son difíciles de distinguir utilizando las técnicas

habituales de difracción de rayos X (XRD). Se revisan métodos de detección alternativos de los cuales se destaca la espectrometría Raman pre-resonante. En tercer lugar, la distribución espacial de las fases secundarias es muy importante para entender y optimizar las propiedades de los dispositivos fotovoltaicos. Si las fases secundarias se encuentran en la interfaz Mo/CZTSSe, una capa barrera encima del Mo o la búsqueda de nuevos materiales para el contacto trasero podrían ser una posible solución. Si las fases secundarias están localizadas en el interior del volumen del absorbedor, probablemente la única solución sea la optimización del tratamiento térmico y/o de la preparación de los precursores. Sin embargo, si las fases secundarias se hallan en la superficie del absorbedor CZTSSe, el problema se simplifica ya que estas fases pueden ser eliminadas mediante ataques químicos selectivos. Los ataques químicos son ampliamente utilizados para la eliminación de las fases secundarias $Cu_x(S,Se)$, Zn(S,Se) y fases relacionadas de Cu-Sn-Se pero no para las fases Sn(S,Se). Para abordar esta cuestión, se ha desarrollado un innovador ataque químico con $(NH_4)_2S$ para eliminar de manera selectiva y eficiente las fases secundarias de Sn(S,Se). Además, también se ha llevado a cabo una investigación sobre el origen de estas fases secundarias y su impacto sobre las células solares de CZTSSe. Esta investigación ha permitido identificar un efecto de pasivación sobre la superficie de los absorbedores. Se propone un mecanismo de pasivación del ataque con $(NH_4)_2S$ para ilustrar este fenómeno. En el artículo "Impact of Sn-(S,Se) secondary phases in $Cu_2ZnSn(S,Se)_4$ solar cells: a chemical route for their selective removal and absorber surface passivation" se detallan todos estos hallazgos.

El quinto capítulo investiga la interfaz CZTSSe/CdS en la cual se forma la unión p-n y la cual es crítica para el buen funcionamiento de las células solares de CZTSSe. En primer lugar, se indaga sobre la dinámica del Na en la interfaz CZTSSe/CdS durante el tratamiento post-recocido a baja temperatura (PLTT, por su siglas en inglés) de los absorbedores de CZTSSe. Este estudio viene motivado por el hecho de que se varios grupos de investigación han demostrado que el proceso PLTT es beneficioso para las células solares de Kesterita de alta eficiencia. Sin embargo, los mecanismos de difusión y distribución del Na durante el tratamiento PLTT no han sido estudiados a pesar de que está ampliamente aceptado que el Na es un elemento crucial tanto en el campo de las calcopiritas como de las Kesteritas. Las grandes variaciones observadas en las propiedades de los dispositivos fotovoltaicos de CZTSSe tras el proceso PLTT se pueden correlacionar con diferentes concentraciones de Na en la región activa de la de la unión p-n en la interfaz CZTSSe/CdS. Se desarrolla un innovador modelo de dinámica de Na basado en dos flujos de Na distintos durante el proceso PLTT: la difusión desde el sustrato de vidrio de sílice (SLG, por sus siglas en inglés) hacia los absorbedores y la pérdida de Na desde la superficie del absorbedor hacia la atmósfera. En función de la magnitud de estos dos flujos a una temperatura dada, designados como $V_{Na\ diffusion}$ y $V_{Na\ loss}$, se obtienen diferentes perfiles de profundidad de Na. Este modelo es validado por cálculos teóricos y, también, por experimentos específicamente diseñados para ello. Los resultados muestran que un contenido apropiado de dopaje con Na, especialmente en la región activa de la interfaz CZTSSe/CdS de las células solares, puede ser crítico para el funcionamiento de los dispositivos fotovoltaicos y que el proceso PLTT puede ser una buena manera de optimizar los perfiles de profundidad del Na. Este trabajo está recogido en el artículo "Impact of Na dynamics at the $Cu_2ZnSn(S,Se)_4$/CdS interface during post low temperature treatment of absorbers". En segundo lugar, se investiga el CdS dopado con Cu para mejorar la calidad del depósito de CdS y obtener una interfaz de alta calidad. Los resultados revelan que el espesor del CdS puede ser reducido considerablemente cuando se introduce un dopaje apropiado de Cu y que, a su vez, se mantiene un comportamiento de los dispositivos fotovoltaicos tanto en CIGS como en CZTSe comparable al proceso estándar.

Este resultado se puede relacionar con el buen recubrimiento de la película delgada de CdS, homogénea y sin agujeros (pin-holes) y puede abrir nuevas posibilidades para paliar los problemas medioambientales asociados a la capa búfer de CdS tan ampliamente utilizada. El artículo "Ultra-thin CdS for highly performing chalcogenides thin film based solar cells" resume este trabajo. En tercer lugar, se ha reportado en numerosas ocasiones que la recombinación en las interfaces es uno de las causas potenciales del gran déficit de V_{oc} que presentan las células solares de Kesterita, en especial de las células de CZTSSe. Para atenuar este problema, se desarrolló un innovador tratamiento químico húmedo usando cloruros del grupo III (III=Al, Ga) y tioacetamida (CH_3CSNH_2). Usando este tratamiento se obtienen dispositivos en los que se reduce el déficit de V_{oc} y se aumenta la eficiencia debido a una mejora en el V_{oc} y el FF relacionadas con una recombinación en las interfaces reducida, un aumento del band gap en la superficie y la disminución de los caminos de deriva de corriente (shunt paths). Se obtuvo una célula solar récord de CZTSSe con una eficiencia del 9.1% y un FF por encima del 69% tras la optimización de un tratamiento químico con $AlCl_3$. Este trabajo se encuentra en proceso de preparación para su publicación.

El sexto capítulo es el resumen de la tesis y analiza las perspectivas de futuro de las células solares de Kesterita.

Finalmente, además de los cuatro artículos mencionados al inicio de este prefacio, Haibing Xie, el autor de esta tesis, ha participado como co-autor en los siguientes artículos relacionados con el trabajo realizado en esta tesis.

1. *M. Dimitrievska, **H. Xie**, A. Fairbrother, X. Fontané, G. Gurieva, E. Saucedo, A. Pérez-Rodríguez, S. Schorr, V. Izquierdo-Roca, "Multiwavelength excitation Raman scattering of $Cu_2ZnSn(S_xSe_{1-x})_4$ $(0 \leq x \leq 1)$ polycrystalline thin films: vibrational properties of sulfoselenide solid solutions", **Applied Physics Letters** 105 (2014) 031913.*

2. *J. López-García, **H. Xie**, V. Izquierdo-Roca, D. Sylla, X. Fontané, M. Blanes-Guardia, F. Ramos, M. Espindola-Rodriguez, S. López-Marino, E. Saucedo, A. Pérez-Rodriguez, "Synthesis of $CuIn(S, Se)_2$ quaternary alloys by screen printing and selenization-sulfurization sequential steps: Development of composition graded absorbers for low cost photovoltaic devices", **Materials Chemistry and Physics** 160 (2015) 237–243.*

3. *M. Dimitrievska, **H. Xie**, A. J. Jackson, X. Fontane, M. Espindola-Rodriguez, E. Saucedo, A. Perez-Rodriguez, A. Walsh, V. Izquierdo-Roca, "Resonant raman scattering of ZnS_xSe_{1-x} solid solutions: the role of S and Se electronic states", **Physical Chemistry Chemical Physics** 18 (2016) 7632-7640.*

4. *M. Dimitrievska, **H. Xie**, G. Gurieva, X. Fontane, A. Fairbrother, R. Gunder, E. Saucedo, A. Perez-Rodriguez, S. Schorr, V. Izquierdo-Roca, "Vibrational and structural properties of $Cu_2ZnSn(S_xSe_{1-x})_4$ $(0 \leq x \leq 1)$ solid solutions", **IEEE 40th Photovoltaic Specialist Conference (PVSC)** (2014) 0033-0036.*

5. *M. Dimitrievska, G. Gurieva, **H. Xie**, A. Carrete, A. Cabot, E. Saucedo, A. Pérez-Rodríguez, S. Schorr, V. Izquierdo-Roca, "Raman scattering quantitative analysis of the anion chemical composition in kesterite $Cu_2ZnSn(S_xSe_{1-x})_4$ solid solutions", **Journal of Alloys and Compounds** 628 (2015) 464–470.*

6. *T. Olar, I. Lauermann, **H. Xie**, M. Neuschitzer, E. Saucedo, W. Calvet, A. Steigert, B. Ümsür, B. Chacko, V. Parvan, M. Gorgoi, B. Senkovskiy, M. Ch Lux-Steiner, "Assessment of chemical and electronic Surface properties of the $Cu_2ZnSn(S,Se)_4$ after different etching procedures by synchrotron-based spectroscopies", **Energy Procedia** 84 (2016) 8-16.*

7. *M. Neuschitzer, Y. Sanchez, S. López-Marino, **H. Xie**, A. Fairbrother, M. Placidi, V. Izquierdo-Roca, A. Perez-Rodriguez, E. Saucedo, "Optimization of CdS Buffer Layer for High Performance CZTSe Solar Cells and the Effects of Light Soaking: Elimination of Cross Over and Red Kink", **Progress in Photovoltaics: Research and Applications** 23(2015)1660 –1667.*

8. *S. Lugo, Y. Sánchez, M. Neuschitzer, **H. Xie**, C. Insignares-Cuello, V. Izquierdo-Roca, Y. Peña, E. Saucedo, "Chemical bath deposition route for the synthesis of ultra-thin $CuIn(S,Se)_2$ based solar cells", **Thin Solid Films** 582 (2015) 74–78.*

9. *M. Dimitrievska, A. Fairbrother, R. Gunder, G. Gurieva, **H. Xie**, E. Saucedo, A. Perez-Rodriguez, V. Izquierdo-Roca, S. Schorr, "Role of S and Se atoms on the microstructural properties of kesterite $Cu_2ZnSn(S_xSe_{1-x})_4$ thin film solar cells", **Physical Chemistry Chemical Physics** 18 (2016)8692-8700.*

10. *S. Lopez-Marino, Y. Sanchez, M. Espindola-Rodriguez, X. Alcobe, **H. Xie**, M. Neuschitzer, I. Becerril, S. Giraldo, M. Dimitrievska, M. Placidi, L. Fourdrinier, V. Izquierdo-Roca, A. Perez-Rodriguez, E. Saucedo, "Alkali doping strategies for flexible and light-weight $Cu_2ZnSnSe_4$ solar cells", **Journal of Materials Chemistry A** 4(2016)1895-1907.*

11. *S. Giraldo, M. Neuschitzer, T. Thersleff, S. López-Marino, Y. Sánchez, **H. Xie**, M. Colina, M. Placidi, P. Pistor, V. Izquierdo-Roca, K. Leifer, A. Pérez-Rodríguez, E. Saucedo, "Large efficiency improvement in $Cu_2ZnSnSe_4$ solar cells by introducing a superficial Ge nanolayer", **Advanced Energy Materials** 5(2015)1501070.*

12. *S. Lopez-Marino, M. Espíndola-Rodríguez, Y. Sánchez, X. Alcobé, F. Oliva, **H. Xie**, M. Neuschitzer, S. Giraldo, M. Placidi, R. Caballero, V. Izquierdo-Roca, A. Pérez-Rodríguez , E. Saucedo, "The importance of back contact modification in $Cu_2ZnSnSe_4$ solar cells: the role of a thin MoO_2 layer", **Nano Energy** (2016). Doi:10.1016/j.nanoen.2016.06.034.*

13. *M. Espindola-Rodriguez, Y. Sanchez, S. López-Marino, D. Sylla, M. Placidi, M. Neuschitzer, **H. Xie**, V. Izquierdo-Roca, O. Vigil-Galán, E. Saucedo, "Selenization of Cu_2ZnSnS_4 thin films obtained by pneumatic spray pyrolysis", **Journal of Analytical and Applied Pyrolysis** (2016) Doi:10.1016/j.jaap.2016.04.008.*

14. *M. Neuschitzer, Y. Sánchez , T. Olar, T. Thersleff, S. López-Marino, F. Oliva, M. Espindola-Rodriguez, **H. Xie,** M. Placidi, V. Izquierdo-Roca, I. Lauermann, K. Leifer, A. Perez-Rodriguez, E. Saucedo, "The complex surface chemistry of kesterites: Cu/Zn re-ordering after low temperature post deposition annealing and its role in high performance devices", **Chemistry of Materials** 27(2015)5279-5287.*

15. *R. Kondrotas, R. Juškėnas, A. Naujokaitis, A. Selskis, R. Giraitis, Z. Mockus, S. Kanapeckaitė, G. Niaura, **H. Xie**, Y. Sánchez, E. Saucedo, "Characterization of*

$Cu_2ZnSnSe_4$ solar cells prepared from electrochemically co-deposited Cu–Zn–Sn alloy", ***Solar Energy Materials & Solar Cells*** *132 (2015) 21–28.*

16. *A.U. Sheleg, V.G. Hurtavy, A.V. Mudryi, V.D. Zhivulko, M. Ya Valakh, V.A. Yuhimchuk, I.S. Babichuk,* ***H. Xie****, E. Saucedo, "Crystallographic and optical characteristics of thin films of $Cu_2ZnSn(S_xSe_{1-x})_4$ solid solutions",* ***Journal of Applied Spectroscopy*** *81(2014)776 –781.*

Contribución del autor a las publicaciones en la tesis

El autor de la tesis, Haibing Xie, es responsable del diseño y la realización de los experimentos, la coordinación de la caracterización y la interpretación de los resultados experimentales presentados en la misma. Ha participado directamente en el desarrollo de un proceso de sulfo-selenización de un solo paso para la fabricación de células solares de CZTSSe de alta eficiencia. Esto incluye el depósito por pulverización catódica de precursores metálicos, la realización de tratamientos térmicos para sintetizar los absorbedores CZTSSe, ataques químicos para eliminar fases secundarias, los tratamientos post-recocido de los absorbedores y dispositivos para optimizar la distribución espacial del Na, la ingeniería de la superficie a través de tratamientos químicos y el depósito por pulverización catódica de capas ventana i-ZnO/ITO por pulverización catódica. Además, ha coordinado el proceso CBD para el depósito de la capa búfer de CdS para la fabricación de dispositivos. Finalmente, el autor ha llevado a cabo las medidas por XRD, SEM, EQE e I-V y coordinado el resto de caracterizaciones pertinentes para entender el proceso e interpretar los resultados experimentales.

Chapter 3:

Haibing Xie*, Mirjana Dimitrievska, Xavier Fontané, Yudania Sánchez, Simon López-Marino, Victor Izquierdo-Roca, Verónica Bermúdez, Alejandro Pérez-Rodríguez, Edgardo Saucedo, "Formation and impact of secondary phases in Cu-poor Zn-rich $Cu_2ZnSn(S_{1-y}Se_y)_4$ ($0 \leq y \leq 1$) based solar cells",* ***Solar Energy Materials & Solar Cells*** *140 (2015) 289 – 298.*

Factor de Impacto (IF): 4.7

1er cuartil en las áreas: Electrónica, Materiales Ópticos y Magnéticos; Energías Renovables.

Este artículo trata sobre la optimización de los tratamientos térmicos para la obtención de absorbedores CZTSSe de alta calidad con una ratio S/(S+Se) apropiada y una menor presencia de fases secundarias en las interfaces. Asimismo, se investiga el impacto de la ratio S/(S+Se) de los absorbedores en la propiedades optoelectrónicas de los dispositivos fotovoltaicos. En este trabajo, Haibing Xie diseñó y llevó a cabo todos los experimentos para la síntesis de los absorbedores de CZTSSe y coordinó la fabricación de células solares de CZTSSe. También realizó las medidas de XRD, EQE e I-V y coordinó el resto de la caracterización. Además, fue responsable de la interpretación de los resultados experimentales y de la redacción de manuscrito.

Chapter 4:

Haibing Xie, *Yudania Sánchez, Simón López-Marino, Moisés Espíndola-Rodríguez, Markus Neuschitzer, Diouldé Sylla, Andrew Fairbrother, Victor Izquierdo-Roca, Alejandro Pérez-Rodríguez, and Edgardo Saucedo*[*]*. "Impact of Sn-(S,Se) secondary phases in* $Cu_2ZnSn(S,Se)_4$ *solar cells: a chemical route for their selective removal and absorber surface passivation",* ***ACS Applied Materials & Interface*** *6 (2014) 12744 – 12751.*

Factor de Impacto: 7.1

1[er] cuartil en las áreas: Nanociencia y Nanotecnología; Ciencia de Materiales; Multidisciplinar.

Este articulo trata, principalmente, de la eliminación de las fases secundarias de Sn(S,Se) de la superficie de los absorbedores de CZTSSe utilizando una disolución amarilla al 22% w/w de $(NH_4)_2S$. Además, se investiga el efecto de este ataque químico en las propiedades de los dispositivos fotovoltaicos y se propone un mecanismo de pasivación. En este trabajo, Haibing Xie diseñó y llevó a cabo todos los experimentos salvo el proceso CBD. También fue responsable de la interpretación de los resultados experimentales y preparó el primer borrador del manuscrito. Además, realizó toda la caracterización de este trabajo.

Chapter 5:

1. ***Haibing Xie****[*], *Simon López-Marino, Tetiana Olar, Yudania Sánchez, Markus Neuschitzer, Florian Oliva, Sergio Giraldo, Victor Izquierdo-Roca, Iver Lauermann, Alejandro Pérez-Rodríguez, Edgardo Saucedo,"Impact of Na dynamics at the* $Cu_2ZnSn(S,Se)_4$*/CdS interface during post low temperature treatment of absorbers",* ***ACS Applied Materials & Interfaces*** *8 (2016) 5017-5024.*

Factor de impacto: 7.1

1er cuartil en la áreas: Nanociencia y Nanotecnología; Ciencia de Materiales; Multidisciplinar.

En este artículo, se estudia el impacto de la dinámica del Na durante el tratamiento post-recocido a baja temperatura (PLTT) de los absorbedores de CZTSSe. Grandes variaciones en el comportamiento de los dispositivos se pueden relacionar con la distribución espacial de Na en la interfaz CZTSSe/CdS. Se propone un innovador modelo para explicar este comportamiento el cual es apoyado por cálculos teóricos y experimentos diseñados para tal fin. Tras la optimización del proceso PLTT, se consiguen dispositivos fotovoltaicos de CZTSSe con eficiencias de 7.1% y 8.3%. En este trabajo, Haibing Xie diseñó y llevó a cabo todos los experimentos excepto el proceso CBD. También realizó las medidas de XRD, SEM, XRF, EQE e I-V y coordinó la caracterización por XPS, Raman, SIMS y C-V. Además, fue responsable de la interpretación de los resultados experimentales y la redacción del manuscrito.

2. *Yudania Sánchez*, Moisés Espíndola-Rodríguez,* ***Haibing Xie****, Simón López-Marino, Markus Neuschitzer, Sergio Giraldo, Mirjana Dimitrievska, Marcel Placidi, Victor Izquierdo-Roca, Fabián Andrés Pulgarín-Agudelo, Osvaldo Vigil-*

*Galán and Edgardo Saucedo, "Ultra-thin CdS for highly performing chalcogenides thin film based solar cells", **Solar Energy Materials and Solar Cells** (2016) Doi:10.1016/j.solmat.2015.12.037.*

Factor de impacto: 4.7

1er cuartil en las áreas: Electrónica, Materiales Ópticos y Magnéticos; Energías Renovables.

En este artículo, se investigó el dopaje con Cu del CdS. Los resultados muestran que el espesor del CdS se puede reducir sustancialmente cuando se introduce un dopaje con Cu adecuado manteniendo un comportamiento comparable de las células solares tanto de CIGS como de CZTSe. En este trabajo, Haibing Xie contribuyó a la preparación de los absorbedores, la fabricación y caracterización de las células solares así como a la preparación de manuscrito y las explicaciones de los resultados experimentales.

Ninguno de estos artículos ha sido utilizado por otros co-autores para sus tesis doctorales.

Barcelona, 9th August, 2016

Prof. Alejandro Pérez Rodríguez Dr. Edgardo Saucedo

Chapter 1

Introduction and objectives

1.1 Solar cells

1.1.1 Fossil fuel: the sword of Damocles

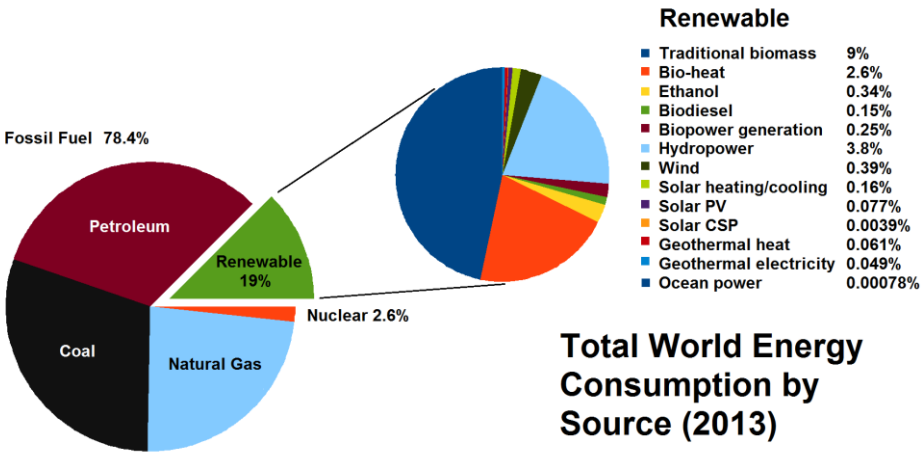

Figure 1.1. Total world energy consumption by source in 2013. Data is from Renewables 2014 Global Status Report of REN21.

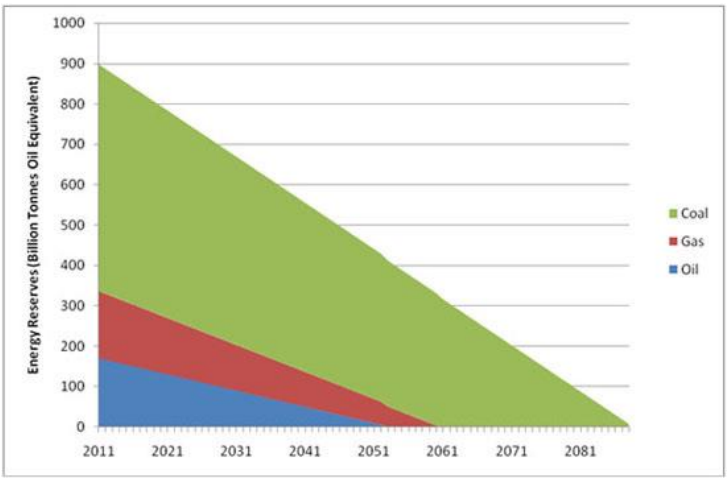

Figure 1.2. Predicted energy reserves as a function of year. All fossil fuel reserve and consumption data is from CIA World Factbook.

Nowadays, fossil fuels including oil, natural gas and coal account for the major share of the world energy consumption. As shown in Figure 1.1, in 2013, 78.4% of the world energy cosumption is from fossil fuels. As it is well known, fossil fuels are considered as non-renewable resources, because they need millions of years under extreme conditions underground to form. As the world energy consumption continues every year, it is just a matter of time that one day the fossil fuels will run out. The predicted ending time of fossil fuels is the year of 2088,

about 70 years away from the present time, as shown in Figure 1.2. This ending point may not be necessarily true due to the change of consumption rate and possible new discovered reserves. Nevertheless, it indeed reminds us the Damocles sword of fossil fuel is hanging above human beings´ heads. In addition, the use of fossil fuels raises serious environmental concerns, such as air pollution by the emission of nitrogen oxides, sulfur dioxide, volatile organic compounds and heavy metals, and global warming due to the emission of carbon oxide. Therefore, concerning the energy time-bomb and environmental protection for the sake of our descendants, renewable energy sources need to be explored urgently.

Solar energy is one of the promissing renewable energy sources. It is clean, easily accessible, and inexhaustible. It is estimated that the power from the sun hits the earth in a single hour is more than humanity uses in an entire year. Solar energy can be converted into heat or electricity. The former is called solar heating while the latter is solar power, either directly using photovoltaics (PV), or indirectly using concentrated solar power (CSP). If the solar energy conversion into electricity is 20% efficient (as it has been in lab tests), we'd only need to cover a land area about the size of Spain with solar panels (PV) to power the entire earth renewably in 2030, as shown in Figure 1.3. Howerver, solar energy only provided 0.24% of the energy consumed in the world in 2013, and solar PV accounts for even samller share of 0.077% (see Figure 1.1). Thus, much work is needed to promote the deployment of solar PV. As the Saudi Oil Minister Sheik Ahmed Zaki Yamani said in the 1970s, "The Stone Age didn't end for lack of stone, and the oil age will end long before the world runs out of oil." We hope the solar PV will be the Terminator soon.

Figure 1.3. Total surface area required to fuel the world with solar panels. Data is from US Energy Information Administration (EIA). In 2030, the projected surface area required to fuel the world with solar panels is about the size of Spain.

1.1.2 Development and commercialization

Solar PV, also refered to as solar cells, has experienced three generations since the first practical silicon solar cells created by Bell Labs in 1954. The first generations include the monocrystalline and polycrystalline silicon solar cells, which are the dominant commerciallized PV technologies in the market currently. Second generation solar cells are thin film solar cells, which are mainly composed of amorphous silicon, CdTe and $Cu(In,Ga)Se_2$ (CIGS) solar cells and are also comerciallized in utility-scale photovoltaic power stations, building integrated

photovoltaics (BIPV) or in small stand-alone power system like portable electronic devices, etc. The third generation of solar cells encompass multiple emerging solar cells that aim at ultra-high efficiency (e.g., breaking the Shockley-Queisser limit) and low cost [1]. The Shockley-Queisser (SQ) limit will be described in section 1.1.5 in detail. These emerging solar cells include: tandem solar cells (multi-junction), solar cells based on photon upconversion and downconversion, dye-sensitized solar cells (DSSC, Grätzel cell), organic solar cells, perovskite solar cells, and quantum dot solar cells, etc. Most of them have not yet been commercially applied and are still in the research or development stage. Figure 1.4 shows the images of the representative solar cells in the three generations.

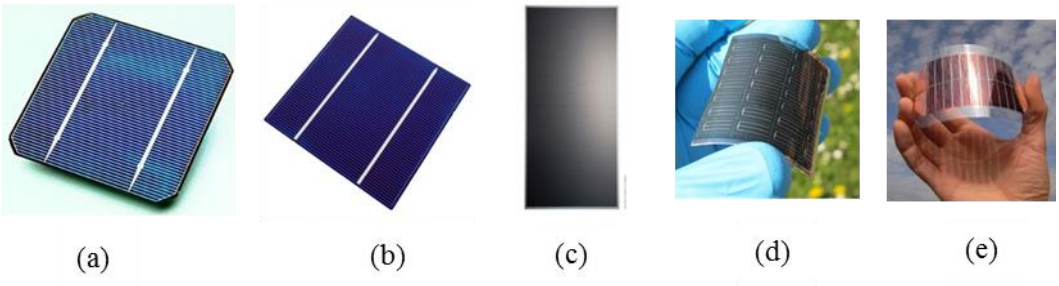

Figure 1.4. Monocrystalline (a), polycrystalline (b), CdTe thin film (c), CIGS flexible thin film (d) and organic semi-trasparent solar cells (e). (a)(b) are from the webpage of Aliexpress, (c) is from First Solar, (d) is from EMPA, and (e) is from the webpage of SINO VOLTAICS.

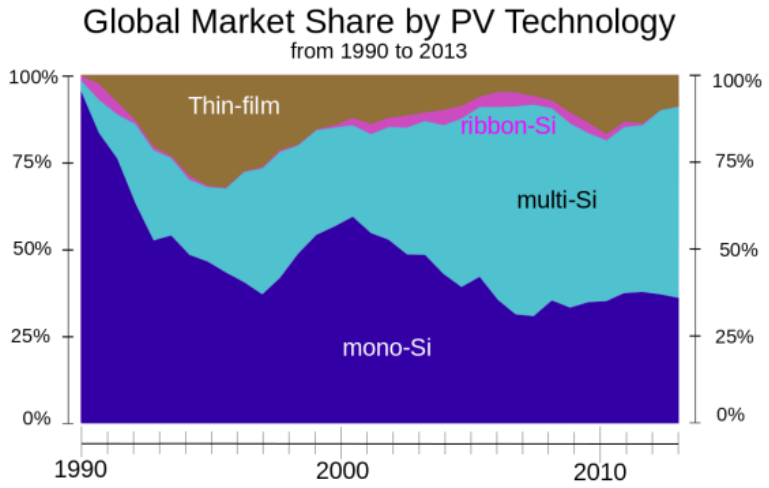

Figure 1.5. Global market share by PV technology as a function of year. The image is from PHOTOVOLTAICS REPORT 2014, Fraunhofer ISE.

The first generation silicon solar cells (mono-Si and multi-Si) have hold the vast majority of maket share (above 70%) for a long time, while the second generation thin film solar cells are still in an absolute inferior position, amounting to around 10% maket share in 2013, as shown in Figure 1.5.

Regarding companies, chinese companies are dominating the PV market by silicon solar cells. Representative companies in China include Trina Solar, JinkoSolar, JA Solar, Yingli Green, SFCE and ReneSola, which are among the top 10 solar module manufacturers in 2015 based on actual module shipments, as shown in Table 1.1. First Solar from USA is leading the production

of CdTe solar cells while Japanese company Solar Frontier is the main CIGS solar cells manufacturer.

Table 1.1. Top 10 solar module manufacturers in 2015 based on actual module shipments.The data is from[2].

	Trina Solar	Canadian Solar	Jinko Solar	JA Solar	Hanwha Q CELLS	First Solar	Yingli Green	SFCE	ReneSola	SunPower Corp
Technology	Silicon	Silicon	Silicon	Silicon	Silicon	CdTe	Silicon	Silicon	Silicon	Silicon
Country	China	Canada	China	China	Korea	USA	China	China	China	USA
Rank	1	2	3	4	5	6	7	8	9	10

1.1.3 P-n junction and photovoltaic effect

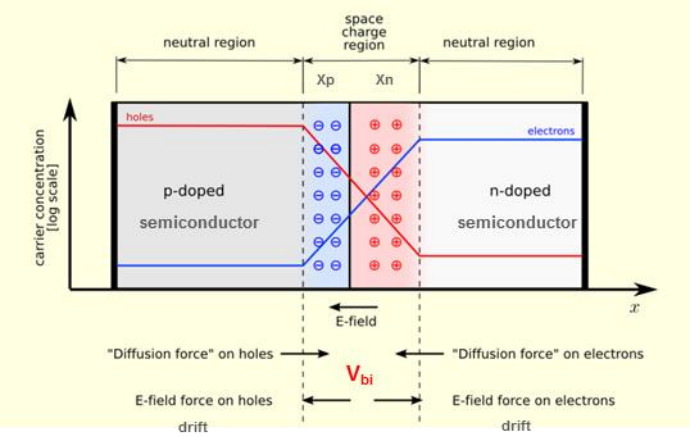

Figure 1.6. Schematic of p-n junction and formation of built-in electric field through the drift-diffusion process. The image is modified from the term of "p-n junction" in wikipedia.

The fundamental of solar cells is a semiconductor p-n junction and its built-in electric field. The p-n junction is formed when joining a p-type semiconductor with a n-type semiconductor. In the boundary region, the marjority carrier holes of p-type semiconductor will diffuse into the n-type semiconductor through the interface due to the concentration gradient, leaving behind negative charges and being recombined with electrons. Likewise, the majority carrier electrons of n-type semiconductor will diffuse into the p-type semiconductor though the interface, leaving behind positive charges and being recombined with holes. The regions near the p–n interface lose their neutrality and most of their mobile carriers, forming the space charge region (SCR) or depletion region. Thus, in the boundary region of these two types of semiconductor, an electric filed is established, with a direction from the n-type one to the p-type one. This electric field will drift the holes back to p-type region and electrons back to n-type region, counteracting with the diffusion process. When this drift-diffusion process reaches an equilibrium, the electric field in the p-n junction is called built-in electric field and the corresponding voltage is denoted as built-in voltage (V_{bi}). Figure 1.6 shows the schematic representation of p-n junction and formation of built-in voltage through drift-diffusion process. In the SCR, with conservation of charge it follows:

$$X_n N_D = X_p N_A \qquad (1.1)$$

$$W=X_n+X_p \qquad (1.2)$$

Where X_n and X_p are the space charge region width W in n-type and p-type semiconductor side, respectively, N_D is the donor concentration in n-type semiconductor and N_A is the acceptor concentration in p-type semiconductor. For CdTe and CIGS thin film solar cells, the absorbers are p-type, $N_D >> N_A$, thus the space charge region width can be approximately expressed as:[3]

$$W \approx X_p \approx \sqrt{\frac{2\varepsilon_p\varepsilon_0}{qN_A}V_{bi}} \qquad (1.3)$$

Where ε_p is the dielectric constant of p-type secmiconductor, ε_0 is the permittivity of vacuum, q is the electron charge.

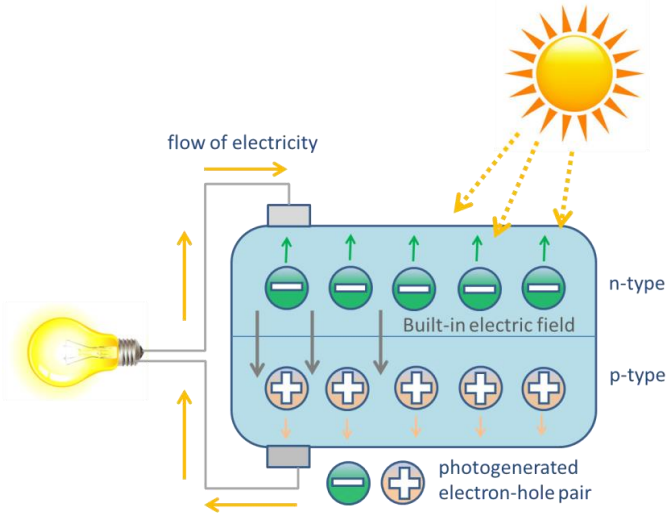

Figure 1.7. Schematic of photovoltaic effect in solar cells.

The solar cells function on the basis of photovoltaic effect of the p-n junction. Figure 1.7 shows the schematic of photovoltaic effect in solar cells. When sunshine is incident on the surface of a p-n junction, photons with energy higher than the E_g of the semiconductor will be asborbed and electrons will be excited from the valence band to the conduction band, leaving behind a hole in the valence band. The electron and hole pair is called a photogenerated electron-hole pair (EHP). The EHPs near the p-n junction region will be separated by the built-in electric field, with electrons to the side of n-type semiconducor and holes to the side of p-type one, leading to a photogenerated electric field in opposition to the built-in electric field. On the other hand, this new electric field will increase the diffusion current, leading to the increase of built-in electric field in turn. Those EHPs far away from the p-n junction could diffuse to the space charge region and be separated. This diffusion distance is named as carrier diffusion length. In equilibrium, a voltage aross the p-n junction is set up under open circuit conditions, which is called "open circuit voltage". This phenomenon is denoted as photovoltaic effect. When in short circuit condition, current will flow in the external circuit. This is how the solar cells work. It should be noted that photovoltaic effect is not necessarily present in p-n junction, it can also be observed in metal-semiconductor junction and photochemical cell. Generally speaking, the photovoltaic effect is the generation of voltage or electric current in a material upon exposure to light.

1.1.4 Configurations of solar cells

Based on the photovoltaic effect of p-n junction, different configurations for the representative solar cells of the three generations are implemented, as shown in Figure 1.8. The p-n junction of crystal silicon solar cells is p-type Si/n^+-type Si homojunction, as shown in Figure 1.8 a. CdTe thin film solar cells are based on the p-type CdTe/n-type CdS heterojunction combined with transparent conductive oxide (TCO) window layer (see Figure 1.8 b). The CIGS thin film solar cells have typical ZnO:Al/ZnO/n-type CdS/p-type CIGS/Mo configurations. Figure 1.8 d shows the typical configuration of planar heterojunction organic solar cells, with p-type P3HT:CNT/n-type PEDOT:PSS as the p-n junction.

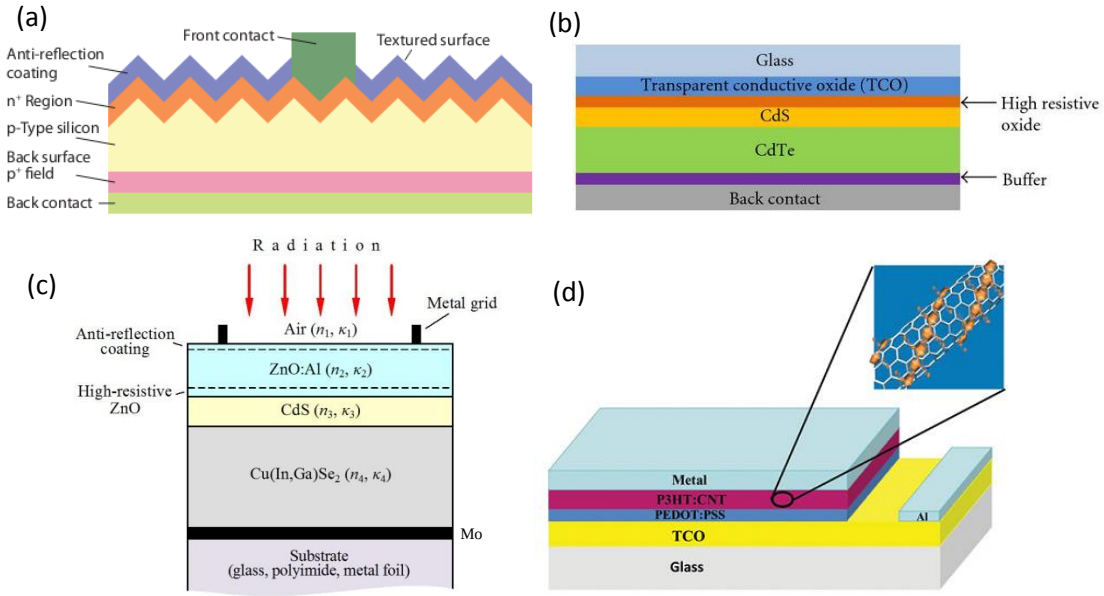

Figure 1.8. The typical configurations of crystal silicon (a), CdTe thin film (b), CIGS thin film (c) and organic (d) solar cells. The images are reproduced from ref [4-7].

1.1.5 Shockley-Queisser limit and band gap

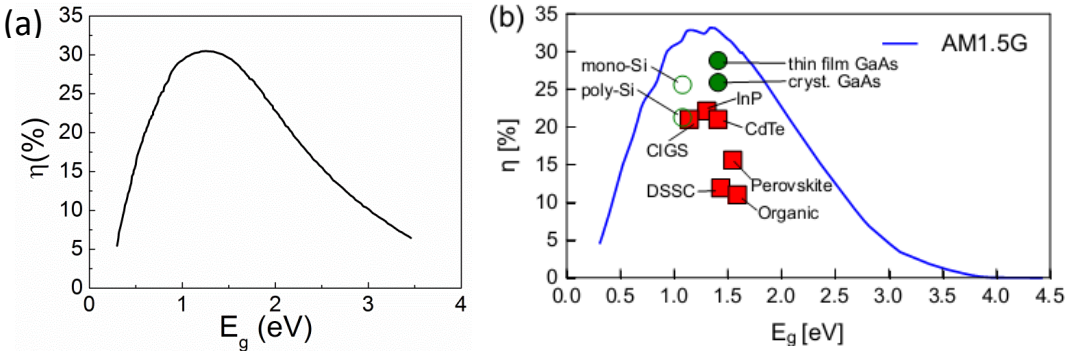

Figure 1.9. Shockley-Queisser (SQ) limit of a single p-n junction solar cell under black body illumination (a) and under AM 1.5G sepectrum with band gap distribution of practical solar cells (b). The images are reproduced from ref [8,9].

The theorectical efficiency for a single p-n junction solar cell was first calculated by Shockley and Queisser in 1961, known as Shockley-Queisser (SQ) limit[8]. The hypothesises and restrictions are as follows:

(1) Black body illumination at 6000 K and solar cell temperature is 300 K.
(2) Step function optical absorptions. Absorbance is zero for $E_{photon} < E_g$ and unity for $E_{photon} \geqslant E_g$.
(3) Only radiative recombination.
(4) One electron–hole pair excited per incoming photon.

Under this circumstances, the maxium efficiency is found to be 30% for E_g =1.1 eV, as shown in Figure 1.9 a. Under AM 1.5G (Reference global spectrum at air mass 1.5), theoretical calculations show two local maxima of 32.85% at 1.15 eV and 33.16% at 1.34 e V (see Figure 1.9 b) [9]. Conversion efficiencies above 30% can be reached for a solar cell band gap between 0.93 and 1.61 eV, where all the three generation of solar cells are located (see Figure 1.9 b). For example, the band gaps of silicon, CdTe, and CIGS solar cells are 1.1, 1.49, 1-1.7 eV (depending on the Ga content), respectively.

To measure the band gap of solar cell absorbers, UV-visible absorption spectra can be applied. This is based on the following equation[10]:

$$(\alpha hv)^n = A(hv - E_g) \quad (1.4)$$

where α is the absorption coefficient, A is a constant, h is Planck's constant, v is photon frequency, and n is transition probability. For direct allowed transition n = 2 while for indirect allowed n = 1/2 [10]. Therefore, this equation can be used to verify the the direct or indirect band gap nature of materials. By ploting $(\alpha hv)^n$ *vs* hv, E_g can be obtained from the horizontal intercept. Figure 1.10 a shows the band gap extraction from UV-visible spectra by Equation 1.1 for direct band gap CZTS absorbers. In addition, E_g can also be obtained by external quantum efficiency measurements of the CZTS devices. The corresponding equation is as follows[11]:

$$EQE = 1 - \exp(-\alpha W) \quad (1.5)$$

Where W is the space charge region width. Combining equation (1.4) and (1.5),we can get:

$$(-hv\ln(1-EQE))^n = AW^n(hv - E_g) \quad (1.6)$$

Likewise, by ploting $(-hv\ln(1-EQE))^n$ *vs* hv, E_g can be achieved from the intercept. Figure 1.10 b shows an example of band gap extraction from the EQE of CZTS solar cells.

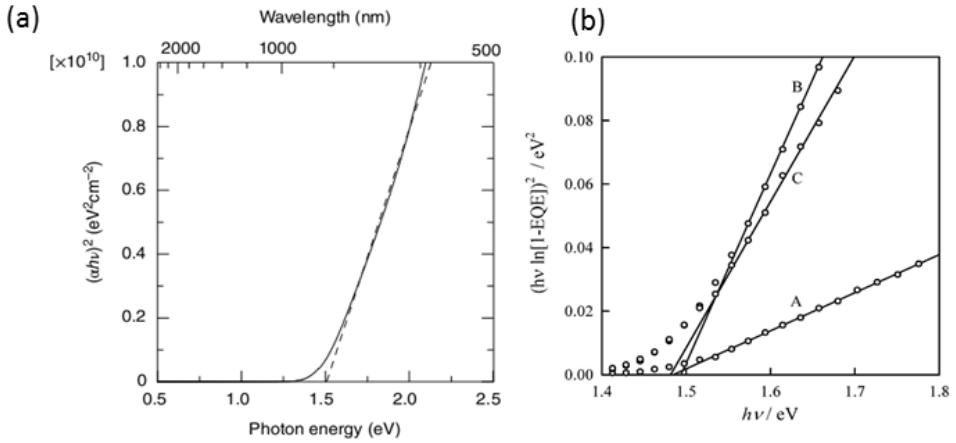

Figure 1.10. Band gap extractration from UV-visible absorption spectra (a) and from EQE (b) for CZTS absorbers. The images are taken from ref [11,12].

1.1.6 Device measurements and analysis

For practical solar cells, the most important measurement is the current density-voltage (J-V) curves and the most important optoelectronic properties are power conversion efficiency (PCE, or Eff.), maximum generated power density (P_m), short circuit current (J_{sc}), open circuit voltage (V_{oc}), and fill factor (FF). Their correlations can be described as the following equations:

$$PCE=\frac{P_m}{P_{light}} \qquad (1.7)$$

$$FF=\frac{P_m}{J_{sc}V_{oc}} \qquad (1.8)$$

Thus, we can get:

$$PCE=\frac{J_{sc}V_{oc}FF}{P_{light}} \qquad (1.9)$$

Where P_{light} is the incident light power density.

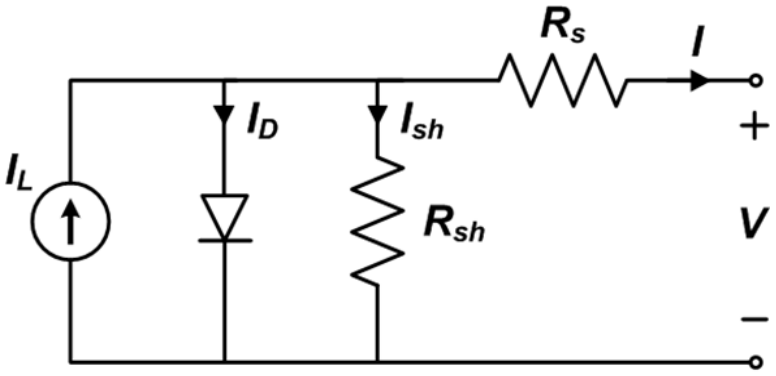

Figure 1.11. The equivalent circuit of single diode model.

A solar cell is essentially a semiconductor diode with p-n junction. The equivalent circuit of the single diode model is shown in Figure 1.11. The governing equation for this equivalent circuit can be described by a general single exponential diode equation:

$$J = J_0 \exp\left(\frac{q}{AkT}(V-R_sJ)\right) + \frac{V}{R_{sh}} - J_L \qquad (1.10)$$

Where J is current density, V is the voltage, J_0 is the reverse saturation current density, J_L is the illuminated current density , A is the ideality factor, R_s is the series resistance, and R_{sh} is the shunt resistance. q and k are constants refered to as electron charge and Boltzmann constant.

Equation 1.10 is the basis of optoelectronic properties analysis. From this equation we can get J_{sc} and V_{oc} when V = 0 and J = 0, respectively. In addition, by further transformations of this equation and assuming certain approximations, other parameters like A, j_0, R_s and R_{sh} can be determined [13]. R_s mainly influences J_{sc} and FF while R_{sh} is related to shunt paths in the p-n junction region that will impact FF considerably. Good devices require low R_s and high R_{sh} and ultimately high FF. Diode factor A is an indicator of the quality of p-n junction in solar cells. Theoretically A has a value between 1 and 2. When A is closer to 1, it means that the p-n junction is limited by neutral region recombination. When A is approaching 2, the junction is limited by space charge region recombination or interface recombination. Finally, A above 2 indicates the junction is incorporating additional tunneling recombination [14]. The ideality factor of a well behaved thin film solar cell is typically in the range $1.3 \leqslant A \leqslant 2$ [13]. J_0 can be further given by:

$$J_0 = J_{00} \exp\left(\frac{\Phi_b}{-AKT}\right) \qquad (1.11)$$

Where J_{00} is the prefactor dependent on the specific recombination mechanism that dominates J_0, and Φ_b is the barrier height or activation energy. Combining Equation 1.10 and 1.11, for $R_{sh} \geqslant V_{oc}/J_L$, the open circuit voltage can be expressed by[13]:

$$V_{oc} = \frac{\Phi_b}{q} - \frac{AkT}{q}\ln\left(\frac{J_{00}}{J_L}\right) \qquad (1.12)$$

This equation is fundamental to the temperature dependent J-V measurements (JV-T). From this equation, by ploting V_{oc} versus T, the barrier height Φ_b can be obtained from the vertical intercept. Φ_b is also called electrical band gap, in contrast with the optical band gap E_g obtained from absorption spectra. This parameter is critical to indentify the location of the dominant recombination. When $\Phi_b < E_g$, the interface recombination is the main recombination mechanism. On the other hand, when $\Phi_b = E_g$, recombinations mainly take place inside the bulk of semiconductors.

In addition, quantum efficiency (QE) measurements are paramount for analyzing photon-electron conversion process, which is the incident photon to converted electron ratio. External quantum efficiency (EQE) counts all the incident photons onto the surface of solar cells, while internal quantum efficiency (IQE) only counts the absorbed photons, getting rid of the reflected phontons from the incident light. The integral of the EQE curve equals the J_{sc}. In fact, the conversion of photons to electrons includes two processes: light absorption and carrier separation and collection. Therefore, this is a combined optical and electrical process. The J_{sc} is directly related to the effective collection length, which is the sum of space charge region width and diffusion length, as shown below:

$$L = W + L_D \qquad (1.13)$$

Where L is the effective collection length, W is the space charge region width and L_D is the diffusion length. L_D is mainly influenced by minority carrier lifetime τ and mobility μ:[15]

$$L_D = \sqrt{\frac{\mu k T \tau}{q}} \qquad (1.14)$$

Where k is the Boltzmann constant and q is the electron charge.

Therefore, high carrier lifetime and mobility are beneficial for EQE and ultimately the J_{sc}.

Figure 1.12 shows the typical QE spectra of a CIGS solar cell with optical loss regions marked.

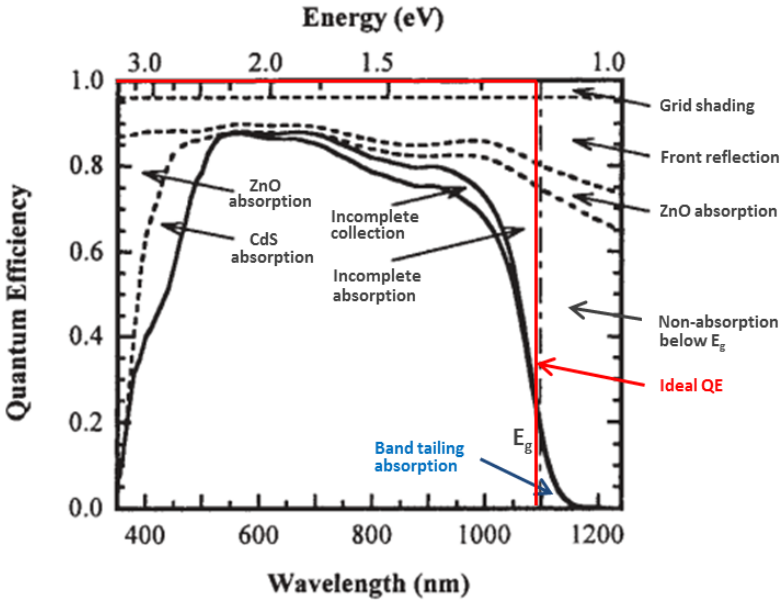

Figure 1.12. Quantum efficiency at 0 V (lower solid curve) and -1 V (upper solid curve) with optical losses region divided by dashed lines for a ZnO/CdS/CIGS/Mo solar cell. The CIGS has a E_g =1.12 eVmarked with a vertical dot-dash line. The ideal QE is ploted with red lines for reference. The optical gain region below E_g is marked with a blue arrow. The image is modified from ref [13].

Grid shading is the only wavelength-independent optical loss. Front reflection accounts for a large part of the optical loss, due to the light reflection from air/ZnO/CdS/CIGS interfaces. This

loss can be minimized by using an arti-reflective coating. ZnO and CdS absorption is mainly in the short wavelength region, due to the approximate 380 nm and 520 nm absorption edge of ZnO and CdS respectively determined from their band gaps (ZnO is 3.3 eV and CdS is 2.42 eV). The absorption ranging from visible to near IR region is ascribed to free carrier absorption[13]. The incomplete absorption in the long wavelength region is related to the band gap gradient in the back of CIGS absorbers, or related to thin asborbers with thickness less than $1/\alpha$, where α is the absorption coefficient. The incomplete collection of photogenerated carriers in the long wavelength region could be correlated to the rear interface (CIGS/Mo) recombination, or correlated to low carrier diffusion length and space charge region width. This incomplete collection is the only electrical loss factor and can be reduced or fully eliminated by applying reverse bias voltage (e.g., -1V). Finally, the fact that the long wavelength light with photon energy below the E_g of CIGS cannot be absorbed is expected. However, there is an interesting optical gain region below E_g, which is due to the band tailing absorption caused by sub-band gap defects or composition/potential fluctuation. This band tailing is typical in kesterite solar cells.

1.2 Kesterite solar cells

1.2.1 Motivation

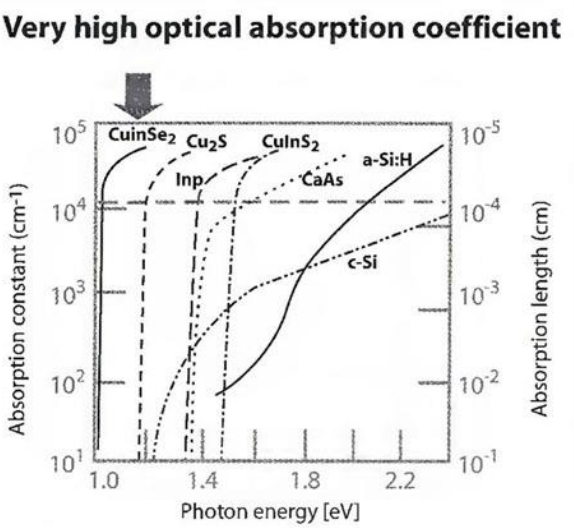

Figure 1.13. Absorption coefficient and absorption length of different absorber materials among the first and the second generation solar cells. The image is taken from the webpage of BEAMS TECHNOLOGY LIMITED.

The first generation silicon solar cells use absorbers with thicknesses more than 100 μm, due to the low absorption coefficient of Si (see Figure 1.13). However, the second generation especially $CuInSe_2$ (CISe) thin film solar cells possess very high absorption coefficient over 10^4 cm^{-1} in the optimal range of 1-1.5 eV, which is more than one order of magnitude higher than that of Si (see Figure 1.13). Therefore, CIGS solar cells can be made into thin films with thicknesses below 2 μm, leading to a substantial reduction of material consumption and potential reduction of production cost. This is the main motivation for the development of thin film solar cells in the early ages. Later other advantages of CIGS solar cells were discovered such as less performance loss at high temperature or low light intensity conditions. In addition,

the felexibility of production routes and the feasibility of using bentable substrates such as polymide and stainless steel also encourage the investment on CIGS solar cells.

As the development of thin film solar cells is moving on, the record efficiency of both CIGS and CdTe thin film solar cells have surpassed the 22% threshhold [16,17], and commerciallization is also successfully achieved. However, another issue that becomes urgent and should be taken into serious account is the availability and toxicity of some of their constituents. Indium in CIGS solar cells has low abundance in the earth´s crust (see Figure 1.14), and maybe cannot meet the needs of mass production in TW level in the future. It is estimated that the worldwide production of indium currently can only support a CIGSSe production capacity of approximately 70 GW/year[18].The siuation may become aggravating when taking into acount that the demand of indium in display panel industry for ITO deposition is increasing. Tellurium in CdTe solar cells is even more scarce than Indium (see Figure 1.14). In addition, cadmium is a toxic element and may cause environmental problems, because it is the culprit of a serious disease in human´s bones called "itai–itai" happened in the early 20th centrury in Japan[19].

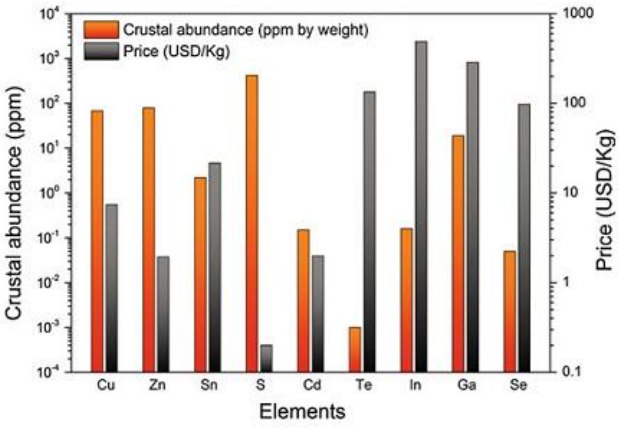

Figure 1.14. Abundance on earth´s crust and cost of constituent elements for CIGS, CdTe, and CZTS absorber materials of thin film solar cells. The image is taken from ref [20].

Therefore, in view of the scarcity of In and Te and the ever growing energy needs, it is necessary to search for absorber materials that possess earth-abundant, non-toxic and low cost constituents, while at the same time keep the high absorption coefficient and suitable band gap. The Cu_2ZnSnS_4 (CZTS) solar cell is an ideal candidate that meets all the requirements. As shown in Figure 1.14, the constituents copper, zinc, tin and sulfur of CZTS solar cells are much more abundant and much cheaper than indium, tellurium and selenium in CIGS and CdTe solar cells. In addition, CZTS has even higher absorption coefficient than that of CIGS and a band gap of 1.5 eV that matches the solar spectrum. Furthermore, the structure of CZTS is very similar to that of CIGS (this will be discussed in the following section), meaning CZTS solar cells could inherit some advantages of CIGS solar cells and learn the knowhow developed in CIGS techonology to facilitate or accelerate their progress.

1.2.2 History

The first efficient CZTS solar cell was made by Katagiri group in Nagaoka National College of Technology (NNCT) at 1996 using electron beam evaporation method [21]. The initial

efficiency 0.66% is a little bit low, but later after more than 10 years´ continuous effort, a 6.77% CZTS solar cell was achieved in his group at 2009 by co-sputtering deposition[22]. Evoked by this pioneer work, several groups began to join in kesterite solar cell investigations. Soon after a breakthrough efficiency of 9.66% on a $Cu_2ZnSn(S_xSe_{1-x})_4$ (CZTSSe, $0 < x < 1$) solar cell was obtained by Todorov et al. from IBM group using a hydrazine solution based process[23]. In addition, Guo et al. from Purdue University also achieved a CZTSSe solar cell with efficiency as high as 7.2% based on a nanocrystal hot injection process[24]. These encouraging successes have aroused the interests of the whole scientific community as well as companies, resulting in more research groups on kesterite solar cells with the aid of more investment. IBM group kept improving the lab record efficiency of CZTSSe solar cells to 10.1% and 11.1% and finally to the 12.6% at the end of 2013[25-27]. The brief record efficiency evolution of kesterite solar cells can be seen from Figure 1.15.

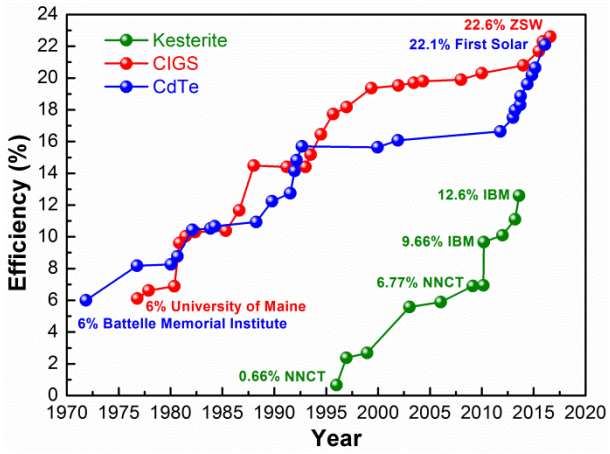

Figure 1.15. Record efficiency of keterite, CIGS and CdTe solar cells as a function of year. Data is from ref [28] and updated NREL efficiency chart. NNCT: Nagaoka National College of Technology.

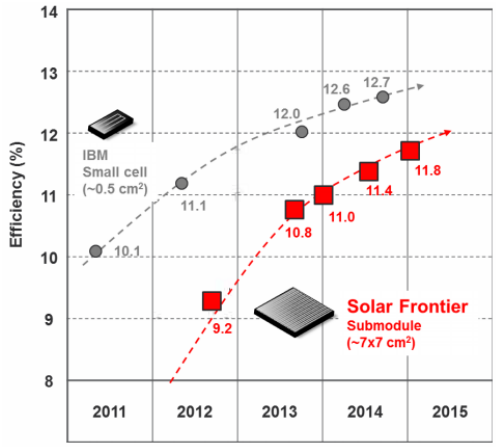

Figure 1.16. Efficiency evolution of kesterite based single cells in IBM and submodules in Solar Frontier. It should be noted that the certified efficiency of the 12.7% solar cell is 12.3% [27]. The image is from ref [29].

At the same time, Solar Frontier applied their know-how from CIGS technologies to kesterite solar cells investigation and achieved 9.2% record efficiency on CZTS submodules at 2012[30]

and 11.8% record efficiency on CZTSSe submodules at the beginning of 2015[29] (see Figure 1.16). In addition, pure selenide $Cu_2ZnSnSe_4$ (CZTSe) solar cells were also developed in NREL, IMEC, IREC and University of Luxembourg[31-38]. Currently the world record CZTS, CZTSe and CZTSSe solar cells have efficiencies of 9.2% (lab cell record by UNSW, submodule record by Solar Frontier)[39,30], 11.6% (IBM)[40] and 12.6% (IBM)[27], respectively. However, the efficiency of kesterite solar cells is still far below those of their counterparts CIGS and CdTe solar cells (see Figure 1.15), evidencing a long way is ahead of kesterite technology to further improve its efficiency. Table 1.2 summarizes the high efficiency kesterite solar cells that have been developed all over the world.

Table 1.2. Summary of high efficiency kesterite solar cells or submodules (CZTS > 8%, CZTSe and CZTSSe >10%) developed ever. SIAT: Shenzhen Institutes of Advanced Technology (China). TCRDL: Toyota Central Research and Development Laboratories Inc. The process is described by precursor deposition method + precursor type + annealing atmosphere, e.g., "sputtering + metallic stacks + H_2Se + H_2S" means sputtering deposition of metallic stack precursors and then annealing the precursors first in H_2Se atmosphere and then in H_2S atmosphere. "S/SnS" means annealing in S and SnS atmosphere simutaneously.

Material	Institution	Process	J_{sc} (mA/cm^2)	V_{oc} (mV)	FF (%)	Eff. (%)	Ref
CZTS (submodule)	Solar Frontier	Sputtering+ Metallic stacks+H_2S	21.6	708	60	9.19	[30]
CZTS	UNSW	Co-sputtering+ S containing precursors+S	19.5	747.8	63.2	9.2	[39]
	TCRDL	Sputtering+ S containing stacks+H_2S	17.5	710	71	8.8	[41]
	UNSW	Co-sputtering + S containing precursors+S/SnS	19.47	666.7	67.51	8.76	[42]
	SIAT	Co-sputtering+ S containing precursors+H_2S	21.1	625	65.1	8.58	[43]
	IBM	Co-evaporation+S	19.5	661	65.8	8.4	[44]
	Konan University	Spray pyrolysis+ Thiourea solution+S	20	670	61	8.1	[45]
	Osaka University	Electrodeposition+ Metallic stacks +S	17.7	719	62.9	8.0	[46]
CZTSSe (submodule)	Solar Frontier	Sputtering+ Metallic stacks +H_2Se+H_2S	35.1	503	66.8	11.8	[29]
CZTSSe	IBM	Spin coating+ Hydrazine solution+Se	35.2	513.4	69.8	12.6	[27]
	DGIST	Sputtering+ Metallic stacks+SeS_2/Se	34.98	521	67.2	12.3	[47]
	University of Washington	Spin coating +DMSO inks+Se	38.8	449	68.1	11.8	[48]
	Ritsumeikan University	Sputtering+ Metallic stacks +H_2Se+H_2S	37.8	437	69.4	11.5	[49]
	EMPA	Spin coating+ DMSO inks+Se	36.5	479	63.8	11.2	[50]
	IMRA	Spray+ Water–ethanol inks +N_2+Se	32.5	510	65	10.8	[51]
	ZSW	Spin coating+ DMSO inks+Se	31.6	471	69.6	10.3	[52]
	Nankai University	Sputtering+ S containing stacks+Ar+Se	34.5	460	64.39	10.23	[53]
	National Tsing Hua University	Spin coating+ Thioacetamide inks+Se/H_2S	33.1	479	63.39	10.05	[54]
CZTSe	IBM	Co-evaporation+Se	40.6	423	67.3	11.6	[40]
	IREC	Sputtering+Metallic stacks+Se	34.4	473	65.4	10.6	[36]
	IMEC	Sputtering+ Metallic stacks+H_2Se	39.7	394.87	66.2	10.4	[34]
	Nankai University	Sputtering+ Metallic stacks+Ar+Se	38.5	419	64.8	10.4	[55]

1.2.3 Configuration

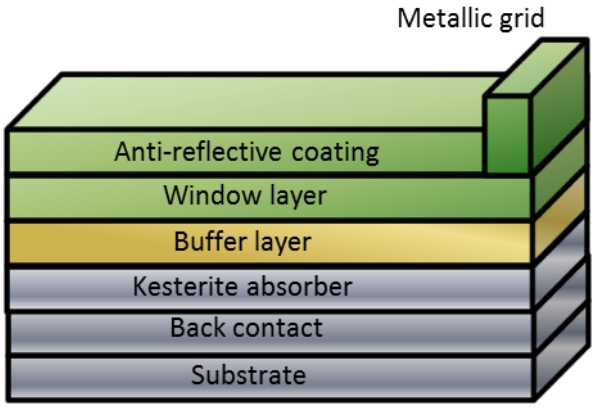

Figure 1.17. The typical configuration of kesterite solar cells.

The typical configuration of kesterite solar cells is shown in Figure 1.17, incluing substrate, back contact, kesterite absorber, buffer layer, window layer, metallic grid, and anti-reflective coating from bottom to top.

The commonly used substrate in kesterite solar cells is soda lime glass (SLG), because it is easily available, cheap, and possesses suitable themal expansion coefficient that matches well the absorbers. In addition, the sodium in SLG substrate can diffuse into kesteite absorbers during high temperature annealing, which helps the crystallization and the passviation of deffects, resulting in better optoelectronic properties[56-60]. The record 12.6% efficiency CZTSSe solar cell is based on SLG substrate. In addition, other substrates such as flexible stainless steel, ceramic tiles and ZrO_2 substrates have also been developed for kesterite solar cells. CZTSe solar cells with best efficiency of 6.1% on stainless steel and 7.5% on ceramic tiles were achieved by IREC group[61,62]. IBM obtained a 11.5% effeiciency CZTSSe solar cell with ZrO_2 based substrate [63].

The back contact allows the photogenerated holes to flow into the external circuit. Mo is an extensively used back contact for CIGS solar cells. Because Mo does not diffuse into CIGS asorbers at elevated temperatures and $MoSe_2$ formation during thermal treatment can form ohmic contact in the back interface via CIGS/$MoSe_2$. In adition, Mo is an inert contact with respect to CIGS absorbers. In view of these advantages, Mo is also applied in kesterite solar cells. However, thermodynamic analysis found that Mo tends to react with kesterite absorbers at elevated temperatures, leading to the decommpostion of absorbers into secondary phases during thermal treatment[64]. In addition, overselenization of Mo is another issue that has to be taken into account seriously. Therefore, new back contacts or inert barrier layers on top of Mo are needed to further improve the performance of kesterite solar cells. Several back contacts including TiN, TiW, Cr, Ti and Al have been tested on CZTSe solar cells by IMEC group and TiN based devices showed higher efficiency than that of the Mo references[65]. This is attributed to a low barrier value which is indicative of a good ohmic contact. In contrast, G. Altamura et al. have studied alternative back contacts like Au, W, Pd, Pt, and Ni, and concluded that although W and Au back contacts allow enhancing the photogenerated current, Mo remains the best back contact in terms of power conversion efficiency[66]. In addition, transparent

conductive oxides like ITO and FTO were also tested in the frame of bifacial solar cells[67-69]. IBM group reported that large efficiency improvements achieved on CZTSe solar cells when TiN was deposited on top of Mo, due to reduced $MoSe_2$ thickness[70]. However, TiN is not successful on CZTS solar cells because it blocks the current[71]. ZnO is found to be effective to prevent the detrimental reaction in the back interface of CZTSe solar cells and to inhibit MoS_2 formation of CZTS solar cells[72,73].

The critical part of kesterite solar cells is the window layer/buffer layer/kesterite absorbers, which forms the p-n junction and is the main part for light absorption, carrier separation and extraction.

The p-type kesterite absorber layer is the most important part in kesterite solar cells, because the light is mainly absorbed in kesterite absorbers and the photogenerated electrons determine the performance of solar cells. Therefore, in the following a detailed introduction of kesterite absorbers is presented.

Kesterite is a sulfide mineral with a formula $Cu_2(Zn,Fe)SnS_4$. In its lattice structure, zinc and iron atoms share the same lattice sites. In this thesis, Zn based keterite is focused, including Cu_2ZnSnS_4 (CZTS) and its derivatives $Cu_2ZnSnSe_4$ (CZTSe) and $Cu_2ZnSn(S,Se)_4$ (CZTSSe). Although the cystal stucture of CZTS is kesterite structure in most cases, it can also possess stannite structure. These two structures can be viewed as derivatives from chalcopyrite structure of $CuInS_2$ (CIS), as shown in Figure 1.18. Kesterite is formed when two trivalent In are replaced by a divalent Zn and a tetravalent Sn while Cu and anions keep in the same position. The difference between keterite and stannite structure lies on the ordering of cations Cu, Zn and Sn. In kesterite structure, Cu and Sn occupy the layers at z = 0 and 1/2, whereas Cu and Zn occupy the layers at z = 1/4 and 3/4. On the contrary, stannite structure is characterized by alternating Zn and Sn layer at z = 0 and 1/2 and Cu layer at z = 1/4 and 3/4. Kesterite structure is favorable for CZTS due to its lower formation energy compared with stannite structure based on theoretical calculations[74] (see Figure 1.19). Structural analysis by neutron powder diffraction confirmed that CZTS and CZTSe powders have kesterite sturcture at room temperature, being consistent with the theoretical results[75].

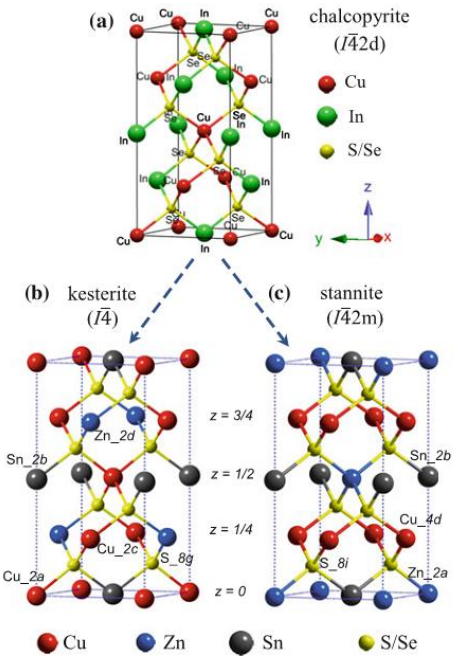

Figure 1.18. Crystal Structures of chalcopyrite CIS(e) (a), kesterite (b) and stannite (c) CZTS(e). The image is from ref[20].

The n-type buffer layer is applied to reduce the shunt paths and interface recommbination of solar cells. CdS is a universal buffer layer for kesterite, CIGS and CdTe solar cells, based on which record efficiencies of those types solar cells were ahieved. The most successful depostion process for CdS is the chemical bath deposition (CBD) process, due to its fast and low cost features, critical role on the removal of oxides, good coverage of the absorbers and benign Cd diffusion effect[76-79]. Other methods such as sputtering were also explored, which showed promissing results on CZTS solar cells[80]. However, concerning the toxic Cd in CdS, several other eco-friendly buffer layers like In_2S_3 and ZnS were developed[81-84]. Furthermore, to adjust the conduction band offset (CBO) of the interface between kesterite asorbers and buffers, $Zn_{1-x}Cd_xS$, $Zn_{1-x}Sn_xO$, $Zn_{1-x}Mg_xO$ and ZnO_xS_{1-x} (ZnS(O,OH)) ($0 < x < 1$) buffer layers were investigated[39, 85-88]. The important role of CZTSSe/CdS interface will be discussed in Chapter 5 in detail.

The window layer usually contains two layers including intrinsic ZnO (i-ZnO) and transparent conductive oxide (TCO). i-ZnO is n-type and usually 20-50 nm thick. The normal TCO includes AZO, ITO, and FTO, etc., which are heavy doped n-type semiconductors. The thickness of TCO varies in the range of 100-300 nm. Sputtering is a typical deposition process for both i-ZnO and TCO.

For metallic grid, Ni/Al eletrode is extensively applied in commercial and lab solar cells by evaporation process after the window layer deposition. The role of metallic grid is to collect current especially in large area solar cells. To form Ni/Al grid usually a mask is used. In the lab, indium pellets or silver pastes can also be used for fast measurements and experimental tests.

The role of anti-relective coating is to reduce the light reflection loss in the front surface and thus increases the quantum efficiency. MgF_2 is an ideal material that can largely reduce the reflection loss. Usually around 100 nm MgF_2 layer is enough to reduce 10-15% light loss.

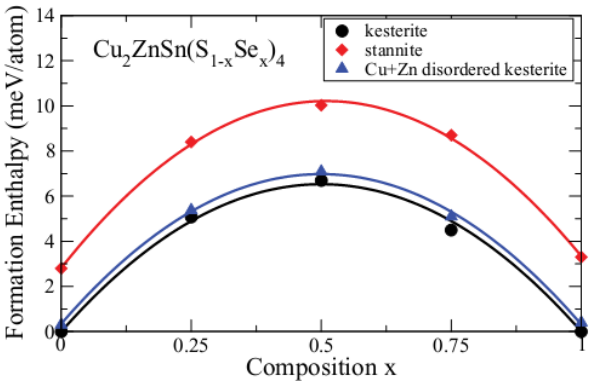

Figure 1.19. Calculated formation enthalpy of kesterite, stannite and Cu+Zn disordered kesterite as a function of S/(S+Se) ratio. The image is from ref [74].

1.2.4 CZTS, CZTSSe and CZTSe solar cells: impact of S/(S+Se) ratio

When S in CZTS is fully or partially substituted by Se, CZTSe and CZTSSe can be formed. Currently, these three types of solar cells coexist in kesterite research field, and each research group has its own focus. Actually, S/(S+Se) ratio has a significant impact on kesterite solar cells, leading to distinct and complex properties of CZTS, CZTSe and CZTSSe solar cells, respectively, as illustrated as follows:

(1) **Crystal structure.** First of all, Se substitution for S will increase the lattice constant of kesterite due to the larger atomic radius of Se than that of S, leading to the expansion of lattice. In consequence, the XRD peaks of kesterite phase will move towards smaller diffraction angles (see Figure 1.20 a), as illustrated by Bragg's law (see Equation 1.15). In addtion, due to the larger atomic mass of Se, Raman A1 peak of kesterite phase will experience a red shift (see Figure 1.20 b), as can be expained by extended Keating's model [89] (see Equation 1.16).

$$\sin\theta = \frac{n\lambda}{2d} \qquad (1.15)$$

Where θ is diffraction angle, n is a positive integer, λ is the wavelength of incident wave, and d is the lattice distance. When lattice distance increases the diffraction angle will decrease.

$$\nu = \sqrt{\frac{2\alpha_{Cu\text{-}S(e)} + \alpha_{Zn\text{-}S(e)} + \alpha_{Sn\text{-}S(e)}}{M_{S(e)}}} \qquad (1.16)$$

Where ν is the frequency of A1 mode and M is the atomic mass. α is the bond stretching force constants related to the interaction between the nearest neighbors, which can be further expressed as $\alpha = a_1 d^{-x}$ (a_1 and x are constants, while d is the bond length). As deduced from XRD results, d will increase as Se content rises, thus α of all the cation-anion pairs will decrease. As a result, the frequency of A1 mode will decrease as M increases and α decreases when Se is introduced.

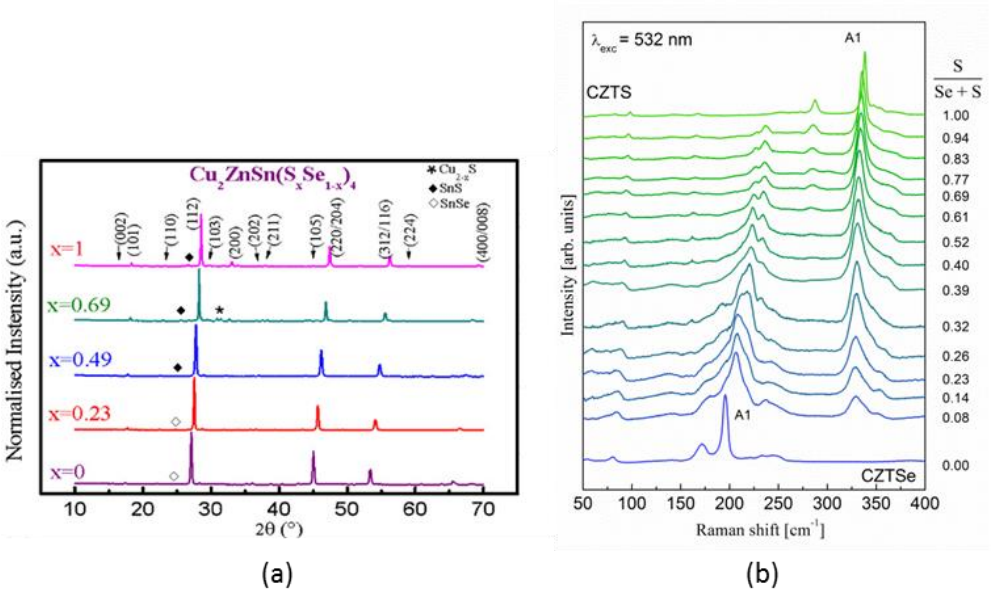

Figure 1.20. XRD patterns (a) and Raman spectra (b) of kesterite thin films as function of S/(S+Se) ratio. The images are from [89,90].

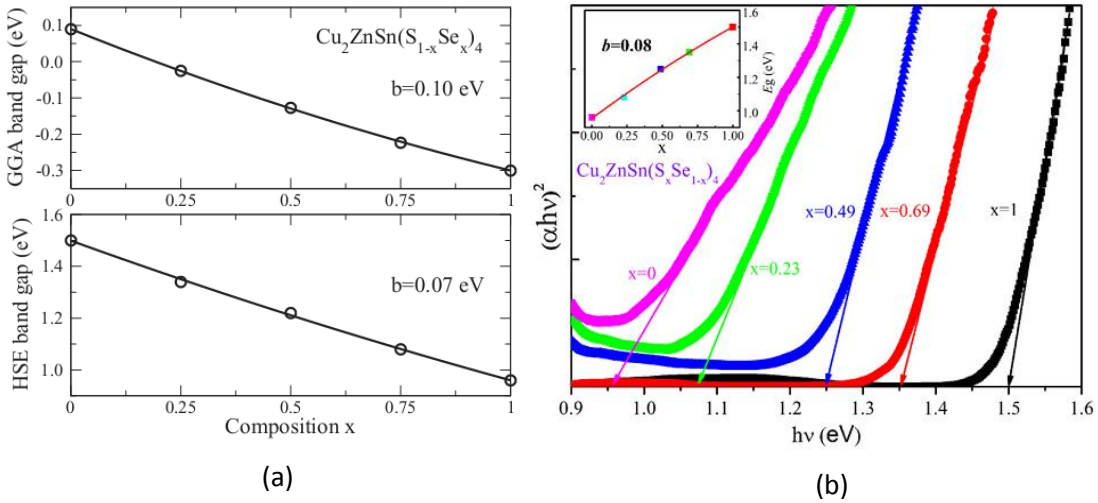

Figure 1.21. Band gap of kesterite absorbers as a function of S/(S+Se) ratio based on theorectical calculations (a) and experimental results (b). The images are from [74,89].

(2) **Band gap and band structure.** The band gap of kesterite solar cells can be modified gradually from 1 to 1.5 eV when the S/(S+Se) ratio rises from 0 to 1. The relationship between kesterite band gap and S content can be written as:

$$E_g\,(CZT(S_{1-x}Se_x)) = (1-x)\,E_g(CZTS) + x\,E_g(CZTSe) - bx(1-x) \quad (0 \leqslant x \leqslant 1) \quad (1.17)$$

Where b is very small, around 0.07-0.1 eV according to theoretical and experimental results, as shown in Figure 1.21[74,89].

The band gap variations as a function of S/(S+Se) ratio is mainly from the change of the conduction band minimum (CBM) and less from the change of valence band maximum (VBM)[74,91-92]. Therefore, the S content can change the CBO between buffer layers and

kesterite absorbers, which is very critical for high efficiency solar cells and will be deeply discussed in Chapter 5.

(3) **Single phase domain.** CZTS and CTZSe have comparable single phase domain while $CZTS_{0.25}Se_{0.75}$ has more than two times single phase domain than that of CZTS and CZTSe according to chemical potential calculations[93,94]. In contrast, NMR investigations showed that stability domain of the copper-poor quaternary phases is wider for selenide kesterites than for sulphides[95]. These results seem to be consistent with the record efficiency of different types of kesterite solar cells shown in Table 1.2.

(4) **Defects**. Theorectically, the energy level of the same type of defect in CZTS is deeper towads the midgap than that in CZTSe (acceptors with respect to VBM while donors with respect to CBM) (see Figure 1.22 a). For example, the prevalent Cu_{Zn} defect is 0.15 eV in CZTS and 0.11 eV in CZTSe, due to the weaker hybridization in the selenide caused by the longer Cu-Se bond[93]. This could result in more carrier recombination in CZTS solar cells especially due to the deeper deep level defects such as V_{Sn}, Cu_{Sn} acceptors and Sn_{Zn}, Sn_{Cu}, and $V_{S(e)}$ donors. CBM and VBM shifts induced by defect complexes give more apparent comparisons, showing the aggravating band gap reduction in CZTS system (see Figure 1.22 b). It is reported that higher S content kesterite devices have higher defect activation energy level and defect density[96], higher urbach energy[97], and worse charge separation and collection efficiency[98], being consistent with the theoretical predictions.

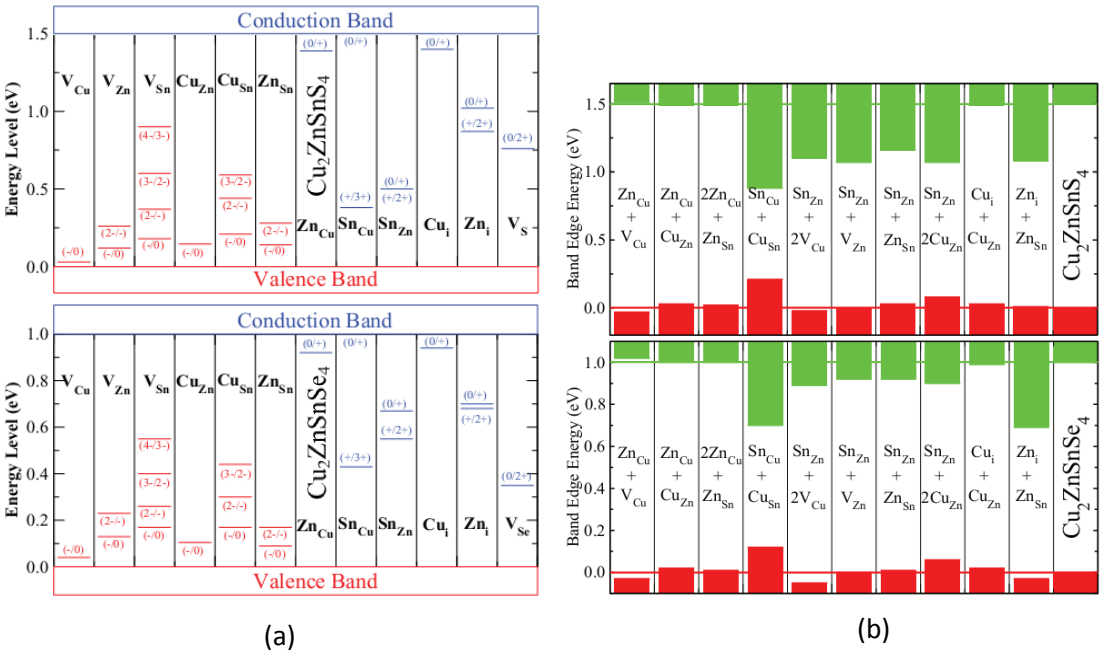

Figure 1.22. Defect energy levels (a) and defect complexes influence on the shift of CBM and VBM (b) of CZTS and CZTSe calculated by first principle theory. The images are from ref[93].

(5) **Optoelectronic properties**. The S/(S+Se) ratio has a large influence on kesterite solar cells. Figure 1.23 shows the optoelectronic properties of kesterite solar cells as a function of band gap[99]. Here the band gap is varied by S/(S+Se) ratio. It is expected that the V_{oc} and R_s increase while J_{sc} decreases in parallel with the increase of band gap

in keterite solar cells (see Figure 1.23 b, c, e). The efficiency first inceases and then decreases, yielding a maximum point at a band gap around 1.13 eV (see Figure 1.23 a). This can be explained by the existence of an optimal FF and diode ideality factor, as can be seen in Figure 1.23 d and f. In addition, 1.13 eV is very close to 1.15 eV where the first SQ limit peak efficiency is located, as shown in section 1.1.5.

(6) **V_{oc} deficit**. As the increase of S/(S+Se) ratio, the V_{oc} deficit of kesterite solar cells increases (see Figure1.24), which could be due to stronger recombination in the interfaces and bulk, associated with Fermi level pinning interface states, as well as band tails and bulk defects [96,100]. In addition, the non-ideal band alignment for devices with increasing S/(S+Se) ratio should also be considered[101]. The typical V_{oc} deficits of high efficiency CZTSe and CZTS solar cells are in the range of 550-600 mV and 700-900 mV, respectively[30,36,39-41,50], which are higher than the 500 mV threshold featured in high efficiency CIGS solar cells. Large V_{oc} deficit is considered as the main hurdle for kesterite solar cells especially for CZTSSe and CZTS solar cells.

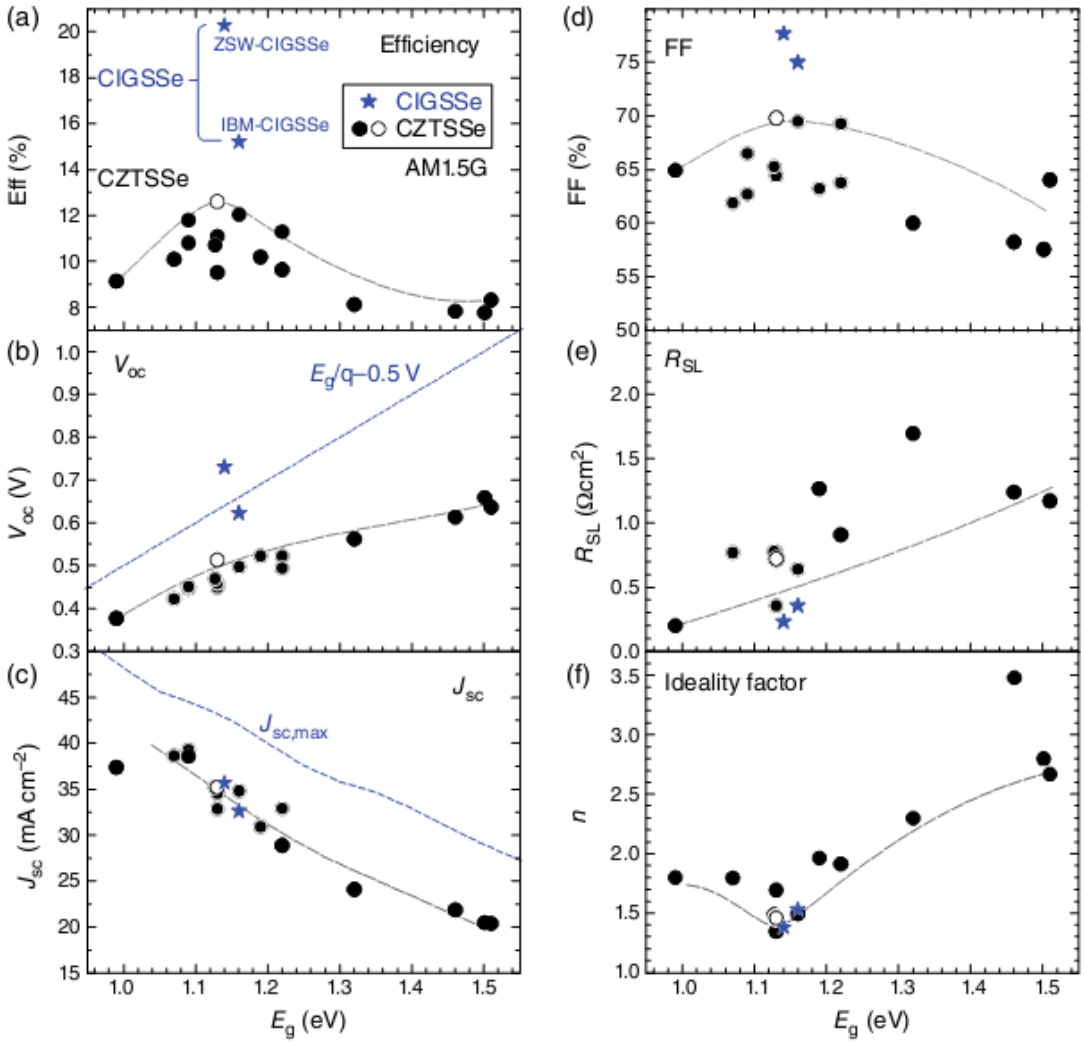

Figure 1.23. Optoelectronic properties of kesterite solar cells as a function of band gap modified by S/(S+Se) ratio. The image is from [99]. The solar cells are prepared from a hydrazine solution based process by IBM.

In summary, S/(S+Se) ratio has substantial influence on the crystal structure, band gap and band structure and defects energy level of kesterite absorbers, which leads to large variations of optoelectronic properties and V_{oc} deficit in kesterite solar cells. Although it is shown that S containing kesterite solar cells have higher defects energy level and severer V_{oc} deficit, CZTSSe solar cells can be adjusted to possess optimal band gap matching the SQ limit peak thus higher potential efficiency than CZTSe solar cells can be achieved. Therefore, in this thesis CZTSSe solar cells are focused and deeply investigated.

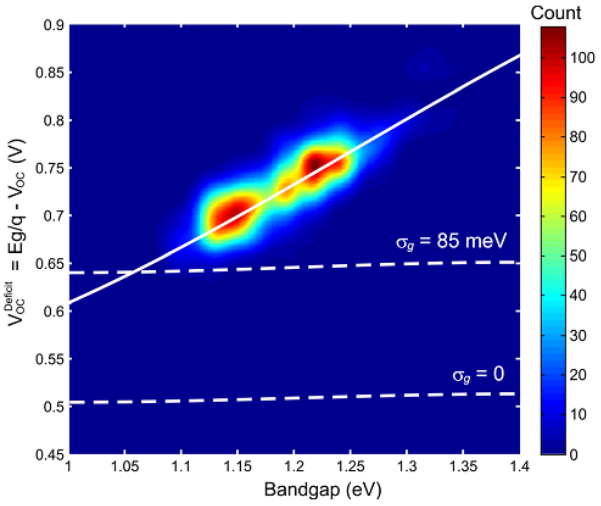

Figure 1.24. V_{oc} deficit of kesterite solar cells as a function of band gap modified by S/(S+Se) ratio. The image is from ref [100].The solar cells are prepared from a hydrazine solution based process by IBM.

1.2.5 Fabrication methods: the single-step sulfo-selenization process

Numerous processes have been developed for the fabrication of kesterite absorbers and kesterite solar cells, including non-vacuum and vacuum based processes. High efficiency kesterite solar cells were achieved by various non-vacuum based processes, e.g., spin coating of hydarzine/thioacetamide/DMSO solution or nanocrystals, spray of water-ethanol inks, sol-gel, electrodeposition, spray pyrolysis, etc.[27,46,48,51,54,102,103] Vacuum based processes such as sputtering and co-evaporation were also applied to obtain kesterite solar cells with efficiencies more than 10% [27,29,30,44,45] (see Table 1.2). In this thesis, a two-step process combining sputtering with subsequent single-step sulfo-selenization will be focused. A general introduction is prensented as follows.

Two-step process. Regarding thin film solar cells, close-spaced sublimation is a typical fabrication method for CdTe solar cells, while co-evaporation is a representative PVD method for the fabrication of CIGS and kesterite solar cells. Close-spaced sublimation and co-evaporation methods are one-step processes that combine the deposition and crystal growth together at the same time by heating the substrate to a certain suitable temperature while deposition of thin films. For CIGS and kesterite solar cells, the two-step process is another typical fabrication process that is more flexible than the one-step process, which performs the thin film deposition and crystal growth, or precursor deposition and absorber formation independently. In detail, precursor deposition (metallic precursors or metal selenides/metal

sulfides) can be realized by sputtering, thermal evaporation, or non-vacuum process based on chemical synthesis of nanocrystal/inks/solution, while absorbers formation is usually accomplished inside furnaces by thermal treatments in chalcogen/inert gas atmosphere. In this way, it is feasible to separate the deposition of metallic elements and chalcogen, with the aim of mass production by sputtering that is popular in semiconductor industry nowadays.

In this thesis, the first step is to prepare metallic precursors with appropriate composition ratio by DC magnetron sputtering. After that, the second step is thermal treatment of the as-prepared metallic precursors in a tube furnace to form CZTSSe absorbers. A single-step sulfo-selenization process is employed to form CZTSSe absorbers. Figure 1.25 shows the sputtering system and the tube furnace used in IREC.

(a) (b)

Figure 1.25. DC magnetron sputtering system (DC 450 Alliance concept) for metallic precursors deposition (a) and the three zone tube furnace for CZTSSe absorbers formation (b) in IREC.

The single-step sulfo-selenization process. The single-step sulfo-selenization process is a process to form CZTSSe absorbers from metallic precursors in S+Se atmosphere simultaneously, without the need for separated and sequential sulfurization/selenization. To supply S/Se atmosphere, H_2S/H_2Se gas, S/Se and SnS/SnSe solid powder mixture, or SeS_2 powder can be used. However, concerning the higher toxicity of H_2S/H_2S gas, solid powders are more favorable for the sake of environmental protection. The advantages of this single-step sulfo-selenization process are as follows. First of all, the expenses of heating will be reduced compared with the sequential sulfurization/selenization process. Secondly, it can avoid the chalcogen corrosion to the sputtering chamber compared with the processes based on sputtered metal sulfide/selenide precursors. Thirdly, it is very convenient and flexible to adjust the S/(S+Se) ratio of the CZTSSe absorbers by varying the added S/(S+Se) weight ratio, annealing temperature and system pressure. Last but not least, as will be shown in the following section, sulfo-selenization process can produce CZTSSe absorbers with less secondary phases especially Zn(S, Se) on the absorber surface and in the back interface.

The single-step sulfo-selenization process was previously applied in $CuIn(S,Se)_2$ (CISS) and $Cu(In,Ga)(S,Se)_2$ (CIGSS) solar cells, but limited devices progress was reported [104-106]. IREC first introduced this process to prepare solid solution CZTSSe solar cells in 2012, using S+Se and SeS_2 powders and achieving an initial encouraging efficiency of 4.4% [107]. Later two groups in Dongguk University and Chonnam Nation University obtained 7% and 9.2% (with ARC) CZTSSe solar cells respectively based on this process using S+Se powders [108,109]. Recently, a breakthrough efficiency of 12.3% for CZTSSe solar cells was achieved by DGIST, South Korea, using SeS_2+Se as the chalcogen sources. This achievement is due to surface S grading and considerable reduction of V_{oc} deficit [47]. This thesis focuses on this process using S+Se powders and a 9.1% Se-rich CZTSSe solar cell with FF over 69% was obtained. All these demonstrate that, the single-step sulfo-selenization process is a promising methodology for the production of high efficiency CZTSSe devices and deserves further investigation.

1.2.6 Comparison of kesterite and chalcopyrite solar cells: challenges and solutions

Kesterite structure is derived from chalcopyrite structure, thus kesterties are expected to inherit some properties of their chalcopyrite analogous. Indeed, kesterites have high absorption coefficient comparable to chalcopyrites. In addition, keterites have very similar band gap range (around 1-1.5 eV) as chalcopyrites (CISS) depending on the S/(S+Se) ratio. Besides these similarities, kesterites also have their peculiarities.

Kesterites have narrower single phase existence region than CIGS[93],which could be supported by the commonly observed secondary phases in the absorbers. Even in the record thin film solar cell and monograin solar cells, secondary phases are detected on the surface or in the bulk[27,110].The challenge of secondary phases will be further discussed in Chapter 4.

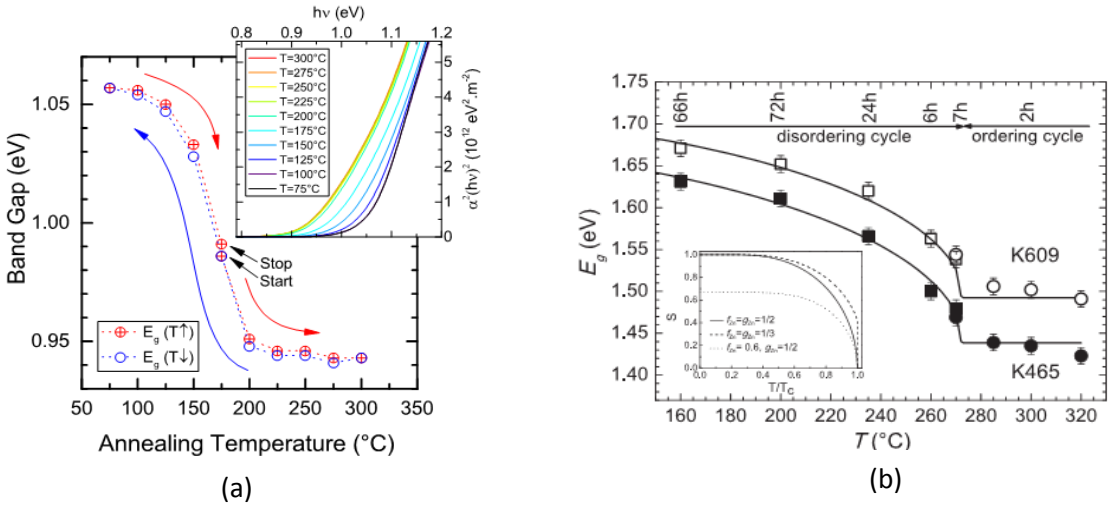

Figure 1.26. Impact of Cu/Zn order-disorder effect on the band gap of CZTSe (a) and CZTS (b) absorbers as a function of post annealing temperature. Critical temperature or transition temperature can be indentified at the point where an abrupt band gap change occurs. The images are from ref[112,114].

In addition, kesterites have a distinct p-type conductivity mechanism. In chalcopyrites, V_{Cu} is the main acceptor that contributes to the p-type conductivity, whereas in kesterites Cu_{Zn} has a lower fomation energy than V_{Cu} and thus is the dominant contributor[93]. Due to the deeper energy level of Cu_{Zn} (0.11-0.15 eV) versus V_{cu} (around 0.05 eV) [93], this singularity makes the kesterite solar cells diverge from chalcopyrite solar cells, in terms of heavier band tails and lower carrier lifetime, etc[26,100]. In addition, carrier freeze out effect that quenches the CZTSSe fill factor and efficiency at low temperatures could also be related to Cu_{Zn}[111].

Besides, due to the similar atomic radius and valence state of Cu and Zn, disordering of Cu and Zn is commonly observed in kesterites, resulting in antisite defect complex [Cu_{Zn}+Zn_{Cu}][75,93]. This is also supported by the small formation energy difference between the ordered and disordered keterite[74] (see Figure 1.19). The Cu/Zn order-disorder effect can cause band gap fluctuations in kesterite solar cells (0.1 eV and 0.2 eV lower band gap at most in disordered CZTSe and CZTS, respectively) (see Figure 1.26)[112-114], but has negligible impact on V_{oc} deficit [115-117]. The critical temperature is about 200 ºC for CZTSe solar cells and 260-270 ºC for CZTS solar cells (see Figure 1.26)[112,114,118].

Furthermore, kesterites are less stable than CIGS at high temperatures, due to the highly volatile nature of Zn, Sn and Sn-S(e), as shown in Table 1.3[119-121]. It is reported that CZTSe quickly decomposed into secondary phases at temperatures higher than 400 ºC in vacuum[120]. At the beginning of kesterite history, kesterite solar cells based on two-step process cannot function well, mainly due to the detrimental decomposition reaction on the surface caused by Sn and chalcogen loss, as illustrated by the following chemical reaction [37]:

$$2Cu_2ZnSnS(e)_4\,(s) \leftrightarrow 2Cu_2S(e)\,(s) + 2ZnS(e)\,(s) + 2SnS(e)\,(g) + S(e)_2\,(g) \qquad (1.18)$$

The Sn and chalcogen loss or defficiency during thermal treatment might also aggravate the detrimental reaction in the back CZTSSe/Mo interface [64]:

$$2Cu_2ZnSnS(e)_4\,(s) + Mo\,(s) \rightarrow 2Cu_2S(e)\,(s) + 2ZnS(e)\,(s) + 2SnS(e)\,(g) + MoS(e)_2\,(s) \qquad (1.19)$$

The SnS(e) loss is considered to be the reason of frequently observed voids in the CZTSSe/Mo interface region which causes delamination problems in some cases[35,122]. Regarding device properties, it is reported that the instability of the CZTS absorbers surface will deteriorate V_{oc} and J_{sc} while the instability of the back interface will cause the loss of J_{sc} [71]. Zn loss has also been reported during thermal treatments[119,120]. These material losses will not only lead to dentrimental sencondary phases in the CZTSSe absorber bulk and interfaces, but also may promote the presence of deep level defects such as $V_{s(e)}$, V_{Sn} and Cu_{Sn} [93], deteriorating the device performance through recombination and degradation of V_{oc}.

Table 1.3. Temperature of vapour pressure of 10^{-4} mbar for different compounds. This table is reproduced from ref [119].

Compound	Temperature (ºC)
Zn	250
ZnS	800
Sn	997
SnS	450
Cu	1017
CuS	500

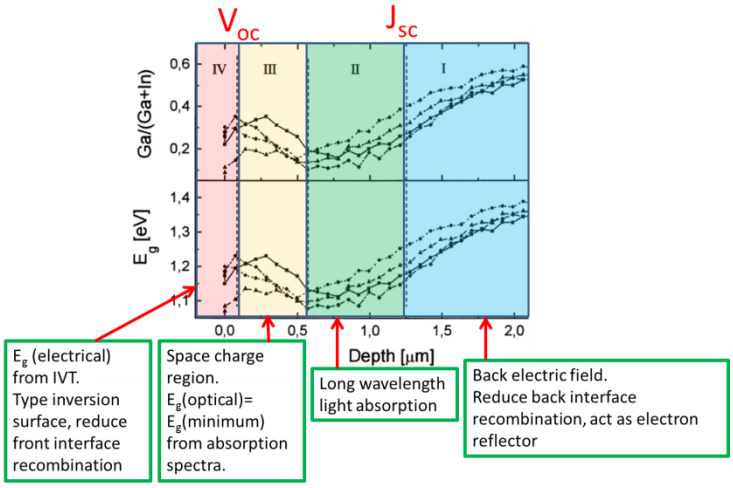

Figure 1.27. Band grading profiles of CIGS solar cells and the impact of each part on V_{oc} and J_{sc}. The image is modified from ref[].

Regarding process technologies, kesterite solar cells have learned the knowhow from CIGS technology since the day they were created, e.g., configurations, KCN etching, alkali doping strategy and band grading, etc. Actually the achitechture of kesterite solar cells is formed just by replacing the CIGS absorbers with kesterite absorbers. KCN etching is also shown to be effective for kesterite solar cells due to selective removal of Cu_x-S(e) secondary phases and metal oxides and increase of surface band gap[38,123,124]. Alkali doping especially Na doping is considered as the milestone technology in the history of CIGS solar cells, which is dicovered in the early 1990´s and is paramount for high efficiency devices. Na doping has been proved to increase the efficiency of CIGS solar cells by increasing the p-type conductivity, enhancing the crystalization, and passivating defects in the GBs[56-60,125-127]. The similar benificial effects of Na doping have also been observed in kesterite solar cells by several groups[61,128-131].

Band grading is another critical technology in CIGS solar cells which leads to the substantial performance enhancement[132-135]. Figure 1.27 shows the typical "V" shape band grading in CIGS solar cells through the fine tuning of Ga/(In+Ga) ratio, with higher band gaps in the front and bottom region while a band gap minimum in the space charge region. Region I with gradual increase of band gap acts as an electron reflector through creating a back electric field which drives the electrons away from the back interface, resulting in the decrease of back interface recombination. Region II is a low band gap notch that can enhance the collection of carriers generated by long wavelength light. These two regions are correlated with the increase of J_{sc}. Region III is the space charge region, which separates the photogenerated electrons and holes. The band gap minimum is located in this region which determines the optical E_g extracted from absorption spectra. Region IV is the front top surface that participates in the formation of absorber/buffer layer interface and p-n junction. In addition, this region is the type inversion region and responsible for the electrical E_g extracted from temperature dependent J-V curves, which has significant impact on the front interface recombination. Therefore, higher optical E_g in Region III and higher electrical E_g in Region IV could increase the V_{oc}. For kesterite solar cells, band grading has also been proved to be benificial for the efficiency enhancement by theorectical[136-138] and experimental results. Front surface band grading by sulfur rich surface was shown to largely enhance V_{oc} of CZTSSe solar cells[47]. Back region band gap grading through gradual increase of S/(S+Se) or Ge/(Ge+Sn) towards the back were also reported to increase the efficiency of kesterite solar cells[139,140]. In addition, Solar Frontier

realized a 11% CZTSSe submoldule based on a "V" shape band grading through the adjustment of S content and careful control of ZnS segregation[141]. Although the increase of efficiency is only 0.2%, considering the considerable factors that can influence the module performance, the band grading is still a promissing technology advance. In sum, the band grading is promissing for kesterite solar cells but accurate adjustment of band grading is still a challenge thus more systematic work needs to be done.

To sum up, although kesterite solar cells inherit several good properties of CIGS solar cells and could learn the knowhow from CIGS technology, their peculiarities or drawbacks appeal for new solutions and thus technologies specially designed for kesterite solar cells are needed to remove the hurdles and to compete with CIGS and CdTe solar cells. Up to now, several new technologies have been developed for kesterite solar cells, as shown in the following.

To minimize the material loss during high temperature thermal treatment, Sn or SnSe was added to the reaction container and large efficiency increase on CZTSe solar cells was realized[37]. Currently Sn or SnSe is extensively used during thermal treatments together with the chalcogen sources in the two-step process, resulting in considerable enhancement of reproducibility of experiments.

To address the secondary phases issue, innovative etchings based on HCl, $KMnO_4/H_2SO_4$+ Na_2S and Br_2/MeOH have been developed to remove ZnS, ZnSe, Cu-Sn-Se secondary phases, respectively[142-144]. To remove Sn-(S,Se) secondary phases, $(NH_4)_2S$ etching was devloped in this thesis[145], which will be presented in Chapter 4.

In the front interface CZTSSe/CdS, ALD deposited Al_2O_3 nanolayer can effectively passivate the CZTSSe absorber surface and reduce the shunt paths[146]. Hybrid buffer layer In_2S_3/CdS can simultaneously enhance the n-type doping of CdS and p-type doping of the kesterite absorbers through In_{Cd} and In_{Sn} point defects respectively and thus increase the efficiency[147]. This hybrid buffer layer technology can also eliminate the carrier freeze out effect (series resistance and efficiency collapse at low temperature).

In the bulk, fine tuning of Sn or Ge doping was found to be effective in increasing crystal quality and possibly minimizing Sn related deep defects (e.g., Cu_{Sn} or Sn_{Cu})[51,148,149]. Ge doping can also control the Na doping level, thus large efficiency enhancement can be achieved[150]. Li doping in CZTSSe can invert the electric field in the GBs and facilitates the holes transport while Sb doping can increase the grain size, decrease series resistance and reduce the trap density[151,152]. Sb+Na co-doping was reported to improve the crystalline quality and efficiency of CZTS solar cells through the formation of alkali antimony chalcogenides flux during the annealing step and reduction of the disorder in specific lattice positions of the CZTS unit cell[153]. 10% Ag doping has been proved to substantially reduce the band tailing effect[154]. Air annealing of absorbers at low temperature around 300 ºC can form SnO_x or $Cu_2ZnSn(Se_xO_{1-x})$ nanolayers in the GBs that passivate the GBs[155,156], which is considered as a key to high efficiency kesterite solar cells by IBM group. Further discussions about this post low temperature treatment (PLTT) of absorbers or devices will be presented in Chapter 5.

In the back interface, the detrimental reaction between kesterite absorber and Mo can be minimized by introducing 10 nm ZnO layer onto the Mo surface[72], while the overselenization of Mo can be controled by prealloying or depositing an appropriate thickness of TiN or MoO_2 layer onto Mo surface[70, 157].

In conclusion, although some new technologies have been developed to address various peculiarities or drawbacks of kesterite solar cells, the V_{oc} deficit is still larger than 500 mV and thus is the main barrier for further efficiency enhancement. In addition, FF (about 70%) is another parameter that needs to be improved compared with that in CIGS technology (FF is around 80%). Therefore, to further level down V_{oc} deficit and improve FF, more technologies from CIGS such as alkali PDT process (recent breakthrough technology for new record CIGS solar cells) should be tested and evaluated and more innovative and feasible technologies specially designed for kesterite solar cells need to be developed.

1.3 Objectives of the thesis

The main subject of this thesis is to develop high efficiency CZTSSe solar cells by the single-step sulfo-selenization process, and to understand the efficiency limitation by characterization and analysis of the chemical and physical properties of absorbers and devices. The specific objectives of this thesis are as follows:

(1) Preparing high quality CZTSSe absorbers with a two-step process based on the single-step sulfo-selenization methodology.
(2) Establishing a thermodynamic equilibrium model to get insights into the single-step sulfo-selenization process.
(3) Developing a customized and facile etching process to tackle Sn-(S,Se) secondary phases.
(4) Optimizing CZTSSe/CdS interface to achieve high efficiency CZTSSe solar cells.
(5) Identifying the efficiency limitations of CZTSSe solar cells.

Chapter 2

Experimental and Methodology

2.1 Experimental

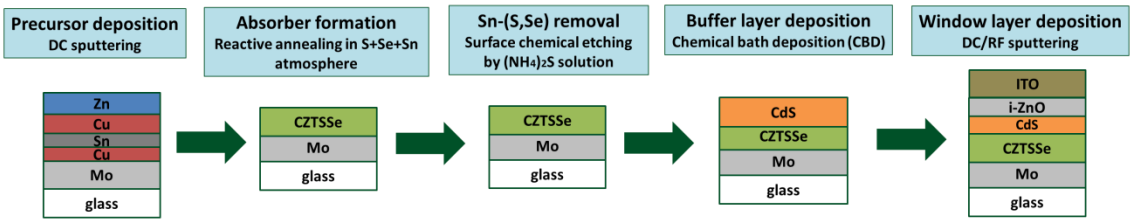

Figure 2.1. The schematic of the typical fabrication process for CZTSSe solar cells in IREC.

Figure 2.1 shows the typical fabrication process for CZTSSe solar cells in IREC, including metallic stack precursors deposition, absorber formation, S-(S,Se) removal, buffer layer and window layer deposition. The following will detail each step of the process.

(1) **Metallic precursor deposition**. Cu/Sn/Cu/Zn precursor stack were deposited by DC-magnetron sputtering (AC 450 Alliance Concepts) onto Mo coated soda lime glass (10×10 cm^2, 600-800 nm Mo + 3mm glass, R□ = 0.25-0.4 Ω/□). Precursor films were approximately 600 nm thick, with compositional ratios of Cu/(Zn+Sn) around 0.75-0.8 and Zn/Sn around 1.15-1.25. This type of stack order is chosen after systematic optimization by our group. Generally speaking, Cu layer on the bottom next to Mo can assist the deposition of Sn layer with smooth surface, Sn layer in the middle is to minimize the Sn loss during thermal treatment, Cu layer in the middle is for promoting elements inter-diffusion through formation of Cu-Sn and Cu-Zn alloys, and Zn top layer is aiming at facilitating the accumulation of Zn(S,Se) secondary phases on the surface for subsequent chemical etchings.

(2) **Absorber formation**. Metallic precursors were reactively annealed in a graphite box inside a tube furnace. The furnace has a homogeneous temperature zone in the middle with a length of 10-15 cm and the maximum temperature can reach 1150 ºC. The graphite box has an interior volume of 23.5 cm^3 and the cover can be closed by graphite screws. To form solid solution CZTSSe films a single-step sulfo-selenization process was used. The process was performed by reactive annealing of the metallic precursors under a S+Se+Sn atmosphere by using two crucibles inside the graphite box, one with a mixture of various ratios of sulfur and selenium powders (Alfa-Aesar, 99.995%) while maintaining the total weight of the mixture of 50 mg, and the other with 5 mg of tin powder (Alfa-Aesar, 99.999%). The addition of elemental tin in the annealing process has been shown to suppress Sn loss from the films during annealing, and can significantly improve the efficiency of kesterite solar cells [37]. The ramp rate was 20 ºC/min while the cooling process was performed naturally till below 300 ºC. Two annealing temperature profiles were employed; one is "one step profile": 550°C, 30 min, 1 mbar or 1bar. The other is "two step profile": first 200 ºC for 15 min in 1mbar atmosphere and then 550°C for 30 min in 1 bar atmosphere, which is proved to be

beneficial to obtain different Se-rich absorbers and good crystal quality as will be shown in Chapter 3.

(3) **Surface Sn-(S,Se) removal**. The as-prepared CZTSSe absorbers were soaked in 22% w/w $(NH_4)_2S$ solution for 1-2 min depending on the quantities of Sn-(S,Se) on the surface. The solution was kept stirring during the etching process. After that the samples were cleaned with DI water to remove the $(NH_4)_2S$ residual and dried by N_2 flow. This $(NH_4)_2S$ etching process is developed by the author during the Ph.D. career and will be discussed in Chapter 4 in detail.

(4) **Buffer layer deposition**. CdS is grown by chemical bath deposition (CBD) in a vertical configuration at 75 ºC for 7 min ($CdSO_4$) or 40 min ($Cd(NO_3)_2$). The chemical bath was composed by $CdSO_4$ or $Cd(NO_3)_2$, $[CH_4N_2S]$ and NH_4OH with pH = 9.5. The thickness of CdS layer can be varied from 30 to 70 nm depending on the different Cd precursors.

(5) **Window layer deposition**. First an i-ZnO layer with about 50 nm thickness was deposited and then a 250-300 nm AZO or ITO layer was deposited by DC pulsed magnetron sputtering (CT100 Alliance). The sheet resistance of the window layer is around 30-100 Ω/□ depending on the deposition time. The transmittance is around 80% in the visible light range.

After the solar cells were finished, 3×3 mm^2 cells were scribed and indium was soldered onto Mo surface to facilitate the contact during the optoelectronic characterization.

It should be noted that, to improve the performance of the CZTSSe solar cells, further optimization such as post low temperature treatment of absorbers or devices and wet chemical treatments of the absorbers surface were integrated into this typical fabrication process, which will be shown in the following chapters.

2.2 Characterizations

2.2.1 Material characterizations

(1) **Scanning electron microscopy (SEM)**. The SEM images were obtained through a ZEISS Series Auriga microscope using accelerating voltage (5-10 kV), with working distance of 5-8 mm and magnification ranging from 1000 × to 20000 ×. EDS (Oxford Instruments, X-Max) was performed using 10kV and 20 kV in the work distance 5-8 mm with the help of Inka software.

(2) **X-ray diffraction (XRD).** XRD measurements were performed using a Siemens D500 diffractometer in θ-2θ configuration. The scanning angle ranges from 10º to 80º and the scanning step is around 0.03º/s.

(3) **Raman spectroscopy.** Raman scattering measurements were performed on the surface and at the back region of the absorbers using three different excitation wavelengths: 532 (green), 458 (blue) and 325 (ultraviolet) nm. Measurements of 532 and 325 nm excitation wavelengths were performed in back scattering configuration with a LabRam HR800-UV Horiba-Jobin Yvon spectrometer, through an Olympus metallographic microscope with a laser spot size of the order of 1 μm. The spot was rastered over an area of 30×30 μm^2 to avoid effects in the spectra related to potential microscopic inhomogeneity. In addition, measurements of 458 nm excitation wavelength were made using a T64000 Horiba–Jobin Yvon spectrometer with a spot size of 100 μm on the samples. In all cases, to avoid the presence of thermal effects in the spectra, the power

excitation density was around 50 W/cm^2. For the detection of secondary phases at the back region of the films, a "lift-off" technic was employed.

(4) **UV-visible Absorption Spectra.** UV-visible absorption spectra were obtained from spectral transmittance and reflectance measurements, which were recorded in the wavelength range 400–1800 nm, using a Perkin Elmer Lambda 950 UV/VIS Spectrometer.

(5) **X-ray fluorescence spectroscopy (XRF).** A Fischerscope XVD system was used for the measurement of the composition and thickness of metallic precursors and absorbers. The system was calibrated with inductively coupled plasma optical-emission spectroscopy (ICP-OES, Perkin–Elmer Optima 3200 RL). Normally average values were obtained by measuring 9 points on a 5×5 cm^2 sample and 16 points on a 10 × 10 cm^2 sample.

(6) **Glow discharge optical emission spectrometer (GD-OES).**The in-depth compositions were obtained by means of a glow discharge optical emission spectrometer (GD-OES) HORIBA GD Profiler 2, powered with a radio frequency source at 3 kHz.

(7) **Time-off-flight secondary ion mass spectrometry (TOF-SIMS).** For in-depth composition, especially Na distribution, time-off-flight secondary ion mass spectrometry (TOF-SIMS) was performed in an ION-TOF IV equipment, equipped with 25 kV Bi cluster primary ion gun for analysis, and O_2 and Cs ion guns for sputtering in-depth profiling modes. The analyzed area was 50×50 μm^2 with a cycle time of 100 μs and a time to digital converter (TDC) resolution of 200 ps.

(8) **X-ray photoelectron spectroscopy (XPS).** For absorbers surface composition, high energy X-ray photoelectron spectroscopy (XPS) measurements were performed at the KMC-1 beamline at the electron storage ring BESSY II Berlin (Germany). The high kinetic energy end station (HIKE) allows to tune excitation the energy (E_{ex}) of the X-ray beam from 2.01 keV up to 12 keV and therefore to increase the information depth from roughly 5 nm up to 25 nm (where information depth is define as three times mean free path of the excited photoelectrons). All measurements were performed in ultra-high vacuum (<8.5×10^{-9} mbar) using an excitation energy E_{ex}=3000eV.

(9) **Photoluminescence Spectroscopy (PL).** The photoluminescence spectra were measured using the *i*HR320 Horiba Jobin Yvon spectrometer coupled with InGaAs detector and He-Ne gas laser with a 632.8 nm laser line was used as excitation source. Spectra were measured in backscattering configuration through the Olympus metallographic objective and using the maximum laser power which ensured the absence of the thermal effects on the samples. Laser power was changed by changing the output slit of the laser. Sample temperature was varied in the close-circle He cryostat and measured by Si-diode.

(10) **High Resolution Transmission Electron Microscopy (HRTEM), Scanning Transmission Electron Microscopy (STEM) and Electron Energy Loss spectroscopy (EELS).** The nanoscale structure and composition were obtained by HRTEM, STEM and EELS mapping using a FEI Tecnai F20 field emission gun microscope operated at 200 kV with a point-to-point resolution of 0.19 nm, which is equipped with a high-angle annular dark field (HAADF) detector.

2.2.2 Device characterizations

(1) **Current density-Voltage measurements** (**J-V).** Dark and illuminated J-V curves were obtained using an ABET Technologies Sun 3000 Class AAA solar simulator calibrated by a reference silicon solar cells at 1sun, AM 1.5G and 25 ºC.

(2) **External Quantum Efficiency (EQE).** The external quantum efficiency (EQE) of the devices is performed on a Bentham PVE300 system, calibrated by Si and Ge photodetectors. The maximum measurement range is 300-1600 nm. Bias EQE were measured by applying a reverse voltage of -1V.

(3) **Capacitance-Voltage measurements (C-V).** Capacitance-Voltage measurements were performed by using an impedance analyzer from Novocontrol Technologies with a frequency of 15 kHz and a modulation voltage of 50 mV in the dark at room temperature.

(4) **Temperature Dependence of J-V measurements (JV-T)**. Temperature dependence of J-V measurements (JV-T) were performed by a Keithley 2400 source meter using a closed-cycle He cryostat (ColdEdge). The illumination source was from a small area Newport solar simulator under AM1.5G light conditions calibrated to 1 sun by using a Si reference cell.

Chapter 3

Thermal treatment: the art of furnace

During the two-step process, thermal treatment is critical for high quality absorbers. The aim of thermal treatment is to prepare CZTSSe absorbers with optimal compositions, less secondary phases and defects and big columnar crystals. This requires the fine tuning of different process parameters in the furnaces, especially under non-equilibrium conditions (temperature less than 600ºC, annealing time less than 1h). The following will show the optimization and thermodynamic analysis of the thermal treatment based on the single-step sulfo-selenization process.

3.1 Optimization of the single-step sulfo-selenization process

3.1.1 Optimization of S/(S+Se) ratio

Until now, CZTSSe solar cells show the best results of 12.6% with S/(S+Se) ≈ 0.25 - 0.3, which is similar to the case of Cu(In,Ga)Se_2 based solar cells, in which the partial substitution of indium by gallium allows for the highest performance of 22.6% [16]. Therefore, the appropriate S/(S+Se) and Ga/(Ga+In) ratio are paramount for high efficiency devices, since they clearly impact relevant features such as band gap and defects.

First of all, to estimate S/(S+Se) ratio in the kesterite phase is a prerequisite. There are many ways to determine it in CZTSSe thin films, e.g., EDS, XRF, ICP, XRD, EQE and Raman, etc. Among them, EDS, XRF and ICP are direct methods to get S/(S+Se) ratio, which allows for the acquisition of the S/(S+Se) ratio from direct calculations of the atomic concentration of each element. XRD, EQE and Raman are indirect methods. XRD and EQE determine the S/(S+Se) ratio through the use of Vegard´s law applied to the lattice constant and band gap evolution with composition[74,89], respectively. Raman determines the S/(S+Se) ratio from the linear correlation between the S/(S+Se) ratio and the integral intensities ratio of the S-related and Se-related Raman peaks: $A_{270\text{-}380cm}^{-1}/(A_{150\text{-}260cm}^{-1}+A_{270\text{-}380cm}^{-1})$ [90].

EDS and XRF usually give higher S/(S+Se) ratios than the real values, due to the fact that the signal of sulfur and Mo overlaps in the measurements. Furthermore, for those indirect methods, some errors are inherent during the evaluation. It should also be mentioned that the values of the anion compositions obtained using different methods could not be interpreted in the same way. For example, EQE and Raman spectroscopy are surface sensitive techniques with a relatively shallow penetration depth. On the other hand, X-ray penetrates completely the film, meaning that the information obtained by XRF and XRD corresponds to that of the whole sample. Also, it is important to note that estimations of chalcogen compositions using EDS, XRF, and ICP give an overall composition of all the phases that are currently present in the sample, and not only of the kesterite phase. In order to evaluate the anion composition of the kesterite phase, the suitable methods are Raman, XRD and EQE, which are based on the integral intensities, shift of kesterite related peaks and bands, respectively. Furthermore, Raman measurements could be performed on the front and the back of each thin film when a “lift-off” technique is applied, thus giving the information about the uniformity of the kesterite phase through the thickness of the layer. On the other hand, ICP is a highly sensitive method for trace analysis of elements. In this work we take it as a reference technique for the evaluation of the indirect methods. Results

show that XRD, EQE and Raman measurements can be used as a facile way to get a rough estimation of S/(S+Se) ratio in this type of materials. A summary of the different methods presented above is included in Table 3.1 and composition measurements by ICP, XRD, EQE, Raman and GD-OES on a typical CZTSSe thin film were compared in Table 3.2.

Table 3.1. Summary of different methods for obtaining the S/(S+Se) ratio in kesterite thin films.

Methods		Detection depth	Total composition	Kesterite composition	Accuracy	Corresponding theory
Direct methods	ICP	The whole bulk	YES	-	High accuracy	Calculation of each element´s concentration
	XRF	>>2μm	YES	-	> real value (Mo and S signals overlap)	
	EDS	1-2μm (5-20 kV applied voltage)	YES	-		
Indirect methods	XRD	>>2μm, The whole bulk	-	YES	Rough estimation	Vegard´s law of lattice constants
	EQE	Normally <500nm (depending on the minority carrier diffusion length)	-	YES		Vegard´s law of band gap (E_g)
	Raman	<100nm (325nm-532nm)	-	YES		Quasi-linear correlation between S/(S+Se) and $A_{270\text{-}380cm}^{-1}/(A_{150\text{-}260cm}^{-1}+A_{270\text{-}380cm}^{-1})$

Table 3.2. Composition measurements by ICP, XRD, EQE, Raman and GD-OES on a typical CZTSSe thin film.

Cu/(Zn+Sn)	Zn/Sn	S/(S+Se)						
ICP		ICP	XRD	EQE	Raman surface	Raman back	GD-OES surface	GD-OES back
0.85	1.17	0.32	0.30	0.26	0.25	0.24	0.29	0.35

The first important role of thermal treatment is to obtain CZTSSe absorbers with appropriate S/(S+Se) ratio. According to the study of IBM group, the optimal S/(S+Se) ratio is around 0.25-0.3, corresponding to a band gap of 1.13 eV, as shown in Figure 1.23. It has been reported by our group that it is feasible to modify S/(S+Se) ratio by varying added S/(S+Se) powder weight ratio, annealing temperature and system pressure[107]. Se-rich CZTSSe absorber can be obtained by increasing the annealing temperature and reducing the added S/(S+Se) weight ratio and the system pressure. Among the three factors, the added S/(S+Se) weight ratio is the most important, then less important is the system pressure, and the least is the annealing temperature.

Table 3.3. CZTSSe absorbers with the whole range of S/(S+Se) ratio (0-1) achieved with various added S/(S+Se) weight ratio and system pressure and Zn(S,Se) distribution on the front and at the back region. Metallic ratios of the absorber were obtained using an XRF method.

No.	Added S/(S+Se) weight ratio	Annealing conditions	Absorber composition						Zn(S,Se)	
			Cu/(Zn+Sn)	Zn/Sn	S/(S+Se)				surface	back
					XRD	EQE	Raman surface	Raman back		
1	1	550℃-1bar	0.85	1.23	1	1	1	1	YES	YES
2	0.4	550℃-1bar	0.87	1.11	0.85	0.82	0.85	0.84	YES	YES
3	0.4	550℃-1mbar	0.86	1.06	0.77	0.77	0.81	0.83	YES	YES
4	0.04	550℃-1mbar	0.84	1.03	0.58	0.55	0.60	0.43	NO	NO
5	0.02	550℃-1bar	0.85	1.08	0.39	0.35	0.31	0.29	NO	YES
6	0.04	200℃-1mbar-550℃-1bar	0.84	1.03	0.27	0.24	0.23	0.18	NO	NO
7	0.02		0.83	1.21	0.15	0.13	0.09	0.08	NO	NO
8	0.02		0.84	1.31	0.15	0.13	0.13	0.07	NO	NO
9	0	550℃-1mbar	0.81	1.16	0	0	0	0	YES	NO

An appropriate annealing temperature is very critical for crystal growth to obtain high quality CZTSSe absorbers. Therefore, to optimize S/(S+Se) ratio for device grade CZTSSe absorbers, it is reasonable to keep the suitable annealing temperature constant, while to change the added S/(S+Se) weight ratio and the system pressure. In this work, the highest annealing temperature is fixed at 550 ºC, due to high quality absorbers and high efficiency CZTSSe solar cells obtained by our group as well as other groups at this temperature. The underlying reason can be explained as follows. Generally speaking, annealing temperature approaching to the melting point of materials is favorable for high quality crystal growth. In addition, annealing temperature should also be lower than the glass transition temperature of the substrate. Here the melting point of CZTS is 990 ºC and the glass transition temperature of the flat soda-lime glass substrate is 564 ºC, thus, 550 ºC is selected and applied. Table 3.3 shows that the whole range of S/(S+Se) ratio in the thin films was achieved by various added S/(S+Se) ratio and system pressure.

3.1.2 Minimization of secondary phases

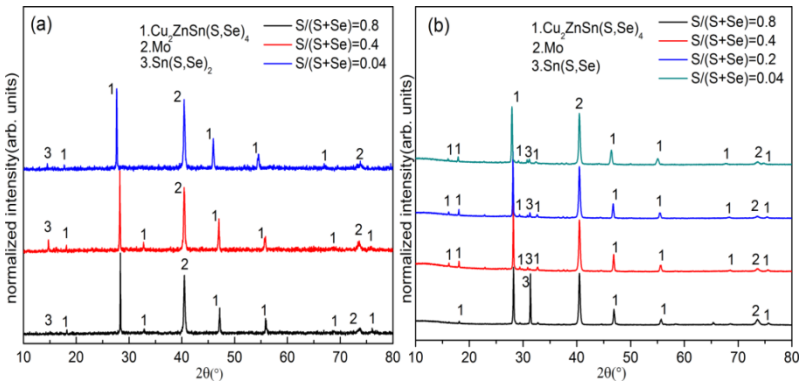

Figure 3.2 . XRD patterns of CZTSSe absorbers annealed under 1bar (a) and 1mbar (b) system pressure at 550 ℃ for 30 min with various added S/(S+Se) weight ratios.

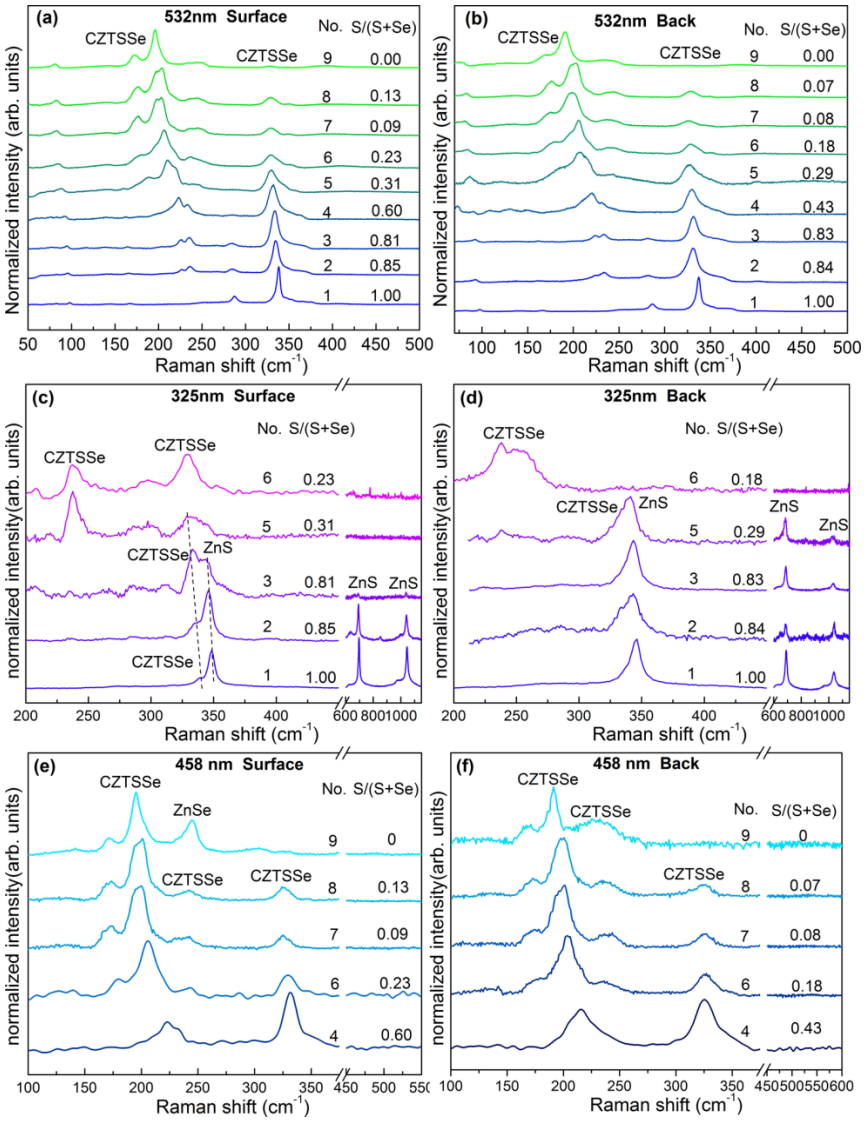

Figure 3.3. Raman spectra measured with 532, 325 and 458 nm excitation wavelengths on the surface (a), (c), (e); and at the back region (b), (d), (f), of CZTSSe samples with S/(S+Se) ratio varying from 0 to 1. Surface and back region S/(S+Se) ratios shown in the spectra are estimated from surface (a) and back (b) Raman spectra with excitation wavelength of 532 nm, respectively. The number and S/(S+Se) ratio in the figure correspond to the information shown in Table 3.3.

Another role of the thermal treatment is to minimize the secondary phases to form a single phase of CZTSSe. Specially, secondary phases on the surface or in the back CZTSSe/Mo interface should be minimized, due to their profound influence on optoelectronic properties. Therefore, to understand secondary phases distribution is important for further optimizations.

However, there are few works focusing on investigating secondary phases in solid solution CZTSSe thin films. An initial work on secondary phases research using XRD with quantitative Rietveld refinement for solid solution CZTSSe thin films with broad metallic composition variation in precursors was presented by R.A. Wibowo et al. [158]. After selenization of ZnS/Cu/Sn stack precursors, Louis Grenet et al. found the presence of Zn(S,Se) at the bottom of $Cu_2ZnSn(S,Se)_4$ thin films via TEM, combined with EDS analysis [159]. Investigation about the influence of S/(S+Se) on the formation and distribution of secondary phases in solid solution CZTSSe solar cells is rarely reported until now. In this work, Raman measurements with green

light (532 nm), blue light (458 nm), UV light (325 nm) as well as XRD were employed to identify secondary phases on the surface and at the back region of absorbers, because green light is suitable to detect kesterite and Cu(S, Se) phases, blue light is effective to detect ZnSe[160], UV light is sensitive to ZnS identification[161], and XRD is useful for the detection of Sn-(S,Se). Detailed discussions about the detection of secondary phases will be presented in Chapter 4.

Figure 3.2 shows the impact of system pressure on Sn-(S,Se) secondary phases formation, indicating that $Sn(S,Se)_2$ appears in the CZTSSe thin films when using high system pressure while Sn(S,Se) is prone to be present under low inert gas pressure. This could be linked with the fact that a lower pressure in the reaction chamber is helpful for the formation of phases with simple stoichiometry [162].

Figure 3.3 shows the secondary phases distribution on the surface and in the back region of CZTSSe absorbers as a function of S/(S+Se) ratio measured by multi-wavelength raman excitaion light. Results display that much fewer secondary phases, especially Zn(S,Se), are prone to be present on the surface and at the back region of Se-rich CZTSSe absorbers when compared with CZTSe, CZTS and S-rich CZTSSe (see the summary of Table 3.3), which may contribute to the higher efficiency for this type of CZTSSe solar cells nowadays. Figure 3.4 shows the schematic of Zn(S,Se) distribution in kesterite absorbers with different S/(S+Se) ratios in this work. It should be noted that, the only exception is Se-rich CZTSSe No.5 with ZnS in the back (see Table 3.3), which is assumed to have experienced a strong sulfurization process in the beginning stage of thermal treatment.

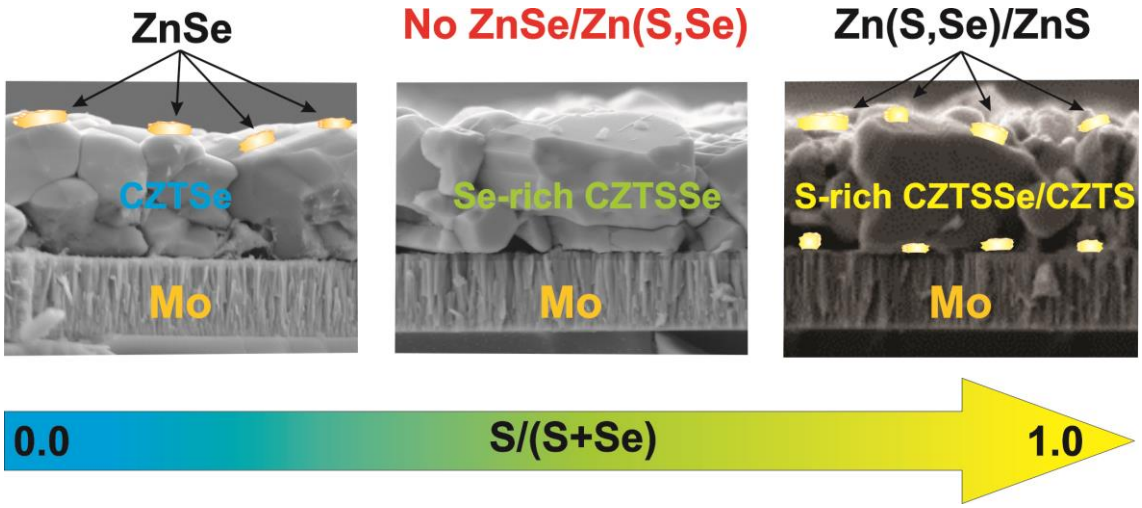

Figure 3.4. Schematic of Zn(S,Se) distribution in the front and back interfaces in kesterite absorbers with different S/(S+Se) ratios.

In summary, CZTSSe absorbers almost free of Zn(S,Se) on the surface and at the back region can be obtained by the appropriate control of different thermal treatment parameters:

(1) Simultaneous sulfo-selenization of the metallic precursors, i.e., avoiding sequential sulfurization and selenization. Once first sulfurized, ZnS will be present at the back and it will hardly be converted to kesterite.
(2) Comparable partial pressure of selenium and sulfur vapor in the atmosphere, i.e., using low Ar pressure (especially in the first stage of the two-step profile thermal treatment) and low added S/(S+Se) ratio to get Se-rich CZTSSe.

For Sn(S,Se) secondary phases, a wet chemical etching was developed to remove them and this will be discussed in Chapter 4.

3.1.3 Influence of S/(S+Se) ratio on the optoelectronic properties

Figure 3.5 shows the impact of S/(S+Se) ratio on optoelectronic properties of CZTSSe solar cells. The samples with S/(S+Se) estimated from EQE deviates from the value from XRD indicating inhomogeneous in-depth distribution of S/(S+Se) (Figure 3.5 a), due to the different penetration depth of these two techniques as shown in Table 3.1. J_{sc} decreases quickly while V_{oc} increases slowly when S/(S+Se) increases, which leads to larger V_{oc} deficit and worse efficiency in higher S/(S+Se) CZTSSe devices (Figure 3.5 b and c), being consistent with the results of kesterite solar cells by hydrazine based process as shown in Figure 1.23. The samples (A, B and C) not following the trends evidence additional efficiency limitation problems like secondary phases, composition fluctuation by in-depth S/(S+Se) non-uniformity in chalcogen distribution (see Figure 3.5 d). Best efficiency of 5.2% was obtained with S/(S+Se) = 0.27, which is consistent with the results of the record CZTSSe solar cells (S/(S+Se) = 0.25-0.3).

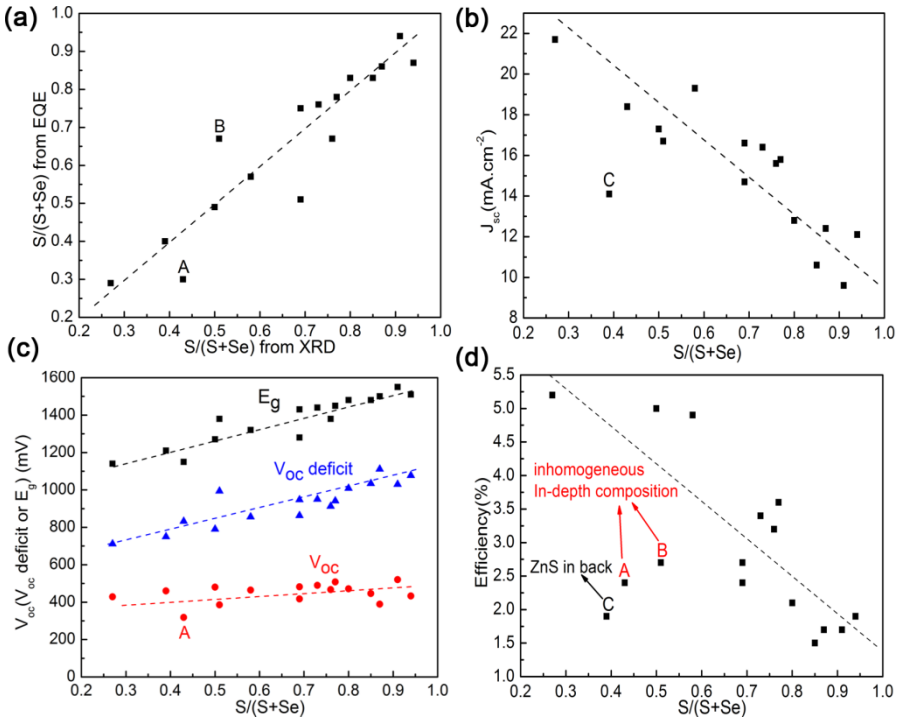

Figure 3.5. Optoelectronic properties of CZTSSe solar cells as a function of S/(S+Se) ratio estimated from XRD in the absorbers: (a) S/(S+Se) estimated from EQE; (b) J_{sc}; (c) V_{oc}, V_{oc} deficit and band gap (E_g); (d) conversion efficiency.

To sum up, the optimization of the single-step sulfo-selenization process during the preparation of CZTSSe solar cells to obtain optimal S/(S+Se) ratio and to minimize secondary phases formation were discussed. The work above, subsection 3.2.1, 3.2.2 and 3.2.3 are included in the paper titled "Formation and impact of secondary phases in Cu-poor Zn-rich $Cu_2ZnSn(S_{1-y}Se_y)_4$ ($0 \leqslant y \leqslant 1$) based solar cells". The paper can be found in the Appendix and is submitted in requirement for the Doctor of Philosophy in Engineering and Advanced Technologies at the University of Barcelona.

3.1.4 Optimization of crystal quality

The third role of thermal treatment is to obtain CZTSSe thin films with big crystals and less grain boundaries, since grain boundaries usually accumulate defects and impurities. In addition to the selection of appropriate high annealing temperature, pre-alloying at low temperature is critical to get columnar crystals across the cross section of the absorbers. Figure 3.6 shows the SEM pictures of CZTSSe absorbers annealed with "one step profile" (550 ºC, 30 min, 1 mbar) and "two step profile" (first 200 ºC, 15 min, 1 mbar and then 550 ºC, 30 min, 1 bar). The S/(S+Se) is around 0.25-0.3 in both samples. It is clearly seen that CZTSSe absorbers annealed with "one step profile" have smaller and rougher crystals than those with "two step profile ". In addition, "one-step profile" samples feature a bilayer configuration with larger crystals on top and much smaller crystals at the bottom, while "two step profile" samples have large comlunar crystals with size comparable to the thickness of the absorbers. Furthermore, there are less voids in the "two step profile" samples. For both samples less than 200 nm $Mo(S,Se)_2$ formed in the interface between CZTSSe absorbers and Mo back contact. The manuscript including this content combined with detailed machanism analysis and device properites is in preparation for publication.

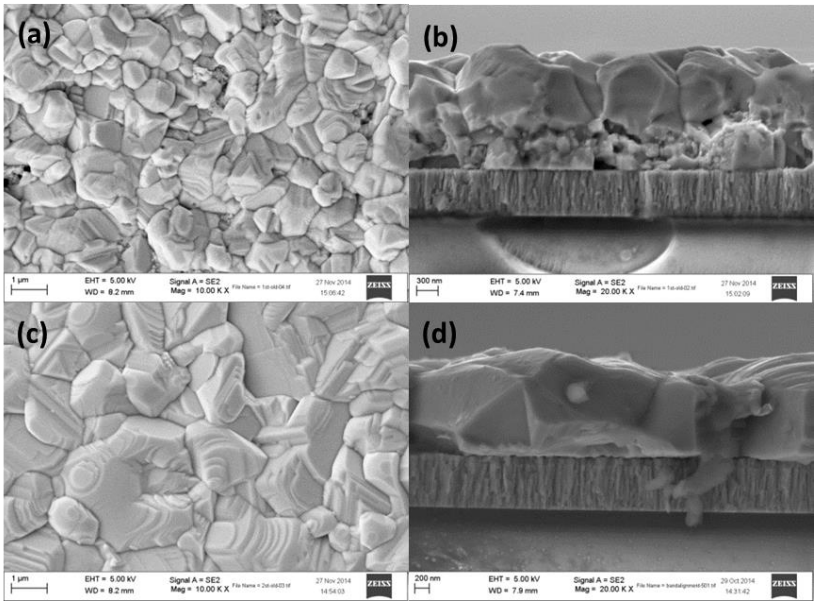

Figure 3.6. SEM pictures of CZTSSe absorbers annealled with "one step profile"(550º C, 30 min, 1 mbar) (a)(b) and "two step profile" (first 200 ºC, 15 min , 1mbar and then 550 ºC,30 min, 1 bar) (c)(d).

3.1.5 Material loss control

It should be noted that material loss from kesterite absorbers must be controled in the thermal treatment for efficient devices. The distinct results in the section 3.2.4 could aslo be related to the supression of Sn and chalcogen loss by atmospheric pressure at high temperature in the "two step profile" case. The material loss has been described in the section 1.2.6. To prevent or minimize the material loss, several techniques can be applied :

(1) Using closed containers. When the constant chalcogen supply is not available as in most of the labs due to limited quantities of S/Se powders being used, annealing precursors inside a closed or semi-closed container is the most effective way to reduce the material loss. Graphite boxes closed with cover fixed by screws can resist the high pressure of chalcogen at high temperatures ($P^*(S_2)$ = 3.9×10^5 Pa at 550 ºC) and restrict the chalcogen vapors inside well. Besides, its benign thermal conductivity can promote the homogeneity of CZTSSe thin flims.

(2) Using Sn or SnS(Se) together with S/Se powder. As can be deduced from the chemical reactions 1.18 and 1.19 in the interfaces discussed in the section 1.2.6, high SnS(Se) vapor can move the reaction towards the left side and suprress the decomposition. This is also supported by experimental studies[163]. Sn has a similar role as SnS(e) because it can react with S(e) vapor easily to form SnS(e).

(3) Using high inert gas pressure. High Ar/N_2 pressure can reduce the evoration rate as well as diffusion rate of volatile SnS, Zn and chalcogen in the atmosphere[121], therefore, less material loss can be achieved.

(4) Using rapid thermal processing (RTP). RTP can accomplish the absorber formation in a fast process with a high vapor of chalcogen, thus could minimize the material loss.

In this thesis, the precursors are annealed together with S, Se and Sn powders inside semi-closed graphite boxes with covers fixed with screws, in order to minimize the material loss.

Other issues, like homogeneity of absorbers, adhesion in the back interface and overselenization/oversulfurization of Mo should also be considered during thermal treatments. However, to address these issues, one should combine the optimization of precursor deposition with the design of thermal treatments. For instance, the homogeneity of absorbers is first correlated to the homogeneity of precursors and then to the thermal treatment profiles. Adhesion in the back can be related to the stress in the interface induced by insuitable cooling rate but also to the crystal orientation of Mo determined by the Mo deposition process[164]. The overselenization of CZTSe solar cells can be minimized by pre-alloying of precursors at low temperatures before high temperature annealing[165], but modifying the Mo configurations or depositing a nanolayer of MoO_2 on top of Mo could be more flexible and controllable[157].

3.2 Thermodynamics equilibrium in the single-step sulfo-selenization process

To understand the S/(S+Se) ratio variations in the CZTSSe thin films as function of added S/(S+Se) ratio, annealing temperature and system pressure, the thermodynamics equilibrium between CZTSSe absorbers and chalcogen vapor is analyzed. The chemical equilibrium equation during the single-step sulfo-selenization process can be written as:

$$Cu_2ZnSnS_4(s)+2Se_2(g)\rightleftharpoons Cu_2ZnSnSe_4(s)+2S_2(g) \qquad (3.1)$$

This is achieved by reasonably assuming:

(1) S_2 and Se_2 first react with the precursors and later other species like S_8 and Se_6 (major species, at 550 ºC) will convert to S_2 and Se_2 by chemical equilibrium $S_8(g)\rightleftharpoons 4S_2(g)$ and $Se_6(g)\rightleftharpoons 3Se_2(g)$ [166-168]. This is reasonable because S_2 and Se_2 have higher reaction activity due to its small molecules nature.

(2) CZTSSe polycrystals form by nucleation-growth process and are the solid solution of CZTS and CZTSe. Therefore, the S/(S+Se) ratio of CZTSSe absorbers is equal to the nominal concentration ratio [CZTS] / ([CZTS] + [CZTSe]).

(3) The final S/(S+Se) ratio of the thin films is the result of chemical equilibrium between CZTSSe and S_2 /Se_2 vapor during the crystal growth process.

Therefore, the chemical equilibrium constant of equation 3.1 can be expressed as below:

$$K^{\theta}(T)=\frac{[\frac{P(S_2)}{P^{\theta}}]^2[Cu_2ZnSnSe_4]}{[\frac{P(Se_2)}{P^{\theta}}]^2[Cu_2ZnSnS_4]} \quad (3.2)$$

$$K^{\theta}(T)=\exp(-\frac{\Delta G^{\theta}(T)}{RT}) \quad (3.3)$$

Then, we have:

$$\frac{[\frac{P(S_2)}{P^{\theta}}]^2[Cu_2ZnSnSe_4]}{[\frac{P(Se_2)}{P^{\theta}}]^2[Cu_2ZnSnS_4]}=\exp(-\frac{\Delta G^{\theta}(T)}{RT}) \quad (3.4)$$

For an ideally sealed system (i.e., the graphite box is assumed to be ideally sealed), assume:

N: Total amount of substance of added sulfur and selenium.
N(S_2) or N(Se_2) : Amount of substance of added sulfur or selenium .
x : Added S/(S+Se) molar ratio.
y : S/(S+Se) molar ratio in CZTSSe thin films.
N*(S_2) or N*(Se_2) : The minimum amount of substance of sulfur or selenium needed to supply to achieve S_2 or Se_2 saturation vapor pressure at a given annealing temperature.
P*(S_2) or P*(Se_2) : Saturation vapor pressure of S_2 and Se_2 at a given annealing temperature.
V : The volume of the container (e.g., graphite box).

We could apply the ideal gas law to estimate the N*(S_2):

$$P^*(S_2)V=N^*(S_2)RT \quad (3.5)$$

Thus, we can get:

$$N^*(S_2)=\frac{P^*(S_2)V}{RT} \quad (3.6)$$

When $N(S_2) \geqslant N^*(S_2)$, $P(S_2)=P^*(S_2)$.

When $N(S_2) < N^*(S_2)$, $P(S_2) = \frac{N(S_2)RT}{V} = \frac{NxRT}{V}$.

For selenium case, similarly we can get:

When $N(Se_2) \geqslant N^*(Se_2)$, $P(Se_2) = P^*(Se_2)$.

When $N(Se_2) < N^*(Se_2)$, $P(Se_2) = \frac{N(Se_2)RT}{V} = \frac{N(1-x)RT}{V}$.

Discussions:

(1) In Equation 3.4, the system pressure P^{θ} will be lost, which means it cannot influence the S/(S+Se) ratio of thin films. This is expected because in a closed container system pressure adjusted by inert gas cannot change the absolute value of $P(S_2)$ or $P(Se_2)$, but can only change the partial pressure of sulfur and selenium.

(2) The Equation 3.4 can be written in different forms depending on $N(S_2)$ and $N(Se_2)$:

Case 1: $N(S_2) < N^*(S_2)$, $N(Se_2) < N^*(Se_2)$:

$$(\frac{x}{1-x})^2 \frac{1-y}{y} = \exp(-\frac{\Delta G^{\theta}(T)}{RT}) \quad (3.7)$$

Case 2: $N(S_2) > N^*(S_2)$, $N(Se_2) > N^*(Se_2)$:

$$(\frac{p^*(S_2)}{P^*(Se_2)})^2 \frac{1-y}{y} = \exp(-\frac{\Delta G^{\theta}(T)}{RT}) \quad (3.8)$$

Case 3: $N(S_2) > N^*(S_2)$, $N(Se_2) < N^*(Se_2)$

$$(\frac{p^*(S_2)}{\frac{N(1-x)RT}{V}})^2 \frac{1-y}{y} = \exp(-\frac{\Delta G^{\theta}(T)}{RT}) \quad (3.9)$$

Case 4: $N(S_2) < N^*(S_2)$, $N(Se_2) > N^*(Se_2)$:

$$(\frac{\frac{NxRT}{V}}{P^*(Se_2)})^2 \frac{1-y}{y} = \exp(-\frac{\Delta G^{\theta}(T)}{RT}) \quad (3.10)$$

From literatures we can obtain by calculations [166,167,170]:

$P^*(S_2) = \exp(-16060.53\ T^{-1} - 1.53\ \ln T - 2.3 \times 10^{-3}\ T + 37.35)$ (torr)

$P^*(Se_2) = \exp(-17559.5\ T^{-1} - 3.537\ \ln T + 41.66)$ (atm)

$\Delta G^{\theta}(T) = 140113.5 - 53.95\ T$ (J/mol) (623 K< T< 813 K)

Therefore, equation 3.7 – 3.10 can further be transferred into equations with only 3 parameters:

added S/(S+Se) ratio x, thin film S/(S+Se) ratio y, and annealing temperature T.

The new versions of equations are as follows:

Case 1: $N(S_2) < N^*(S_2)$, $N(Se_2) < N^*(Se_2)$:

$$y = \frac{1}{(\frac{1}{x}\text{-}1)^2 \exp(\text{-}16851.7T^{-1}\text{+}6.49)\text{+}1} \quad (3.11)$$

Case 2: $N(S_2) > N^*(S_2)$, $N(Se_2) > N^*(Se_2)$:

$$y = \frac{1}{\frac{\exp(\text{-}16851.7T^{-1}\text{+}6.49)}{(\exp(1498.7T^{-1}\text{+}2.007\ \ln T\text{-}2.3*10^{-3}T\text{-}10.84))^2}\text{+}1} \quad (3.12)$$

Case 3: $N(S_2) > N^*(S_2)$, $N(Se_2) < N^*(Se_2)$:

$$y = \frac{1}{\frac{\exp(\text{-}16851.7T^{-1}\text{+}6.49)(\frac{N(1\text{-}x)RT}{V})^2}{(\exp(\text{-}16060.53T^{-1}\text{-}1.53\ln T\text{-}2.3*10^{-3}T\text{+}42.24))^2}\text{+}1} \quad (3.13)$$

Case 4: $N(S_2) < N^*(S_2)$, $N(Se_2) > N^*(Se_2)$:

$$y = \frac{1}{\frac{\exp(\text{-}16851.7T^{-1}\text{+}6.49)(\exp(\text{-}17559.5T^{-1}\text{-}3.537\ln T\text{+}53.17))^2}{(\frac{NxRT}{V})^2}\text{+}1} \quad (3.14)$$

By partial derivative, it is found that for all the cases $y'(x) > 0$ except for Case 2, meaning that the S/(S+Se) ratio in the thin films increases in parallel with the added S/(S+Se) ratio, which is consistent with the experimental results.

In Case 2, the S/(S+Se) in the thin films is independent of added S/(S+Se) ratio. This is very interesting because this means when both of the added amounts of S and Se are over $N^*(S_2)$ and $N^*(Se_2)$, the added S/(S+Se) ratio becomes invalid for adjusting the chalcogen content of the thin films. In other words, in order to modify the S content inside the CZTSSe absorbers, S or Se, at least one of their quantities should be controlled to be lower than the $N^*(S_2)$ or $N^*(Se_2)$.

However, by applying partial derivative to the temperature, only in case 1 we can determine $y'(T) < 0$, indicating higher temperature can reduce the S/(S+Se) ratio in the thin films, being consistent with the experimental observation. For the other three cases, it is very difficult to draw a clear conclusion due to the complexity of those equations. In addition, as the graphite box is actually not an ideally sealed system, chalcogen loss from leakages is unavoidable. Therefore, Se-richer absorbers obtained at higher temperatures could be mainly due to higher loss of S vapour compared with that of Se vapour, and less to the inherent thermodynamics factors.

It should be noted that, experimental results show that the system pressure can clearly influence the absorbers S content. According to the theoretical analysis above, this must be achieved due to the chalcogen diffusion into outer space that changes the vapour pressure of chalcogen inside the graphite box.

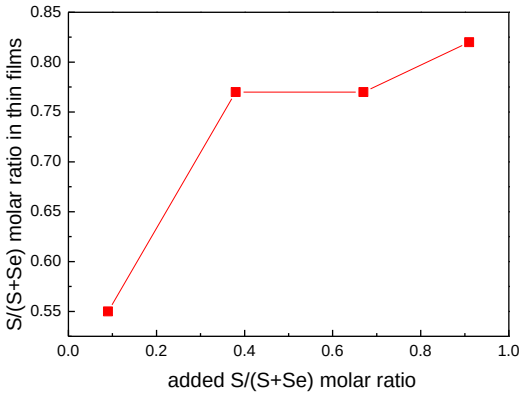

Figure 3.7. S/(S+Se) ratio in the CZTSSe thin films as a function of added S/(S+Se) molar ratio. The S/(S+Se) ratios of the thin films were estimated by EQE. The annealing temperature is fixed at 550 ºC and the total amount of S+Se was kept constant to 50 mg.

Figure 3.7 shows the S/(S+Se) ratio in the CZTSSe thin films as a function of added S/(S+Se) ratio. The curve is composed of three stages: the rapid increase stage at low added S/(S+Se) ratio, the plateau stage at medium added S/(S+Se) ratio, and finally the slow increase stage at high added S/(S+Se) ratio.

Based on the thermodynamics analysis, we may explain this behaviour qualitatively. At low added S/(S+Se) ratio stage, probably $N(S_2) < N^*(S_2)$ while $N(Se_2) > N^*(Se)$, leading to the increase of S/(S+Se) in the films. Continually raising the S quantities will lead to $N(S_2) > N^*(S_2)$ and $N(Se_2) > N^*(Se)$, being invalid for the adjustment of S/(S+Se) ratio of the absorbers. Finally, high S/(S+Se) ratio included in the box means the Se could be deficient to achieve saturation vapour pressure. In other words, $N(S_2) > N^*(S_2)$ while $N(Se_2) < N^*(Se)$ in this stage start to increase the absorbers S/(S+Se) again. The more rapid increase in the first stage compared with the last stage could be due to faster loss of S compared with that of Se due to its smaller molar mass and high molecule speed, as shown in equation (15):

$$V_{rms} = \sqrt{\frac{3RT}{M}} \qquad (3.15)$$

Where V_{rms} is the root-mean-square speed, T is the kelvin temperature, R is the ideal gas constant, and M is the molar mass. These explanations are also supported by theoretical calculations of N*(S) and N*(Se) in this specific case.

To sum up, the thermodynamics equilibrium during the single-step sulfo-selenization process was analyzed. The basic chemical equilibrium equation was established based on several reasonable assumptions. Equations including added S/(S+Se) ratio, S/(S+Se) ratio in the CZTSSe thin films as well as the annealing temperature were achieved in different cases depending on the supplied S and Se. Finally, the thermodynamic model was applied to explain the experimental results. Further specially designed experiments inside sealed ampoules are in progress to confirm the validity of the proposed equations quantitatively. This work will be included in a future publication.

In conclusion, in this chapter the important role of thermal treatment and its optimization were discussed. CZTSSe absorbers with optimal S/(S+Se) and minimized Zn(S,Se) secondary phases

in the front and back interface as well as good crystal quality were obtained by varing the added S/(S+Se) ratio, system pressure and thermal treatment profiles. Finally, thermodynamics analysis was performed to get insights into this single-step sulfo-selenization process. This work paves a way for the further optimization to achieve high efficiency CZTSSe solar cells.

Chapter 4

Secondary phases: a big challenge

4.1 Introduction

4.1.1 Secondary phases in kesterite

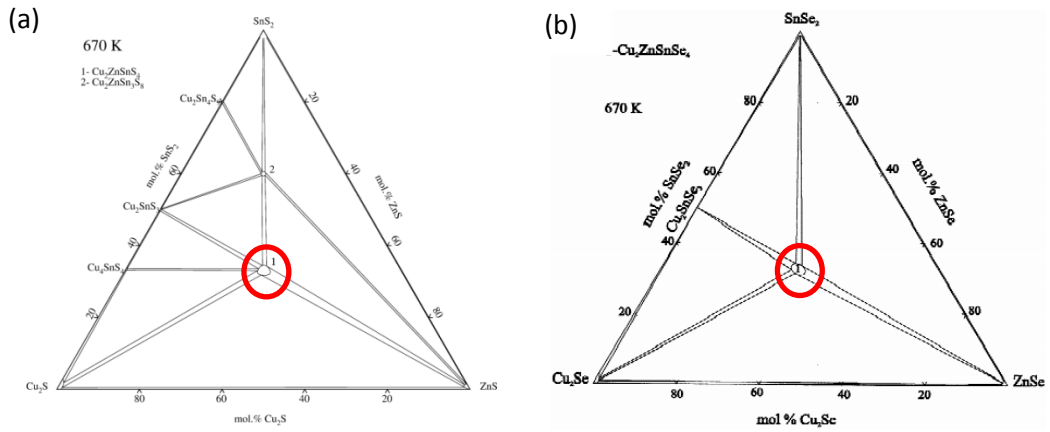

Figure 4.1. Isothermal section of the Cu_2S–SnS_2–ZnS system (a) and Cu_2Se–$SnSe_2$–ZnSe system (b) at 670 K. The zone 1 marked with a red circle in both images represents the single phase zone of CZTS and CZTSe, respectively. The images are taken from ref [171,172].

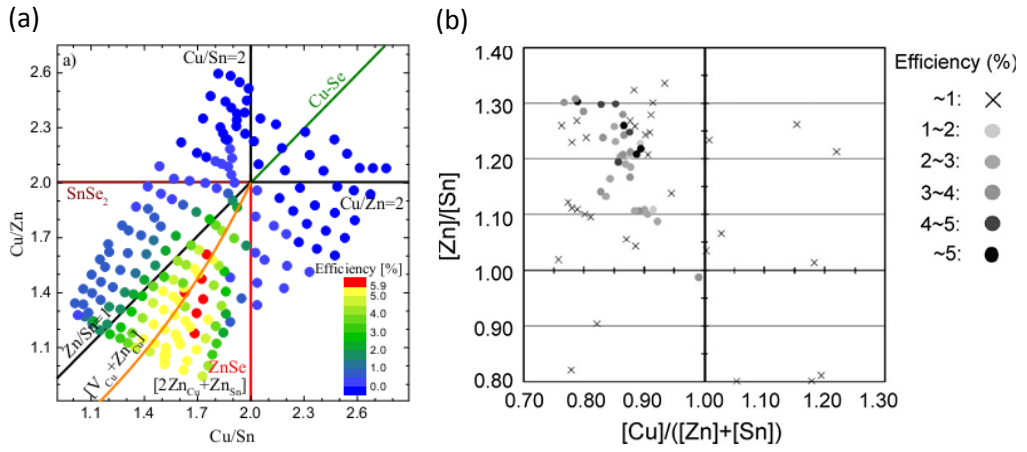

Figure 4.2. Dependence of optoelectronic properties of CZTSe (a) and CZTS (b) solar cells on composition. The images are taken from ref[173] and ref[174], respectively.

Kesterite CZTS and CZTSe have very narrow single phase exsistence zone in the phase diagrams, as shown in Figure 4.1. This is also supported by the composition study of CZTS, CZTSe and $CZTS_{0.7}Se_{0.3}$ monograins by K. Muska et al[175-177] as well as the first principle calculation of stable chemical potential region by Chen et al[93]. In addition, non-stoichiometry Cu-poor Zn-rich compositional condition is accepted as the critical factor to achieve high efficiency kesterite solar cells, due to the avoidance of Cu-S(Se) secondary phases and the

beneficial effect of the donor-acceptor pair (DAP) [V_{cu}+Zn_{Cu}], as shown in Figure 4.2 [173]. Furthermore, relatively low annealing temperature compared with the melting point of kesterite and short dewelling time mean the thermal treatment is somehow under non-equilibrium conditions. All those three factors make the formation of secondary phases in CZTSSe thin films inevitable. Due to these peculiarities, secondary phases like ternary Cu-Sn-(S,Se), binary Zn(S,Se), Cu-(S,Se) and Sn-(S,Se) are prone to appear in the as-prepared absorbers, and have already been detected in several works[27,124,178,179].

$Cu_xS(Se)$ is considered highly detrimental in CIGS films, and may appear as well on the surface of CZTSe films when Cu/(Zn+Sn)＞0.9, which will severely increase the hole concentration and cause short circuits of the p-n junction, reducing the efficiency considerably [124,180,181]. Low band gap phases SnS(Se) (Sn:S(Se) = 1:1, $E_g \approx$ 1-1.3 eV) and $Cu_2SnS(Se)_3$ ($E_g \approx$ 0.8-1 eV) may limit the open circuit voltage of the solar cells, due to a band gap lower than that of the kesterites. It has been reported that only 100 meV of band gap reduction can decrease the maximum achievable efficiency by 8% absolute [182]. The most commonly found and reported secondary phases are Zn(S,Se) because the Cu-poor Zn-rich composition is extensively employed in high efficiency devices. They are assumed to be the reason for high series resistance, which decreases the fill factor and the short circuit current [44,142,143,183]. Table 4.1 summarizes the potential dentrimental impact of secondary phases on kesterite solar cells.

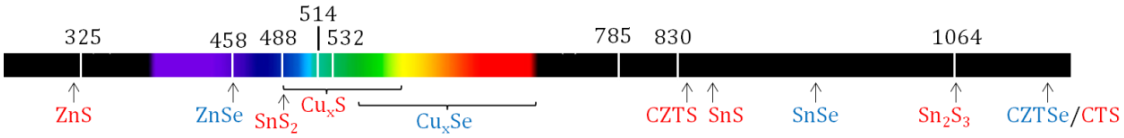

Figure 4.3. Detection of different secondary phases in kesterite system by pre-resonant Raman spectra with appropriate excitation wavelengths. The image is generated from [184] and reproduced from the IEEE poster of X. Fontané et al.

In addition, to detect secondary phases in kesterite system is a challenge. For example, the extensively used XRD is not an effective tool for distinguishing quaternary $Cu_2ZnSnS(Se)_4$, ZnS(Se) and $Cu_2SnS(Se)_3$, as they have highly similar crystalline structures[185,186]. Raman with green excitation wavelength (514.5 or 532 nm) is not sensitive to identify Zn(S,Se) because of low Raman scattering efficiency[161]. Several methods have been developed to detect ZnS(Se), including X-ray absorption near edge structure (XANES)[187,188], room temperature PL[189], TEM[64,183], atom probe tomography (APT)[38,190], EDS mapping[27,191] and pre-resonant Raman spectra[160,161,184,192], etc. Among them, pre-resonant Raman methodology is fast, non-destructive, and sensitive to detect secondary phases. The key is to employ excitation lights with photon energy close to the band gap of secondary phases to get resonant excitation conditions. It is found that UV light (325 nm) is effective to identify ZnS [161], blue light (458 nm) is sensitive to inspect ZnSe[160] , green light (514.5 or 532 nm) is sensitive for the detection of $Cu_xS(Se)$[124,184], and red light (785 nm) can effectively detect SnS(Se)[192]. Figure 4.3 summarizes the detection of different secondary phases in kesterite system by pre-resonant Raman spectra with appropriate excitation wavelengths.

Finally, the distribution of secondary phases is also critical. The secondary phases may be present either at the interfaces (surface and back contact) [64,142,143], in the bulk or grain boundaries[27,191,193,194], and in fact there are several reports confirming their possible

presence along the whole thickness of the films[38,190]. When present in the back region or in the bulk, the detrimental effects of secondary phases cannot be avoided, and in fact, prevention is probably the only solution, by choosing idealized synthesis conditions: precursors, composition, processes parameters, post treatments, etc., as discussed in Chater 3. Conversely, when present on the surface, one of the solutions is to remove them by etching.

4.1.2 Etchings in kesterite technology

Table 4.1. Summary of etching procedures for CIGSSe and CZTSSe solar cells.

Secondary Phases	E_g (eV)	Potential detriment	Etching routes	Etching reactions	Reference
$Cu_x(S,Se)$ $(1\leq x\leq 2)$	1.2–2.2	Shunted devices	5%-10%w/v KCN,RT,0.5-30min	2 CuS(Se)(s) + 5 KCN(aq) + 2 KOH (aq)= 2 $KCu(CN)_2$ (aq)+ 2 K_2S(Se)(aq) + KCNO(aq) + H_2O(l)	[124,180, 181]
ZnS	3.7	Decrease J_{sc}, Increase R_s	5%-10% v/v HCl,75℃, 5-10 min	2HCl(aq)+ZnS(s)=$ZnCl_2$(aq)+ H_2S(g)	[142]
ZnSe	2.7	Decrease J_{sc}, Increase R_s	$KMnO_4$(0.01M)/H_2SO_4 (1M) 30-40 s then Na_2S(1M)1 min, RT	8H_2SO_4(aq)+2$KMnO_4$(aq)+5ZnSe(s)=5Se(s)+5$ZnSO_4$(aq) +2$MnSO_4$(aq)+K_2SO_4(aq)+8H_2O(l) 6NaOH(aq)+3Se(s)=Na_2SeO_3(aq)+2Na_2Se(aq)+3H_2O(l)	[143]
Cu-Sn-Se (Cu_2SnSe_3, Cu_3SnSe_4)	0.8-1.0	Reduce V_{oc}	0.02M Br_2/MeOH, RT	____	[144]

Etchings can be categorized into physical and chemical etchings. Physical etchings include plasma and laser etchings, which use sputtering or laser induced local utral-high temperature to remove the surface layer of materials[196-198]. In fact, usually these ethcings are not selective and are energy consuming. In contrast, chemical etchings are based on chemical reactions between the etching agents and the materials, thus, normally it is possible to find a selective and effective chemical route for each material. For kesterite CZTSSe thin films, the aim is to find customized chemical etchings to remove ZnS, ZnSe, Cu-(S,Se), Cu-Sn-(S,Se) and Sn-(S,Se) secondary phases present on the surface. KCN etching is now a daily routine for CIGSSe processing, which can effectively remove Cu-(S,Se) also for kesterites[180,181]. Br_2/MeOH was reported to remove Cu-Sn-Se related secondary phases[144]. For ZnS, 5-10 % hot (75℃) HCl solution is a useful way to selectively remove it [142]. For ZnSe removal, an oxidation route using $KMnO_4/H_2SO_4$ followed by Na_2S solution rinse was developed and its effectiveness was shown[143]. Table 4.1 shows the summary of most interesting etching routes developed until now for CIGSSe and CZTSSe solar cells.

However, the development of a method for the removal of Sn-(S,Se) secondary phases, is still a pending task, presumably because this secondary phase occurs to a lesser extent than Cu-(S,Se) in CIGSSe and Zn(S,Se) in CZTSSe absorbers. Nevertheless, its presence has been noticed in several literature cases [199,200].

4.2 $(NH_4)_2S$ etching

4.2.1 Removal of Sn-(S,Se) secondary phases

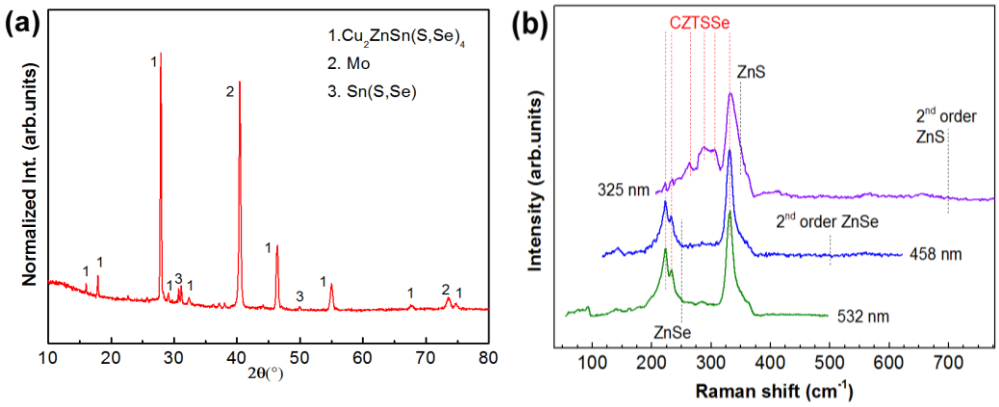

Figure 4.4. (a) XRD patterns of representative CZTSSe absorbers. (b) Raman spectra of representative CZTSSe absorbers with 532 nm, 458 nm and 325 nm excitation light.

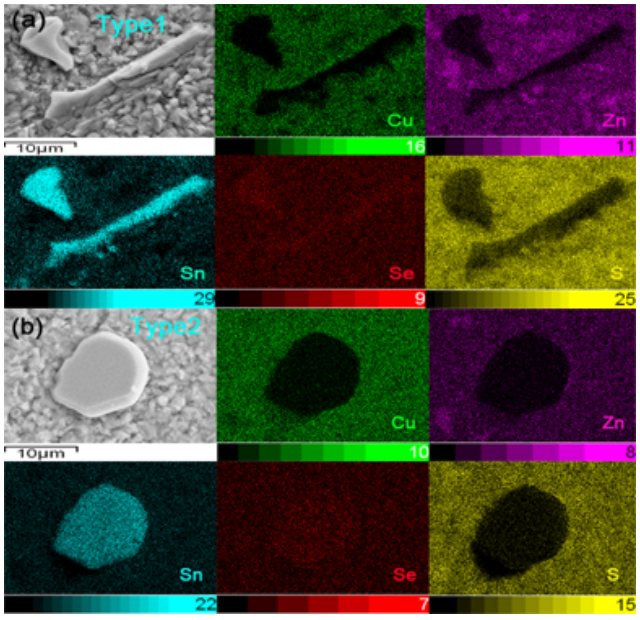

Figure 4.5. SEM images and EDS mappings of features with different morphologies observed on the surface of $Cu_2ZnSn(S,Se)_4$ absorbers. (a) Type 1– rod-like Sn(S,Se) and (b) Type 2– round or semicircular Sn(S,Se).

First of all, to study the etching of secondary phases it is necessary to know what kind of secondary phases on the surface of CZTSSe absorbers. Figure 4.4 shows the XRD patterns and Raman spectra with 532, 458 and 325 nm of a representative Se-rich CZTSSe thin films. XRD patterns indicate that Sn(S,Se) is present in the absorbers. Raman spectra display that the

surface of the CZTSSe samples under study in this work is Cu_xS, Cu_xSe (x<1.8), ZnSe, and ZnS free. The presence of ternary Cu-Sn-(S,Se) phases cannot be discarded, but considering the imposed Zn-rich and Cu-poor compositional conditions, their formation is highly non-expected.

In addition, SEM images and EDS mapping were measured on the CZTSSe absorbers to cofirm the presence of Sn(S,Se) secondary phases on surface, as shown in Figure 4.5. Two types of Sn(S,Se) were found: type 1 with a rod-like shape, integrated in the surface of the CZTSSe film whereas type 2 with approximately round or semicircular shape.

To remove the Sn(S,Se) secondary phases, KCN (2 % w/v), Na_2S (1M), and $(NH_4)_2S$ (22% w/w) solution were tested. Results show that $(NH_4)_2S$ is very effective to remove the Sn(S,Se) secondary phases, as shown by XRD patterns (Figure 4.6) and SEM images (Figure 4.7).

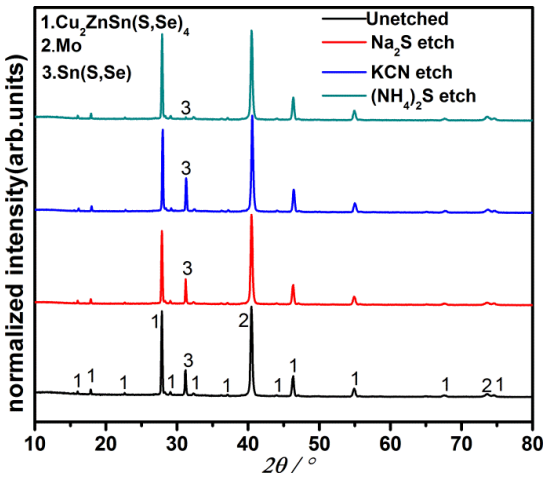

Figure 4.6. XRD patterns of $Cu_2ZnSn(S,Se)_4$ absorbers before and after etching with KCN, Na_2S and $(NH_4)_2S$ solutions.

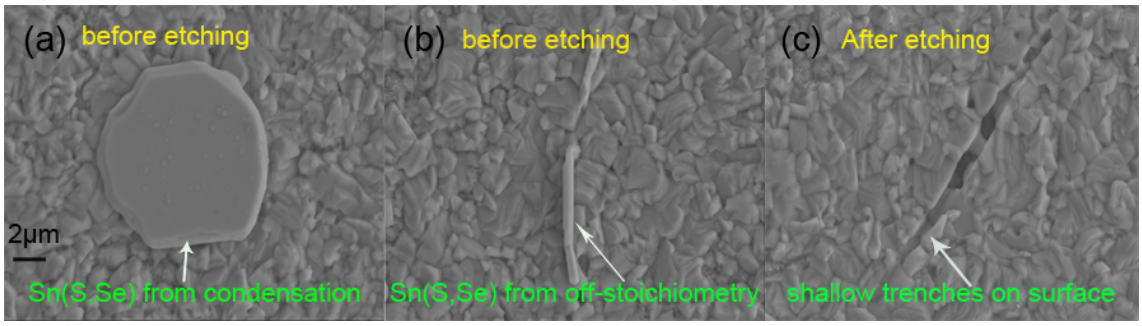

Figure 4.7. SEM images of Type 2 (a) and Type 1 (b) Sn-(S,Se) secondary phases before etching on $Cu_2ZnSn(S,Se)_4$ absorbers, and (c) Surface image after removal of Sn-(S,Se) secondary phase with 22% $(NH_4)_2S$ chemical etching, showing the formation of shallow trenches, which is related to type 1 Sn(S,Se).

The formation of shallow trenches on the CZTSSe absorbers surface after $(NH_4)_2S$ etching as shown in Figure 4.7 c is apparently related to type 1 Sn(S,Se) secondary phases removal. On the other hand, removal of type 2 Sn(S,Se) does not leave any traces. The different morphorlogies

after etching of these two types of Sn(S,Se) could indicate distinct origin for each type. The phase with elongated shape are most probably formed during the synthesis process, explaining why they are encrusted in the surface, while the other one may come from the condensation of Sn-(S,Se) during the cooling process, explaining why it is on the surface of the films. When the annealing furnace is cooled down under vacuum, there are less Type 2 secondary phases on the surface, which also support this conclusion.

In addition, etching rates on SnSe, $SnSe_2$, SnS, SnS_2 as well as CZTSSe thim films with 22 % w/w $(NH_4)_2S$ solution were estimated, which comfirms the high selectivity of $(NH_4)_2S$ on SnS and SnSe secondary phases (Table 4.2). The etching rate is lower for $SnSe_2$ and SnS_2 than that of SnSe and SnS in this experiments, but it is still higher than that of kesterite absorbers, indicating relative selectivity on these two secondary phases. It should be noted that the effectiveness of $(NH_4)_2S$ solution on removal of $SnSe_2$ was later verified by a collaborative work on electrodeposited CZTSe solar cells with efficiency above 8%[192, 201]. The effective and selective ethcing of Sn-(S,Se) with $(NH_4)_2S$ solution is ascribed to the formation of soluble complexes ammonium thiostannate(IV) specie by means of the following reactions (the reactions are illustrated for the Se pure compounds but are analogues for the sulfide and sulfo-selenide ones)[202,203]:

$$SnSe + S^{2-}S = SnSeS_2^{2-} \quad (4.1)$$

$$2NH_4^+ + SnSeS_2^{2-} = (NH_4)_2SnSeS_2 \text{ (soluble)} \quad (4.2)$$

Table 4.2. Etching rate of 22% w/w $(NH_4)_2S$ on Sn-S, Sn-Se and CZTSSe thin films. SnSe mixes with a little $SnSe_2$, and SnS_2 mixes with a little SnS. However, the conclusion is not affected.

Thin film compound	**$Cu_2ZnSn(S,Se)_4$**	**SnSe**	**$SnSe_2$**	**SnS**	**SnS_2**
Etching rate ($nm.s^{-1}$)	< 0.13	1.2	0.2	1.1	0.5

4.2.2 Improvement in optoelectronic properties

The impact of Sn(S,Se) removal by $(NH_4)_2S$ etching on the optoelectronic properties of CZTSSe solar cells was investigated, as shown in Figure 4.8 and Table 4.3. All the parameters have been improved after $(NH_4)_2S$ etching. Especially, the V_{oc} and FF are improved cosiderably. In addition, EQE and Bias EQE indicate the improvement of carrier collection efficiency, which contributes to the higher J_{sc} achieved in etched devices. The FF increase can be attributed to the improved $R_{sh.}$ The V_{oc} improvement could be due to the removal of low band gap Sn(S,Se) and the passivation of the CZTSSe surface by S species.

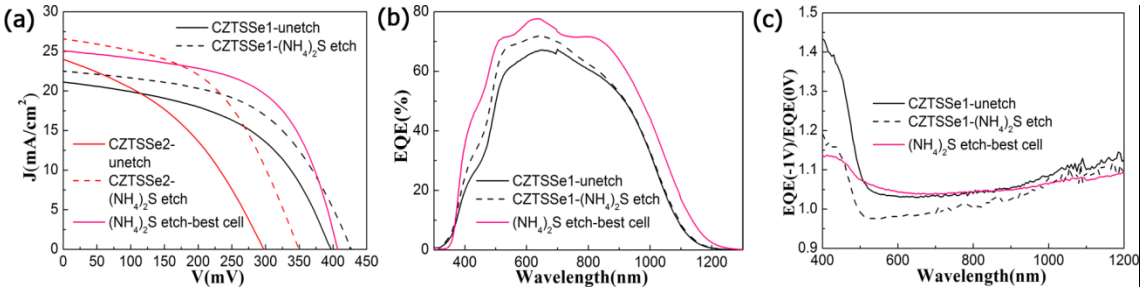

Figure 4.8. Illuminated J-V curves of CZTSSe1 and CZTSSe2 solar cells before and after 22% w/w $(NH_4)_2S$ etching, and the best solar cell obtained with the optimized process, producing a 5.9% efficiency device (a). EQE curves of CZTSSe1 and the best cell (b) and EQE(-1V)/EQE(0V) for CZTSSe1 and the best cell (c).

Table 4.3. Optoelectronic properties of devices before and after 22% w/w $(NH_4)_2S$ etching.

Type	absorber	etching	J_{sc} ($mA.cm^{-2}$)	V_{oc} (mV)	FF (%)	Eff. (%)	R_s ($\Omega.cm^2$)	R_{sh} ($\Omega.cm^2$)	A	J_0 ($mA.cm^{-2}$)
CZTSSe1	Little Sn-(S,Se) content on surface	unetch	21.1	397	49.8	4.2	1.5	91	2.0	1.2×10^{-2}
		$(NH_4)_2S$ etch	22.4	427	52.9	5.1	2.6	142	1.7	2.1×10^{-3}
CZTSSe2	High Sn-(S,Se) content on surface	unetch	23.9	296	39.3	2.8	_	_	_	_
		$(NH_4)_2S$ etch	26.5	349	49.5	4.6	_	_	_	_
	Best cell	$(NH_4)_2S$ etch	25.1	406	57.6	5.9	0.7	109	1.7	1.4×10^{-3}

4.2.3 Passivation mechanism

The passivation effect by $(NH_4)_2S$ etching can be supported by the decrease of diode factor A and saturation current J_0. In addition, XPS measurements show that after $(NH_4)_2S$ etching, the surface S content of the Se-rich CZTSSe samples is much higher than that of the samples before ething[204]. Furthermore, this passivation effect promoted by $(NH_4)_2S$ has already been observed in III-V semiconductors and reasonable mechanisms were proposed[205,206]. Taking the mechanisms as a reference, to clarify the passivation of $(NH_4)_2S$ ethcing on CZTSSe absorbers, we propose an updated route which implies the elimination of surface oxides and the formation of S passivated species on the surface. The mechanism is based on a three steps process as shown in Figure 4.9. In the first step the sulfur ions (preferentially HS^- due to the pH of the solution) react with the surface metallic oxides, breaking the bond between the chalcogen and the metals as is presented in Figure 4.9 a, forming soluble metal chalcogenides species, and leaving a H^+ ions in the solution. This process produces free bonds at the surface for subsequent bond formation with sulfur ions from the $(NH_4)_2S$ solution. After the dissolution of the native oxides, in a second step, the electrons from the conduction band of the semiconductor are transferred to the solution to neutralize the hydrogen ions created in the previous step (Fig 4.9 b). This electron transfer allows for the formation of chemical bonds between the S^{2-} free in the

solution and the chalcogen atoms of the semiconductor (Fig 4.9 c), explaining the passivation of the surface.

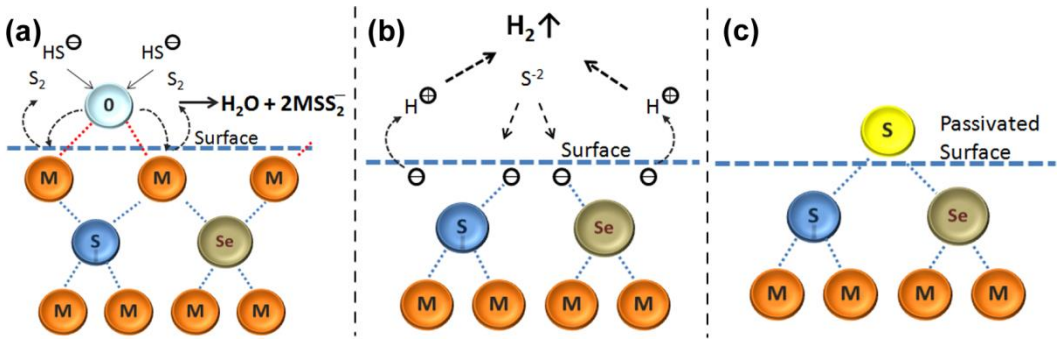

Figure 4.9. Schematic representation of the passivation of CZTSSe surface using yellow $(NH_4)_2S$ solutions. Removal of the native oxides with the HS^- ions (a); electron transfer from the semiconductor towards the H^+ ions of the solution and production of H_2 (b); and formation of the bond between the sulfur and the dissolved chalcogen (c).

In conclusion, in this chapter the big challenge of secondary phases formation in CZTSSe thin films and their removal by chemical etchings were discussed. The secondary phases are somehow inevitable, due to the extremely narrow single phase existence zone in the phase diagram of kesterites, the off-stoichiometry conditions used for the preparation of high efficiency devices (Zn-rich and Cu-poor composition), and the non-equilibrium conditions used during thermal treatments. However, it is feasible to minimize them by thermal treatment optimization as shown in Chater 3, and particularly, if the sencondary phases are present on the surface, they can be removed by suitable wet chemical etchings.

Sn(S,Se) are the only secondary phases found on the Se-rich CZTSSe absorbers surface explored in this work, which can form either from stoichiometric deviations during synthesis process or by condensation from the annealing atmosphere containing Sn and the chalcogens. 22% yellow $(NH_4)_2S$ solution can effectively and selectively remove Sn-(S,Se) secondary phases via the formation of soluble complexes ammonium thiostannate (IV) sepecie.

The presence of Sn(S,Se) secondary phases in the front CZTSSe/CdS interface clearly degrade the performance of devices mainly due to reduction of V_{oc} and FF. Additionally, the yellow $(NH_4)_2S$ solution is not only effective for the selective removal of Sn-(S,Se), but also can passivate the surface, decrease interface recombination, and ultimately improve the p-n junction quality and the conversion efficiency of CZTSSe based solar cells. Finally, a surface passivation mechanism of CZTSSe with $(NH_4)_2S$ solution was proposed.

This work is included in the paper titled "Impact of Sn-(S,Se) secondary phases in $Cu_2ZnSn(S,Se)_4$ solar cells: a chemical route for their selective removal and absorber surface passivation". The paper can be found in the Appendix and is submitted in requirement for the Doctor of Philosophy in Engineering and Advanced Technologies at the University of Barcelona.

Chapter 5

CZTSSe/CdS interface: the holy grail for engineering

5.1 Introduction

5.1.1 Interfaces in CZTSSe solar cells

The most important interface in CZTSSe solar cells is the front interface CZTSSe/CdS, because it is the p-n junction region, which forms built-in electric field that separates electrons and holes, leading to the so-called photovoltaic effect. There are several basic requirements for a good quality CZTSSe/CdS interface.

First of all, good coverage of CdS onto the surface of CZTSSe absorber is necessary to reduce the shunt paths. This can be realized by optimization of CdS deposition process and CZTSSe absorber surface. The most popular method to deposite CdS nowadays is chemical bath deposition (CBD). Through optimization of deposition temperature and time, pH, and Cd precursor (different Cd salts) as well as extrinsic doping, it is possible to to promote the ion by ion growth of CdS and ultimately form good coverage of high quality CdS onto CZTSSe absorbers. Our group has achieved better coverage of CdS by substituting $CdSO_4$ with $Cd(NO_3)_2$ as Cd precursor[207]. In addition, Cu doping in the CBD process can also improve the quality of CdS layer and this will be discussed in the following section. On the other hand, CZTSSe absorbers with smoother surface are favorable for the coverage of CdS.

Secondly, good epitaxial quality of CZTSSe/CdS interface is very important in reducing the interface recombination. The dangling bonds and structural defects on the surface can severly degrade the performance of kesterite solar cells. It is reported that by air annealing of absorbers or optimization of absorbers formation process the surface structural defects of CZTS absorbers can be cured and good epitaxial growth of CdS onto CZTS thin films can be achieved[42]. Additionally, suitable crystal orientation of CZTSSe surface could also be beneficial for the CZTSSe/CdS quality as less lattice mismatch could be expected, although no reports are available. However, the fact that (220)/(204) oriented CIGS surface enables favorable CIGS/CdS junction than (112) oriented one could be an example[208].

Last but not least, the band alignment of CZTSSe/CdS, especially the conduction band offset (CBO), should be seriously considered. Generally speaking, there are three types of band alignment for heterojunctions, including straddling gap (type I), staggered gap (type II) and broken gap (type III), as can be seen in Figure 5.1.

The favorable band alignment for solar cells is type I with a “spike” like conduction band offset (CBO) less than 0.4 eV[209,210]. Because a “cliff” like CBO will reduce the barrier between the conduction band of buffer layer and the valence band of the absorber, increasing the interface recombination. Additionally, CBO higher than 0.4 eV will block the short circuit current. Figure 5.2 shows the simulation results of the impact of CBO on the optoelectronic properties of $CuInSe_2$ solar cells, which is also valid for CZTSSe solar cells.

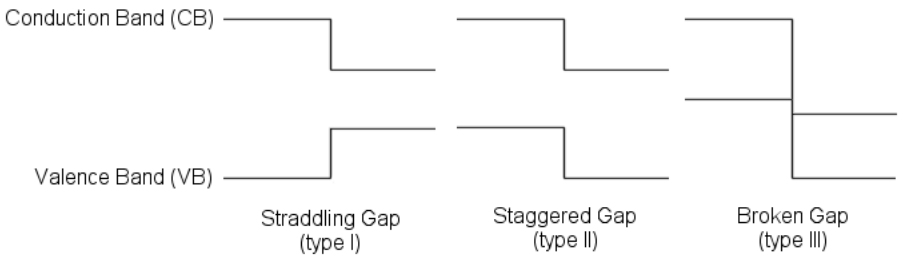

Figure 5.1. The three types of semiconductor heterojunctions organized by band alignment.

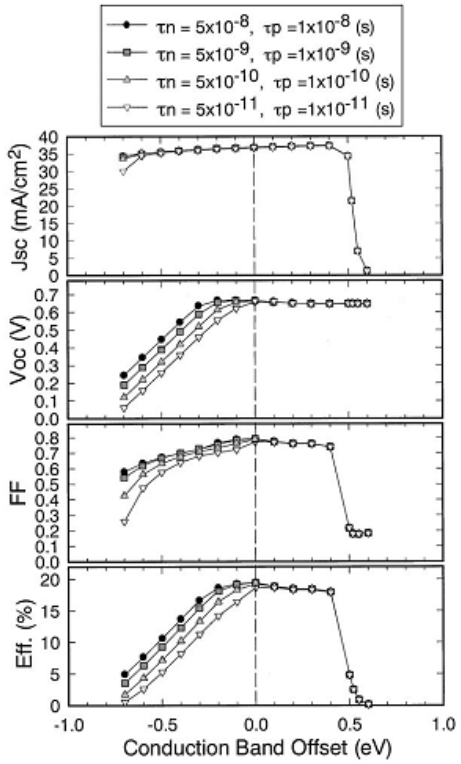

Figure 5.2. Calculated solar cell parameters as a function of the conduction band offset of window/CIGS layers. τ_n and τ_p are lifetime of electron and hole at the interface between window and OVC layers, respectively. The image is taken from ref [209].

The back interface CZTSSe/Mo is the exit of holes in the devices, which also has large influence on the optoelectronic properties. A good back interface requires an ohmic contact to facilitate the current flow and benign adhesion to prevent absorbers delamination. In addition, $Mo(S,Se)_2$ usually forms on the surface of Mo during crystalization process by thermal treatment. The thickness and orientation of this layer have crucial influence on the performance of CZTSSe solar cells. It is reported that a too thick $MoSe_2$ layer can increase the series resistance, leading to the deterioration of FF and J_{sc} [70]. In addition, $Mo(S,Se)_2$ with c-axis parallel to the substrate is favorable for the adhesion and optoelectronic properties of solar cells [157,211].

In this work, the front interface CZTSSe/CdS is focused and studied, which will be discussed in the next sections.

5.1.2 Na doping and distribution

As discussed in Chapter 1, Na is paramount for high efficiency CIGS and CZTSSe solar cells, mainly due to passivation of defects in the grain boundaries and interfaces. The impact of Na concentration on device properties is frequently reported and the optimal concentration is considered to be around 0.1at% [212,213]. However, the impact of Na spatial distribution, i.e., Na in-depth distribution in absorbers, interfaces and buffer/window layer, on devices is rarely investigated. Recently, V. Fjallstrom et al. reported the important role of Na distribution in active CIGS/CdS interface region during potential induced degradation (PID) process, which gives insight into the impact of Na spatial distribution on CIGS solar cells performance[214].

5.2 Na dynamics in the CZTSSe/CdS interface

5.2.1 Motivation

IBM has reported on the introduction of a post low temperature treatment (PLTT) of CZTSSe absorbers at 375 ºC in air before buffer layer deposition as a key step for high efficiency solar cells exceeding 10% [215]. The efficiency enhancement was ascribed to Cu-depleted and SnO_x-rich grain boundaries. Moreover, an air PLTT of pure selenide $Cu_2SnZnSe_4$ (CZTSe) solar cells under 200ºC for large improvement of performance was reported as well[216], which correlates the efficiency increase mainly with Cu-poorer Zn-richer surface and grain boundaries. Additionally, PLTT of pure sulfide Cu_2ZnSnS_4 (CZTS) solar cells or CZTS/CdS was proved to improve efficiency through changing ITO resistivity or forming a hetero-phase epitaxial junction at the CZTS/CdS interface, respectively[217,218]. Furthermore, another work showed that PLTT of CZTSSe absorbers under an inert atmosphere at 200 ºC can improve the efficiency considerably due to the increase of Na concentration in the bulk[219]. All this suggests that, independently of the S/Se content, the processes employed and the characteristics of the solar cell architecture, the absorbers seem to respond distinctly to the PLTT process. However, no investigation about alkali doping during PLTT process are available, although alkali dynamics, especially Na, are systematically reported as crucial within the field. Thus, in this work, the impact of Na during PLTT process and Na dynamics were studied, indicating a close correlation between the performance of CZTSSe solar cells and the Na distribution in the CZTSSe/CdS interface.

5.2.2 Impact of PLTT temperature on CZTSSe solar cells

A as-fabricated CZTSSe absorber was immediately cut into 7 pieces equally, 1 as reference without PLTT process and the other 6 for PLTT in a quartz boat at temperatures ranging from 150 ºC to 400 ºC under 1 bar N_2 atmosphere for 1 h, respectively. Figure 5.3 shows the normalized conversion efficiency, the band gap (E_g), the Urbach energy (E_u) and the normalized EQE spectra as a function of the temperatures employed during the PLTT process of CZTSSe absorbers. Results indicate that 200 ºC is a critical temperature in this study due to the distinct behavior of solar cells properties before and after this temperature. Efficiency and EQE decrease while E_g and E_u increase in the range 150-200 ºC. In contrast, the opposite behaivor of these parameters is observed in the range 200-400 ºC.

To confirm this phenomenon, experiments were repeated to rule out errors or possible accidents during the process. Results of these complementary experiments confirm that PLTT of CZTSSe

absorbers under 200 ºC degrades the efficiency considerably while at 400ºC usually 0.8-1.5% absolute higher efficiency could be achieved compared with the reference cells (see Table 5.1).

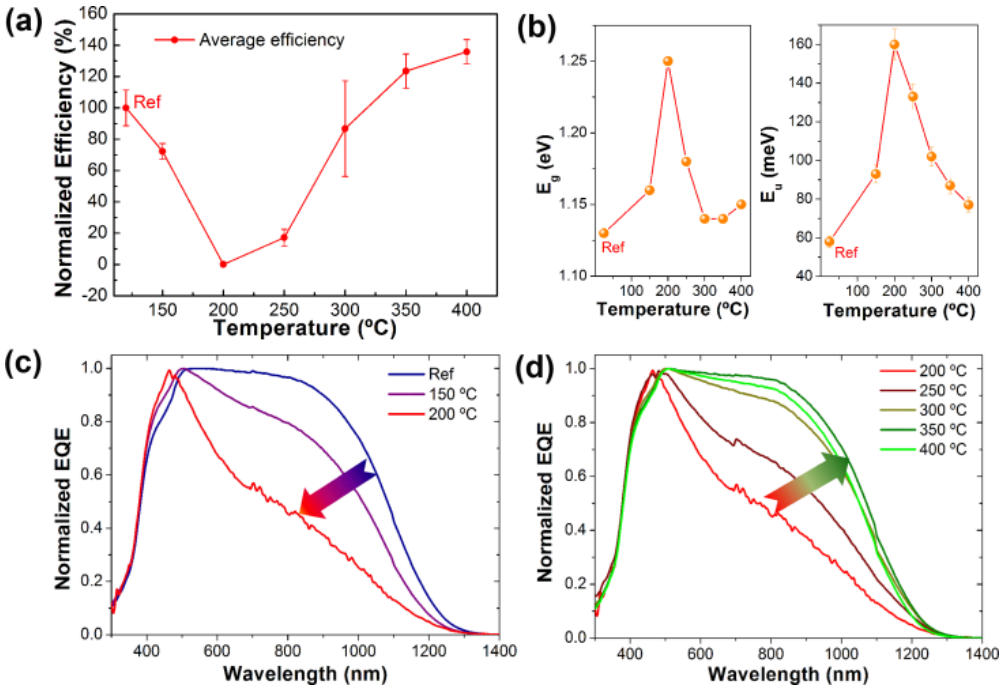

Figure 5.3. Normalized efficiency evolution with the PLTT temperature including the standard deviation determined from 9 different cells (a), band gap (E_g) and Urbach Energy (E_u) extracted from the EQE curves as a function of the PLTT temperature (b), EQE plots showing the degradation of the devices when submitted to a PLTT process in the range of 150-200 ºC (c) and EQE plots showing the recovery of the device properties when submitted to a PLTT process in the range of 200-400 ºC (d). Conversion efficiencies are normalized to the reference solar cell (without PLTT process) and EQE are normalized to the highest value of each spectrum, aiming to get a better comparison.

Table 5.1. Optoelectronic properties of CZTSSe solar cells without PLTT process (reference cells) or with PLTT of CZTSSe absorbers at 200ºC and 400ºC under 1bar N_2 atmosphere.

Batch of experiments	Temperature	J_{sc} (mA/cm^2)	V_{oc} (mV)	FF (%)	Eff. (%)	Average Eff. (9) (%)
1	Ref	23.4	348	44.9	3.7	3.3
	200ºC	0	0	0	0	0
	400ºC	24.5	389	52.1	5.0	4.5
2	Ref	25.1	361	53.3	4.8	4.6
	200ºC	21.0	198	38.0	1.6	1.5
	400ºC	24.3	441	57.2	6.1	6.0
3	Ref	24.2	359	53.2	4.6	4.3
	200ºC	18.1	72.6	32.3	0.4	0.3
	400ºC	23.2	432	58.2	5.8	5.1

5.2.3 Na in-depth profiles and Na dynamics model

To understand the unusual behavior of CZTSSe solar cell performance during PLTT process, the bulk composition, crystalline structure and morphology of these samples under different

PLTT temperatures were checked by XRF, XRD, Raman and SEM. However, no remarkable changes were observed. Therefore, the variations of the performance could be related to cationic composition change (Cu re-distribution) on the surface or in the grain boundaries[215,216], or defects modification induced by post thermal treatments, i.e., order-disorder, extrinsic doping, etc.

Order-disorder effect is not likely responsible for the dramatic change in performance of this work. The observed E_g variations could be related to Cu-Zn order-disorder of kesterites[113]. However, it is reported by several groups that order-disorder effect cannot change the V_{oc} deficit[115-117]. Here the performance seems to have a negative relation with the band gap, with the highest band gap correlating with the lowest efficiency at 200ºC, leading to considerable V_{oc} deficit increase. The composition variations on the surface of CZTSSe absorbers during PLTT process were checked by XPS measurements.Very Cu-poor and Zn-rich surfaces were observed on both the CZTSSe absorbers under 200 ºC and 400 ºC PLTT, which might not necessarily explain the drastic efficiency change, especially for the nearly zero efficiency at 200ºC.

The use of SLG substrates without any chemical barrier layer implies that substrates act as extrinsic alkali doping source for CZTSSe absorbers. Figure 5.4 a and b shows the 3D and 2D TOF-SIMS of Na concentration profiles for the as-fabricated solar cells as well as those with 200 ºC and 400 ºC PLTT processes. The in-depth distribution of other elements (Cu, Zn, Sn, S, and Se) has no changes among the in-depth resolution of this technique.

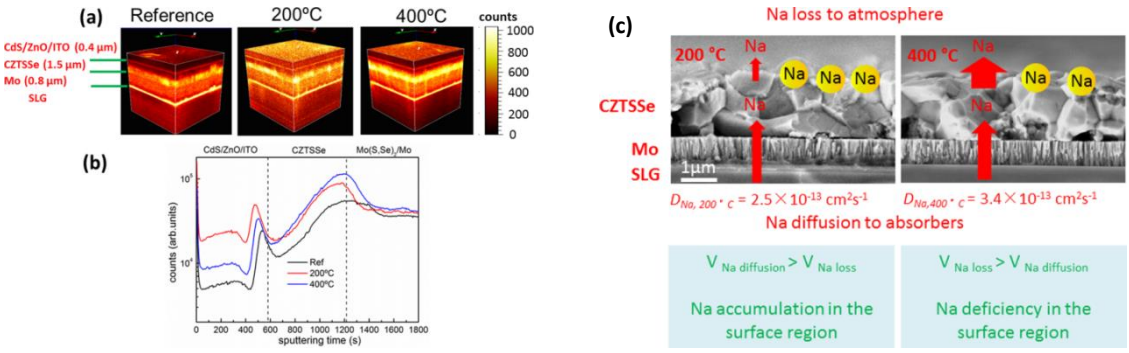

Figure 5.4. 3D (a) and 2D (b) TOF-SIMS of Na concentration in the reference solar cell without PLTT and solar cells with 200 ºC and 400 ºC PLTT. Proposed Schematic of Na dynamics during PLTT process of CZTSSe absorbers (c).

Results show that higher Na concentration in the absorber surface, CZTSSe/CdS interface and window layer but lower Na concentration in the back of the absorber is observed at 200ºC, while lower Na concentration in the upper layer but higher Na concentration in the back of the absorbers is detected at 400ºC. The lower Na content in the back of the absorber at 200 ºC compared with 400 ºC is reasonable as Na diffusion rate from the substrate is enhanced by higher temperature, which is supported by thermal dynamic calculations, yelding Na diffusion coefficient at two key PLTT temperatures: $D_{Na,200ºC} = 2.5\times10^{-13}$ cm^2s^{-1} and $D_{Na,400ºC} = 3.4\times10^{-13}$ cm^2s^{-1}. However, the Na concentration at the surface is unexpectedly higher for the sample treated at 200ºC. In consequence, if theoretical calculations point towards a higher Na flux at higher temperatures, the only plausible cause is that Na is lost from the surface at high

temperatures in a large extent due to a higher vapor pressure of possible Na containing species like Na_2CO_3, Na_2O, $Na_2Se(S)$, or $Na_2Se(S)O_3$…etc.[220] Based on the analysis obove, an innovative Na dynamics model is proposed to explain the Na profiles under 200 ºC and 400 ºC PLTT processes, as shown in Figure 5.4 c. At 200ºC, the diffusion rate of Na ($V_{Na\ diffusion}$) from the SLG to the absorber is higher than the loss rate of Na ($V_{Na\ loss}$) from the absorber surface to the atmosphere, leading to the accumulation of Na in the surface region. On the other hand, at 400 ºC, higher temperature accelerates both $V_{Na\ diffusion}$ and $V_{Na\ loss}$, but seems that $V_{Na\ loss}$ is more enhanced than $V_{Na\ diffusion}$, thus leading to the relative deficiency of Na in the surface region compared with that at 200 ºC.

5.2.4 Mechanism discussion

The efficiency variations during PLTT process could be correlated with the Na re-distribution in the CZTSSe/CdS p-n junction region. The effect of PLTT on the performance of CZTSSe solar cells in this work is mainly from the change of V_{oc} and FF and partially from the change of J_{sc} (see Table 5.1).

(1) **V_{oc} variations**. At 200ºC, high level of Na concentration in the active region could cause severe recombination in the CZTSSe/CdS interface and in the n-type buffer/window layer and change the n-type doping of the layer, since Na acts as acceptor in CdS and ZnO buffer/window layer[221,222]. Thus, according to the well-known diffusion-drift equilibrium in the p-n junction region, the built-in voltage could be weakened drastically, leading to severe degradation of V_{oc} in CZTSSe solar cells. At 400ºC, less Na in the active region compared with that in 200ºC leads to the recovery of the p-n junction quality and V_{oc}. The V_{oc} increase compared with that of the reference cells could be among other factors associated to the passivation of non-radiative defects in the bulk or CZTSSe/CdS interface through an appropriate content of Na[213,223-226]. Furthermore, 400ºC PLTT devices have a Zn-richer surface than that of the reference devices measured by XPS spectra, which can decrease the interface recombination and increase the V_{oc} [227,228]. Finally, Na could also influence the sub-band gap states in the active region of CZTSSe solar cells[223], which may be partially responsible for the E_u variations, and ultimately have an impact on V_{oc}, to a certain extent.

(2) **FF variations**. Devices under 200 ºC PLTT process are heavily shunted (see Figure 5.5 a). Bias EQE measurements at -1V for 200 ºC PLTT devices show a large EQE increase in the range of 300-500 nm, which implies a drastic change of photoconductivity in the buffer/window layer (see Figure 5.5 b). According to Hsu et al., this sharp increase of EQE in the short wavelength region could be related to shunt paths through CZTSSe/CdS interface caused by lateral distributed defects induced by an excessive amount of Zn[229]. However, in this work Zn keeps almost constant during PLTT at 200 ºC as confirmed by XPS, thus an excess of Na in the CZTSSe/CdS interface region could be a possible explanation, leading to the severe degradation of FF.

(3) **J_{sc} variations.** The J_{sc} change can be explained by the depletion width and band gap variations as confirmed by C-V and EQE measurements (see Figure 5.3).

In summary, the severe degradation of performance at 200ºC is mainly because of the degradation of Voc and FF, due to a possible weakening of built-in voltage and shunting in the

interface as well as higher E_u caused by high concentration of Na in the active CZTSSe/CdS interface region. Note that the 400 ºC PLTT devices have the best performance but with the medium Na concentration in the active region among these three devices, which indicates the importance of appropriate Na distribution in CZTSSe/CdS p-n junction region. This also could be explained by the need of appropriate absorber/emitter doping ratio for highly efficient solar cells.

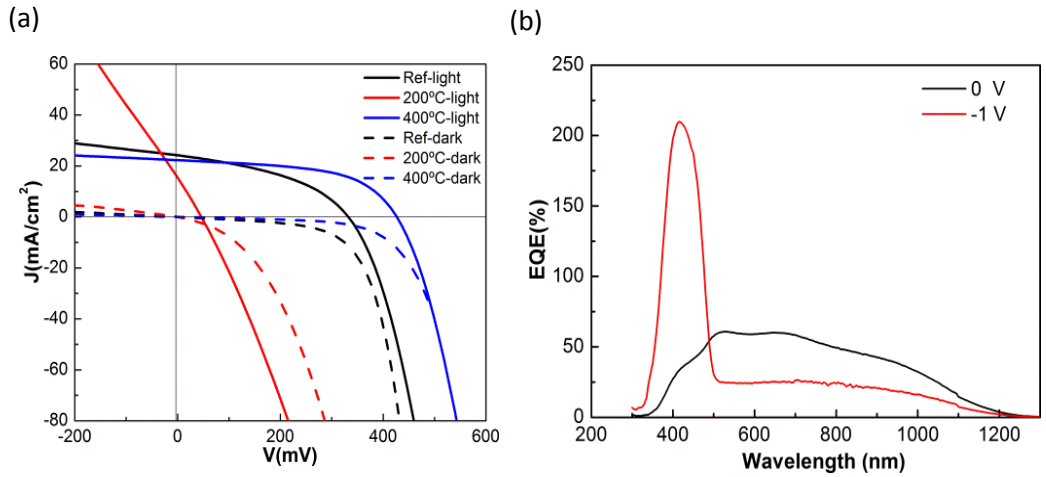

Figure 5.5. Light and dark J-V curves of the reference solar cell without PLTT and solar cells with 200 ºC and 400 ºC PLTT processes (a). EQE of one representative device under 200ºC PLTT at 0V and -1V(b).

The crucial role of Na distribution in the active region can be supported by the results of the potential induced degradation effect on CIGS solar cells[214,230]. The efficiency of CIGS solar cells decreases from more than 15% to nearly zero with an increased Na concentration in the CdS buffer layer and the top third of the CIGS absorbers, and recovers to the same level of the devices before degradation with a decreased Na concentration. Another work reported by C. M. Sutter-Fella et al. also shows the considerable increase of Na concentration in the active CZTSSe/CdS interface region of CZTSSe solar cells and degraded efficiency when 200 nm NaF was introduced[131], which is consistent with the results of 200ºC PLTT process in this work.

Two special designed experiments further support the model of Na dynamics and its important role on the performance of CZTSSe solar cells: (1) When a 10 nm of ZnO was introduced onto Mo surface before metallic precursor deposition and an absorber was completed, the performance of the device was less deteriorated compared with the one without ZnO barrier layer in the control group under 200ºC PLTT process; (2) samples annealed in 1 bar atmosphere degraded considerably while those annealed in 1×10^{-6} bar were nearly not affected under 200ºC. These results possibly can be explained by the decrease of $V_{Na\ diffusion}$ and increase of $V_{Na\ loss}$ in experiment 1 and 2, respectively, which ultimately leads to less Na accumulation in the active region.

In conclusion, in this section Na dynamics during PLTT process was discussed. Large variations of device properties of CZTSSe solar cells during PLTT process can be correlated with different Na concentration in the active CZTSSe/CdS p-n junction region. A model of Na dynamics is developed, featuring two Na fluxes including Na diffusion from the SLG to the absorbers and Na loss from the surface to the atmosphere. Depending on the rate of these two fluxes at a given temperature, namely $V_{Na\ diffusion}$ and $V_{Na\ loss}$, different Na in-depth profiles could be obtained.

This model is validated by theoretical calculations, which allows to estimate the Na diffusion coefficient at two key PLTT temperatures: $D_{Na,200^oC}$ = 2.5×10^{-13} cm^2s^{-1} and $D_{Na,400^oC}$ = 3.4×10^{-13} cm^2s^{-1}. Results show that appropriate content of Na doping especially in the active CZTSSe/CdS interface region of solar cells could be critical for device performance, and PLTT process can be a way to optimize Na in-depth profiles.

This work is included in the paper titled "Impact of Na Dynamics at the $Cu_2ZnSn(S,Se)_4$/CdS Interface During Post Low Temperature Treatment of Absorbers". The paper can be found in the Appendix and is submitted in requirement for the Doctor of Philosophy in Engineering and Advanced Technologies at the University of Barcelona.

5.3 Cu doping in CdS buffer layer

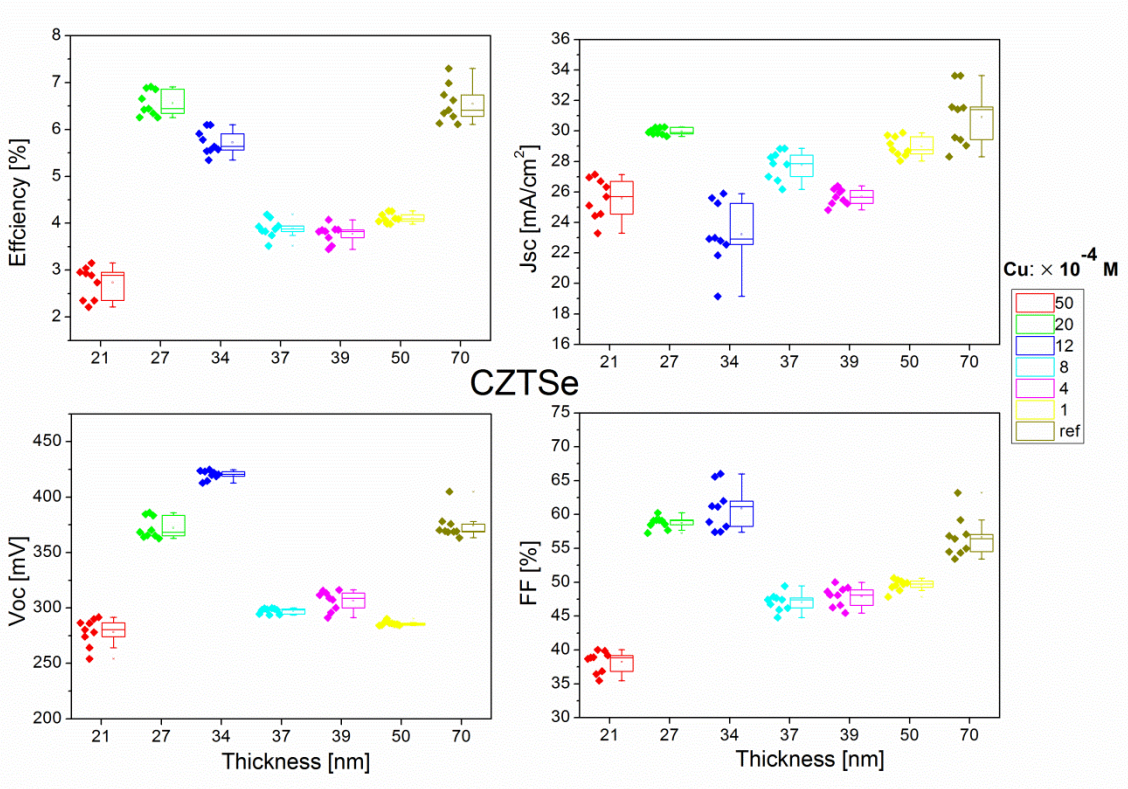

Figure 5.6. Optoelectronic parameters for CZTSe solar cells with different Cu doping concentration in CdS deposition.

Although CdS buffer layer is used extensively in CdTe, CIGS and CZTSSe solar cells, its toxic constituent Cd raises serious environmental concerns. Alternative buffer layers are systematically studied but limited success has been achieved[81-84]. Another solution is to reduce the thickness of CdS buffer layer while keeping or even improving the performance of chalcopyrite solar cells. A successful example is the reduction of CdS thickness by potassium PDT of CIGS absorbers [231]. In this work, an innovative process based on Cu doping of CdS was developed to reduce the thickness of CdS (from 70 nm to around 30 nm) while keeping the same highly performing efficiency level of CIGS and CZTSe solar cells .Various Cu dopings ware performed by adding different concentration of $CuSO_4.5H_2O$ into the CBD solution of CdS and opimial concentration of 2×10^{-3} M was determined (see Figure 5.6). This was achieved

by homogeneous and pin hole free CdS layer, allowing for good coverage and epitaxial CZTSe/CdS interface quality when thinner CdS was deposited, as shown in Figure 5.7.

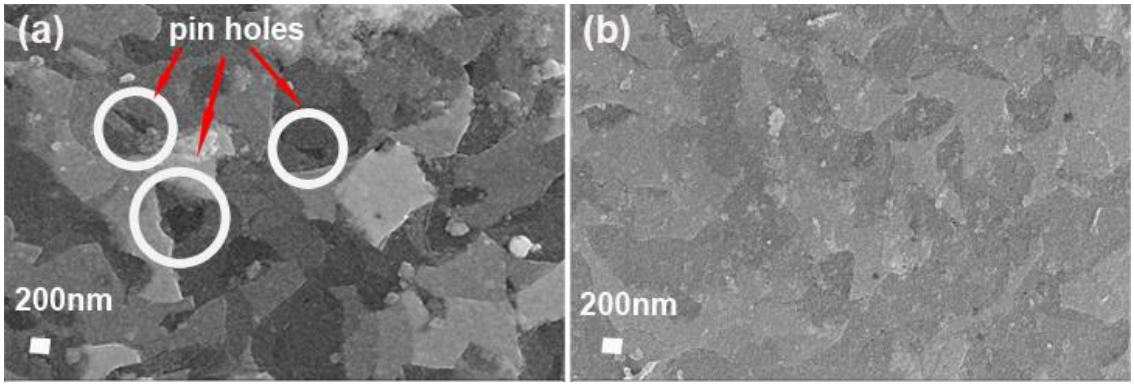

Fig. 5.7. SEM images of the CdS layers grown onto glass. Undoped (a) and Cu doped CdS (5×10^{-3} M)(b).

This work is included in the paper entiltled "Ultra-thin CdS for highly performing chalcogenides thin film based solar cells". The paper can be found in the Appendix and is the only co-authored paper submitted in requirement for the Doctor of Philosophy in Engineering and Advanced Technologies at the University of Barcelona.

5.4 CZTSSe/CdS p-n junction quality improvement by wet chemical treatments

5.4.1 Motivation

As discussed in section 1.2.4, V_{oc} deficit is considered as the main hurdle for kesterite solar cells, with band tailing and interface recombination as plausible causes[36,50,232]. In particular, the CZTSSe/CdS interface is usually reported as the source of the dominant recombination pathway in highly efficient CZTSSe solar cells with band gap above 1.1 eV, including the current record kesterite solar cell [26,27,51]. Thus, engineering the CZTSSe/CdS interface can be a reasonable and effective way to reduce the V_{oc} deficit and further improve the efficiency of CZTSSe solar cells. However, interface engineering of kesterite solar cells are still not well investigated up to date. Na_2S and $(NH_4)_2S$ solutions were reported to have surface passivation effect on the CZTSSe solar cells, but the V_{oc} and FF increase of the solar cells were mainly associated with the removal of ZnSe and Sn(S,Se) secondary phases[143,145]. Additionally, Wu et al. reduced interface recombination and increased the V_{oc} of CZTSSe based solar cells by introducing an ultra-thin layer of TiO_2 by atom layer deposition (ALD) inbetween the absorbers and CdS[233]. However, the conversion efficiency of the devices was only slightly improved due to a deterioration of J_{sc} and almost unaffected FF. Recently, IBM reported that ALD of Al_2O_3 nanolayer onto the surface of CZTSSe absorbers can effectively passivate the surface and improve the performance as well as leveling down the V_{oc} deficit[234]. The ALD process seems promissing, but it is expensive and time consuming (minutes to hours) thus exploring low cost ways is of key relevant for kesterite solar cells. In contrast, Nakada et al. reported that surface modification of the CIGS absorbers through coverage of a layer of metal sulfides or S atoms by using aqueous solutions with group Ⅲ chlorides (Ⅲ=In, Ga, Al, Y) and

thioacetamide (CH_3CSNH_2) can improve all the parameters of the devices. [235] In addition, when this chemical passivation process was applied to CIGS/Zn(O,S) solar cells, considerable V_{oc} and efficiency improvement was observed, due to reduced interface recombination and enhanced minority carrier lifetime.[236,237] This chemical process is fast (seconds to several mins), facile to control, and low cost with respect to ALD process, thus it shows very promising perspectives for the demonstration of this chemical treatment on CZTSSe solar cells.

Therefore, with the aim of reducing interface recombination and improving the p-n junction quality, hence the performance of the CZTSSe solar cells, the impact of the group-III (III=Al, Ga) chemical treatment on the CZTSSe solar cells was systematically evaluated by X-ray photoelectron spectroscopy (XPS), STEM and EELS mapping, J-V curves, External quantum efficiency (EQE), Capacitance-Voltage (C-V), temperature-dependent current-voltage (JV-T) and photoluminescence (PL) measurements.

5.4.2 Wet chemical treatments

The as-prepared CZTSSe absorbers with S/(S+Se) of 0.25-0.3 are etched in 22% w/w $(NH_4)_2S$ solution at room temperature for 2 min to remove Sn(S,Se) secondary phases, and then are immersed in the aqueous solution with group-III chlorides (III=Al, Ga, 0.005-0.1 M) and thioacetamide (CH_3CSNH_2, 0.1-0.5 M) at 80 ºC for 10 s-5 min.

5.4.3 As-treated absorbers surface

Figure 5.8 shows the XPS measurements onto $AlCl_3/GaCl_3$ treated samples with different soaking time. It is difficult to identify the Al peak due to the overlap of Al2p and Cu3p peak, while Ga2p3 and Ga2p1 peaks are clearly visible after10 s treatment (See Figure 5.8 a and 5.8 b). Samples after 60s treatment are selected as representatives for further analysis. Scrutiny of the Al2p-Cu3p overlapped peak reveals that the peak is composed by 3 peaks located at 76.9, 74.7 and 72.7 eV, being related to Cu3p, Cu3p overlapping with Al-O/OH and possible Al-S or metallic bonds, respectively (see Figure 5.8 c) [238,239]. The symmetric Ga2p peak located at 1118.3 eV is assigned to Ga-O/OH (see Figure 5.8 d)[240]. The relative surface concentrations of Al , Ga and S were carefully extracted from the XPS data through integral area of related peaks (see Figure 5.8 e and 5.8 f). It should be noted that the integral area of Al was obtained by subtracting the peak area of the reference sample from those of the chemical treated ones, based on the fact that the reference sample is absent of Al. There is a small amount of Al concentration on the surface, around 1% for all deposition times, while Ga concentration increases in parallel with the increase of deposition time, up to 16% at 120s. S concentration seems to be stable for both $AlCl_3$ and $GaCl_3$ processes, varying between 9-11%, although higher values are observed compared with the reference samples. The existence of S layer on the surface was also reported by other groups [235-237].

STEM and EELS mapping were performed onto $AlCl_3$-thioacetamide 60 s treated samples (see Figure 5.9), which clearly confirms the existence of Al after the wet chemical treatment. In addition, HRTEM micrographs and SAED patterns further identify that Al is deposited in the form of $Al(OH)_3$, as is shown in Figure 5.10, being consistent with the XPS results.

Results indicate that during the chemical treatments the absorber surfaces were covered mainly by group III hydroxides and S layer, which is in contrast with the results of Nakada et al., probably due to the lack of deep analysis of their XPS data. The low concentration of Al-S and

Ga-S is attributed to the high instability of Al_2S_3 and Ga_2S_3 in aqueous solution (e.g., reacting with H_2O to form hydroxides and H_2S). In contrast, $Al(OH)_3$ and $Ga(OH)_3$ are approximately insoluble in H_2O, with solubility product constant K_{sp} equals to 3×10^{-34} and 7.28×10^{-36} at 25ºC, respectively.

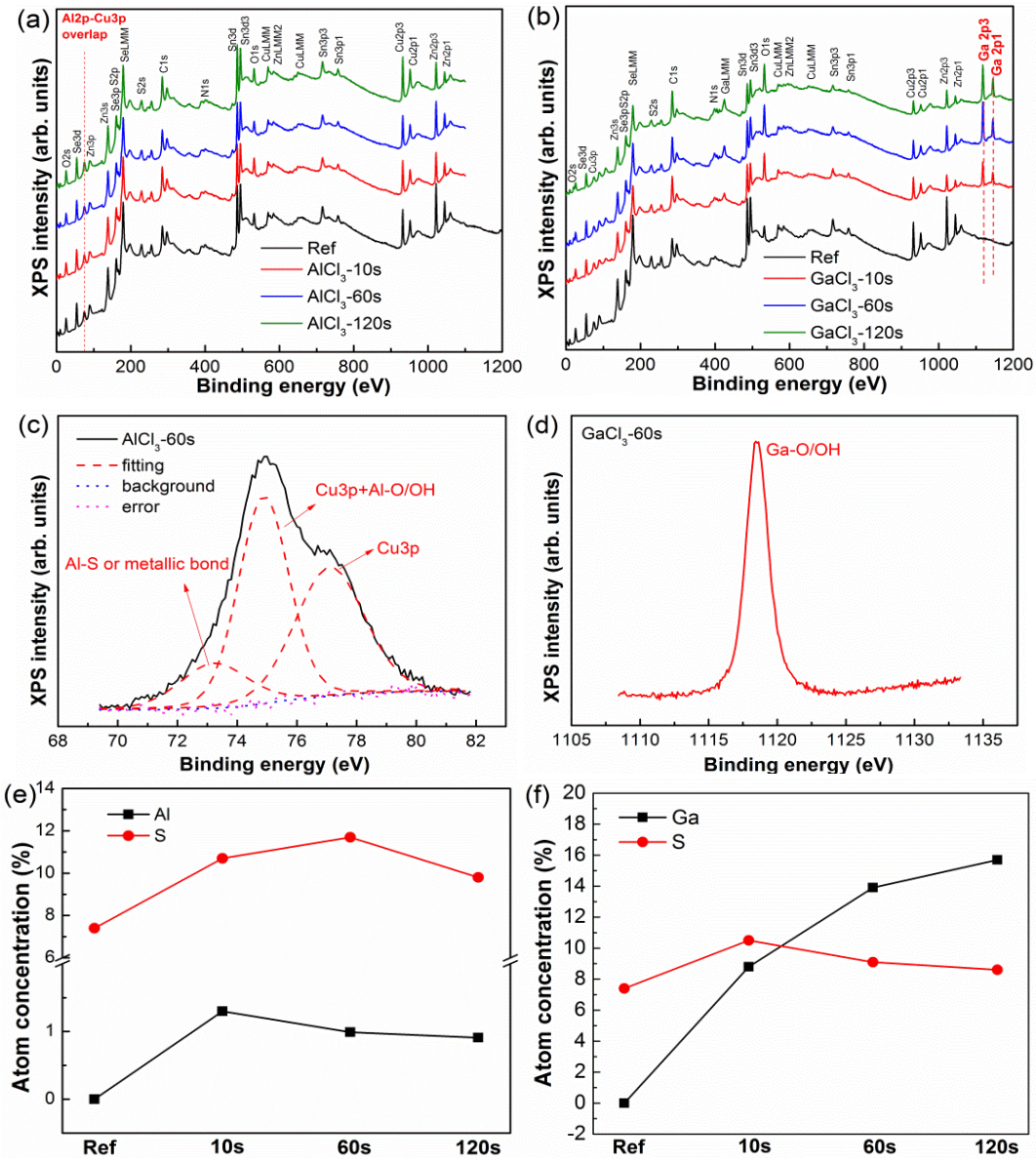

Figure 5.8. XPS spectra and element concentrations of $AlCl_3$ (a)(e) and $GaCl_3$ (b)(f) treated samples with different deposition times; analysis of Al (c) and Ga (d) related peaks after 60s passivation by fitting. $AlCl_3$/$GaCl_3$ (0.005M) + Thioacetamide (0.1M).

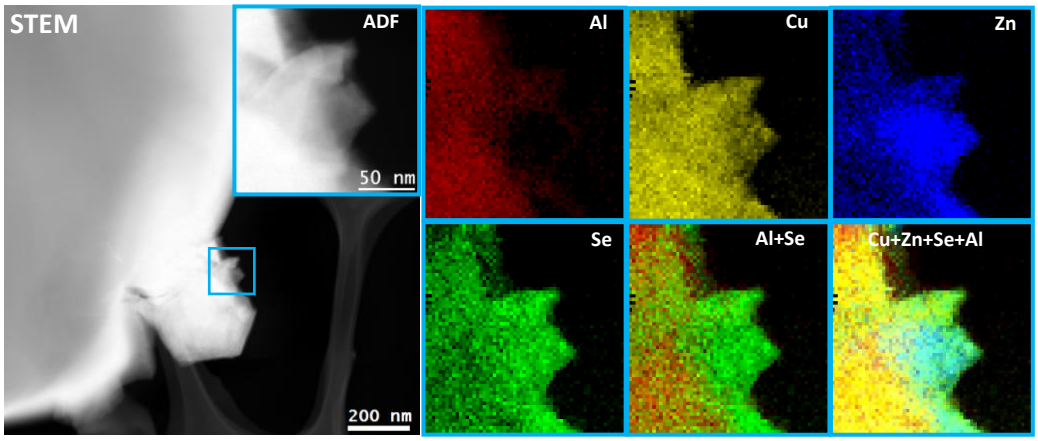

Figure 5.9. EELS chemical composition maps obtained from the indigo rectangled area of the ADF-STEM micrograph. Individual Al (red), Zn (blue), Se (green), Cu (yellow) maps and their composite.

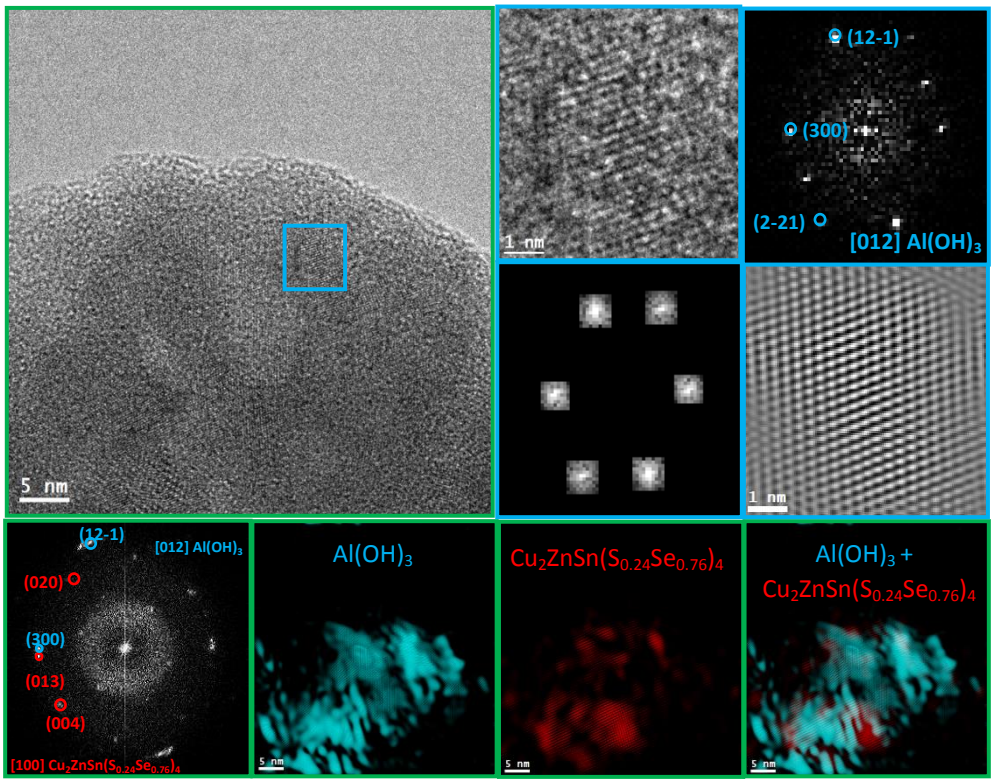

Figure 5.10. Left panel: HRTEM micrograph of the nanoparticles. Right panel: The magnified HRTEM image of the indigo squared area; the corresponding reduced FFT spectrum indicate that the species is monoclinic $Al(OH)_3$, [P121/N1]-space group 14, with lattice parameters of a =0.86676 nm, b= 0.50741 nm, c=0.9728 nm, and α = 90 °, β=94.54 °, γ=90 °as visualized along the [012] direction; the spot mask filtered reduced FFT and the IFFT image. Bottom panel, the reduced FFT of the whole HRTEM image, the IFFT of $Al(OH)_3$, $Cu_2ZnSn(S_{0.24}Se_{0.76})_4$ and their RGB composite.

5.4.4 Impact on solar cells and mechanism analysis

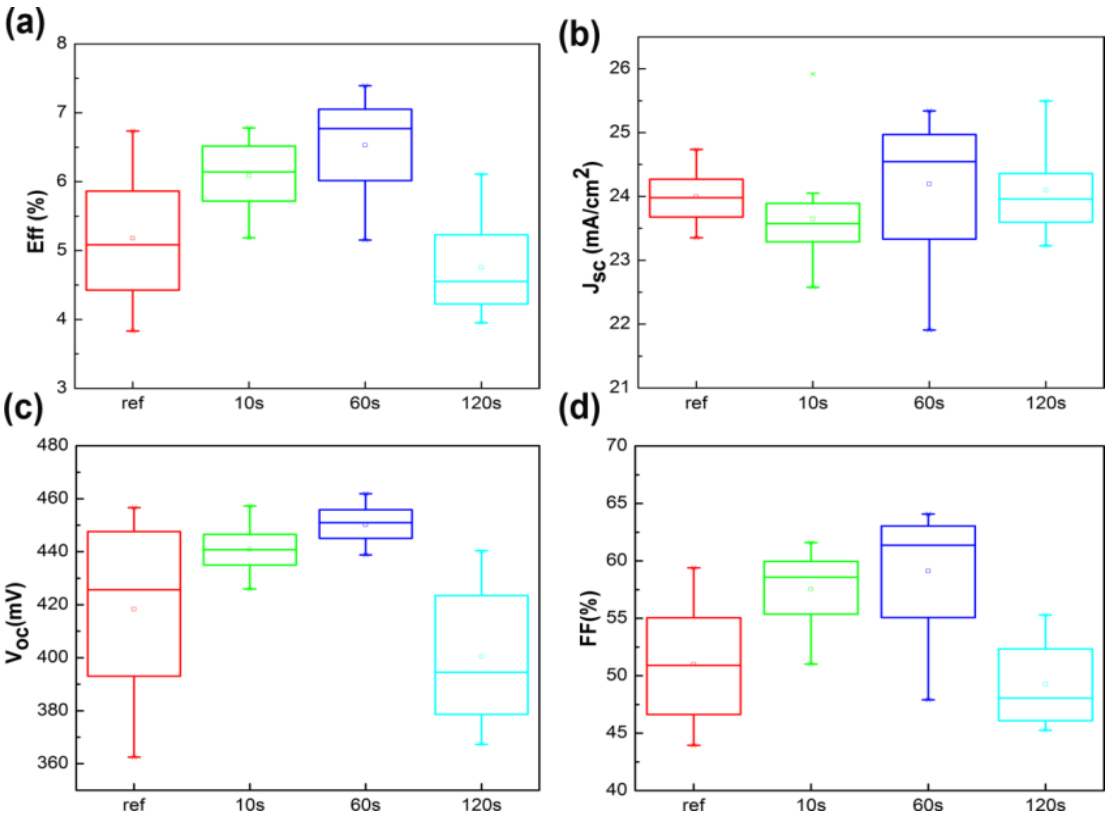

Figure 5.11. Coversion efficiency (a), short circuit current (b), open circuit voltage (c) and fill factor (d) of CZTSSe solar cells after $AlCl_3$ treatment with different deposition times. For each deposition time, more than 9 cells were included.

Figure 5.11 displays the optoelectronic properties of CZTSSe solar cells after $AlCl_3$ treatment. It has to be noted that $GaCl_3$ treated solar cells provided very similar results, and thereby the results are not shown. It can be easily observed that deposition time of 60 s allowed for the best results, with a significant improvement of all optoelectronic parameters with the exception of J_{sc}. In average, V_{oc} and FF of the devices are improved by 30-40 mV and 8-10%, respectively, while J_{sc} is almost unaffected, leading to 1-1.5 % increased efficiency in absolute. Table 5.2 shows the optoelectronic properties and diode parameters extracted from illuminated J-V curves of reference and $AlCl_3/GaCl_3$ treated CZTSSe solar cells [13]. Results show the decrease of diode ideality factor A and reverse saturation current J_0 after chemical treatment, indicating a better p-n junction quality and CZTSSe/CdS interface properties. The reduced R_s and increased R_{sh} might explain the considerable increase of FF in the devices. The increase of shunt resistance could be due to the decrease of shunt paths by the coverage of colloid $Al(OH)_3/Ga(OH)_3$. The reason for the reduction of series resistance will be discussed later.

Table 5.2. Optoelectronic properties and diode parameters of reference and $AlCl_3/GaCl_3$ treated CZTSSe solar cells. Cells with conversion efficiency close to the average values (9 cells) were selected as the representatives, aiming to get a better comparison.

Name	J_{sc} ($mA.cm^{-2}$)	V_{oc} (mV)	FF (%)	Eff. (%)	R_s ($\Omega.cm^2$)	R_{sh} ($\Omega.cm^2$)	A	J_0 ($mA.cm^{-2}$)
$AlCl_3$-ref	23.6	422.8	50.9	5	1.73	158.9	2.4	2.1×10^{-2}
$AlCl_3$-60s	23.4	457	58.3	6.2	1.58	248.6	1.9	2.3×10^{-3}
$GaCl_3$-ref	24.3	413	49	4.9	1.1	134	2.7	3.7×10^{-2}
$GaCl_3$-60s	25	454.7	57.8	6.6	0.44	237	2.4	2.7×10^{-2}

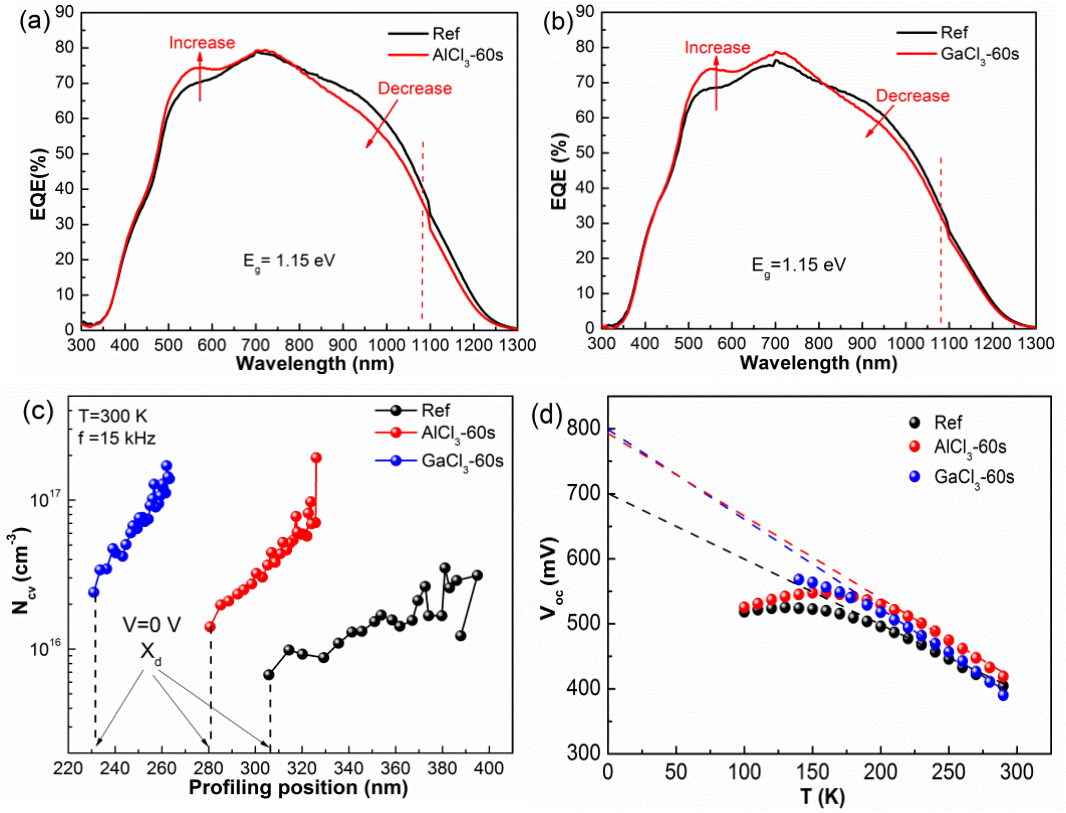

Figure 5.12. EQE of $AlCl_3$ (a) and $GaCl_3$ (b) treated devices compared with reference devices, hole concentration profiles obtained from C-V measurements (c) and temperature dependence of V_{oc} curves (d) of reference and $AlCl_3/GaCl_3$ treated devices.

To shed more light on the chemical treatment process, EQE, C-V and JV-T measurements were performed. An increase of EQE in the range of 500-800 nm coupled with a decrease of EQE in the range 800-1200 nm were observed after chemical treatment with $AlCl_3$ as well as $GaCl_3$ (See Figure 5.12 a and 5.12 b). The band gaps extracted from EQE remain unchanged (E_g =1.15 eV) before and after the chemical treatment process, which is consistent with the fact that the chemical treatments affect only the surface. C-V measurements show that after the treatment, the hole concentrations increased from 6.7×10^{15} to 1.4×10^{16} ($AlCl_3$) and 2.4×10^{16} cm^{-3}($GaCl_3$). Accordingly, the space charge region (SCR) widths (X_d, at zero voltage) decreased from 306 to 281 ($AlCl_3$) and 231 nm ($GaCl_3$), which could be due to possible removal of interface deep donors such as $V_{se}(V_s)$ or p-type doping via Al_{Sn}/Ga_{Sn} (see Figure 5.12 c)[60,93,147]. Thus, the enhancement of EQE in the short wavelength region can be attributed to a better p-n junction quality while the deterioration of EQE in the long wavelength region could be ascribed to a

shorter SCR width. The increased p-type doping could be responsible for the decrease of the series resistance due to the inverse proportion between resistivity and carrier concentration.

Temperature-dependent V_{oc} was measured to determine the dominant recombination mechanism (see Figure 5.12 d). The activation energy can be extracted from the vertical intercept at T = 0 of the linear fitting plot according to the following equation: [13]

$$V_{oc} = \frac{\Phi_b}{q} - \frac{AkT}{q} \ln\left(\frac{J_{00}}{J_L}\right) \qquad (5.1)$$

with Φ_b as the barrier height or activation energy, A the diode ideality factor, J_L the light current, and J_{00} the prefactor dependent on the specific recombination mechanism that dominates the saturation current J_0. Theoretically the main recombination mechanism varies from depletion region or neutral region recombination when $\Phi_b = E_g$ to interface recombination when $\Phi_b < E_g$[13,26]. Results show that after treatment with $AlCl_3$ or $GaCl_3$ chemical solutions, the activation energy increased from 700 to 800 mV approximately. The values are lower than the optical band gap at around 1.15 V, indicating interface recombination is the dominant recombination path of these devices. Nevertheless, the improved activation energy by nearly 100 mV after treatment with respect to the reference cells shows promising prospects addressing the issue of the interface recombination for CZTSSe solar cells. Therefore, V_{oc} enhancement after treatment can be explained by the decrease of interface recombination and a better diode ideality factor as well as increased a p-type doping.

To obtain more information about the origin of the interface recombination suppression after the chemical treatment process, PL spectra with various excitation powers and temperatures were measured.

Figure 5.13a displays the excitation power dependence study of PL spectra in a reference device and devices treated with $AlCl_3$ and $GaCl_3$ solution for 60s, respectively. Analysis of these spectra shows a strong blue shift of the maximum with excitation power increase for about 15meV/decade. Additionally, the analysis of the integrated PL intensity versus excitation power shows the exponential dependence in accordance with formulae $I_{PL} \sim I_{ex}^{k}$. The exponent k is found to be lower than 1 (see Figure 5.13b). This indicates the defect related nature of the observed PL spectra, while the strong blue shift of the maximum indicates the quasi donor-acceptor pair (QDAP) recombination as irradiative processes in the analyzed samples[241]. The QDAP recombination was previously found in pure $Cu_2ZnSnSe_4$ [242] and Cu_2ZnSnS_4 [243,244] compounds, as well as in their solid solution CZTSSe thin films [242]. It is characterized by a strong influence of the bands bending, due to a fluctuating potential, to the PL band maximum, which could be described by [241]:

$$E_{PL} = E_g - (E_A + E_D) + 2\Gamma \qquad (5.2)$$

Here E_g is the band gap energy, E_A and E_D are the activation energies of the acceptor and donor, respectively, involved in the irradiative process and coefficient Γ is average potential well depth related with bands bending [241].

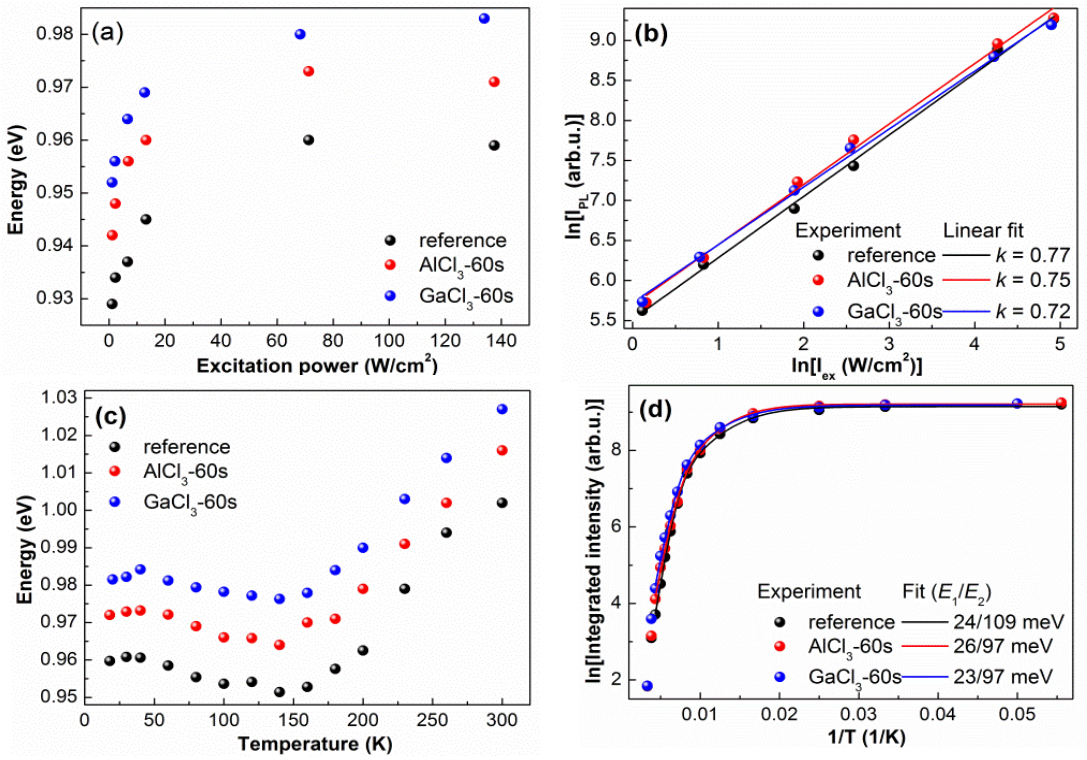

Figure 5.13. PL band maximum position (a) and integrated PL intensity (b) as a function of excitation power, PL band maximum position (c) and integrated PL intensity (d) as a function of sample temperature. Solid lines in the panels (b) and (d) are the fitting to the respective Eqs.

The analysis of temperature dependence of PL spectra showed the red shift of the band maximum up to ~ 150 K and blue shift at higher temperatures (see Figure 4c). Similar dependencies were observed previously for the CZTSSe solid solutions with the QDAP emission [242,245] and is well explained elsewhere [242]. It is notable that the PL peak exhibits blue shift in the whole range of temperatures after treated with $AlCl_3$ or $GaCl_3$ process. This is normally attributed to the increased E_g of the absorbers. As the E_g extracted from EQE plots represent the in-depth minimum of E_g, we assume that the surface E_g of the absorbers increased after the treatment process, probably due to O(S) or Al(Ga) substitution for anion vacancy or Sn sites, respectively. [60,93] The increased surface E_g could be partially responsible for the V_{oc} enhancement shown above.

A strong quenching of PL intensity of about 3 orders of magnitude in the analyzed temperature range 20 – 300 K is also found in the samples. This quenching could be described using the equation with two activation energies [246]:

$$I_{PL} = \frac{I_0}{1 + a_1 \exp(-E_1 / k_B T) + a_2 \exp(-E_2 / k_B T)} \qquad (5.3)$$

where a_1 and a_2 are the rate parameters of the non-irradiative process with activation energies E_1 and E_2. I_0 is PL intensity at lowest temperature and k_B is Boltzmann constant. Note that in the framework of QDAP recombination model the lower E_1 energy is attributed to the average value

of the valley depth, Γ, from which the carriers should be thermally activated for the subsequent recombination, rather than to the activation energy of some shallow defect levels [242]. In Figure 5.13d it is seen that obtained values of the valley depth by fitting in analyzed samples are almost independent on passivation.

The higher activation energy E_2 could be attributed shallower level from donor or acceptor involved in the recombination process. At temperatures higher than 250 K the irradiative mechanism of the observed PL spectra was found to be changed from QDAP to the band to impurity (BI) recombination, which is proved by the constant maximum position with excitation power change at 300 K [242,243]. As CZTSSe absorber has *p*-type of conductivity the conduction band-acceptor transition is a more favorable origin of the observed PL band near the room temperatures. Here from the band gap energy found in EQE (see Figure 3) and position of PL band maximum at 300 K the activation energy of the involved acceptor level (E_A) was roughly estimated to be 0.148, 0.134 and 0.123 eV for reference, $AlCl_3$ and $GaCl_3$ treated samples, respectively. The found transformation of PL spectra close to the room temperatures yields the assignment of E_2 energy to the donor defect level (E_D). Using the empirical equation for the band gap change found in the CZTSSe single crystals at 80 K [247] and the Eq. (5) we estimated the activation energy of acceptor level involved in the QDAP process. The values are quite close to that obtained for the acceptor level involved in BI transitions, thus we can suppose that similar acceptor levels are involved both in QDAP and BI irradiative transitions. According to theoretical studies two found in the PL study levels E_A and E_D could be associated with different defects, however taking into account the formation energy and conditions of Cu-poor Zn-rich samples the most probable are Cu_{Zn} and Zn_{Cu} [93]. The slightly shallower Zn_{Cu} donor level after chemical treatments indicate less minor carrier recombination in the p-n junction region, which is beneficial for V_{oc} enhancement.

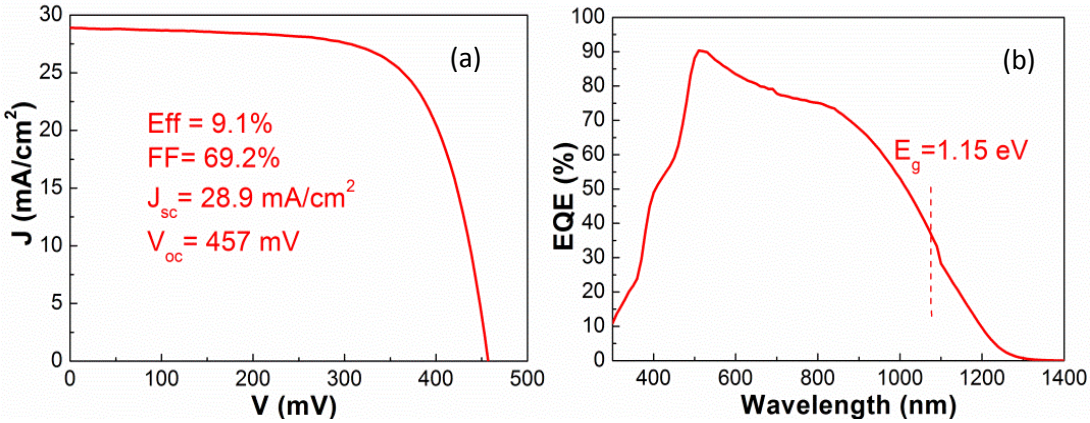

Figure 5.14. J-V curves (a) and EQE plot (b) of the champion Se-rich CZTSSe solar cell with efficiency of 9.1% after $AlCl_3$ chemical treatment.

In summary, results show that $AlCl_3$ and $GaCl_3$ chemical treatments have very similar impact on CZTSSe solar cells. This is not surprising when considering the similar chemical properties and radii of Al and Ga. However, Al is more earth-abundant and cheaper than Ga, thus it is reasonable to focus on $AlCl_3$ chemical treatment process to maintain the advantage of kesterite solar cells. After optimization of the thermal treatment and $AlCl_3$ based chemical treatment (concentration and soaking time, etc.), best efficiency of 9.1% was obtained for a Se-rich

CZTSSe solar cell. Figure 5.14a shows the optoelectronic properties of this champion device, with J_{sc} = 28.9 mA.cm^{-3}, V_{oc} = 457 mV, and FF = 69.2 %. Figure 5.14b shows the EQE reaches nearly 90 % in the 500-600 nm range, indicating good carrier collection in the p-n junction region. Band gap of 1.15 eV was extracted from the inflection point of EQE plot. Considering that no anti-reflective coating was used, further improvement of J_{sc} and hence higher efficiency could be foreseen.

5.4.5 Conclusions

In this work, we managed to engineer CZTSSe absorbers surface with group III hydroxides (III =Al, Ga) and S layer by a facile wet chemical treatment, which is verified by XPS, EELS mapping and HRTEM measurements. Considerable enhancement of V_{oc} and conversion efficiency of CZTSSe solar cells was observed after the treatment process. This effect can be explained by: (1) V_{oc} increase and less V_{oc} deficit. Better p-n junction quality, less interface recombination and increased hole concentration are linked to a decrease of diode ideality factor and reverse saturation current and possible removal of deep donors, which are confirmed by J-V, JV-T and C-V measurements. In addition, increased surface band gap and shallower donor level revealed by temperature and excitation power dependent PL spectra could also be partially responsible for the V_{oc} enhancement; (2) FF increase. Lower series resistance and higher shunt resistance could be related to higher p-type doping and decrease of shunt paths; (3) J_{sc} unaffected. Higher EQE for the p-n junction wavelength region while lower EQE for photogenerated carriers deeper in the absorber can be ascribed to better p-n junction quality and shorter depletion width, respectively. This work has demonstrated the importance of engineering the kesterite surface in order to improve the voltage deficit of the devices, and it is feasible to engineer the kesterite surface using a simple solution based methodology.

This work is in preparation for publication.

Chapter 6

Conclusions and outlook

6.1 Conclusions

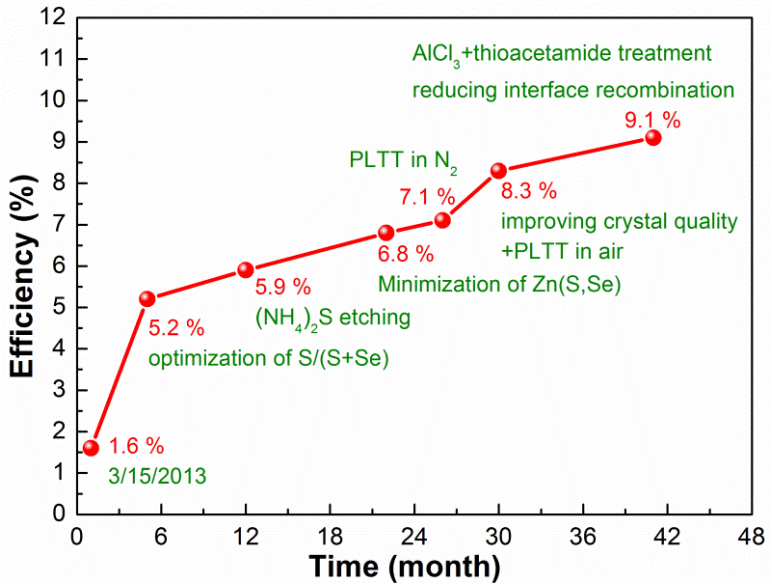

Figure 6.1. Efficiency evolution of CZTSSe solar cells developed during the Ph.D. career in IREC. The technology related to each record efficiency is marked.

In this thesis, starting from efficiency less than 5%, CZTSSe kesterite solar cells with high efficiency over 9 % have been achieved based on a single-step sulfo-selenization process, through the optimization of the thermal treatment, surface secondary phases control by etching, and CZTSSe/CdS interface engineering. This demonstrates that the single-step sulfo-selenization methodology is promising and feasible for obtaining high efficiency CZTSSe solar cells.

High quality absorbers with appropriate S/(S+Se) ratio and good crystal quality are paramount for high efficiency CZTSSe devices. Achieving this requires careful and systematic tuning of different parameters during the thermal treatment, i.e., the single-step sulfo-selenization process, especially under non-equilibrium conditions: low annealing temperature, short holding time and discontinuous supply of chalcogen sources. These parameters include added S/(S+Se) powder ratio, annealing temperature, system pressure, holding time, ramp and cooling rate, and steps of thermal treatment profile, etc. Among them, the first three factors are the most important. Se-rich CZTSSe absorbers (S/(S+Se) = 0.25-0.3) can be achieved by using low added S/(S+Se) powder ratio, high annealing temperature (550 ºC) and low system pressure in "one step" thermal profile. The system pressure serves to adjust the evaporation rate of S and Se powder by inert gas (Ar or N_2) and pumping system. Thermodynamic equilibrium analysis shows that, in an ideal closed reactor, the absorber S/(S+Se) ratio is mainly controlled by added S/(S+Se)

powder ratio and annealing temperature and is independent of system pressure. However, in a real partial closed graphite box, S loss can be more enhanced than Se during low system pressure due to its higher saturation vapour and diffusion rate thus low system pressure is favourable for the formation of Se-rich CZTSSe. Multiwavelength Raman spectra indicate Se-rich CZTSSe absorbers in this work have less Zn(S,Se) secondary phases in the front and back interface than CZTS, CZTSe and S-rich CZTSSe absorbers, which could explain the higher efficiency of this type of kesterite solar cells. In addition, columnar crystal with size comparable to the cross section can be achieved by using a "two step" thermal profile (first 200-250 ºC and then 550 ºC), due to the accelerate and homogeneous reactions after prealloying in the low temperature step. Finally, material loss and detrimental decompositions at the front and back surface can be controlled by using a closed graphite box with a narrow space, supplying Sn powder together with S and Se, and employing a high system pressure.

Secondary phases are big challenges for kesterite solar cells. If present in the front interface, they will severely deteriorate the p-n junction quality and ultimately the efficiency. CZTSSe absorber surface in this work was found to have only Sn-(S,Se) secondary phases. An innovative etching process based on 22% w/w $(NH_4)_2S$ solution was developed for the effective and selective removal of Sn-(S,Se). Sn-(S,Se) can be originated from composition deviation during the crystal growth process or by condensation from the Sn containing atmosphere during the cooling process. If present in the front interface, Sn-(S,Se) can degrade the device performance mainly through the reduction of V_{oc} and FF. In addition, the $(NH_4)_2S$ solution also has a passivation effect on the absorbers surface. A passivation mechanism was developed, featuring removal of metal oxides and passivation of the surface with S layer. After this $(NH_4)_2S$ etching, efficiency can be improved by 1-2.5% in absolute value averagely depending on the quantities of Sn-(S,Se) on the surface.

To further improve the efficiency of CZTSSe solar cells, engineering of CZTSSe/CdS interface was explored, because this interface is the p-n junction region and is paramount for the performance of devices.

Based on the post low temperature treatment process, it was firstly found in the kesterite research field that Na spatial distribution especially in the CZTSSe/CdS interface region has crucial impact on the solar cells efficiency. Efficiency can be varied from more than 7% to nearly 0% by different content of Na in the interface region, indicating the critical and subtle role of Na distribution other than Na concentration in kesterite solar cells. This behaviour could be due to the modification of built-in voltage by the p-type doping of CdS and ZnO layer and alteration of buffer/absorber doping ratio. In addition, the Na profile shows surprising results at 200 ºC and 400 ºC PLTT, with higher Na content at 200 ºC while lower Na content at 400 ºC on the surface region of CZTSSe layers. To elucidate this behaviour, an innovative Na dynamic model was developed, featuring Na diffusion from the SLG substrate and Na loss from the absorbers surface during PLTT process. Depending on the diffusion and loss rate at a given temperature, different Na profiles could be obtained. This model is validated by theoretical calculations, yielding Na diffusion coefficient at two key PLTT temperatures: $D_{Na,200ºC} = 2.5\times10^{-13}$ cm^2s^{-1} and $D_{Na,400ºC} = 3.4\times10^{-13}$ cm^2s^{-1}. Best conversion efficiency of 7.1% and 8.3% for Se-rich CZTSSe solar cells were obtained after PLTT of absorbers in N_2 at 400 ºC and air atmosphere at 300 ºC, respectively. This would point again towards the relevance of Na dynamics since Na diffusion is enhanced in oxidation processes.

In addition, CdS doped with different Cu was investigated. Results showed that the thickness of CdS decreased from 70 nm in the reference case to less than 30 nm after appropriate Cu doping, while the efficiency keeps the same level for both CIGS and CZTSe solar cells. Although the efficiency was not improved by this process, the reduction of CdS thickness could provide new possibilities to address the environmental concern of Cd.

Finally, to reduce the interface recombination and improve the V_{oc}, wet chemical treatments based on $AlCl_3/GaCl_3$ + thioacetamide solution were developed. Results show that this process can increase the efficiency and reduce the V_{oc} deficit through the improvement of V_{oc} and FF, while J_{sc} and the band gap extracted from EQE are unaffected. This is mainly related to the reduction of interface recombination and shunt resistance by the colloid $Al(OH)_3/Ga(OH)_3$ coverage of the absorbers surface after the chemical treatments. In addition, the increase of surface band gap and decrease of donor level could also be possible reasons for the V_{oc} enhancement. This process is facile and lost cost and could open new perspectives for the engineering of CZTSSe/CdS interface of S containing kesterite solar cells to tackle the interface recombination.

Figure 6.1 shows the efficiency evolution of CZTSSe solar cells developed during my Ph.D. career in IREC. The technologies or reasons related to each record efficiency are marked.

6.2 Outlook

Table 6.1. Comparisons between the champion 9.1% CZTSSe solar cell in this work and the 12.6% CZTSSe record solar cell.

	E_g (eV)	J_{sc} (mA/cm^2)	V_{oc} (mV)	FF (%)	Efficiency (%)	R_s (Ω.cm^2)	R_{sh} (Ω.cm^2)	J_0 (mA/cm^2)	A	Ref
CZTSSe Record	1.13	35.2	513	69.8	12.6	0.72	621	$7*10^{-8}$	1.45	[]
CZTSSe	1.15	28.9	457	69.2	9.1	0.58	527	$2*10^{-4}$	1.52	This work
Loss	-	- 6.3	-56	-0.6	-3.5	-	-	-	-	-
Loss (%)	-	-17.9	-10.9	-0.9	-27.8	-	-	-	-	-

The champion 9.1% CZTSSe solar cell in this work has comparable FF as the world record CZTSSe solar cell, while suffering substantial J_{sc} and V_{oc} loss, as can be seen in Table 6.1. There is a large EQE loss in the long wavelength range (see Figure 5.14), which could be due to short diffusion length caused by secondary phases or deep defects. TEM indeed found Sn-S-O inclusions in the back region of the absorbers. However, deep defects identification needs measurements like admittance spectra and DLTS spectra. Therefore, further optimization of CZTSSe absorber quality to reduce the secondary phases and possible deep defects can be a plausible solution. In addition, the J_{sc} can be enhanced by optimization of window layer and using anti-reflective coating. The V_{oc} loss could be related to interface recombination and bulk recombination due to deep defects, as indicated by the four orders lower J_0 value than that of the record CZTSSe solar cell. Although by wet chemical treatments the activation energy of the interface recombination has been improved to 1.02 eV, comparable to that in the world record CZTSSe solar cell (1.03 eV), still a 0.13 eV gap exists with respect to the optical band gap. This evidences that it is necessary to further engineer the CZTSSe/CdS (e.g., CBO, type inversion layer) with the aim of fully removing the interface recombination and thereby increase the V_{oc}. As discussed above, the bulk defects need more measurements to identify. Actually they are

considered as big challenges in the kesterite technology and more innovative solutions need to be developed.

Up to now, the record 12.6% efficiency for kesterite solar cells has lasted for nearly 3 years. The main hurdle is the V_{oc} deficit compared with CIGS technology and the SQ limit, as shown in Table 6.2. Theoretical and experimental results point towards the band tailing and bulk defects as the key culprits that limit V_{oc}. In addition, for S containing kesterite solar cells, interface recombination can be another plausible reason. The question is, to what extent these assumed efficiency limiting factors can influence the V_{oc} and V_{oc} deficit? Taking CZTSe solar cells for an example, the V_{oc} of the high efficiency CZTSe solar cells (E_g =1 eV) is typically around 400 mV[34,40,54], while its analogy CISe solar cells typically have V_{oc} around 500 mV[248,249]. It is well known that CISe solar cells have very less band tailing, thus it means that the band tailing could at most account for around 100 mV V_{oc} loss. Band tailing is proved to be correlated to the prevalent Cu_{Zn} defect, which is about 0.11 eV in CZTSe. This energy level is around 80 mV higher than the prevalent V_{Cu} (0.03-0.04 eV) in CISe, being consistent with the V_{oc} discrepancy. This Cu_{Zn} defect also causes order-disorder effect in the kesterite materials in terms of anti-sites defect complex [Cu_{Zn}+Zn_{Cu}]. Reannealing the absorbers below their critical temperatures could partially reorder the Cu and Zn sites and increase the band gap but cannot change the V_{oc} deficit. Full ordering is impossible due to basic thermodynamic reasons. Partially Ag or Cd substitution for Cu or Zn can be more effective to reduce the band tailing and V_{oc} deficit [154,250], but it seems deviate the targeting non-toxic and earth-abundant constituents of kesterite. Therefore, new solutions are needed to address this Cu_{Zn} defects. In addition, it is reported that after the fine tuning of Sn content or appropriate Ge doping, all the optoelectronic properties of the kesterite devices can be largely enhanced. The reason is assumed to be the suppression of Sn related bulk deep defects like Cu_{Sn} and Sn_{Cu} based on admittance spectra. These results clearly show the importance of minimization of deep defects in the bulk. However, the deep defects in actual kesterite solar cells are still challenging to identify. Therefore, more advanced characterizations of deep defects should be implemented, based on which new solutions may be developed. Furthermore, the GBs play an important role in thin film solar cells. Passive GBs can facilitate the carrier transportation and increase the V_{oc}. However, the role of GBs, e.g., facilitating transportation of electrons or holes or repelling both, is controversial in kesterite solar cells[48,155,156,251,252]. Thus, advanced characterization is needed to figure out the composition (including oxygen and alkali elements) and electrical properties of GBs especially in high efficiency devices.

Table 6.2. Comparisons among the world record CZTSSe solar cell, record CIGS solar cell and SQ limit.

	E_g (eV)	**J_{sc} (mA/cm^2)**	**V_{oc} (mV)**	**FF (%)**	**Efficiency (%)**	**Ref**
SQ limit	1.15	42.3	887	87	32.7	[]
CIGS record	1.13-1.15	37.8	741	80.6	22.6	[]
CZTSSe record	1.13	35.2	513	69.8	12.6	[]
Loss (to CIGS) (%)	-	-6.9	-30.8	-13.4	-44.2	-
Loss (to SQ limit) (%)	-	-16.8	-42.2	-17.8	-61.5	-
CZTSSe expected 1	1.13	35.2	641	69.8	15.7	-
CZTSSe expected 2	1.13	37.8	641	75	18.2	-

Besides, the back interface recombination at CZTSSe/Mo is assumed to be another reason for V_{oc} deficit, due to secondary phases and defects caused by detrimental reactions, non-ohmic

contact, and possible non-optimized band alignment. Some pioneer work using new barrier layers like TiN, ZnO and MoO_2 has been demonstrated to be beneficial for the V_{oc} enhancement of CZTSe solar cells, but the back contact is far from optimization for kesterite solar cells especially for those S containing ones. Furthermore, some fundamental issues, e.g., the band alignment of CZTSSe/$MoS(e)_2$ and the exact recombination rate are still pending, which requires deeper investigation on both experiments and theory.

Furthermore, as is well known, CIGS solar cells largely increase the V_{oc} and efficiency by band grading and alkali (K, Rb, Cs) PDT process[16,231]. Therefore, to increase the V_{oc} deficit, band grading should be carefully tuned by Ge or S and alkali PDT process should be deeply investigated. As alkali PDT mainly leads to Cu-poor surface that facilitate Cd diffusion to form type inversion top layer in CIGS solar cells, it could also be valid for kesterite devices.

Finally, from the point of view of material itself, the fundamental bottleneck of kesterite solar cells is the prevalent [Cu_{Zn}+Zn_{Cu}] defect cluster, as long as Cu or Zn is not totally substituted by other elements (if totally, it is another material). As discussed above, this defect cluster is somehow tough to tackle, leading to 100 mV V_{oc} deficit at the most. Therefore, taking the CIGS record solar cell as a reference, if all the other V_{oc} limiting issues of kesterite solar cells, e.g., other deep defects, interfaces and GBs, are successfully resolved with an effort, the V_{oc} may reach 641 mV. Assuming the J_{sc} and FF keep constant as those of the record kesterite solar cell, the expected efficiency of kesterite solar cells could reach 15.7% (see Table 6.2 "CZTSSe expected 1"), surpassing the commercial threshold slightly. Furthermore, if the J_{sc} and FF could reach the same level of the record CIGS solar cell, 18.2 % efficiency for kesterite solar cells could be expected (see Table 6.2 "CZTSSe expected 2". FF could also be limited by V_{oc} thus conservative value is applied), which is high enough to compete with other photovoltaic technologies.

To sum up, although the efficiency of kesterite solar cells is far below those of their counterparts CIGS and CdTe solar cells, taking into acount the relatively short history and the rapid progress (see Figure 1.15), this photovoltaic technology is promissing for further investigation and bright prospects could be expected.

Acknowledgements

How time flies! Just a blink, the four years have passed by, and now is the moment that I need to write this exciting but a little sad part. I am excited because I am about to finish the Ph.D. career and the Ph.D. degree of my dreams is in front of me; I am a little sad because I am about to finish the Ph.D. career and I am leaving my respectable supervisors and tutor, my beloved friends and my sincere and kind colleagues in IREC, especially those people in the Solar Energy Materials and Systems Group. The four-year duration is just like a wonderful movie for me, I really enjoyed it, sometimes when I look back it seems not real. The movie begins like this: a guy, who is the 99th generation of Xie living 2500 years ago, from the mysterious orient, China, travelled 10,000 miles to the passionate and international Mediterranean pearl, Barcelona, aiming to feel and understand the magic force of Apollo…

The movie seems a "Cuento Chino", but it is not limited to that. The people involved including investors, directors, actors and actresses make the movie wonderful. First of all, I would like to thank the investor Chinese government that offered me the "China Scholarship Council (CSC)" Fellowship, with which I am able to focus on my study and investigations. In addition, I would like to express my sincere appreciation to the directors Edgardo and Alejandro, who gave me the opportunity to perform in the stage of IREC, supervised my work and helped me to address the difficulties that I met in science and in the university. Especially, I owe a lot to Edgardo, not only because he helped me with the heavy luggage on the first day, knocked my door to wake me up for the oral presentation in Tallinn, and invited me mojitos in the bar near La Rambla, but also because he trained and taught me a lot on ideas conception, experiments design, data analysis, presentation preparation and paper writing, which are critical for a young Ph.D. student to grow into a scientific researcher.

Of course the wonderful movie cannot go without the participation of all the nice and talented actors and actresses, my colleagues, also called "monas" in the group, including Simón, Yudania, Moisés, Markus, Nacho, Florian, Andrew, Mira, Marcel, Diouldé, Sergio, Laura, Victor, Alex, Monica, Rokas, Juan and Max, et al. I enjoyed the benign atmosphere in the lab, sharing ideas and talking jokes in the interval of hard lab work. Another thing I have to note is the delicious cakes and drinks in the "afternoon group meeting" almost every week. I really enjoyed a lot but maybe because of that I got fatter and maybe even developed the cholesterol? LOL. I also cannot forget the "flow and reflow" parties on Friday nights in the Mexico restaurant after one week´s intensive work. Most of the time the parties helped me to release some pressure and remove frustrations on the solar cells efficiency, while sometimes they witnessed my success and glorious time of good results.

It seems that I am a Potential heavy Drinker, but actually I am one of those People have Dreams. In a solar lab, hard work is always the main stream, and for me I am motivated to try different new ideas and ready to learn new things that can improve my scientific knowledge and experiences. As Confucius said, "If three of us are walking together, at least one of the other two is good enough to be my teacher". I have learned a lot from the "monas" around me, because the lab is international and they have different backgrounds and think in a different way. In addition, I have improved my English due to the practice in the group, but as a coin has two faces, on the other hand my Spanish has limited success. Anyway, I can speak some highly "clin clin" five star Spanish words, e.g., "Culebra Vonsoñosa" "Rata de Dos Patas", etc. I also appreciate the opportunities that I got in our lab to attend scientific conferences in different

countries and to collaborate with scientists outside, like people from HZB, ICN2, UB and university of Uppsala, which really broadened my horizon and enriched my network.

In addition, I want to thank my Chinese friends Jun Tang, Weiyi Zhang, Wenhua Li, Jiandong Fan, Zhishan Luo, Feng Shao, Yu Liu, Junfeng Liu, and Xiaoting Yu, with whom I have enjoyed a lot the life in Barcelona.

Finally, no matter where I am, my heart always goes with my family, which is my motivation, safe port and eternal support. Mom, dad, grandma, grandpa, sister, sister in law and the lovely niece and nephew, I love you!

As every movie has an end, the four-year Ph.D. is approaching the last moment, what is the next? No idea, but I will try my best to make it wonderful again.

References

1. M.A. Green, Third generation photovoltaics: Ultra-high conversion efficiency at low cost, Progress in Photovoltaics: Research and Applications, 9 (2001) 123-135.
2. Mark Osborne, Top 10 solar module manufacturers in 2015, PVTECH, http://www.pv-tech.org/editors-blog/top-10-solar-module-manufacturers-in-2015.
3. H. Lewerenz, H.J. Jungblut, Photovoltaik- Grundlagen und Anwendungen, first ed., Springer-Verlag Berlin Heidelberg, 1995.
4. T. Saga, Advances in crystalline silicon solar cell technology for industrial mass production, NPG Asia Mater, 2 (2010) 96-102.
5. Z. Fang, X.C. Wang, H.C. Wu, C.Z. Zhao, Achievements and Challenges of CdS/CdTe Solar Cells, International Journal of Photoenergy, 2011 (2011) 8.
6. L. A. Kosyachenko, A theoretical description of thin-film Cu(In,Ga)Se_2 solar cell performance, in: L. A. Kosyachenko (Ed), Solar cells-new approaches and reviews, INTECH, 2015. http://www.intechopen.com/books/solar-cells-new-approaches-and-reviews/a-theoretical-description-of-thin-film-cu-in-ga-se2-solar-cell-performance.
7. O.A. Abdulrazzaq, V. Saini, S. Bourdo, E. Dervishi, A.S. Biris, Organic Solar Cells: A Review of Materials, Limitations, and Possibilities for Improvement, Particulate Science and Technology, 31 (2013) 427-442.
8. W. Shockley, H.J. Queisser, Detailed Balance Limit of Efficiency of p-n Junction Solar Cells, Journal of Applied Physics, 32 (1961) 510-519.
9. S. Rühle, Tabulated values of the Shockley-Queisser limit for single junction solar cells, Solar Energy, 130 (2016) 139-147.
10. D.-J. Xue, B. Yang, Z.-K. Yuan, G. Wang, X. Liu, Y. Zhou, L. Hu, D. Pan, S. Chen, J. Tang, $CuSbSe_2$ as a Potential Photovoltaic Absorber Material: Studies from Theory to Experiment, Advanced Energy Materials, 5 (2015) 1501203.
11. J.J. Scragg, P.J. Dale, L.M. Peter, G. Zoppi, I. Forbes, New routes to sustainable photovoltaics: evaluation of Cu_2ZnSnS_4 as an alternative absorber material, physica status solidi (b), 245 (2008) 1772-1778.
12. K. Tanaka, CZTS thin films prepared by a non-vacuum process, in: K. Ito, Copper zinc tin sulfide-based thin-film solar cells, John Wiley & Sons, Ltd, Hoboken, 2015, pp. 272-287.
13. S.S. Hegedus, W.N. Shafarman, Thin-film solar cells: device measurements and analysis, Progress in Photovoltaics: Research and Applications, 12 (2004) 155-176.
14. M.A. Contreras, K. Ramanathan, J. AbuShama, F. Hasoon, D.L. Young, B. Egaas, R. Noufi, Diode characteristics in state-of-the-art ZnO/CdS/Cu($In_{1-x}Ga_x$)Se_2 solar cells, Progress in Photovoltaics: Research and Applications, 13 (2005) 209-216.
15. G. Hodes, P.V. Kamat, Understanding the Implication of Carrier Diffusion Length in Photovoltaic Cells, The Journal of Physical Chemistry Letters, 6 (2015) 4090-4092.
16. P. Jackson, R. Wuerz, D. Hariskos, E. Lotter, W. Witte, M. Powalla, Effects of heavy alkali elements in Cu(In,Ga)Se_2 solar cells with efficiencies up to 22.6%, physica status solidi (RRL) – Rapid Research Letters, 10 (2016) 583-586.
17. First solar, First solar achieves yet another cell conversion efficiency world record, press released, http://investor.firstsolar.com/releasedetail.cfm?releaseid=956479.
18. B.A. Andersson, Materials availability for large-scale thin-film photovoltaics, Progress in Photovoltaics: Research and Applications, 8 (2000) 61-76.
19. D.B. Mitzi, O. Gunawan, T.K. Todorov, K. Wang, S. Guha, The path towards a high-performance solution-processed kesterite solar cell, Solar Energy Materials and Solar Cells, 95 (2011) 1421-1436.
20. Sandip Das, Krishna C. Mandal, Raghu N. Bhattacharya, Earth-abundant $Cu_2ZnSn(S,Se)_4$ (CZTSSe) solar cells, in: M. P. Paranthaman, W. Wong-Ng , R. N. Bhattacharya (Eds), Semiconductor materials for solar photovoltaic cells, Springer International Publishing, New York, 2016, pp. 25-74.

21. H. Katagiri, K. Jimbo, W.S. Maw, K. Oishi, M. Yamazaki, H. Araki, A. Takeuchi, Development of CZTS-based thin film solar cells, Thin Solid Films, 517 (2009) 2455-2460.
22. K. Hironori, J. Kazuo, Y. Satoru, K. Tsuyoshi, M. Win Shwe, F. Tatsuo, I. Tadashi, M. Tomoyoshi, Enhanced conversion efficiencies of Cu_2ZnSnS_4-based thin film solar cells by using preferential etching technique, Applied Physics Express, 1 (2008) 041201.
23. T.K. Todorov, K.B. Reuter, D.B. Mitzi, High-efficiency solar cell with earth-abundant liquid-processed absorber, Advanced Materials, 22 (2010) E156-E159.
24. Q. Guo, G.M. Ford, W.-C. Yang, B.C. Walker, E.A. Stach, H.W. Hillhouse, R. Agrawal, Fabrication of 7.2% efficient CZTSSe solar cells using CZTS nanocrystals, Journal of the American Chemical Society, 132 (2010) 17384-17386.
25. D.A.R. Barkhouse, O. Gunawan, T. Gokmen, T.K. Todorov, D.B. Mitzi, Device characteristics of a 10.1% hydrazine-processed $Cu_2ZnSn(Se,S)_4$ solar cell, Progress in Photovoltaics: Research and Applications, 20 (2012) 6-11.
26. T.K. Todorov, J. Tang, S. Bag, O. Gunawan, T. Gokmen, Y. Zhu, D.B. Mitzi, Beyond 11% efficiency: characteristics of state-of-the-art $Cu_2ZnSn(S,Se)_4$ solar cells, Advanced Energy Materials, 3 (2012) 34-38.
27. W. Wang, M.T. Winkler, O. Gunawan, T. Gokmen, T.K. Todorov, Y. Zhu, D.B. Mitzi, Device characteristics of CZTSSe thin-film solar cells with 12.6% efficiency, Advanced Energy Materials, 4 (2014) 1301465.
28. R. Scheer, H. Schock, Chalcogenide photovoltaics: physics, technologies, and thin film devices, first ed., Wiley-VCH Verlag & Co. KGaA, Weinheim, 2011.
29. H. Hiroi, N. Sakai, Y. Iwata, T. Kato and H. Sugimoto, Impact of Buffer Layer on Kesterite Solar Cells, in: Proceedings of the 42th IEEE Photovoltaic Specialists Conference (PVSC), 2015, 10.1109/PVSC.2015.7356415.
30. T. Kato, H. Hiroi, N. Sakai, S. Muraoka, H. Sugimoto, Characterization of front and back interfaces on Cu_2ZnSnS_4 thin-film solar cells, in: Proceedings of the 27th European Photovoltaic Solar Energy Conference and Exhibition, 2012, pp.2236– 2239.
31. I. Repins, C. Beall, N. Vora, C. DeHart, D. Kuciauskas, P. Dippo, B. To, J. Mann, W.-C. Hsu, A. Goodrich, R. Noufi, Co-evaporated $Cu_2ZnSnSe_4$ films and devices, Solar Energy Materials and Solar Cells, 101 (2012) 154-159.
32. S.G. Choi, T.J. Kim, S.Y. Hwang, J. Li, C. Persson, Y.D. Kim, S.H. Wei, I.L. Repins, Temperature dependent band-gap energy for Cu2ZnSnSe4: A spectroscopic ellipsometric study, Solar Energy Materials and Solar Cells, 130 (2014) 375-379.
33. G. Brammertz, M. Buffière, S. Oueslati, H. ElAnzeery, K. Ben Messaoud, S. Sahayaraj, C. Köble, M. Meuris, J. Poortmans, Characterization of defects in 9.7% efficient $Cu_2ZnSnSe_4$-CdS-ZnO solar cells, Applied Physics Letters, 103 (2013) 163904.
34. S. Oueslati, G. Brammertz, M. Buffière, H. ElAnzeery, O. Touayar, C. Köble, J. Bekaert, M. Meuris, J. Poortmans, Physical and electrical characterization of high-performance $Cu_2ZnSnSe_4$ based thin film solar cells, Thin Solid Films, 582 (2014) 224-228.
35. A. Fairbrother, X. Fontané, V. Izquierdo-Roca, M. Placidi, D. Sylla, M. Espindola-Rodriguez, S. López-Mariño, F.A. Pulgarín, O. Vigil-Galán, A. Pérez-Rodríguez, E. Saucedo, Secondary phase formation in Zn-rich $Cu_2ZnSnSe_4$-based solar cells annealed in low pressure and temperature conditions, Progress in Photovoltaics: Research and Applications, 22 (2014) 479-487.
36. S. Giraldo, T. Thersleff, G. Larramona, M. Neuschitzer, P. Pistor, K. Leifer, A. Pérez-Rodríguez, C. Moisan, G. Dennler, E. Saucedo, Cu2ZnSnSe4 solar cells with 10.6% efficiency through innovative absorber engineering with Ge superficial nanolayer, Progress in Photovoltaics: Research and Applications, (2016). DOI: 10.1002/pip.2797.
37. A. Redinger, D.M. Berg, P.J. Dale, S. Siebentritt, The Consequences of Kesterite Equilibria for Efficient Solar Cells, Journal of the American Chemical Society, 133 (2011) 3320-3323.
38. M. Mousel, T. Schwarz, R. Djemour, T.P. Weiss, J. Sendler, J.C. Malaquias, A. Redinger, O. Cojocaru-Mirédin, P.-P. Choi, S. Siebentritt, Cu-rich precursors improve kesterite solar cells, Advanced Energy Materials, 4 (2013) 1300543.

39. K. Sun, C. Yan, F. Liu, J. Huang, F. Zhou, J.A. Stride, M. Green, X. Hao, Over 9% efficient kesterite Cu_2ZnSnS_4 solar cell fabricated by using $Zn_{1-x}Cd_xS$ buffer layer, Advanced Energy Materials, 6 (2016). DOI: 10.1002/aenm.201600046.
40. Y.S. Lee, T. Gershon, O. Gunawan, T.K. Todorov, T. Gokmen, Y. Virgus, S. Guha, $Cu_2ZnSnSe_4$ thin-film solar cells by thermal co-evaporation with 11.6% efficiency and improved minority carrier diffusion length, Advanced Energy Materials, 5 (2015). DOI: 10.1002/aenm.201401372.
41. T. Shin, I. Tadayoshi, H. Hirofumi, O. Keiichiro, A. Ryoji, Improvement of the open-circuit voltage of Cu_2ZnSnS_4 solar cells using a two-layer structure, Applied Physics Express, 8 (2015) 082302.
42. F. Liu, C. Yan, J. Huang, K. Sun, F. Zhou, J.A. Stride, M.A. Green, X. Hao, Nanoscale microstructure and chemistry of Cu_2ZnSnS_4/CdS interface in kesterite Cu_2ZnSnS_4 solar cells, Advanced Energy Materials, 6 (2016). DOI: 10.1002/aenm.201600706.
43. Y. Feng, T.-K. Lau, G. Cheng, L. Yin, Z. Li, H. Luo, Z. Liu, X. Lu, C. Yang, X. Xiao, A low-temperature formation path toward highly efficient Se-free Cu2ZnSnS4 solar cells fabricated through sputtering and sulfurization, CrystEngComm, 18 (2016) 1070-1077.
44. B. Shin, O. Gunawan, Y. Zhu, N.A. Bojarczuk, S.J. Chey, S. Guha, Thin film solar cell with 8.4% power conversion efficiency using an earth-abundant Cu_2ZnSnS_4 absorber, Progress in Photovoltaics: Research and Applications, 21 (2011) 72-76.
45. T.H. Nguyen, S. Fujikawa, T. Harada, J. Chantana, T. Minemoto, S. Nakanishi, S. Ikeda, Impact of precursor compositions on the structural and photovoltaic properties of spray-deposited Cu_2ZnSnS_4 thin films, ChemSusChem, 9 (2016) 2414-2420.
46. F. Jiang, S. Ikeda, T. Harada, M. Matsumura, Pure sulfide Cu_2ZnSnS_4 thin film solar cells fabricated by preheating an electrodeposited metallic stack, Advanced Energy Materials, 4 (2014). DOI: 10.1002/aenm.201301381.
47. K.J. Yang, D.H. Son, S.J. Sung, J.H. Sim, Y.I. Kim, S.N. Park, D.H. Jeon, J. Kim, D.K. Hwang, C.W. Jeon, D. Nam, H. Cheong, J.K. Kang, D.H. Kim, A band-gap-graded CZTSSe solar cell with 12.3% efficiency, Journal of Materials Chemistry A, 4 (2016) 10151-10158.
48. H. Xin, S.M. Vorpahl, A.D. Collord, I.L. Braly, A.R. Uhl, B.W. Krueger, D.S. Ginger, H.W. Hillhouse, Lithium-doping inverts the nanoscale electric field at the grain boundaries in $Cu_2ZnSn(S,Se)_4$ and increases photovoltaic efficiency, Physical Chemistry Chemical Physics, 17 (2015) 23859-23866.
49. Daisuke Hironiwa, High quality hetero junction formation of $Cu_2ZnSn(S,Se)_4$ solar cells, Ph.D. thesis, 2015.
50. S.G. Haass, M. Diethelm, M. Werner, B. Bissig, Y.E. Romanyuk, A.N. Tiwari, 11.2% efficient solution processed kesterite solar cell with a low voltage deficit, Advanced Energy Materials, 5 (2015) 1500712.
51. G. Larramona, S. Levcenko, S. Bourdais, A. Jacob, C. Choné, B. Delatouche, C. Moisan, J. Just, T. Unold, G. Dennler, Fine-tuning the Sn content in CZTSSe thin films to achieve 10.8% solar cell efficiency from spray-deposited water–ethanol-based colloidal inks, Advanced Energy Materials, 5 (2015) 1501404.
52. T. Schnabel, T. Abzieher, T.M. Friedlmeier, E. Ahlswede, Solution-based preparation of $Cu_2ZnSn(S,Se)_4$ for solar cells-comparison of $SnSe_2$ and elemental Se as chalcogen source, IEEE Journal of Photovoltaics, 5 (2015) 670-675.
53. J. Li, H. Wang, M. Luo, J. Tang, C. Chen, W. Liu, F. Liu, Y. Sun, J. Han, Y. Zhang, 10% efficiency $Cu_2ZnSn(S,Se)_4$ thin film solar cells fabricated by magnetron sputtering with enlarged depletion region width, Solar Energy Materials and Solar Cells, 149 (2016) 242-249.
54. S.Y. Wei, Y.C. Liao, C.H. Hsu, C.H. Cai, W.C. Huang, M.C. Huang, C.H. Lai, Achieving high efficiency $Cu_2ZnSn(S,Se)_4$ solar cells by non-toxic aqueous ink: defect analysis and electrical modeling, Nano Energy, 26 (2016) 74-82.
55. J. Li, H. Wang, L. Wu, C. Chen, Z. Zhou, F. Liu, Y. Sun, J. Han, Y. Zhang, Growth of $Cu_2ZnSnSe_4$ film under controllable Se vapor composition and impact of low Cu content on solar cell efficiency, ACS Applied Materials & Interfaces, 8 (2016) 10283-10292.

56. N. Janke, O. Grassme, R. Wwissmann, Alkali ion migration control from flat glass substrates, Glass Sci. Technol., 73(2000) 143 – 155.
57. G. Hanna, S. Schleussner, G. Bilder, H.W. Schock , U. Rau, J. H. Werner, Na diffusion in the Cu(In,Ga)Se_2/Mo/Glass system, in: Proceedings of the 3rd World Conference on Photovoltaic Energy Conversion, May 11– 18, 2003,Osaka Japan, pp 368– 371.
58. A. Rockett, J.S. Britt, T. Gillespie, C. Marshall, M.M. Al Jassim, F. Hasoon, R. Matson, B. Basol, Na in selenized Cu(In,Ga)Se_2 on Na-containing and Na-free glasses: distribution, grain structure, and device performances, Thin Solid Films, 372 (2000) 212-217.
59. D. Braunger, D. Hariskos, G. Bilger, U. Rau, H.W. Schock, Influence of sodium on the growth of polycrystalline Cu(In,Ga)Se_2 thin films, Thin Solid Films, 361-362 (2000) 161-166.
60. L. Kronik, D. Cahen, H.W. Schock, Effects of sodium on polycrystalline Cu(In,Ga)Se_2 and its solar cell performance, Advanced Materials, 10 (1998) 31-36.
61. S. Lopez-Marino, Y. Sanchez, M. Espindola-Rodriguez, X. Alcobe, H. Xie, M. Neuschitzer, I. Becerril, S. Giraldo, M. Dimitrievska, M. Placidi, L. Fourdrinier, V. Izquierdo-Roca, A. Perez-Rodriguez, E. Saucedo, Alkali doping strategies for flexible and light-weight $Cu_2ZnSnSe_4$ solar cells, Journal of Materials Chemistry A, 4 (2016) 1895-1907.
62. I. Becerril-Romero, S. Giraldo, S. López-Marino, M. Placidi, Y. Sánchez, D. Sylla, A. Pérez-Rodríguez, E. Saucedo, P. Pistor, Vitreous enamel as sodium source for efficient kesterite solar cells on commercial ceramic tiles, Solar Energy Materials and Solar Cells, 154 (2016) 11-17.
63. T. Todorov, J. Olenick, K. AOlenick, O. Gunawan, T. Gershon, C. Sturdevant, L. Yun Seog, C. Liang-yi, S. Guha, Flexible kesterite solar cells on ceramic substrates for advanced thermal processing, in: Photovoltaic Specialist Conference (PVSC), 2015 IEEE 42nd, pp. 1-3.
64. J.J. Scragg, J.T. Wätjen, M. Edoff, T. Ericson, T. Kubart, C. Platzer-Björkman, A Detrimental Reaction at the Molybdenum Back Contact in $Cu_2ZnSn(S,Se)_4$ Thin-Film Solar Cells, Journal of the American Chemical Society, 134 (2012) 19330-19333.
65. O. Souhaib, B. Guy, B. Marie, E. Hossam, M. Denis, E. Ounsi, T. Oualid, K. Christine, M. Marc, P. Jef, Study of alternative back contacts for thin film $Cu_2ZnSnSe_4$-based solar cells, Journal of Physics D: Applied Physics, 48 (2015) 035103.
66. G. Altamura, L. Grenet, C. Roger, F. Roux, V. Reita, R. Fillon, H. Fournier, S. Perraud, H. Mariette, Alternative back contacts in kesterite $Cu_2ZnSn(S_{1-x}Se_x)_4$ thin film solar cells, Journal of Renewable and Sustainable Energy, 6 (2014) 011401.
67. J. Ge, Y. Yu, W. Ke, J. Li, X. Tan, Z. Wang, J. Chu, Y. Yan, Improved performance of electroplated CZTS thin-film solar cells with bifacial configuration, ChemSusChem, 9 (2016) 2149-2158.
68. M. Espindola-Rodriguez, Y. Sánchez, S. López, H. Xie, V. Izquierdo-Roca, D. Sylla, M. Neuschitzer, O. Vigil-Gal, E. Saucedo, M. Placidi, Efficient bifacial $Cu_2ZnSnSe_4$ solar cells, in: Photovoltaic Specialist Conference (PVSC), 2015 IEEE 42nd, 2015, pp. 1-3.
69. J.S. Kim, J.K. Kang, D.K. Hwang, High efficiency bifacial $Cu_2ZnSnSe_4$ thin-film solar cells on transparent conducting oxide glass substrates, APL Materias, 4 (2016) 096101.
70. B. Shin, Y. Zhu, N.A. Bojarczuk, S. Jay Chey, S. Guha, Control of an interfacial $MoSe_2$ layer in $Cu_2ZnSnSe_4$ thin film solar cells: 8.9% power conversion efficiency with a TiN diffusion barrier, Applied Physics Letters, 101 (2012) 053903.
71. J.J. Scragg, T. Kubart, J.T. Wätjen, T. Ericson, M.K. Linnarsson, C. Platzer-Björkman, Effects of back contact instability on Cu_2ZnSnS_4 devices and processes, Chemistry of Materials, 25 (2013) 3162-3171.
72. S. Lopez-Marino, M. Placidi, A. Perez-Tomas, J. Llobet, V. Izquierdo-Roca, X. Fontane, A. Fairbrother, M. Espindola-Rodriguez, D. Sylla, A. Perez-Rodriguez, E. Saucedo, Inhibiting the absorber/Mo-back contact decomposition reaction in $Cu_2ZnSnSe_4$ solar cells: the role of a ZnO intermediate nanolayer, Journal of Materials Chemistry A, 1 (2013) 8338-8343.
73. W. Li, J. Chen, H. Cui, F. Liu, X. Hao, Inhibiting MoS_2 formation by introducing a ZnO intermediate layer for Cu_2ZnSnS_4 solar cells, Materials Letters, 130 (2014) 87-90.

74. S. Chen, A. Walsh, J. Yang, X. Gong, L. Sun, P. Yang, J. Chu, S. Wei, Compositional dependence of structural and electronic properties of $Cu_2ZnSn(S,Se)_4$ alloys for thin film solar cells, PHYSICAL REVIEW B, 83(2011)125201.
75. S. Schorr, The crystal structure of kesterite type compounds: A neutron and X-ray diffraction study, Solar Energy Materials and Solar Cells, 95 (2011) 1482-1488.
76. J.M. Doña, J. Herrero, Chemical bath deposition of CdS thin films: electrochemical in situ kinetic studies, Journal of The Electrochemical Society, 139 (1992) 2810-2814.
77. D. Regesch, L. Gütay, J.K. Larsen, V. Deprédurand, D. Tanaka, Y. Aida, S. Siebentritt, Degradation and passivation of $CuInSe_2$, Applied Physics Letters, 101 (2012) 112108.
78. J. Kessler, K.O. Velthaus, M. Ruckh, R. Laichinger, H.W. Schock, D. Lincot, R. Ortega, J. Vedel, Chemical bath deposition of CdS on $CuInSe_2$, etching effects and growth kinetics, In: the 6 th International Photovoltaic Solar Energy Conference, New Delhi, 1992, 1005.
79. D. Abou-Ras, G. Kostorz, A. Romeo, D. Rudmann, A.N. Tiwari, Structural and chemical investigations of CBD- and PVD-CdS buffer layers and interfaces in $Cu(In,Ga)Se_2$-based thin film solar cells, Thin Solid Films, 480-481 (2005) 118-123.
80. J. Tao, J. Liu, L. Chen, H. Cao, X. Meng, Y. Zhang, C. Zhang, L. Sun, P. Yang, J. Chu, 7.1% efficient co-electroplated Cu_2ZnSnS_4 thin film solar cells with sputtered CdS buffer layers, Green Chemistry, 18 (2016) 550-557.
81. S. Spiering, A. Eicke, D. Hariskos, M. Powalla, N. Naghavi, D. Lincot, Large-area Cd-free CIGS solar modules with In_2S_3 buffer layer deposited by ALCVD, Thin Solid Films, 451-452 (2004) 562-566.
82. D.A.R. Barkhouse, R. Haight, N. Sakai, H. Hiroi, H. Sugimoto, D.B. Mitzi, Cd-free buffer layer materials on $Cu_2ZnSn(S_xSe_{1-x})_4$: Band alignments with ZnO, ZnS, and In_2S_3, Applied Physics Letters, 100 (2012) 193904.
83. D.B. Khadka, S. Kim, J. Kim, A nonvacuum approach for fabrication of $Cu_2ZnSnSe_4/In_2S_3$ thin film solar cell and optoelectronic characterization, The Journal of Physical Chemistry C, 119 (2015) 12226-12235.
84. H. Hiroi, N. Sakai, S. Muraoka, T. Katou, H. Sugimoto, Development of high efficiency Cu_2ZnSnS_4 submodule with Cd-free buffer layer, in: Photovoltaic Specialists Conference (PVSC), 38th IEEE, 2012, pp. 001811-001814.
85. X. Li, Z. Su, S. Venkataraj, S.K. Batabyal, L.H. Wong, 8.6% efficiency CZTSSe solar cell with atomic layer deposited Zn-Sn-O buffer layer, Solar Energy Materials and Solar Cells, 157 (2016) 101-107.
86. D. Hironiwa, N. Matsuo, J. Chantana, N. Sakai, T. Kato, H. Sugimoto, T. Minemoto, Annealing effect on $Cu_2ZnSn(S,Se)_4$ solar cell with $Zn_{1-x}Mg_xO$ buffer layer, physica status solidi (a), 212 (2015) 2766-2771.
87. K.X. Steirer, R.L. Garris, J.V. Li, M.J. Dzara, P.F. Ndione, K. Ramanathan, I. Repins, G. Teeter, C.L. Perkins, Co-solvent enhanced zinc oxysulfide buffer layers in kesterite copper zinc tin selenide solar cells, Physical Chemistry Chemical Physics, 17 (2015) 15355-15364.
88. N. Markus, L. Karla, G. Maxim, B. Lorenzo Calvo, H. Stefan, P. Jose Marquez, S. Yudania, E.R. Moises, R. Yaroslav, P.R. Alejandro, I.R. Victor, S. Edgardo, Towards high performance Cd-free CZTSe solar cells with a ZnS(O,OH) buffer layer: the influence of thiourea concentration on chemical bath deposition, Journal of Physics D: Applied Physics, 49 (2016) 125602.
89. J. He, L. Sun, S. Chen, Y. Chen, P. Yang, J. Chu, Composition dependence of structure and optical properties of Cu2ZnSn(S,Se)4 solid solutions: An experimental study, Journal of Alloys and Compounds, 511 (2012) 129-132.
90. M. Dimitrievska, G. Gurieva, H. Xie, A. Carrete, A. Cabot, E. Saucedo, A. Pérez-Rodríguez, S. Schorr, V. Izquierdo-Roca, Raman scattering quantitative analysis of the anion chemical composition in kesterite $Cu_2ZnSn(S_xSe_{1-x})_4$ solid solutions, Journal of Alloys and Compounds, 628 (2015) 464-470.
91. M. Aslani, C.M. Garner, S. Kumar, D. Nordlund, P. Pianetta, Y. Nishi, Characterization of electronic structure of $Cu_2ZnSn(S_xSe_{1-x})_4$ absorber layer and $CdS/Cu_2ZnSn(S_xSe_{1-x})_4$ interfaces

by in-situ photoemission and inverse photoemission spectroscopies, Applied Physics Letters, 107 (2015) 183507.
92. R. Haight, A. Barkhouse, O. Gunawan, B. Shin, M. Copel, M. Hopstaken, D.B. Mitzi, Band alignment at the $Cu_2ZnSn(S_xSe_{1-x})_4$/CdS interface, Applied Physics Letters, 98 (2011) 253502.
93. S. Chen, A. Walsh, X.G. Gong, S.H. Wei, Classification of lattice defects in the kesterite Cu_2ZnSnS_4 and $Cu_2ZnSnSe_4$ earth-abundant solar cell absorbers, Advanced Materials, 25 (2013) 1522-1539.
94. E. Chagarov, K. Sardashti, R. Haight, D.B. Mitzi, A.C. Kummel, Density-functional theory computer simulations of $CZTS_{0.25}Se_{0.75}$ alloy phase diagrams, The Journal of Chemical Physics, 145 (2016) 064704.
95. L. Choubrac, A. Lafond, M. Paris, C. Guillot-Deudon, S. Jobic, The stability domain of the selenide kesterite photovoltaic materials and NMR investigation of the Cu/Zn disorder in $Cu_2ZnSnSe_4$ (CZTSe), Physical Chemistry Chemical Physics, 17 (2015) 15088-15092.
96. H. Duan, W. Yang, B. Bob, C. Hsu, B. Lei, Y. Yang. The role of sulfur in solution-processed $Cu_2ZnSn(S,Se)_4$ and its effect on defect properties, Advanced Functional Material 23(2013) 1466 – 1471.
97. D. W. Miller, C. W. Warren, O. Gunawan, T. Gokmen, D. B. Mitzi, J. D. Cohen. Electronically active defects in the $Cu_2ZnSn(Se,S)_4$ alloys as revealed by transient photocapacitance spectroscopy, Appl. Phys. Lett. 101(2012) 142106.
98. X. Z. Lin, T. Dittrich, S. Fengler, M. C. Lux-Steiner, A. Ennaoui, Correlation between processing conditions of $Cu_2ZnSn(S_xSe_{1-x})_4$ and modulated surface photovoltage, Appl. Phys. Lett. 102 (2013) 143903.
99. Oki Gunawan, Tayfun Gokmen and David B. Mitzi, Device characteristics of hydrazine-processed CZTSSe, in: K. Ito, Copper zinc tin sulfide-based thin-film solar cells, John Wiley & Sons, Ltd, Hoboken, 2015, pp. 388-411.
100. T. Gokmen, O. Gunawan, T. K. Todorov, D. B. Mitzi, Band tailing and efficiency limitation in kesterite solar cells, Appl. Phys. Lett. 103 (2013) 103506.
101. A. Redinger, M. Mousel, M. H. Wolter, N. Valle, S. Siebentritt, Influence of S/Se ratio on series resistance and on dominant recombination pathway in $Cu_2ZnSn(SSe)_4$ thin film solar cells, Thin Solid Films, 535 (2013) 291–295.
102. C.K. Miskin, W.-C. Yang, C.J. Hages, N.J. Carter, C.S. Joglekar, E.A. Stach, R. Agrawal, 9.0% efficient $Cu_2ZnSn(S,Se)_4$ solar cells from selenized nanoparticle inks, Progress in Photovoltaics: Research and Applications, 23 (2014) 654-659.
103. F. Liu, F. Zeng, N. Song, L. Jiang, Z. Han, Z. Su, C. Yan, X. Wen, X. Hao, Y. Liu, Kesterite $Cu_2ZnSn(S,Se)_4$ solar cells with beyond 8% efficiency by a sol-gel and selenization process, ACS Applied Materials & Interfaces, 7 (2015) 14376-14383.
104. F.O. Adurodija, J. Song, I. O. Asia, K.H. Yoon, Formation of $CuIn(S,Se)_2$ thin film by thermal diffusion of sulfur and selenium vapours into Cu-In alloy within a closed graphite container, Solar Energy Materials and Solar Cells, 58 (1999) 287-297.
105. T. Yamaguchi, T. Naoyama, H.S. Lee, A. Yoshida, T. Kobata, S. Niiyama, T. Nakamura, Preparation of $CuIn(S,Se)_2$ thin films by thermal crystallization in sulfur and selenium atmosphere, Journal of Physics and Chemistry of Solids, 64 (2003) 1831-1834.
106. T. Yamaguchi, M. Nakashima and A. Yoshida. Characterization of $CuIn(S,Se)_2$ thin films prepared by thermal crystallization from Cu-In-Se precursor in S/Se atmosphere, in: Proceedings of the 3rd World Conference on Photovoltaic Energy Conversion, May 11– 18, 2003,Osaka, Japan, p.p. 410-413.
107. A. Fairbrother, X. Fontané, V. Izquierdo-Roca, M. Espindola-Rodriguez, S. López-Mariño, M. Placidi, J. López-García, A. Pérez-Rodríguez, E. Saucedo, Single-step sulfo-selenization method to synthesize $Cu_2ZnSn(S_ySe_{1-y})_4$ absorbers from metallic stack precursors, ChemPhysChem 14(2013) 1836 − 1843.
108. S.M. Pawar, A.I. Inamdar, K.V. Gurav, S.W. Shin, J. Gwak, Y. Jo, J. Yun, H. Pak, S. Kwon, H. Kim, J.H. Kim, H. Im, Fabrication of $Cu_2ZnSn(S_xSe_{1-x})_4$ thin film solar cell by single step sulfo-selenization of stacked metallic precursors, Current Applied Physics, 15 (2014) 59-63.

109. M.G. Gang, S.W. Shin, C.W. Hong, K.V. Gurav, J. Gwak, J.H. Yun, J.Y. Lee, J.H. Kim, Sputtering processed highly efficient $Cu_2ZnSn(S,Se)_4$ solar cells by a low-cost, simple, environmentally friendly, and up-scalable strategy, Green Chemistry, 18 (2016) 700-711.
110. K. Muska, M. Kauk, M. Altosaar, M. Pilvet, M. Grossberg, O. Volobujeva, Synthesis of Cu2ZnSnS4 monograin powders with different compositions, Energy Procedia, 10 (2011) 203-207.
111. O. Gunawan, T. Gokmen, C.W. Warren, J.D. Cohen, T.K. Todorov, D.A.R. Barkhouse, S. Bag, J. Tang, B. Shin, D.B. Mitzi, Electronic properties of the $Cu_2ZnSn(Se,S)_4$ absorber layer in solar cells as revealed by admittance spectroscopy and related methods, Applied Physics Letters, 100 (2012) 253905.
112. G. Rey, A. Redinger, J. Sendler, T.P. Weiss, M. Thevenin, M. Guennou, B. El Adib, S. Siebentritt, The band gap of $Cu_2ZnSnSe_4$: effect of order-disorder, Applied Physics Letters, 105 (2014) 112106.
113. C. Krämmer, C. Huber, C. Zimmermann, M. Lang, T. Schnabel, T. Abzieher, E. Ahlswede, H. Kalt, M. Hetterich, Reversible order-disorder related band gap changes in $Cu_2ZnSn(S,Se)_4$ via post-annealing of solar cells measured by electroreflectance, Applied Physics Letters, 105 (2014) 262104.
114. M. Valentini, C. Malerba, F. Menchini, D. Tedeschi, A. Polimeni, M. Capizzi, A. Mittiga, Effect of the order-disorder transition on the optical properties of Cu_2ZnSnS_4, Applied Physics Letters, 108 (2016) 211909.
115. G. Rey, T.P. Weiss, J. Sendler, A. Finger, C. Spindler, F. Werner, M. Melchiorre, M. Hála, M. Guennou, S. Siebentritt, Ordering kesterite improves solar cells: a low temperature post-deposition annealing study, Solar Energy Materials and Solar Cells, 151 (2016) 131-138.
116. S. Bourdais, C. Choné, B. Delatouche, A. Jacob, G. Larramona, C. Moisan, A. Lafond, F. Donatini, G. Rey, S. Siebentritt, A. Walsh, G. Dennler, Is the Cu/Zn disorder the main culprit for the voltage deficit in kesterite solar cells? Advanced Energy Materials, 6 (2016) 1502276.
117. C. Krämmer, C. Huber, T. Schnabel, C. Zimmermann, M. Lang, E. Ahlswede, H. Kalt, M. Hetterich, Order-disorder related band gap changes in $Cu_2ZnSn(S,Se)_4$: Impact on solar cell performance, in: Photovoltaic Specialist Conference (PVSC), 2015 IEEE 42nd, pp. 1-4.
118. J.J.S. Scragg, L. Choubrac, A. Lafond, T. Ericson, C. Platzer-Björkman, A low-temperature order-disorder transition in Cu_2ZnSnS_4 thin films, Applied Physics Letters, 104 (2014) 041911.
119. P.M.P. Salomé, J. Malaquias, P.A. Fernandes, M.S. Ferreira, J.P. Leitao, A.F. da Cunha, J.C. González, F.N. Matinaga, G.M. Ribeiro, E.R. Viana, The influence of hydrogen in the incorporation of Zn during the growth of Cu_2ZnSnS_4 thin films, Solar Energy Materials and Solar Cells, 95 (2011) 3482-3489.
120. A. Redinger, S. Siebentritt, Coevaporation of $Cu_2ZnSnSe_4$ thin films, Applied Physics Letters, 97 (2010) 092111.
121. A. Weber, R. Mainz, H.W. Schock, On the Sn loss from thin films of the material system Cu-Zn-Sn-S in high vacuum, Journal of Applied Physics, 107 (2010) 013516.
122. A. Fairbrother, E. Saucedo, X. Fontane, V. Izquierdo-Roca, D. Sylla, M. Espindola-Rodriguez, F.A. Pulgarin-Agudelo, O. Vigil-Galan, A. Perez-Rodriguez, Preparation of 4.8% efficiency Cu2ZnSnSe4 based solar cell by a two step process, in: Photovoltaic Specialists Conference (PVSC), 2012 38th IEEE, 2012, pp. 002679-002684.
123. M. Buffière, G. Brammertz, S. Sahayaraj, M. Batuk, S. Khelifi, D. Mangin, A.-A. El Mel, L. Arzel, J. Hadermann, M. Meuris, J. Poortmans, KCN chemical etch for interface engineering in $Cu_2ZnSnSe_4$ solar cells, ACS Applied Materials & Interfaces, 7 (2015) 14690-14698.
124. T. Tanaka, T. Sueishi, K. Saito, Q. Guo, M. Nishio, K.M. Yu, W. Walukiewicz, Existence and removal of Cu_2Se second phase in coevaporated $Cu_2ZnSnSe_4$ thin films, Journal of Applied Physics, 111 (2012) 053522.
125. K. Granath, M. Bodegard, L. Stolt, The effect of NaF on $Cu(In,Ga)Se_2$ thin film solar cells, Solar Energy Materials and Solar Cells, 60 (2000) 279-293.

126. R. Caballero, C.A. Kaufmann, T. Eisenbarth, T. Unold, R. Klenk, H.-W. Schock, High efficiency low temperature grown Cu(In,Ga)Se_2 thin film solar cells on flexible substrates using NaF precursor layers, Progress in Photovoltaics: Research and Applications, 19 (2011) 547-551.
127. D. Rudmann, D. Brémaud, H. Zogg, A.N. Tiwari, Na incorporation into Cu(In,Ga)Se_2 for high-efficiency flexible solar cells on polymer foils, Journal of Applied Physics, 97 (2005) 084903.
128. J.V. Li, D. Kuciauskas, M.R. Young, I.L. Repins, Effects of sodium incorporation in co-evaporated $Cu_2ZnSnSe_4$ thin-film solar cells, Applied Physics Letters, 102 (2013) 163905.
129. W.M. Hlaing Oo, J.L. Johnson, A. Bhatia, E.A. Lund, M.M. Nowell, M.A. Scarpulla, Grain size and texture of Cu_2ZnSnS_4 thin films synthesized by cosputtering binary sulfides and annealing: effects of processing conditions and sodium, Journal of Electronic Materials, 40 (2011) 2214-2221.
130. T. Gershon, B. Shin, N. Bojarczuk, M. Hopstaken, D.B. Mitzi, S. Guha, The role of sodium as a surfactant and suppressor of non-radiative recombination at internal surfaces in Cu_2ZnSnS_4, Advanced Energy Materials, 5 (2014) 1400849.
131. C.M. Sutter-Fella, J.A. Stückelberger, H. Hagendorfer, F. La Mattina, L. Kranz, S. Nishiwaki, A.R. Uhl, Y.E. Romanyuk, A.N. Tiwari, Sodium assisted sintering of chalcogenides and its application to solution processed $Cu_2ZnSn(S,Se)_4$ thin film solar cells, Chemistry of Materials, 26 (2014) 1420-1425.
132. A. Chirilă, S. Buecheler, F. Pianezzi, P. Bloesch, C. Gretener, A.R. Uhl, C. Fella, L. Kranz, J. Perrenoud, S. Seyrling, R. Verma, S. Nishiwaki, Y.E. Romanyuk, G. Bilger, A.N. Tiwari, Highly efficient Cu(In,Ga)Se_2 solar cells grown on flexible polymer films, Nature Materials, 10 (2011) 857-861.
133. T. Dullweber, G.H. anna, U. Rau, H.W. Schock, A new approach to high-efficiency solar cells by band gap grading in Cu(In,Ga)Se_2 chalcopyrite semiconductors, Solar Energy Materials and Solar Cells, 67 (2001) 145-150.
134. M. Gloeckler, J.R. Sites, Band-gap grading in Cu(In,Ga)Se_2 solar cells, Journal of Physics and Chemistry of Solids, 66 (2005) 1891-1894.
135. T. Dullweber, O. Lundberg, J. Malmström, M. Bodegård, L. Stolt, U. Rau, H.W. Schock, J.H. Werner, Back surface band gap gradings in Cu(In,Ga)Se_2 solar cells, Thin Solid Films, 387 (2001) 11-13.
136. M. Olopade, A. Adewoyin, D. Olorode, M. Chendo, Effect of band gap grading on the performance characteristics of Cu_2ZnSnS_4 solar cell, in: 2014 IEEE 40th Photovoltaic Specialist Conference (PVSC), pp. 2394-2396.
137. H. Daisuke, M. Masashi, A. Naoki, T. Zeguo, M. Takashi, Simulation of optimum band-gap grading profile of $Cu_2ZnSn(S,Se)_4$ solar cells with different optical and defect properties, Japanese Journal of Applied Physics, 53 (2014) 071201.
138. G. Altamura, Development of CZTSSe thin films based solar cells, Ph.D. thesis, 2014, pp. 112-119.
139. K. Woo, Y. Kim, W. Yang, K. Kim, I. Kim, Y. Oh, J.Y. Kim, J. Moon, Band-gap-graded $Cu_2ZnSn(S_{1-x},Se_x)_4$ solar cells fabricated by an ethanol-based, particulate precursor ink route, Scientific Reports, 3 (2013) 3069.
140. I. Kim, K. Kim, Y. Oh, K. Woo, G. Cao, S. Jeong, J. Moon, Bandgap-graded $Cu_2Zn(Sn_{1-x}Ge_x)S_4$ thin-film solar cells derived from metal chalcogenide complex ligand capped nanocrystals, Chemistry of Materials, 26 (2014) 3957-3965.
141. T. Kato, N. Sakai, H. Sugimoto, Efficiency improvement of $Cu_2ZnSn(S,Se)_4$ submodule with graded bandgap and reduced backside ZnS segregation, in: 2014 IEEE 40th Photovoltaic Specialist Conference (PVSC), pp. 0844-0846.
142. A. Fairbrother, E. García-Hemme, V. Izquierdo-Roca, X. Fontané, F.A. Pulgarín-Agudelo, O. Vigil-Galán, A. Pérez-Rodríguez, E. Saucedo, Development of a selective chemical etch to improve the conversion efficiency of Zn-rich Cu_2ZnSnS_4 solar cells, Journal of the American Chemical Society, 134 (2012) 8018-8021.
143. S. López-Marino, Y. Sánchez, M. Placidi, A. Fairbrother, M. Espindola-Rodríguez, X. Fontané, V. Izquierdo-Roca, J. López-García, L. Calvo-Barrio, A. Pérez-Rodríguez, E. Saucedo, ZnSe

etching of Zn-rich $Cu_2ZnSnSe_4$: an oxidation route for improved solar-cell efficiency, Chemistry–A European Journal, 19 (2013) 14814-14822.
144. M. Mousel, A. Redinger, R. Djemour, M. Arasimowicz, N. Valle, P. Dale, S. Siebentritt, HCl and Br_2-MeOH etching of $Cu_2ZnSnSe_4$ polycrystalline absorbers, Thin Solid Films, 535 (2013) 83-87.
145. H. Xie, Y. Sánchez, S. López-Marino, M. Espíndola-Rodríguez, M. Neuschitzer, D. Sylla, A. Fairbrother, V. Izquierdo-Roca, A. Pérez-Rodríguez, E. Saucedo, Impact of Sn(S,Se) secondary phases in $Cu_2ZnSn(S,Se)_4$ solar cells: a chemical route for their selective removal and absorber surface passivation, ACS Applied Materials & Interfaces, 6 (2014) 12744-12751.
146. Y.S. Lee, T. Gershon, T.K. Todorov, W. Wang, M.T. Winkler, M. Hopstaken, O. Gunawan, J. Kim, Atomic layer deposited aluminum oxide for interface passivation of $Cu_2ZnSn(S,Se)_4$ thin-film solar cells, Advanced Energy Materials, 6 (2016) 1600198.
147. J. Kim, H. Hiroi, T.K. Todorov, O. Gunawan, M. Kuwahara, T. Gokmen, D. Nair, M. Hopstaken, B. Shin, Y.S. Lee, W. Wang, H. Sugimoto, D.B. Mitzi, High efficiency $Cu_2ZnSn(S,Se)_4$ solar cells by applying a double In_2S_3/CdS emitter, Advanced Materials, 26 (2014) 7427-7431.
148. S. Giraldo, M. Neuschitzer, T. Thersleff, S. López-Marino, Y. Sánchez, H. Xie, M. Colina, M. Placidi, P. Pistor, V. Izquierdo-Roca, K. Leifer, A. Pérez-Rodríguez, E. Saucedo, Large efficiency improvement in $Cu_2ZnSnSe_4$ solar cells by introducing a superficial Ge nanolayer, Advanced Energy Materials, 5 (2015) 1501070.
149. M. Neuschitzer, J. Marquez, S. Giraldo, M. Dimitrievska, M. Placidi, I. Forbes, V. Izquierdo-Roca, A. Pérez-Rodriguez, E. Saucedo, V_{oc} boosting and grain growth enhancing Ge-doping strategy for $Cu_2ZnSnSe_4$ photovoltaic absorbers, The Journal of Physical Chemistry C, 120 (2016) 9661-9670.
150. S. Giraldo, M. Neuschitzer, M. Placidi, P. Pistor, A. Pérez-Rodríguez, E. Saucedo, $Cu_2ZnSnSe_4$ based solar cells with efficiency exceeding by adding a superficial Ge nanolayer: the interaction between Ge and Na, IEEE Journal of Photovoltaics, 6 (2016) 754-759.
151. H. Xin, S.M. Vorpahl, A.D. Collord, I.L. Braly, A.R. Uhl, B.W. Krueger, D.S. Ginger, H.W. Hillhouse, Lithium-doping inverts the nanoscale electric field at the grain boundaries in $Cu_2ZnSn(S,Se)_4$ and increases photovoltaic efficiency, Physical Chemistry Chemical Physics, 17 (2015) 23859-23866.
152. K.F. Tai, D. Fu, S.Y. Chiam, C.H.A. Huan, S.K. Batabyal, L.H. Wong, Antimony doping in solution-processed $Cu_2ZnSn(S,Se)_4$ solar cells, ChemSusChem, 8 (2015) 3504-3511.
153. D. Tiwari, T. Koehler, X. Lin, R. Harniman, I. Griffiths, L. Wang, D. Cherns, R. Klenk, D.J. Fermin, Cu_2ZnSnS_4 thin films generated from a single solution based precursor: The effect of Na and Sb doping, Chemistry of Materials, 28 (2016) 4991-4997.
154. T. Gershon, Y.S. Lee, P. Antunez, R. Mankad, S. Singh, D. Bishop, O. Gunawan, M. Hopstaken, R. Haight, Photovoltaic materials and devices based on the alloyed kesterite absorber $(Ag_xCu_{1-x})_2ZnSnSe_4$, Advanced Energy Materials, 6 (2016) 1502468.
155. K. Sardashti, R. Haight, T. Gokmen, W. Wang, L.Y. Chang, D.B. Mitzi, A.C. Kummel, Impact of nanoscale elemental distribution in high-performance kesterite solar cells, Advanced Energy Materials, 5 (2015) 1402180.
156. J.H. Kim, S.Y. Choi, M. Choi, T. Gershon, Y.S. Lee, W. Wang, B. Shin, S.Y. Chung, Atomic-scale observation of oxygen substitution and its correlation with hole-transport barriers in $Cu_2ZnSnSe_4$ thin-film solar cells, Advanced Energy Materials, 6 (2016) 1501902.
157. S. Lopez-Marino, M. Espíndola-Rodríguez, Y. Sánchez, X. Alcobé, F. Oliva, H. Xie, M. Neuschitzer, S. Giraldo, M. Placidi, R. Caballero, V. Izquierdo-Roca, A. Pérez-Rodríguez, E. Saucedo, The importance of back contact modification in $Cu_2ZnSnSe_4$ solar cells: The role of a thin MoO_2 layer, Nano Energy, 26 (2016) 708-721.
158. R.A. Wibowo, H. Yoo, A. Hölzing, R. Lechner, S. Jost, J. Palm, M. Gowtham, B. Louis, R. Hock, A study of kesterite $Cu_2ZnSn(Se,S)_4$ formation from sputtered Cu–Zn–Sn metal precursors by rapid thermal processing sulfo-selenization of the metal thin films, Thin solid films 535 (2013) 57–61.

159. L. Grenet, S. Bernardi, D. Kohen, C. Lepoittevin, S. Noël, N. Karst, A. Brioude, S. Perraud, H. Mariette, $Cu_2ZnSn(S_{1-x}Se_x)_4$ based solar cell produced by selenization of vacuum deposited precursors, Solar Energy Materials and Solar Cells 101 (2012) 11–14.
160. A. Redinger, K. Hones, X. Fontané, V. Izquierdo-Roca, E. Saucedo, N. Valle, A. Perez-Rodriguez, S. Siebentritt, Detection of a ZnSe secondary phase in coevaporated $Cu_2ZnSnSe_4$ thin films, Applied Physics Letters, 98 (2011) 101907-101903.
161. X. Fontané, L. Calvo-Barrio, V. Izquierdo-Roca, E. Saucedo, A. Pérez-Rodriguez, J.R. Morante, D.M. Berg, P.J. Dale, S. Siebentritt, In-depth resolved Raman scattering analysis for the identification of secondary phases: Characterization of Cu_2ZnSnS_4 layers for solar cell applications, Applied Physics Letters, 98 (2011) 181905-181903.
162. W. Albers, C. Haas, H. J. Vink, J. D. Wasscher, Investigations on SnS, Journal of Applied Physics, 32 (1961) 2220.
163. J.J. Scragg, T. Ericson, T. Kubart, M. Edoff, C. Platzer-Björkman, Chemical Insights into the Instability of Cu2ZnSnS4 Films during Annealing, Chemistry of Materials, 23 (2011) 4625-4633.
164. J.H. Yoon, W.M. Kim, J.K. Park, Y.J. Baik, T.Y. Seong, J.h. Jeong, Control of the preferred orientations of $Cu(In,Ga)Se_2$ films and the photovoltaic conversion efficiency using a surface-functionalized molybdenum back contact, Progress in Photovoltaics: Research and Applications, 22 (2014) 69-76.
165. J. Li, Y. Zhang, W. Zhao, D. Nam, H. Cheong, L. Wu, Z. Zhou, Y. Sun, A temporary barrier effect of the alloy layer during selenization: tailoring the thickness of $MoSe_2$ for efficient $Cu_2ZnSnSe_4$ solar cells, Advanced Energy Materials, 5 (2015) 1402178.
166. H. Rau, T.R.N. Kutty, J.R.F. Guedes De Carvalho, Thermodynamics of sulphur vapour, The Journal of Chemical Thermodynamics, 5 (1973) 833-844.
167. Y.K. Rao, Composition of liquid-saturated selenium vapor, Metallurgical Transactions B, 14 (1983) 308-311.
168. J. Berkowitz, J.R. Marquart, Equilibrium Composition of Sulfur Vapor, The Journal of Chemical Physics, 39 (1963) 275-283.
169. G. Simon, E.J. Essene, Phase relations among selenides, sulfides, tellurides, and oxides; I, Thermodynamic properties and calculated equilibria, Economic Geology, 91 (1996) 1183-1208.
170. X. Yin, C. Tang, L. Sun, Z. Shen, H. Gong, Study on phase formation mechanism of non- and near-stoichiometric $Cu_2ZnSn(S,Se)_4$ film prepared by selenization of Cu-Sn-Zn-S precursors, Chemistry of Materials, 26 (2014) 2005-2014.
171. I.D. Olekseyuk, et al., Phase equilibria in the Cu_2S-ZnS-SnS_2 system., Journal of Alloys and Compounds, 368 (2004) 135-143.
172. I.V. Dudchak, L.V. Piskach, Phase equilibria in the Cu_2SnSe_3-$SnSe_2$-ZnSe system, Journal of Alloys and Compounds, 351 (2003) 145-150.
173. A. Fairbrother, M. Dimitrievska, Y. Sanchez, V. Izquierdo-Roca, A. Perez-Rodriguez, E. Saucedo, Compositional paradigms in multinary compound systems for photovoltaic applications: a case study of kesterites, Journal of Materials Chemistry A, 3 (2012) 9451-9455.
174. H. Katagiri, K. Jimbo, M. Tahara, H. Araki, K. Oishi, The influence of the composition ratio on CZTS-based thin film solar cells, Materials Research Society Symposium Proceedings 1165 (2009) M04–01.
175. K. Muska, M. Kauk, M. Altosaar, M. Pilvet, M. Grossberg, O. Volobujeva, Synthesis of Cu_2ZnSnS_4 monograin powders with different compositions, Energy Procedia, 10 (2011) 203-207.
176. K. Muska, M. Kauk, M. Grossberg, M. Altosaar, J. Raudoja, O. Volobujeva, Influence of compositional deviations on the properties of $Cu_2ZnSnSe_4$ monograin powders, Energy Procedia, 10 323-327.
177. K. Muska, M. Kauk-Kuusik, M. Grossberg, M. Altosaar, M. Pilvet, T. Varema, K. Timmo, O. Volobujeva, A. Mere, Impact of $Cu_2ZnSn(Se_xS_{1-x})4$ (x = 0.3) compositional ratios on the monograin powder properties and solar cells, Thin Solid Films, 535 (2013) 35-38.

178. V. Chawla, B. Clemens, Effect of composition on high efficiency CZTSSe devices fabricated using co-sputtering of compound targets, in: Photovoltaic Specialists Conference (PVSC), 2012 38th IEEE, 2012, pp. 002990-002992.
179. W.C. Hsu, I. Repins, C. Beall, C. DeHart, G. Teeter, B. To, Y. Yang, R. Noufi, The effect of Zn excess on kesterite solar cells, Solar Energy Materials and Solar Cells, 113 (2013) 160-164.
180. S. Niki, P.J. Fons, A. Yamada, Y. Lacroix, H. Shibata, H. Oyanagi, M. Nishitani, T. Negami, T. Wada, Effects of the surface $Cu_{2-x}Se$ phase on the growth and properties of $CuInSe_2$ films, Applied Physics Letters, 74 (1999) 1630-1632.
181. B.A. Schubert, B. Marsen, S. Cinque, T. Unold, R. Klenk, S. Schorr, H.W. Schock, Cu_2ZnSnS_4 thin film solar cells by fast coevaporation, Progress in Photovoltaics: Research and Applications, 19 (2011) 93-96.
182. S. Siebentritt, Why are kesterite solar cells not 20% efficient? Thin Solid Films, 535 (2013) 1-4.
183. J.T. Wätjen, J.J. Scragg, T. Ericson, M. Edoff, C. Platzer-Björkman, Secondary compound formation revealed by transmission electron microscopy at the Cu_2ZnSnS_4/Mo interface, Thin Solid Films, 535 (2013) 31-34.
184. X. Fontané, V. Izquierdo-Roca, A. Fairbrother, M. Espíndola-Rodríguez, Simón Lòpez-Marino, M. Placidi, T. Jawhari, E. Saucedo, A. Pérez-Rodríguez, Selective detection of secondary phases in $Cu_2ZnSn(S,Se)_4$ based absorbers by pre-resonant Raman spectroscopy, in: 2013 IEEE 39th Photovoltaic Specialists Conference (PVSC), pp. 2581-2584.
185. P.A . Fernandes, P.M.P. Salomé, A .F. da Cunha, Growth and Raman scattering characterization of Cu_2ZnSnS_4 thin films, Thin Solid Films, 517 (2009)2519–2523.
186. A .J. Cheng, M. Manno, A . Khare, C. Leighton, S.A. Campbell, E.S. Aydil, Imaging and phase identification of Cu_2ZnSnS_4 thin films using confocal Raman spectroscopy, Journal of Vacuum Science & Technology A, 29 (2011) 051203.
187. J. Just, D. Lützenkirchen-Hecht, R. Frahm, S. Schorr, T. Unold, Determination of secondary phases in kesterite Cu_2ZnSnS_4 thin films by x-ray absorption near edge structure analysis, Applied Physics Letters, 99 (2011) 262105.
188. J. Just, C.M. Sutter-Fella, D. Lutzenkirchen-Hecht, R. Frahm, S. Schorr, T. Unold, Secondary phases and their influence on the composition of the kesterite phase in CZTS and CZTSe thin films, Physical Chemistry Chemical Physics, 18 (2016) 15988-15994.
189. R. Djemour, A. Redinger, M. Mousel, L. Gütay, S. Siebentritt, Multiple phases of $Cu_2ZnSnSe_4$ detected by room temperature photoluminescence, Journal of Applied Physics, 116 (2014) 073509.
190. T. Schwarz, O. Cojocaru-Mirédin, P. Choi, M. Mousel, A. Redinger, S. Siebentritt, D. Raabe, Atom probe study of $Cu_2ZnSnSe_4$ thin-films prepared by co-evaporation and post-deposition annealing, Applied Physics Letters, 102 (2013) 042101.
191. A. Ennaoui, M. Lux-Steiner, A. Weber, D. Abou-Ras, I. Kötschau, H.W. Schock, R. Schurr, A. Hölzing, S. Jost, R. Hock, T. Voβ, J. Schulze, A. Kirbs, Cu_2ZnSnS_4 thin film solar cells from electroplated precursors: Novel low-cost perspective, Thin Solid Films, 517 (2009) 2511-2514.
192. L. Vauche, L. Risch, M. Arasimowicz, Y. Sánchez, E. Saucedo, M. Pasquinelli, T. Goislard de Monsabert, P.P. Grand, S. Jaime-Ferrer, Detrimental effect of Sn-rich secondary phases on $Cu_2ZnSnSe_4$ based solar cells, Journal of Renewable and Sustainable Energy, 8 (2016) 033502.
193. A. Alvarez Barragan, H. Malekpour, S. Exarhos, A.A. Balandin, L. Mangolini, Grain-to-grain compositional variations and phase segregation in copper–zinc–tin–sulfide films, ACS Applied Materials & Interfaces, 8 (2016) 22971-22976.
194. B.G. Mendis, M.C.J. Goodman, J.D. Major, A.A. Taylor, K. Durose, D.P. Halliday, The role of secondary phase precipitation on grain boundary electrical activity in Cu_2ZnSnS_4 (CZTS) photovoltaic absorber layer material, Journal of Applied Physics, 112 (2012) 124508.
195. L. Weinhardt, O. Fuchs, D. Groβ, E. Umbach, C. Heske, N.G. Dhere, A.A. Kadam, S.S. Kulkarni, Surface modifications of $Cu(In,Ga)S_2$ thin film solar cell absorbers by KCN and H_2O_2/H_2SO_4 treatments, Journal of Applied Physics, 100 (2006) 024907.
196. R.P.H. Chang, C.C. Chang, S. Darack, Hydrogen plasma etching of semiconductors and their oxides, Journal of Vacuum Science & Technology, 20 (1982) 45-50.

197. K. Ozono, M. Obara, A. Usui, H. Sunakawa, High-speed ablation etching of GaN semiconductor using femtosecond laser, Optics Communications, 189 (2001) 103-106.
198. A. Haruhiko, Y. Masahiro, F. Nobuo, Developments of plasma etching technology for fabricating semiconductor devices, Japanese Journal of Applied Physics, 47 (2008) 1435.
199. S.W. Shin, S.M. Pawar, C.Y. Park, J.H. Yun, J.-H. Moon, J.H. Kim, J.Y. Lee, Studies on Cu_2ZnSnS_4 (CZTS) absorber layer using different stacking orders in precursor thin films, Solar Energy Materials and Solar Cells, 95 (2011) 3202-3206.
200. M. Xie, D. Zhuang, M. Zhao, B. Li, M. Cao, J. Song, Fabrication of Cu_2ZnSnS_4 thin films using a ceramic quaternary target, Vacuum, 101 (2014) 146-150.
201. L. Vauche, L. Risch, Y. Sánchez, M. Dimitrievska, M. Pasquinelli, T. Goislard de Monsabert, P.P. Grand, S. Jaime-Ferrer, E. Saucedo, 8.2% pure selenide kesterite thin-film solar cells from large-area electrodeposited precursors, Progress in Photovoltaics: Research and Applications, 24 (2015) 38-51.
202. G. Raj., Advanced inorganic chemistry, Krishna Prakashan Media, Meerut, 2008, p.600.
203. A. Arora, Text book of inorganic chemistry, Discovery Publishing House, New Delhi, 2005, p. 444.
204. T. Olar, I. Lauermann, H. Xie, M. Neuschitzer, E. Saucedo, W. Calvet, A. Steigert, B. Ümsür, B. Chacko, V. Parvan, M. Gorgoi, B. Senkovskiy, M.C. Lux-Steiner, Assessment of chemical and electronic surface properties of the $Cu_2ZnSn(SSe)_4$ after different etching procedures by synchrotron-based spectroscopies, Energy Procedia, 84 (2015) 8-16.
205. C.Y. Tseng, C.T. Lee, Mechanisms of $(NH4)_2S_x$-treated III-V compound triple-junction solar cells incorporating with hybrid electrode, Applied Physics Letters, 101 (2012) 033902.
206. V. N. Bessolov, M. Lebedev, Chalcogenide passivation of III–V semiconductor surfaces. Semiconductors, 32 (1998) 1141–1156.
207. M. Neuschitzer, Y. Sanchez, S. López-Marino, H. Xie, A. Fairbrother, M. Placidi, S. Haass, V. Izquierdo-Roca, A. Perez-Rodriguez, E. Saucedo, Optimization of CdS buffer layer for high-performance $Cu_2ZnSnSe_4$ solar cells and the effects of light soaking: elimination of crossover and red kink, Progress in Photovoltaics: Research and Applications, 23 (2015) 1660-1667.
208. J.H. Yoon, W.M. Kim, J.K. Park, Y.J. Baik, T.Y. Seong, J.h. Jeong, Control of the preferred orientations of $Cu(In,Ga)Se_2$ films and the photovoltaic conversion efficiency using a surface-functionalized molybdenum back contact, Progress in Photovoltaics: Research and Applications, 22 (2014) 69-76.
209. T. Minemoto, T. Matsui, H. Takakura, Y. Hamakawa, T. Negami, Y. Hashimoto, T. Uenoyama, M. Kitagawa, Theoretical analysis of the effect of conduction band offset of window/CIS layers on performance of CIS solar cells using device simulation, Solar Energy Materials and Solar Cells, 67 (2001) 83-88.
210. M. Gloeckler, J.R. Sites, Efficiency limitations for wide-band-gap chalcopyrite solar cells, Thin Solid Films, 480-481 (2005) 241-245.
211. C.M. Ruiz, A. Pérez-Rodríguez, J. Arbiol, J.R. Morante, V. Bermúdez, Impact of the structure of $Mo(S,Se)_2$ interfacial region in electrodeposited $CuIn(S,Se)_2$ solar cells, physica status solidi (a), 212 (2015) 61-66.
212. J.E. Granata, J.R. Sites, S. Asher, R.J. Matson, Quantitative incorporation of sodium in $CuInSe_2$ and $Cu(In,Ga)Se_2$ photovoltaic devices, in: Photovoltaic Specialists Conference, 1997., Conference Record of the Twenty-Sixth IEEE, 1997, pp. 387-390.
213. F. Pianezzi, P. Reinhard, A. Chirila, B. Bissig, S. Nishiwaki, S. Buecheler, A.N. Tiwari, Unveiling the effects of post-deposition treatment with different alkaline elements on the electronic properties of CIGS thin film solar cells, Physical Chemistry Chemical Physics, 16 (2014) 8843-8851.
214. V. Fjallstrom, P. Szaniawski, B. Vermang, P.M.P. Salome, F. Rostvall, U. Zimmermann, M. Edoff, Recovery after potential-induced degradation of $CuIn_{1-x}$ $GaxSe_2$ solar cells with CdS and Zn(O,S) buffer layers, IEEE Journal of Photovoltaics, 5 (2015) 664-669.

215. K. Sardashti, R. Haight, T. Gokmen, W. Wang, L.Y. Chang, D.B. Mitzi, A.C. Kummel, Impact of nanoscale elemental distribution in high-performance kesterite solar cells, Advanced Energy Materials, 5 (2015) 1402180.
216. M. Neuschitzer, Y. Sanchez, T. Olar, T. Thersleff, S. Lopez-Marino, F. Oliva, M. Espindola-Rodriguez, H. Xie, M. Placidi, V. Izquierdo-Roca, I. Lauermann, K. Leifer, A. Pérez-Rodriguez, E. Saucedo, Complex surface chemistry of kesterites: Cu/Zn reordering after low temperature postdeposition annealing and its role in high performance devices, Chemistry of Materials, 27 (2015) 5279-5287.
217. K. Wang, O. Gunawan, T. Todorov, B. Shin, S.J. Chey, N.A. Bojarczuk, D. Mitzi, S. Guha, Thermally evaporated Cu_2ZnSnS_4 solar cells, Applied Physics Letters, 97 (2010) 143508.
218. S. Tajima, R. Asahi, D. Isheim, D.N. Seidman, T. Itoh, M. Hasegawa, K. Ohishi, Atom-probe tomographic study of interfaces of Cu_2ZnSnS_4 photovoltaic cells, Applied Physics Letters, 105 (2014) 093901.
219. D. Hironiwa, N. Sakai, T. Kato, H. Sugimoto, Z. Tang, J. Chantana, T. Minemoto, Impact of annealing treatment before buffer layer deposition on $Cu_2ZnSn(S,Se)_4$ solar cells, Thin Solid Films, 582 (2015) 151-153.
220. K. Granath, M. Bodegård, L. Stolt, The effect of NaF on Cu(In, Ga)Se_2 thin film solar cells, Solar Energy Materials and Solar Cells, 60 (2000) 279-293.
221. B. Tell, Properties of the alkalis in CdS, Journal of Applied Physics, 42 (1971) 2919-2924.
222. S.S. Lin, J.G. Lu, Z.Z. Ye, H.P. He, X.Q. Gu, L.X. Chen, J.Y. Huang, B.H. Zhao, p-type behavior in Na-doped ZnO films and ZnO homojunction light-emitting diodes, Solid State Communications, 148 (2008) 25-28.
223. B.T. Gershon, Y.S. Lee, R. Mankad, O. Gunawan, T. Gokmen, D. Bishop, B. McCandless, S. Guha, The impact of sodium on the sub-bandgap states in CZTSe and CZTS, Applied Physics Letters, 106 (2015) 123905.
224. T. Gershon, B. Shin, N. Bojarczuk, M. Hopstaken, D.B. Mitzi, S. Guha, The Role of Sodium as a Surfactant and Suppressor of Non-Radiative Recombination at Internal Surfaces in Cu_2ZnSnS_4, Advanced Energy Materials, 5 (2014) 1400849.
225. S. Lopez-Marino, Y. Sanchez, M. Espindola-Rodriguez, X. Alcobe, H. Xie, M. Neuschitzer, I. Becerril, S. Giraldo, M. Dimitrievska, M. Placidi, L. Fourdrinier, V. Izquierdo-Roca, A. Perez-Rodriguez, E. Saucedo, Alkali doping strategies for flexible and light-weight $Cu_2ZnSnSe_4$ solar cells, Journal of Materials Chemistry A, 4 (2016) 1895-1907.
226. K.J. Yang, J.H. Sim, B. Jeon, D.H. Son, D.H. Kim, S.J. Sung, D.K. Hwang, S. Song, D.B. Khadka, J. Kim, J.K. Kang, Effects of Na and MoS_2 on Cu_2ZnSnS_4 thin-film solar cell, Progress in Photovoltaics: Research and Applications, 23 (2015) 862-873.
227. I.L. Repins, J.V. Li, A. Kanevce, C.L. Perkins, K.X. Steirer, J. Pankow, G. Teeter, D. Kuciauskas, C. Beall, C. Dehart, J. Carapella, B. Bob, J.S. Park, S.H. Wei, Effects of deposition termination on $Cu_2ZnSnSe_4$ device characteristics, Thin Solid Films, 582 (2015) 184-187.
228. W.C. Hsu, H. Zhou, S. Luo, T.B. Song, Y.T. Hsieh, H.S. Duan, S. Ye, W. Yang, C.J. Hsu, C. Jiang, B. Bob, Y. Yang, Spatial element distribution control in a fully solution-processed nanocrystals-based 8.6% $Cu_2ZnSn(S,Se)_4$ device, ACS Nano, 8 (2014) 9164-9172.
229. W.C. Hsu, I. Repins, C. Beall, C. DeHart, G. Teeter, B. To, Y. Yang, R. Noufi, The effect of Zn excess on kesterite solar cells, Solar Energy Materials and Solar Cells, 113 (2013) 160-164.
230. B. Vermang, F. Rostvall, V. Fjällström, M. Edoff, Potential-induced optimization of ultra-thin rear surface passivated CIGS solar cells, physica status solidi (RRL) – Rapid Research Letters, 8 (2014) 908-911.
231. A. Chirilă, P. Reinhard, F. Pianezzi, P. Bloesch, A.R. Uhl, C. Fella, L. Kranz, D. Keller, C. Gretener, H. Hagendorfer, D. Jaeger, R. Erni, S. Nishiwaki, S. Buecheler, A.N. Tiwari, Potassium-induced surface modification of Cu(In,Ga)Se_2 thin films for high-efficiency solar cells, Nature Materials, 12 (2013) 1107-1111.
232. T. Gokmen, O. Gunawan, T.K. Todorov, D.B. Mitzi, Band tailing and efficiency limitation in kesterite solar cells, Applied Physics Letters, 103 (2013) 103506.

233. W. Wu, Y. Cao, J.V. Caspar, Q. Guo, L.K. Johnson, R.S. McLean, I. Malajovich, K.R. Choudhury, Characterization of CZTSSe photovoltaic device with an atomic layer-deposited passivation layer, Applied Physics Letters, 105 (2014) 042108.
234. Y.S. Lee, T. Gershon, T.K. Todorov, W. Wang, M.T. Winkler, M. Hopstaken, O. Gunawan, J. Kim, Atomic layer deposited aluminum oxide for interface passivation of $Cu_2ZnSn(S,Se)_4$ thin-film solar cells, Advanced Energy Materials, 6 (2016) 1600198.
235. T. Nakada, K. Matsumoto, M. Okumura, Improved efficiency of $Cu(In,Ga)Se_2$ thin film solar cells by surface sulfurization using wet process, in: Photovoltaic Specialists Conference, 2002. Conference Record of the Twenty-Ninth IEEE, 2002, pp. 527-530.
236. C.W. Chen, H.W. Tsai, T.T. Wu, Y.T. Yen, Y.C. Wang, C.H. Hsu, W.C. Tsai, H.S. Tsai, C.H. Shen, J.M. Shieh, Y.L. Chueh, Enhanced solar performance of chemical bath deposited-$Zn(O,S)/Cu(In,Ga)Se_2$ solar cells via interface engineering by a wet soaking process, Journal of Materials Chemistry A, 3 (2015) 14985-14990.
237. W.H. Ho, C.H. Hsu, T.H. Yeh, Y.H. Chang, S.Y. Wei, T.Y. Lin, C.H. Lai, Room-temperature chemical solution treatment for flexible $ZnS(O,OH)/Cu(In,Ga)Se_2$ solar cell: improvements in interface properties and metastability, ACS Applied Materials & Interfaces, 8 (2016) 6709-6717.
238. J.A. Taylor, An XPS study of the oxidation of AlAs thin films grown by MBE, Journal of Vacuum Science & Technology, 20 (1982) 751-755.
239. M.T. Anthony, M.P. Seah, XPS: energy calibration of electron spectrometers. 1—an absolute, traceable energy calibration and the provision of atomic reference line energies, Surface and Interface Analysis, 6 (1984) 95-106.
240. G. Schön, Auger and direct electron spectra in X-ray photoelectron studies of zinc, zinc oxide, gallium and gallium oxide, Journal of Electron Spectroscopy and Related Phenomena, 2 (1973) 75-86.
241. P.W. Yu, Excitation-dependent emission in Mg-, Be-, Cd-, and Zn-implanted GaAs, Journal of Applied Physics, 48 (1977) 5043-5051.
242. S. Levcenko, J. Just, A. Redinger, G. Larramona, S. Bourdais, G. Dennler, A. Jacob, T. Unold, Deep defects in $Cu_2ZnSn(S,Se)_4$ solar cells with varying Se content, Physical Review Applied, 5 (2016) 024004.
243. T. Gershon, B. Shin, N. Bojarczuk, T. Gokmen, S. Lu, S. Guha, Photoluminescence characterization of a high-efficiency Cu_2ZnSnS_4 device, Journal of Applied Physics, 114 (2013) 154905.
244. T. Gershon, B. Shin, T. Gokmen, S. Lu, N. Bojarczuk, S. Guha, Relationship between Cu_2ZnSnS_4 quasi donor-acceptor pair density and solar cell efficiency, Applied Physics Letters, 103 (2013) 193903.
245. X. Lin, A. Ennaoui, S. Levcenko, T. Dittrich, J. Kavalakkatt, S. Kretzschmar, T. Unold, M.C. Lux-Steiner, Defect study of $Cu_2ZnSn(S_xSe_{1-x})_4$ thin film absorbers using photoluminescence and modulated surface photovoltage spectroscopy, Applied Physics Letters, 106 (2015) 013903.
246. F. Luckert, D.I. Hamilton, M.V. Yakushev, N.S. Beattie, G. Zoppi, M. Moynihan, I. Forbes, A.V. Karotki, A.V. Mudryi, M. Grossberg, J. Krustok, R.W. Martin, Optical properties of high quality $Cu_2ZnSnSe_4$ thin films, Applied Physics Letters, 99 (2011) 062104.
247. I.V. Bodnar, On the band gap of $Cu_2ZnSn(S_xSe_{1-x})_4$ alloys, Semiconductors, 49 (2015) 1145-1148.
248. J.A.M. AbuShama, S. Johnston, T. Moriarty, G. Teeter, K. Ramanathan, R. Noufi, Properties of $ZnO/CdS/CuInSe_2$ solar cells with improved performance, Progress in Photovoltaics: Research and Applications, 12 (2004) 39-45.
249. J. AbuShama, R. Noufi, S. Johnston, S. Ward, X. Wu, Improved performance in $CuInSe_2$ and surface-modified $CuGaSe_2$ solar cells, NREL Report, 2004.
250. Z. Su, J.M.R. Tan, X. Li, X. Zeng, S.K. Batabyal, L.H. Wong, Cation substitution of solution-processed Cu_2ZnSnS_4 thin film solar cell with over 9% efficiency, Advanced Energy Materials, 5 (2015) 1500682.

251. J.B. Li, V. Chawla, B.M. Clemens, Investigating the role of grain boundaries in CZTS and CZTSSe thin film solar cells with scanning probe microscopy, Advanced Materials, 24 (2012) 720-723.
252. G.Y. Kim, A.R. Jeong, J.R. Kim, W. Jo, D.H. Son, D.H. Kim, J.K. Kang, Surface potential on grain boundaries and intragrains of highly efficient $Cu_2ZnSn(S,Se)_4$ thin-films grown by two-step sputtering process, Solar Energy Materials and Solar Cells, 127 (2014) 129-135.

Appendix

All the articles as well as their corresponding supporting information referenced in previous chapters are included in this section.

Chapter 3:

Haibing Xie*, Mirjana Dimitrievska, Xavier Fontané, Yudania Sánchez, Simon López-Marino, Victor Izquierdo-Roca, Verónica Bermúdez, Alejandro Pérez-Rodríguez, Edgardo Saucedo, "Formation and impact of secondary phases in Cu-poor Zn-rich $Cu_2ZnSn(S_{1-y}Se_y)_4$ ($0 \leqslant y \leqslant 1$) based solar cells",* ***Solar Energy Materials & Solar Cells*** *140 (2015) 289 – 298.*

Chapter 4:

Haibing Xie, *Yudania Sánchez, Simón López-Marino, Moisés Espíndola-Rodríguez, Markus Neuschitzer, Diouldé Sylla, Andrew Fairbrother, Victor Izquierdo-Roca, Alejandro Pérez-Rodríguez, and Edgardo Saucedo*. "Impact of Sn-(S,Se) secondary phases in $Cu_2ZnSn(S,Se)_4$ solar cells: a chemical route for their selective removal and absorber surface passivation",* ***ACS Applied Materials & Interface*** *6 (2014) 12744 – 12751.*

Chapter 5:

1. ***Haibing Xie****, Simon López-Marino, Tetiana Olar, Yudania Sánchez, Markus Neuschitzer, Florian Oliva, Sergio Giraldo, Victor Izquierdo-Roca, Iver Lauermann, Alejandro Pérez-Rodríguez, Edgardo Saucedo,"Impact of Na dynamics at the $Cu_2ZnSn(S,Se)_4$/CdS interface during post low temperature treatment of absorbers",* ***ACS Applied Materials & Interfaces*** *8 (2016) 5017-5024.*
2. *Yudania Sánchez*, Moisés Espíndola-Rodríguez,* ***Haibing Xie****, Simón López-Marino, Markus Neuschitzer, Sergio Giraldo, Mirjana Dimitrievska, Marcel Placidi, Victor Izquierdo-Roca, Fabián Andrés Pulgarín-Agudelo, Osvaldo Vigil-Galán and Edgardo Saucedo, "Ultra-thin CdS for highly performing chalcogenides thin film based solar cells",* ***Solar Energy Materials and Solar Cells*** *(2016) Doi:10.1016/j.solmat.2015.12.037.*

Solar Energy Materials & Solar Cells 140 (2015) 289–298

Contents lists available at ScienceDirect

Solar Energy Materials & Solar Cells

journal homepage: www.elsevier.com/locate/solmat

Formation and impact of secondary phases in Cu-poor Zn-rich $Cu_2ZnSn(S_{1-y}Se_y)_4$ $(0 \le y \le 1)$ based solar cells

Haibing Xie [a,*], Mirjana Dimitrievska [a], Xavier Fontané [a], Yudania Sánchez [a], Simon López-Marino [a], Victor Izquierdo-Roca [a], Verónica Bermúdez [b], Alejandro Pérez-Rodríguez [a,c], Edgardo Saucedo [a]

[a] Catalonia Institute for Energy Research, IREC, Jadins de les Dones de Negre 1, 08930 Sant Adrià de Besòs, Barcelona, Spain
[b] EDF R&D, 6 Quai Watier, 78401 Chatou, France
[c] IN2UB, Departament d'Electrònica, Universitat de Barcelona, C. Martí i Franquès 1, 08028 Barcelona, Spain

ARTICLE INFO

Article history:
Received 14 January 2015
Received in revised form
15 March 2015
Accepted 14 April 2015

Keywords:
$Cu_2ZnSn(S$
$Se)_4$
Secondary phases
Pre-resonant Raman
Kesterite
Solar cell

ABSTRACT

$Cu_2ZnSn(S_{1-y}Se_y)_4$ (CZTSSe, $0 \le y \le 1$) based solar cells relying on earth abundant and low toxic elements are attracting a lot of research interest for photovoltaic applications. Currently, the record efficiency (12.6%) is still far away from the required value (15–18%) for future commercialization. One of the main issues concerning the performance limitation of the devices is certainly the formation of secondary phases, coupled with the off-stoichiometric growth conditions used for high efficiency solar cells. In this work, we prepared Cu-poor and Zn-rich CZTSSe absorbers and solar cells in the whole S–Se compositional range, with the aim of analyzing the formation of secondary phases and their impact on the optoelectronic properties of the devices. The results show that much less secondary phases (especially Zn(S,Se)) are prone to be present on the surface and at the back region of Se-rich CZTSSe absorbers, when compared with other types of kesterites like Cu_2ZnSnS_4, $Cu_2ZnSnSe_4$ and S-rich CZTSSe. CZTSSe solid solutions almost free of secondary phases on the surface and at the back region can be obtained by the appropriate control of different process parameters: thermal treatment (low Ar pressure), composition (simultaneous sulfo-selenization) and surface etching (using $(NH_4)_2S$ solutions). Based on this absorber with very low secondary phases content, best efficiency of 6.8% for a Se-rich CZTSSe solar cell was achieved using a single-step sulfo-selenization process.

1. Introduction

$Cu_2ZnSn(S_{1-y}Se_y)_4$ (CZTSSe, $0 \le y \le 1$) kesterite based solar cells are currently developing fast and have achieved a great improvement, 9.2% efficiency for Cu_2ZnSnS_4 (CZTS) solar cells [1], 11.6% efficiency for $Cu_2ZnSnSe_4$ (CZTSe) solar cells [2] and 12.6% efficiency for solid solution CZTSSe solar cells [3] were demonstrated. Until now, Se-rich solid solution CZTSSe solar cells show the best results (S/(S+Se) ≈ 0.3), which is similar to the case of $Cu(In,Ga)Se_2$ (CIGS) based solar cells, in which the partial substitution of indium by gallium allows for the highest performance of 21.7% [4]. Therefore, the appropriate S/(S+Se) and Ga/(Ga+In) ratio are paramount for high efficiency devices, since they clearly impact relevant features such as band gap, defects and secondary phases. Thus, it is highly relevant to understand the inner limitation mechanism concerning performance in kesterites based devices. Some preliminary works addressing these issues have demonstrated that Se-rich CZTSSe solar cells have lower defect energy level and bulk defect density, better charge separation and carrier collection efficiency than S-rich CZTSSe solar cells [5,6]. In addition, it was found that the Urbach energy is lower for CZTSSe devices with $E_g \le 1.2$ eV, when compared to devices based on absorbers with higher band gap [7].

Secondary phases clearly limit the efficiency of kesterites, and are commonly present on the surface, bulk or at the back of the films, due to a very narrow single phase existence region shown in the pseudoternary phase diagrams [8,9], off-stoichiometry and non-equilibrium thermodynamics conditions used in the typical kesterites synthesis processes. $Cu_xS(Se)$ is considered highly detrimental in CIGS films, and may appear as well on the surface of CZTSe films when Cu/(Zn+Sn) > 0.9, which will severely increase the hole concentration and cause short circuits of the p–n junction, reducing the efficiency considerably [10–12]. Low band gap phases SnS(Se) (Sn:S(Se) = 1:1, $E_g \approx 1$–1.3 eV) and $Cu_2SnS(Se)_3$ ($E_g \approx 0.8$–1 eV) may limit the open circuit voltage of the solar cells, due to a band gap lower than that of the kesterites. It has been reported that only 100 meV of band gap reduction can decrease the maximum achievable efficiency

* Corresponding author. Tel.: +34 933 562 615; fax: +34 933 563 802.
E-mail address: xhaibing@irec.cat (H. Xie).

http://dx.doi.org/10.1016/j.solmat.2015.04.023
0927-0248/

by 8% absolute [13]. The most commonly found and reported secondary phases are Zn(S,Se) because the Cu-poor Zn-rich composition is usually accepted as suitable to achieve high efficiency devices and thus extensively employed. They are often detected on the surface or at the back region of absorbers, and are assumed to be the reason for high series resistance, which decreases the fill factor and the short circuit current [14–17].

However, there are few works focusing on investigating secondary phases in solid solution CZTSSe thin films, probably due to the complexity of this type of material and the technical issues to effectively detect some secondary phases. An initial work on secondary phases research using XRD with quantitative Rietveld refinement for solid solution CZTSSe thin films with broad metallic composition variation in precursors was presented by Wibowo et al. [18]. After selenization of ZnS/Cu/Sn stack precusors, Grenet et al. found the presence of Zn(S,Se) at the bottom of $Cu_2ZnSn(S,Se)_4$ thin films via TEM, combined with EDS analysis [19]. No investigation about the influence of S/(S+Se) on the formation and distribution of secondary phases in solid solution CZTSSe solar cells is reported until now.

For an effective discrimination in the presence of secondary phases in kesterites, it is very important to choose appropriate detection techniques. As it is well known, XRD is not an effective tool for distinguishing quaternary $Cu_2ZnSnS(Se)_4$, ZnS(Se) and $Cu_2SnS(Se)_3$, as they have highly similar crystalline structures [20,21]. Raman with green excitation wavelength (514.5 or 532 nm) is useful to detect kesterites, Cu–(S,Se), and Sn–(S,Se), but it is not sensitive to identify Zn (S,Se) because of low Raman scattering efficiency [22]. To solve the problem, a pre-resonant Raman methodology for detecting Zn(S,Se) in kesterites was developed. The key is to employ excitation lights with photon energy close to the band gap of secondary phases to get resonant excitation conditions. It was found that UV light (325 nm) is effective to identify ZnS, while blue light (458 nm) is sensitive to inspect ZnSe [23,24]. Another relevant issue is that, Zn(S,Se) usually presents at the Mo/$Cu_2ZnSn(S,Se)_4$ interface, which can be difficult to detect by Raman measurements performed on the surface, taking into account that the penetration depth of the Raman excitation light is only about 100 nm. Therefore, a "lift-off" technique is necessary to expose the back of the absorber for Raman detection [25,26].

In this work, $Cu_2ZnSn(S,Se)_4$ thin films with various S/(S+Se) and Zn/Sn ratios were synthesized through single-step sulfo-selenization annealing of glass/Mo/ZnO/Cu/Sn/Cu/Zn metallic stacks deposited by direct current (DC) magnetron sputtering [27,28]. Raman measurements with green light (532 nm), blue light (458 nm), and UV light (325 nm) as well as XRD were employed to identify secondary phases on the surface and at the back region of absorbers. Their formation and distribution as a function of different process parameters were analyzed, as well as its possible impact on devices performance.

2. Materials and methods

Cu/Sn/Cu/Zn metallic stack precursors were deposited by DC-magnetron sputtering onto Mo coated soda-lime glass substrates. With respect to the stacking sequence, as has been demonstrated by Altamura et al. [29], the composition of CZTSSe films is relatively homogenous and almost independent of the precursor stacking order (at least using ZnS/Cu/Sn or ZnS/Sn/Cu precursors). In our case, we use Zn metallic precursor instead ZnS and a detailed explanation for the selection of this sequence is published in our previous works [16,27,28]. Precursor films were approximately 600 nm thick, with compositional ratios of Cu/(Zn+Sn) around 0.8 and Zn/Sn varying from 1.2 to 1.3.

Quaternary CZTS absorbers were produced by reactive annealing of the metallic precursors under a sulfur atmosphere at 550 °C, 1 bar Ar pressure for 30 min, and using two crucibles, one with 50 mg of sulfur powder (Alfa-Aesar, 99.995%) and the other with 5 mg of tin powder (Alfa-Aesar, 99.999%). CZTSe absorbers were produced by reactive annealing under a selenium atmosphere at 550 °C for 30 min under a flow of Ar to maintain a pressure of 1 mbar, and also with two crucibles, one containing 50 mg of selenium powder (Alfa-Aesar, 99.999%) and the other with 5 mg of tin powder. The heating rate for all thermal treatments was 20 °C/min. The cooling process was allowed to proceed naturally. To form solid solution CZTSSe films a single-step sulfo-selenization anneal was used [27,28]. The process is similar to that used for the pure CZTS or CZTSe films, with 5 mg tin powder added but varying the ratio of a mixture of sulfur and selenium. Five different added S/(S+Se) weight ratios, 0.02, 0.04, 0.2, 0.4 and 0.8 were used while maintaining the total weight of the mixture of 50 mg. Two annealing temperature profiles were employed; one is "one step profile": 550 °C, 30 min, 1 mbar or 1 bar. The other is "two step profile": first 200 °C for 15 min in 1 mbar atmosphere and then 550 °C for 30 min in 1 bar atmosphere, which is proved to be beneficial to obtain different Se-rich absorbers. Compared to other methodologies including sequential sulfurization and selenization of metallic precursors (or the opposite sequence) and sulfurization (selenization) of chalcogen containing precursors, the single-step sulfo-selenization process employed here is easier and simpler, allowing for a precise control of the S/(S+Se) ratio of solid solution CZTSSe absorbers [27].

The as-annealed CZTSSe absorbers were characterized by means of X-ray diffraction (XRD), scanning electron microscope (SEM), Raman spectroscopy, and glow discharge optical emission spectroscopy (GD-OES). XRD measurements were performed using a Siemens D500 diffractometer in θ–2θ configuration. The SEM images were obtained with a ZEISS Series Auriga microscope using 10 kV accelerating voltage. Raman scattering measurements were performed on the surface and at the back region of the absorbers using three different excitation wavelengths: 532 (green), 458 (blue) and 325 (ultraviolet) nm. Measurements of 532 and 325 nm excitation wavelengths were performed in back scattering configuration with a LabRam HR800-UV Horiba–Jobin Yvon spectrometer, through an Olympus metallographic microscope with a laser spot size of the order of 1 μm. The spot was rastered over an area of $30 \times 30\ \mu m^2$ to avoid effects in the spectra related to potential microscopic inhomogeneity. In addition, measurements of 458 nm excitation wavelength were made using a T64000 Horiba–Jobin Yvon spectrometer with a spot size of 100 μm on the samples. In all cases, to avoid the presence of thermal effects in the spectra, the power excitation density was around 50 W/cm^2. More details about the Raman measurements can be found in our previous works [30,31]. For the detection of secondary phases at the back region of the films, a "lift-off" technic was employed. The in-depth compositions were obtained by means of a glow discharge optical emission spectrometer (GD-OES) HORIBA GD Profiler 2, powered with a radio frequency source at 3 kHz.

Finally, solar cells were fabricated by depositing 50–60 nm of CdS by chemical bath deposition (CBD), followed by the pulsed DC-magnetron sputtering deposition of 50 nm of intrinsic ZnO and 450 nm of ZnO:Al (CT100 Alliance Concepts). For the optoelectronic characterization 3×3 mm^2 cells were scribed and the area was determined using an optical microscope. The illuminated *J–V* curves were obtained using an ABET Technologies Sun 3000 Class AAA solar simulator calibrated by a reference silicon solar cells. The external quantum efficiency (EQE) of the devices was performed on a Bentham PVE300 system with a spot size equal to the area of each cell of 3×3 mm^2.

3. Results and discussion

3.1. Determination of the S/(S+Se) ratios and evaluation of the in-depth S/(S+Se) ratios uniformity in CZTSSe thin films

Prior to the secondary phases discussion in CZTSSe thin films, it is necessary to know the S/(S+Se) ratio of the absorbers, because this ratio has a strong influence on secondary phase formation as it will be shown next. Moreover, the S/(S+Se) ratio is one of the most important parameters for CZTSSe or other materials, since this ratio allows for band gap tuning. There are many ways to determine it in CZTSSe thin films, i.e., energy dispersive spectrometer (EDS), X-ray fluorescence (XRF), inductively coupled plasma optical emission spectrometry (ICP-OES), XRD, EQE, Raman spectroscopy, etc. Among them, EDS, XRF and ICP are direct methods to get S/(S+Se) ratio, which allows for the acquisition of the S/(S+Se) ratio from direct calculations of the atomic concentration of each element. XRD, EQE and Raman are indirect methods. XRD and EQE determine the S/(S+Se) ratio through the use of Vegard´s law applied to the lattice constant and band gap evolution with composition [32,33], respectively. Raman determines the S/(S+Se) ratio from the linear correlation between the S/(S+Se) ratio and the integral intensities ratio of the S-related and Se-related Raman peaks: $A_{270-380\ cm^{-1}}/(A_{150-260\ cm^{-1}}+A_{270-380\ cm^{-1}})$ [30]. In addition, it should be mentioned that the values of the anion compositions obtained using different methods could not be interpreted in the same way. For example, EQE and Raman spectroscopy are surface sensitive techniques with a relatively shallow penetration depth. On the other hand, X-ray penetrates completely the film, meaning that the information obtained by XRF and XRD corresponds to that of the whole sample. Also, it is important to note that estimations of chalcogen compositions using EDS, XRF, and ICP give an overall composition of all the phases that are currently present in the sample, and not only of the kesterite phase. In order to evaluate the anion composition of the kesterite phase, the suitable methods are Raman, XRD and EQE, which are based on the integral intensities or shift of kesterite related peaks or bands. Furthermore, Raman measurements could be performed on the front and the back of each thin film, thus giving the information about the uniformity of the kesterite phase through the thickness of the layer. Finally, regarding the accuracy, EDS and XRF usually give higher S/(S+Se) ratios than the real values, due to the fact that the signal of sulfur and Mo overlaps in the measurements, while those indirect methods could have some inherent errors during the evaluation. On the other hand, ICP is a highly sensitive method for trace analysis of elements. Therefore, in this work we take it as a reference technique for the evaluation of the indirect methods. A summary of the different methods presented above is included in Table S1 of supporting information (SI) Part 1.

At this point, it is important to remark that the absolute measurements of S and Se are of key importance for the validation of the composition estimation, because they give a fingerprint of the single phase compound with a given alloy composition. The agreement of the value of S+Se with that expected in the stoichiometric $Cu_2ZnSn(S,Se)_4$ is paramount for a single phase, and this value can only be obtained by direct methods like XRF, EDS and ICP. Using XRF calibrated with ICP-OES standards, it is corroborated that all the CZTSSe samples in this work have a total anion composition in the range of (49.0 ± 0.5)% (obtained from 9 independent measurements in the whole sample area), in close agreement with the expected 50% value of S+Se in the stoichiometric $Cu_2ZnSn(S,Se)_4$. Table 1 shows the metallic composition and sulfur content of one representative CZTSSe absorber obtained from ICP-OES, XRD, EQE, surface and back Raman measurements and GD-OES. This representative sample was annealed at 550 °C for 30 min in 1 mbar atmosphere and solar cells based on this type of absorber achieve efficiency above 6%. For more details on the estimations of S/(S+Se) from XRD and EQE, see SI Part 1 (different ways of extracting band gap from EQE are compared and discussed). From Table 1 it is possible to observe that the S/(S+Se) ratio calculated from XRD, EQE and surface and back Raman measurements are consistent with ICP-OES results, which confirms that the estimation of S/(S+Se) ratios from XRD, EQE and Raman is reliable. The results show that XRD, EQE and Raman measurements can be used as a facile way to get a rough estimation of S/(S+Se) ratio in this type of materials.

Table 1
Composition measurements by ICP, XRD, EQE, Raman and GD-OES on a representative CZTSSe thin film.

Cu/(Zn+Sn)	Zn/Sn	S/(S+Se)						
ICP		ICP	XRD	EQE	Raman surface	Raman back	GD-OES Surface (1 nm)	GD-OES back (1.5 μm)
0.85	1.17	0.32	0.30	0.26	0.25	0.24	0.29	0.35

In addition, it is important to check the in-depth composition uniformity of CZTSSe absorbers, especially for the S/(S+Se) ratio. This is one of the crucial issues of CZTSSe solid solutions thin films, which will considerably influence the band gap, secondary phases, and optoelectronic properties of the final solar cells. Fig. 1 shows the top view and cross section SEM pictures and the corresponding GD-OES depth profile of a representative CZTSSe sample (same sample present in Table 1). The layer has 1.5 μm in thickness and is formed by 1–2 μm compact grains. However, there are voids at the absorber/Mo interface and in the bulk, which is a common problem even in the record CZTSe and CZTSSe solar cells [2,3]. Fig. 1(c) shows the GD-OES profile of the absorber, which demonstrates a slight decrease of selenium and increase of sulfur from the surface to the back region. Calculations show that the S/(S+Se) ratio on the surface (1 nm) is 0.29 while in the bottom (1.5 μm) is 0.35 (see Table 1, both detection depths are estimated from the surface), which may be due to the higher sulfur vapor pressure in the initial step of the reaction [34,35]. Nevertheless, the in-depth distribution of S/(S+Se) is relatively uniform, which is also supported by the surface and back Raman results (see Table 1).

Note that the surface S/(S+Se) ratio obtained with GD-OES, is in accordance with the values predicted by EQE (see Table 1). As XRD generally gives information from the whole bulk, and EQE is limited to the first hundreds nanometers top layer, in this sense, a comparison of S/(S+Se) ratio obtained from these two methods can give a simple evaluation of the in-depth uniformity of S/(S+Se). Thus, similar EQE and XRD results could mean a relatively homogeneous in-depth distribution of S/(S+Se) in the absorber, already proved by the GD-OES in-depth profile. It has to be noted that, in our XRD patterns symmetric peaks of kesterite phase are always observed when the S/(S+Se) ratios of samples estimated from EQE and XRD are comparable. As it is known, symmetric peaks in XRD usually correspond to a single phase, based on which it could be reasonably deduced that the in-depth S/(S+Se) in the corresponding samples are homogeneous. Additionally, grazing incidence X-ray diffraction (GIXRD) measurements with different angles were also performed on several samples (these results will be published elsewhere). From GIXRD the same values of lattice parameters for each angle were obtained supporting the homogeneous S/(S+Se) ratio through the sample layers.

In summary, two ways of estimating in-depth S/(S+Se) uniformity are presented: the comparison of S/(S+Se) ratio from XRD and EQE, or from the Raman spectra performed on the surface and at the back region of the films. The in-depth S/(S+Se) uniformity

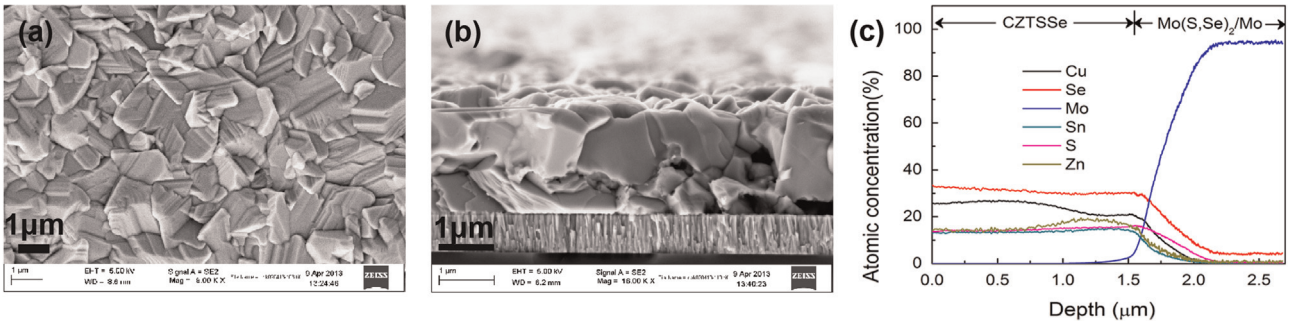

Fig. 1. SEM pictures of the top view (a), cross section (b), and GD-OES depth profile (c) of a representative CZTSSe thin film (same sample in Table 1).

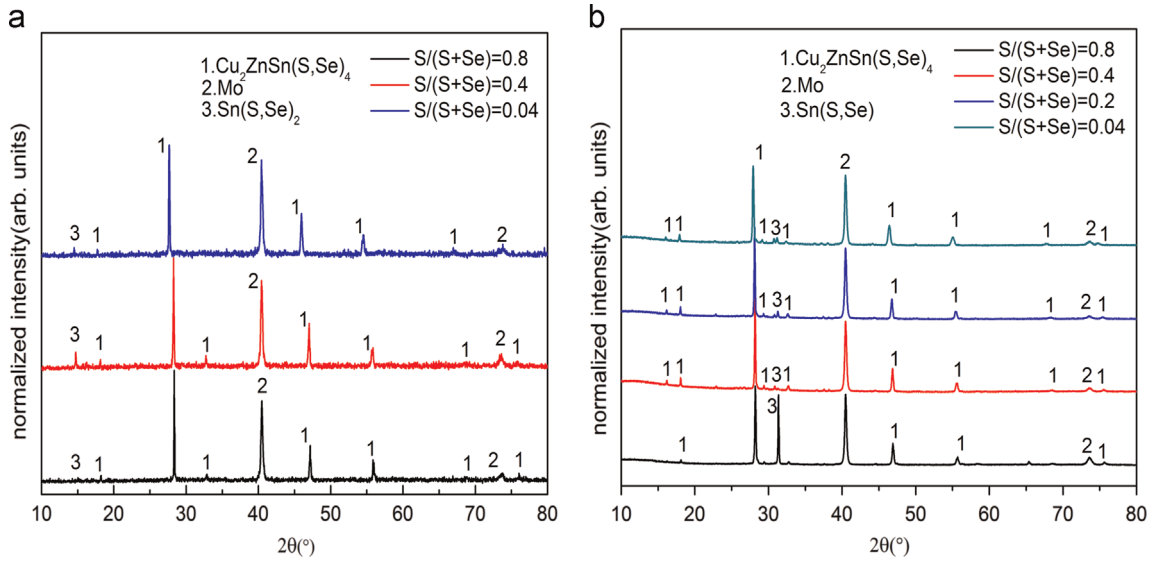

Fig. 2. XRD patterns of CZTSSe absorbers annealed under 1 bar (a) and 1 mbar (b) Ar pressure at 550 °C for 30 min with various added S/(S+Se) weight ratios. See SI Table S2 for more detailed description of the different samples.

of the representative sample is confirmed by GD-OES, which is in agreement with the results from the two described methods. Based on this conclusion, in the following parts, these two methods will be applied to evaluate the in-depth S/(S+Se) uniformity of the samples. Finally, with respect to the cations distribution, Cu decreases and Zn increases at the back region, correlating with the expected existence of Zn(S,Se) at the back [36]. However, this kind of behavior is also observed in the single phase region of CZTS and CZTSe [37,38], and could be an indication of the formation of Zn related defects like Zn_{Cu} antisites.

3.2. *Influence of the Ar pressure and S/(S+Se) ratios on the presence of secondary phases in CZTSSe thin films*

Fig. 2(a) and (b) show the XRD patterns of CZTSSe absorbers annealed under different Ar pressure and added S-Se powders weight ratio (namely $S/(S+Se)_P$ ratio) (a detailed description of these samples with the corresponding composition and thermal treatment conditions are presented in Table S2 of SI Part 2). Samples present in Fig. 2(a) were annealed under 1 bar Ar pressure and with $S/(S+Se)_P$ ratios equal to 0.8, 0.4 and 0.04. The most intense peaks are attributed to CZTSSe, Mo and $Sn(S,Se)_2$ secondary phases. When the $S/(S+Se)_P$ ratio decreases from 0.8 to 0.04, the peaks related to CZTSSe phase shift towards lower diffraction angles, indicating that more selenium are incorporated in the kesterite lattice, which is also in agreement with a previous published work [27]. Peak labeled as 3 in the figure is assigned to $Sn(S,Se)_2$ phase, as the peak is located between the (001) diffraction peak of $SnSe_2$ (ICDD # 01-089-3197) and SnS_2 (ICDD # 00-023-0677). The peak corresponding to $Sn(S,Se)_2$ shifts in the same way as those observed for CZTSSe with respect to the $S/(S+Se)_P$. Samples present in Fig. 2(b) were annealed under 1 mbar Ar pressure, and $S/(S+Se)_P$ are equal to 0.8, 0.4, 0.2, and 0.04. From the diffractogram we can see that the main phases of these samples are CZTSSe, Mo and Sn(S,Se). The peak labeled as 3 is assigned to Sn(S,Se) phase and is located between the (111) diffraction peak of SnSe (ICDD # 00-048-1224) and SnS (ICDD # 00-039-0354). Also as it is expected, with the increase of $S/(S+Se)_P$ ratio the peaks of CZTSSe and Sn(S,Se) shift to higher diffraction angles. Those Sn-(S,Se) secondary phases can be originated from two sources and mainly located on the surface [28]. One is from the composition deviation during the reaction process, due to the very narrow single phase region existence of kesterite, non-ideal temperature for the formation of single phase kesterites and Zn-loss due to the volatility of Zn [39]. The other can be the condensation of Sn-(S,Se) from the atmosphere during cooling processes, due to the use of Sn or Sn-(S,Se) during the annealing to suppress the tin loss. The secondary phase formed at 1 bar is $Sn(S,Se)_2$ while for 1 mbar is Sn(S,Se), which can be linked with the fact that a lower pressure in the reaction chamber is helpful for the formation of phases with simple stoichiometry [40].

To investigate the influence of S/(S+Se) on the presence of secondary phases in CZTSSe absorbers, Raman measurements were done on a series of as-annealed absorbers on the surface as well as at the back region, covering a range of S/(S+Se) from 0 to 1. Fig. 3 shows the Raman spectra of these samples measured with 532, 325

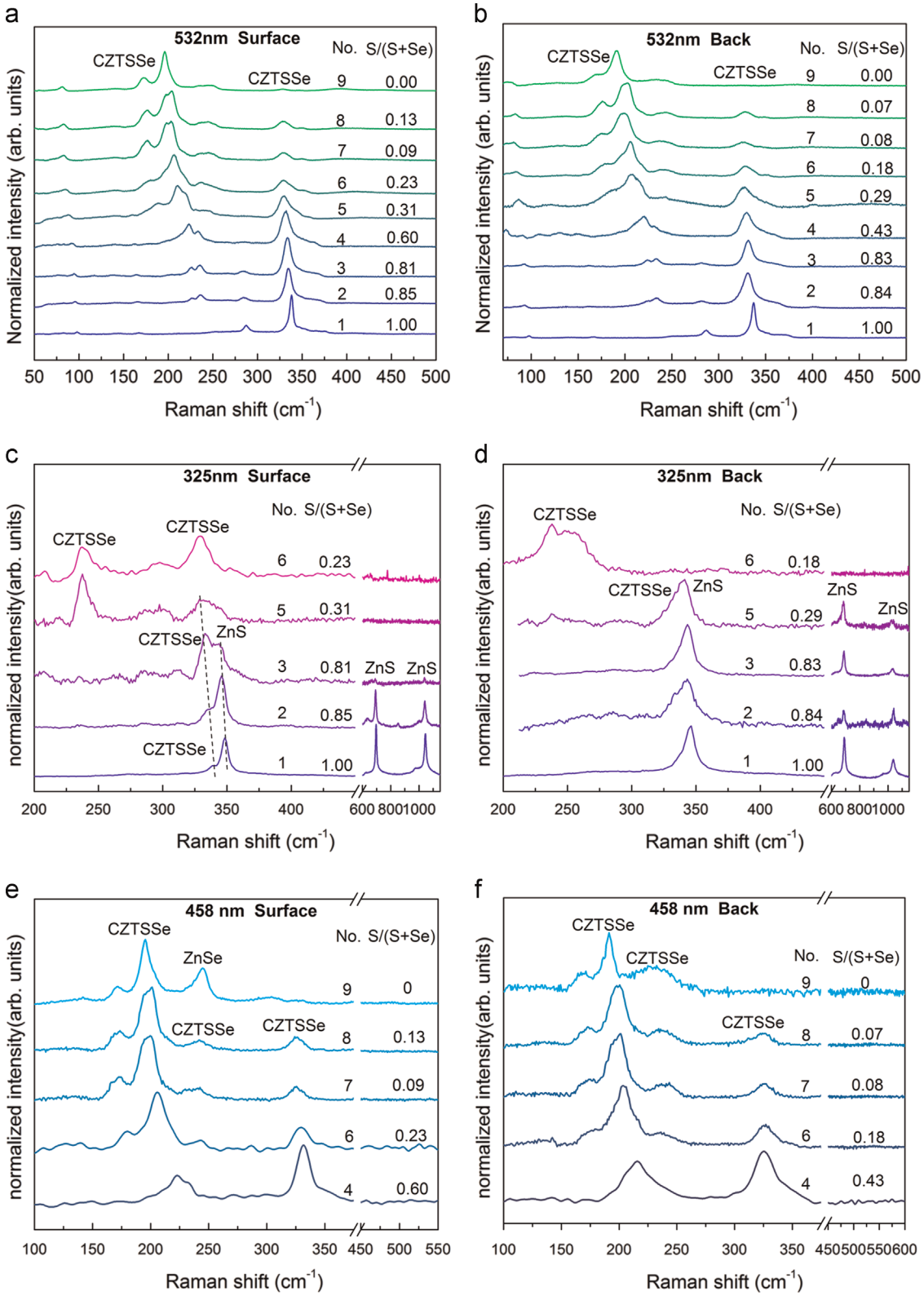

Fig. 3. Raman spectra measured with 532, 325 and 458 nm excitation wavelengths on the surface (a), (c), (e) respectively; and at the back region (b), (d), (f) of CZTSSe samples with S/(S+Se) ratio varying from 0 to 1. Surface and back region S/(S+Se) ratios shown in the spectra are estimated from the surface (a) and back (b) Raman spectra with excitation wavelength of 532 nm, respectively. The number and S/(S+Se) ratio in the figure correspond to the information shown in Table 2.

and 458 nm excitation wavelengths, and Table 2 summarizes the thermal treatments, composition and secondary phases of these samples. No evidences of the formation of Cu-(S,Se) or Sn-(S,Se) secondary phases was found either on the surface or back region of the films according to the Raman measurements performed with 532 nm excitation wavelength (see Fig. 3(a) and (b)). This is in contrast with the fact that the Sn-(S,Se) secondary phases are mainly located on the surface shown in our previous work [28] and also XRD results. The low sensitivity of the Raman scattering measurements performed with 532 nm excitation to the presence of Sn-(S,Se)

Table 2
Zn(S,Se) on the front and at the back region of CZTSe, solid solution CZTSSe and CZTS absorbers. Metallic ratios of the absorber were obtained using an XRF method.

no.	Added S/(S+Se) weight ratio	Annealing conditions	Absorber composition						Zn(S,Se)	
					S/(S+Se)				Surface	Back
			Cu/(Zn+Sn)	Zn/Sn	XRD	EQE	Raman surface	Raman back		
1	1	550 °C , 1bar	0.85	1.23	1	1	1	1	YES	YES
2	0.4	550 °C , 1 bar	0.87	1.11	0.85	0.82	0.85	0.84	YES	YES
3	0.4	550 °C , 1mbar	0.86	1.06	0.77	0.77	0.81	0.83	YES	YES
4	0.04	550 °C , 1mbar	0.84	1.03	0.58	0.55	0.60	0.43	NO	NO
5	0.02	550 °C , 1bar	0.85	1.08	0.39	0.35	0.31	0.29	NO	YES
6	0.04	200 °C , 1mbar	0.84	1.03	0.27	0.24	0.23	0.18	NO	NO
7	0.02	550 °C , 1bar	0.83	1.21	0.15	0.13	0.09	0.08	NO	NO
8	0.02		0.84	1.31	0.15	0.13	0.13	0.07	NO	NO
9	0	550 °C , 1mbar	0.81	1.16	0	0	0	0	YES	NO

secondary phases is related to low optical absorption of green photons in this compound, in contrast with very high optical absorption of CZTSSe. This is also an indication of the low overall amount of Sn-(S,Se) formed on the surface of the samples investigated. Nevertheless, XRD is sensitive to the Sn-(S,Se) detection. All the Raman peaks observed in the spectra measured with 532 nm wavelength are attributed to the kesterite CZTSSe phase with peak positions in agreement with the work of Dimitrievska et al. [41]. To clarify the discussion later on, several typical Raman spectra of 325 and 458 nm are chosen as illustrative references. For further information see the SI Part 2. From Fig. 3(c) and (e), it can be easily observed the presence of Zn(S,Se) as a function of S/(S+Se) on the surface of the samples: Se-rich CZTSSe do not have Zn(S,Se) while S-rich CZTSSe, pure CZTS and CZTSe have it, which is independent of the thermal treatment conditions (see Table 2). At the back region or Mo/absorbers interface, the analysis is slightly complicated, due to the possible detrimental reactions between Mo and kesterites absorber [42], and the possible inhomogeneous distribution of in-depth S/(S+Se) caused by diffusion of chalcogen atoms (sulfur and selenium) through the absorbers from the surface to the back region. This diffusion process is controlled by thermal kinetics and mainly related to the thermal history. Nevertheless, the S/(S+Se) estimated from XRD and EQE for each single sample is very similar, indicating relatively homogeneous in-depth distribution of S/(S+Se), which is also supported by surface and back Raman measurements. The correlation is also evident at the back region, where Se-rich CZTSSe samples do not have Zn(S,Se) with the only exception of sample no. 5. Regarding S-rich CZTSSe and CZTS, these type of samples always present Zn(S,Se) at the back interface. It should be noted that sample no. 5 was annealed under 1 bar Ar atmosphere but with very low $S/(S+Se)_P$ ratio (see Table 2), and higher Ar pressure can suppress the evaporation and loss of sulfur and selenium. Since sulfur is less affected compared with selenium due to its higher saturation vapor pressure, then it is likely that at the very beginning the metallic precursors were first mainly sulfurized. ZnS is the most stable secondary phase during low sulfur pressure and often lies at the back of the absorbers at high temperature [36,43]. Once ZnS is formed at the back, it is hardly converted into kesterite, which means that to prevent the presence of ZnS at the back of the CZTSSe samples, it is important to avoid the sulfurization at the very beginning of the thermal treatment. In other words, mixture of sulfur and selenium vapor and low Ar pressure are beneficial for the prevention of the presence of Zn(S,Se) at the back region of the absorbers.

In addition, even when the Zn/Sn ratio increases from 1.21 (sample no. 7) to 1.31 (sample no. 8), no Zn(S,Se) on the surface and at the back region for these Se-rich absorbers was detected (see SI Part 2). In order to understand this behavior, one possible explanation is that Zn(S,Se) is more prone to be present in the grain boundaries or in the bulk of Se-rich CZTSSe absorbers, as was previously reported [44,45]. Another reasonable explanation can be that Se-rich CZTSSe is more tolerant to compositional deviations, i.e., Zn/Sn ratio deviation. In this way, Se-rich CZTSSe may have broader single phase existence region than pure CZTS and CZTSe. Pseudoternary phase diagrams of CZTS and CZTSe have been already reported, while the phase diagram for the solid solution CZTSSe is still pending. Studies on monograins to determine the exact composition limits of single phase zone of CZTS, CZTSe and $Cu_2ZnSn(S_{0.7}\ Se_{0.3})_4$ were carried out by Muska et al., which confirm the rather narrow single phase region for these three types of kesterites [37,38,46], but no reports about Se-rich solid solutions are available yet.

In summary, Se-rich CZTSSe absorbers are almost Zn(S,Se) and Cu_x(S,Se) free on the surface and at the back region. The presence of ternary Cu–Sn–(S,Se) phases cannot be discarded, but taking into account the imposed Zn-rich and Cu-poor compositional conditions, their formation is not expected. Thus, in this type of absorbers, Sn-(S,Se) seems to be the only secondary phase on the surface, which can be selectively removed by $(NH_4)_2S$ etching [28]. Therefore, some requirements can be drawn to obtain CZTSSe absorbers without Zn (S,Se) on the surface and at the back region prepared from Cu-poor and Zn-rich metallic precursors: (i)- simultaneous sulfo-selenization of the metallic precursors, i.e., avoiding sequential sulfurization and selenization; (ii)-comparable partial pressure of selenium and sulfur vapor in the atmosphere, i.e., using low Ar pressure (especially in the first stage of the two step profile thermal treatment) and low added S/(S+Se) ratio to get Se-rich CZTSSe.

3.3. *Influence of the S/(S+Se) ratios on the optoelectronic properties of CZTSSe thin film solar cells and their efficiency limitation problems*

Fig. 4 shows the optoelectronic properties of CZTSSe solar cells as a function of S/(S+Se) ratio estimated from XRD. The dashed lines in these pictures can be used as eye guides, indicating some correlations. Fig. 4(a) shows the S/(S+Se) ratio estimated from EQE as a function of those estimated from XRD. It can be easily noticed that most of the samples have homogeneous in-depth S/(S+Se) distribution, having very similar S/(S+Se) ratios obtained from EQE and XRD. From Fig. 4(b) to (d), apart from individual samples, it is clear that as the S/(S+Se) ratio increase, J_{sc} and efficiency decrease while the band gap, V_{oc} and V_{oc} deficit increase accordingly. J_{sc} decreases quickly while V_{oc} increases slowly when the S/(S+Se) ratio rises, which leads to larger V_{oc} deficit and smaller $J_{sc} \times V_{oc}$ values in higher band gap CZTSSe devices, deteriorating the efficiency as a consequence. The increase of V_{oc} deficit with S/(S+Se) ratio or band gap is possibly dominated by Fermi level pinning associated with interface states, as well as band tails and bulk defects [5,47]. In addition, the non-ideal band alignment for devices with increasing S/(S+Se) should also be

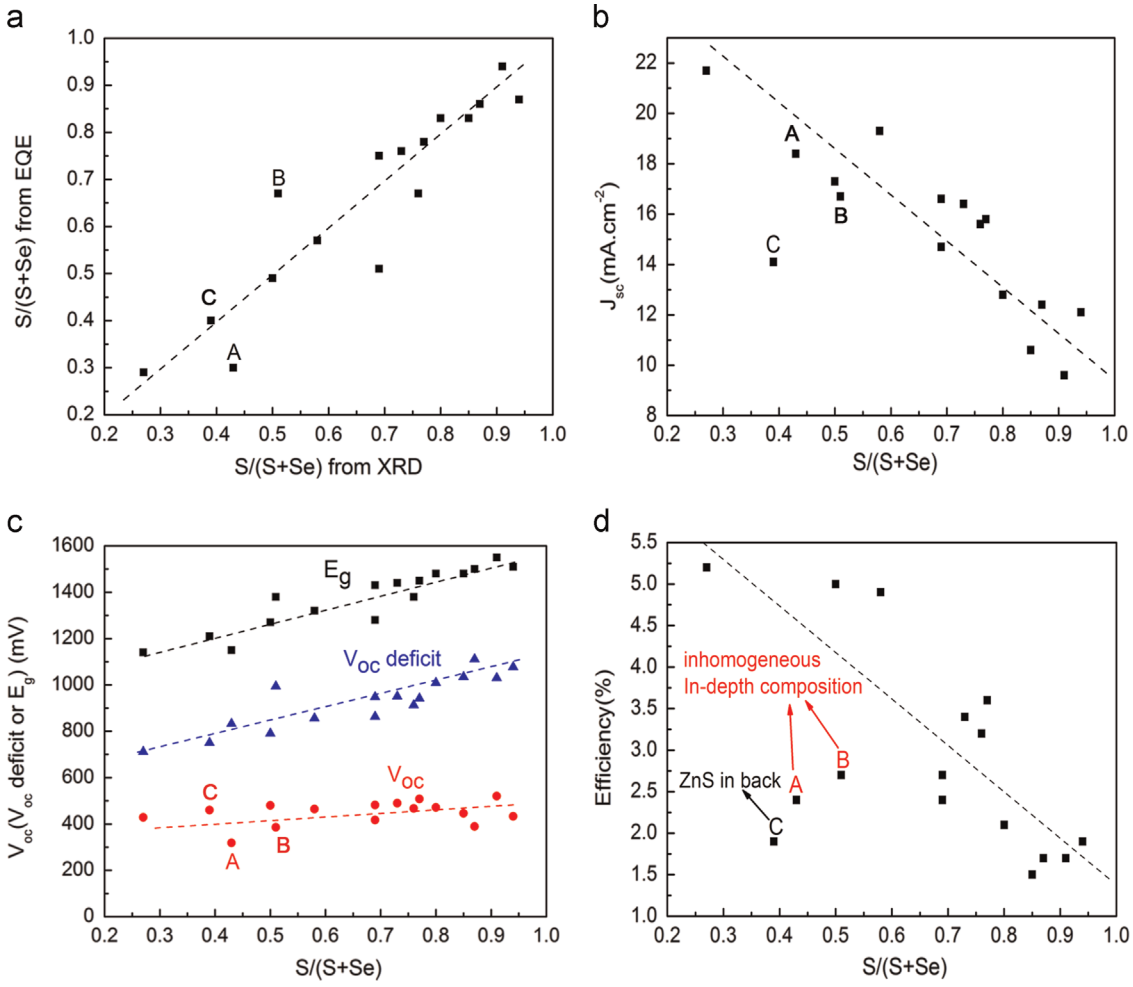

Fig. 4. S/(S+Se) ratio estimated from EQE (a) and optoelectronic properties of CZTSSe solar cells as a function of S/(S+Se) ratio estimated from XRD in the absorbers: (b) J_{sc}; (c) V_{oc}, V_{oc} deficit and band gap (E_g); (d) conversion efficiency.

considered [48]. The fact that the efficiency decreases when S/(S+Se) increases seems to be inconsistent with those reported by Chawla et al. In their work, S/(S+Se) ratio does not have a significant impact on the efficiency of CZTSSe devices in the range of 0.43–0.79 [49]. However, when taking a careful examination of Fig. 4(d), it can be observed that devices with similar efficiency of about 5% are obtained as well in a fairly similar S/(S+Se) ratio range (from 0.27 to 0.6). In addition, there is no obvious correlation between grain size and efficiency in these CZTSSe solar cells. According to SEM pictures (not shown here), the grain size of CZTSSe decreases in the range of $0 \leq S/(S+Se) < 0.5$ approximately (Se-rich layers), while starts to increase again in the range of $0.5 \leq S/(S+Se) < 1$ (S-rich layers) with the increase of S/(S+Se) ratio. The best efficiency in this series of devices is 5.2% with S/(S+Se)=0.27 and E_g=1.14 eV, which is consistent with the results of the record CZTSSe solar cells (S/(S+Se) ≈ 0.3, and E_g=1.13 eV) [3]. The ideality factor A and diode saturation current density J_0 are also plotted as a function of S/(S+Se) ratio (see SI Part 3, Fig. S3) according to the methods suggested by Hegedus and Shafarman [50], which shows that both A and J_0 increase when S/(S+Se) rises. All the values of A are above 2, indicating space charge region (SCR) and additional tunneling recombination in the devices, being more severe in higher sulfur content samples [51]. Nevertheless, we have to take into account that for devices that exhibit A values larger than 2, the one diode equation applied here could not be realistic because the electron transport is limited by other mechanisms.

Table 3
Compositions of samples A–C.

Sample	Cu/(Zn+Sn)	Zn/Sn	S/(S+Se)	
			XRD	EQE
A	0.86	1.20	0.43	0.26
B	0.74	1.20	0.51	0.65
C	0.85	1.08	0.39	0.35

The samples not following a correlation are marked with A, B and C, which may evidence additional efficiency limitation problems. From Table 3 we can see that for sample A, the surface S/(S+Se) ratio is lower than the bulk one (Se-rich surface), indicating a lower band gap at the surface, which leads to the reduction of the V_{oc} as shown in Fig. 4(c). For sample B, the surface S/(S+Se) ratio is higher than the bulk one (S-rich surface). In this case, the J_{sc} is little affected and V_{oc} seems not be affected at all (see Figs. 4(b) and (c)). Nevertheless, the R_{sh} is deteriorated (not shown in the manuscript), which also leads to the decrease of the efficiency (see Fig. 4(d)). Although appropriate graded band gap can be beneficial for the performance of solar cells [52,53], in this work it is observed that inhomogeneous in-depth distribution of S/(S+Se) might deteriorate the efficiency. This observation can be connected to possible compositional/band-gap fluctuations that are accepted to be detrimental for the devices performance [47]. Finally, sample C has relatively homogeneous in-depth S/(S+Se)

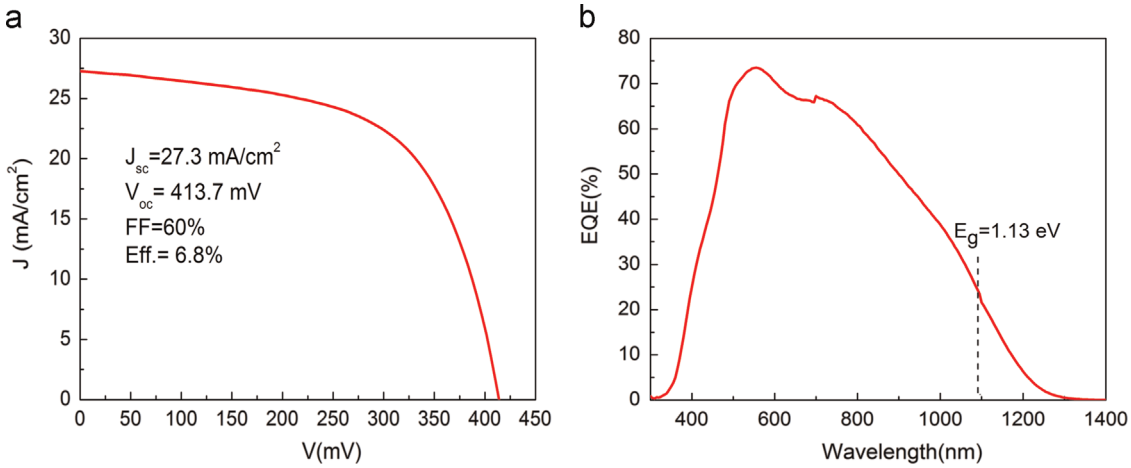

Fig. 5. *J–V* (a) and EQE (b) curves of the best efficiency (6.8%) Se-rich CZTSSe device.

ratio (see Table 3) but suffering considerable J_{sc} and efficiency deterioration (see Figs. 4(b) and (d)). To determine the reason, this sample was analyzed with Raman spectroscopy and ZnS was detected at the back region (see sample no. 5 in Table 2). It is important to note that sample C is Se-rich, thus ZnS will have much more influence than in the S-rich case. Therefore, compared with other Se-rich samples without ZnS, sample C has lower J_{sc} and efficiency. In summary, many factors can influence the efficiency of solar cells, among them secondary phases and compositional/band-gap fluctuation by inhomogeneous chalcogen distribution have been revealed as paramount factors in this work.

After optimization of the thermal treatment process and the CdS buffer layer [54], and including an etching step with $(NH_4)_2S$ solution, best efficiency of 6.8% for a Se-rich CZTSSe solar cell was achieved (S/(S+Se)=0.25 estimated from XRD). *J–V* and EQE curves of this device are shown in Fig. 5(a) and (b), respectively. The parameters of this device are also presented in Fig. 5(a), with J_{sc}=27.3 mA/cm^2, V_{oc}=413.7 mV and FF=60%. A band gap of 1.13 eV is extracted from EQE curve through the derivative way (see SI Part 1) and the integrated current from EQE is 24.5 mA/cm^2, slightly lower than the J_{sc} from *J–V* curve. The reason may be related to the presence of a barrier for the photocurrent that is large under low light intensity or monochromatic illumination, but becomes lowered by photo doping of the buffer at AM1.5 G illumination, namely light soaking effect [54,55]. Although the efficiency is still limited by several factors, the results are encouraging, indicating that a single-step sulfo-selenization of metallic precursor technology is a promising method for the production of high efficiency CZTSSe devices.

4. Conclusion

In this work we have investigated the secondary phases of Cu-poor and Zn-rich CZTSSe absorbers with S/(S+Se) ratios varying from 0 to 1 on the surface and at the back region, using Raman measurements with 325, 458 and 532 nm excitation lights as well as XRD. The impact of the S/(S+Se) ratios on the optoelectronic properties and efficiency limitation issues of the devices were also discussed. The following conclusions were drawn:

1. XRD, EQE and Raman are simple and effective ways for estimating S/(S+Se) ratio in CZTSSe thin films. The comparison of S/(S+Se) ratio from XRD and EQE, or from the Raman spectra performed on the surface and at the back region of the films, can be two quick ways for a rough evaluation of the uniformity of in-depth distribution of S/(S+Se).
2. Much less secondary phases, especially Zn(S,Se), are prone to be present on the surface and at the back region of Se-rich CZTSSe absorbers when compared with CZTSe, CZTS and S-rich CZTSSe, suggesting that Se-rich CZTSSe seems to be more tolerant to composition deviations and possibly has broader single phase existence region, which may contribute to the higher efficiency for this type of CZTSSe solar cells nowadays.
3. $Sn(S,Se)_2$ appears on the surface of CZTSSe thin films when using high inert gas pressure while Sn(S,Se) is prone to be present under low inert gas pressure. Solid solution kesterites almost free of secondary phases on the surface and at the back region can be obtained by the appropriate control of different process parameters: thermal treatment (low Ar pressure, simultaneous sulfo-selenization) and surface etching (using $(NH_4)_2S$ solutions). Based on this absorber with very low secondary phases content, best efficiency of 6.8% for a Se-rich CZTSSe solar cell was achieved.
4. ZnS at the back of Se-rich solar cells can deteriorate J_{sc} and efficiency. Inhomogeneous in-depth distribution of S/(S+Se) ratio influences the band gap and V_{oc}, which in some cases will decrease the efficiency and is probably connected to detrimental compositional/band-gap fluctuations effects.

Acknowledgments

The research leading to these results has received funding from the People Program (Marie Curie Actions) of the European Union's Seventh Framework Program FP7/2007-2013/ under REA grant agreement no. 316488 (KESTCELLS) and by European Regional Development Founds (ERDF, FEDER Programa Competitivitat de Catalunya 2007–2013). Authors from IREC and IN2UB belong to the M-2E (Electronic Materials for Energy) Consolidated Research Group and the XaRMAE Network of Excellence on Materials for Energy of the "Generalitat Generalitat de Catalunya". H. Xie thanks the "China Scholarship Council" fellowship (CSC no. 201206340113), Y. S. for the PTA fellowship (PTA2012-7852-A), V.I. for the "Juan de la Cierva" Fellowship (JCI-2011-10782), and E.S. the "Ramon y Cajal" fellowship (RYC-2011-09212). Finally, many thanks to Ophélie Rogée (NEXCIS) for the assistance with the GD-OES measurement.

Appendix A. Supplementary material

Supplementary material associated with this article can be found in the online version at http://dx.doi.org/%2010.1016/j.solmat.2015.04.023

References

[1] T. Kato, H. Hiroi, N. Sakai, S. Muraoka, H. Sugimoto, Characterization of front and back interfaces on Cu_2ZnSnS_4 thin-film solar cells, in: Proceedings of the 27th European Photovoltaic Solar Energy Conference and Exhibition, 2012, pp. 2236–2239.

[2] Y.S. Lee, T. Gershon, O. Gunawan, T.K. Todorov, T. Gokmen, Y. Virgus, S. Guha, $Cu_2ZnSnSe_4$ thin-film solar cells by thermal co-evaporation with 11.6% efficiency and improved minority carrier diffusion length,, Adv. Energy Mater. 5 (7) (2014), http://dx.doi.org/10.1002/aenm.201401372 1401372.

[3] W. Wang, M.T. Winkler, O. Gunawan, T. Gokmen, T.K. Todorov, Y. Zhu, D. B. Mitzi, Device characteristics of CZTSSe thin-film solar cells with 12.6% efficiency,, Adv. Energy Mater. 4 (2014) 1301465.

[4] Solar Energy and Hydrogen Research Baden-Württemberg (ZSW), "ZSW brings world record back to Stuttgart," press release, 09/19/2014. ⟨http://www.zsw-bw.de/en/support/news/news-detail/zsw-brings-world-record-back-to-stuttgart.html⟩.

[5] H. Duan, W. Yang, B. Bob, C. Hsu, B. Lei, Y. Yang, The role of sulfur in solution-processed $Cu_2ZnSn(S,Se)_4$ and its effect on defect properties, Adv. Funct. Mater. 23 (2013) 1466–1471.

[6] X.Z. Lin, Th. Dittrich, S. Fengler, M.Ch. Lux-Steiner, A. Ennaoui, Correlation between processing conditions of $Cu_2ZnSn(S_xSe_{1-x})_4$ and modulated surface photovoltage, Appl. Phys. Lett. 102 (2013) 143903.

[7] D.W. Miller, C.W. Warren, O. Gunawan, T. Gokmen, D.B. Mitzi, J.D. Cohen, Electronically active defects in the $Cu_2ZnSn(Se,S)_4$ alloys as revealed by transient photocapacitance spectroscopy, Appl. Phys. Lett. 101 (2012) 142106.

[8] I.V. Dudchak, L.V. Piskach, Phase equilibria in the Cu SnSe–SnSe–ZnSe system, J. Alloy. Compd. 351 (2003) 145–150.

[9] I.D. Olekseyuk, I.V. Dudchak, L.V. Piskach, Phase equilibria in the Cu_2S–ZnS–SnS_2 system, J. Alloy. Compd. 368 (2004) 135–143.

[10] S. Niki, P.J. Fons, A. Yamada, Y. Lacroix, H. Shibata, H. Oyanagi, M. Nishitani, T. Negami, T. Wada, Effects of the surface $Cu_{2-x}Se$ phase on the growth and properties of $CuInSe_2$ films, Appl. Phys. Lett. 74 (1999) 1630.

[11] B. Schubert, B. Marsen, S. Cinque, T. Unold, R. Klenk, S. Schorr, H.W. Schock, Cu_2ZnSnS_4 thin film solar cells by fast coevaporation, Prog. Photovolt.: Res. Appl. 19 (2011) 93–96.

[12] T. Tanaka, T. Sueishi, K. Saito, Q. Guo, M. Nishio, K.M. Yu, W. Walukiewicz, Existence and removal of Cu_2Se second phase in coevaporated $Cu_2ZnSnSe_4$ thin films, J. Appl. Phys. 111 (2012) 053522.

[13] S. Siebentritt, Why are kesterite solar cells not 20% efficient? Thin Solid Films 535 (2013) 1–4.

[14] B. Shin, O. Gunawan, Y. Zhu, N.A. Bojarczuk, S.J. Chey, S. Guha, Thin film solar cell with 8.4% power conversion efficiency using an earth-abundant Cu_2ZnSnS_4 absorber, Photovolt.: Res. Appl. 21 (2013) 72–76.

[15] A. Fairbrother, E. García-Hemme, V. Izquierdo-Roca, X. Fontané, F.A. Pulgarín-Agudelo, O. Vigil-Galán, A. Peérez-Rodríguez, E. Saucedo, Development of a selective chemical etch to improve the conversion efficiency of Zn-rich Cu_2ZnSnS_4 solar cells, J. Am. Chem. Soc. 134 (2012) 8018–8021.

[16] S. Lopez-Marino, M. Placidi, A. Perez-Tomas, J. Llobet, V. Izquierdo-Roca, X. Fontane, A. Fairbrother, M. Espindola-Rodriguez, D. Sylla, A. Perez-Rodriguez, E. Saucedo, Inhibiting the absorber/Mo-back contact decomposition reaction in $Cu_2ZnSnSe_4$ solar cells: the role of a ZnO intermediate nanolayer, J. Mater. Chem. A 1 (2013) 8338–8343.

[17] J. Wätjen, J.J. Scragg, T. Ericson, M. Edoff, C. Platzer-Björkman, Secondary compound formation revealed by transmission electron microscopy at the Cu_2ZnSnS_4/Mo interface, Thin Solid Films 535 (2013) 31–34.

[18] R.A. Wibowo, H. Yoo, A. Hölzing, R. Lechner, S. Jost, J. Palm, M. Gowtham, B. Louis, R. Hock, A study of kesterite $Cu_2ZnSn(Se,S)_4$ formation from sputtered Cu–Zn–Sn metal precursors by rapid thermal processing sulfo-selenization of the metal thin films, Thin Solid Films 535 (2013) 57–61.

[19] L. Grenet, S. Bernardi, D. Kohen, C. Lepoittevin, S. Noël, N. Karst, A. Brioude, S. Perraud, H. Mariette, $Cu_2ZnSn(S_{1-x}Se_x)_4$ based solar cell produced by selenization of vacuum deposited precursors, Sol. Energy Mater. Sol. Cells 101 (2012) 11–14.

[20] P.A. Fernandes, P.M.P. Salomé, A.F. da Cunha, Growth and Raman scattering characterization of Cu_2ZnSnS_4 thin films, Thin Solid Films 517 (2009) 2519–2523.

[21] A.J. Cheng, M. Manno, A. Khare, C. Leighton, S.A. Campbell, E.S. Aydil, Imaging and phase identification of Cu_2ZnSnS_4 thin films using confocal Raman spectroscopy, J. Vac. Sci. Technol. A 29 (2011) 051203.

[22] X. Fontané, L. Calvo-Barrio, V. Izquierdo-Roca, E. Saucedo, A. Pérez-Rodriguez, J.R. Morante, D.M. Berg, P.J. Dale, S. Siebentritt, In-depth resolved Raman scattering analysis for the identification of secondary phases: characterization of Cu_2ZnSnS_4 layers for solar cell applications, Appl. Phys. Lett. 98 (2011) 181905.

[23] A. Fairbrother, V. Izquierdo, X. Fontané, M. Ibáñez, A. Cabot, E. Saucedo, A. Pérez-Rodríguez, ZnS grain size effects on near-resonant Raman scattering: optical non-destructive grain size estimation, CrystEngComm 16 (2014) 4120–4125.

[24] X. Fontané, V. Izquierdo-Roca, A. Fairbrother, M. Espíndola-Rodríguez, S. López-Marino, M. Placidi, T. Jawhari, E. Saucedo, A. Pérez-Rodríguez, Selective detection of secondary phases in $Cu_2ZnSn(S,Se)_4$ based absorbers by pre-resonant Raman spectroscopy, in: Proceedings of the 39th IEEE Photovoltaic Specialists Conference (PVSC), 2013, pp. 2581–2584.

[25] A. Fairbrother, X. Fontané, V. Izquierdo-Roca, M. Placidi, D. Sylla, M. Espindola-Rodriguez, S. López-Mariño, F.A. Pulgarín, O. Vigil-Galán, A. Pérez-Rodríguez, E. Saucedo, Secondary phase formation in Zn-rich $Cu_2ZnSnSe_4$ based solar cells annealed in low pressure and temperature conditions, Prog. Photovolt.: Res. Appl. 22 (2014) 479–487.

[26] A. Fairbrother, L. Fourdrinier, X. Fontané, V. Izquierdo-Roca, M. Dimitrievska, A. Pérez-Rodrígue, E. Saucedo, Precursor stack ordering effects in $Cu_2ZnSnSe_4$ thin films prepared by rapid thermal processing, J. Phys. Chem. C 118 (2014) 17291–17298.

[27] A. Fairbrother, X. Fontané, V. Izquierdo-Roca, M. Espindola-Rodriguez, S. López-Mariño, M. Placidi, J. López-García, A. Pérez-Rodríguez, E. Saucedo, Single-step sulfo-selenization method to synthesize $Cu_2ZnSn(S_ySe_{1-y})_4$ absorbers from metallic stack precursors, ChemPhysChem 14 (2013) 1836–1843.

[28] H. Xie, Y. Sánchez, S. López-Marino, M. Espíndola-Rodríguez, J. López-García, M. Neuschitzer, D. Sylla, A. Fairbrother, A. Pérez-Rodríguez, E. Saucedo, Impact of Sn(S,Se) secondary phases in $Cu_2ZnSn(S,Se)_4$ solar cells: a chemical route for their selective removal and absorber surface passivation, ACS Appl. Mater. Interfaces 6 (2014) 12744–12751.

[29] G. Altamura, L. Grenet, C. Bougerol, E. Robin, D. Kohen, Hln Fournier, A. Brioude, S. Perraud, H. Mariette, $Cu_2ZnSn(S_{1-x}Se_x)_4$ thin films for photovoltaic applications: influence of the precursor stacking order on the selenization process, J. Alloy. Compd. 588 (2013) 310–315.

[30] M. Dimitrievska, A. Fairbrother, X. Fontané, T. Jawhari, V. Izquierdo-Roca, E. Saucedo, A. Pérez-Rodríguez, Multiwavelength excitation Raman scattering study of polycrystalline kesterite Cu_2ZnSnS_4 thin films, Appl. Phys. Lett. 104 (2014) 021901.

[31] M. Dimitrievska, G. Gurieva, H. Xie, A. Carrete, A. Cabot, E. Saucedo, A. Pérez-Rodríguez, S. Schorr, V. Izquierdo-Roca, Raman scattering quantitative analysis of the anion chemical composition in kesterite $Cu_2ZnSn(S_xSe_{1-x})_4$ solid solutions, J. Alloy. Compd. 628 (2015) 464–470.

[32] J. He, L. Sun, S.Y. Chen, Y. Chen, P.X. Yang, J.H. Chu, Composition dependence of structure and optical properties of $Cu_2ZnSn(S,Se)_4$ solid solutions: an experimental study, J. Alloy. Compd. 511 (2012) 129–132.

[33] S. Chen, A. Walsh, J. Yang, X.G. Gong, L. Sun, P. Yang, J. Chu, S. Wei, Compositional dependence of structural and electronic properties of $Cu_2ZnSn(S,Se)_4$ alloys for thin film solar cells, Phys. Rev. B 83 (2011) 125201.

[34] Y.K. Rao, Composition of liquid-saturated selenium vapor, Metall. Trans. B 14 (1983) 308–311.

[35] H. Rau, T.R.N. Kutty, J.R.F. Guedes de Carvalho, High temperature saturated vapour pressure of sulphur and the estimation of its critical quantities, J. Chem. Thermodyn. 5 (1973) 291–302.

[36] A. Fairbrother, X. Fontané, V. Izquierdo-Roca, M. Espíndola-Rodríguez, S. López, M. Placidi, L. Calvo-Barrio, A. Pérez-Rodríguez, E. Saucedo, On the formation mechanisms of Zn-rich Cu_2ZnSnS_4 films prepared by sulfurization of metallic stacks, Sol. Energy Mater. Sol. Cells 112 (2013) 97–105.

[37] K. Muska, M. Kauk, M. Altosaar, M. Pilvet, M. Grossberg, O. Volobujeva, Synthesis of Cu_2ZnSnS_4 monograin powders with different compositions, Energy Procedia 10 (2011) 203–207.

[38] K. Muska, M. Kauk, M. Grossberg, M. Altosaar, J. Raudoja, O. Volobujeva, Influence of compositional deviations on the properties of $Cu_2ZnSnSe_4$ monograin powders, Energy Procedia 10 (2011) 323–327.

[39] A. Redinger, S. Siebentritt, Coevaporation of $Cu_2ZnSnSe_4$ thin films, Appl. Phys. Lett. 97 (2010) 092111.

[40] W. Albers, C. Haas, H.J. Vink, J.D. Wasscher, Investigations on SnS, J. Appl. Phys. 32 (1961) 2220.

[41] M. Dimitrievska, H. Xie, A. Fairbrother, X. Fontané, G. Gurieva, E. Saucedo, A. Pérez-Rodríguez, S. Schorr, V. Izquierdo-Roca, Vibrational and structural properties of $Cu_2ZnSn(S_xSe_{1-x})_4$ $(0 \le x \le 1)$ solid solutions, Appl. Phys. Lett. 105 (2014) 031913.

[42] J.J. Scragg, J.T. Wätjen, M. Edoff, T. Ericson, T. Kubart, C. Platzer-Björkman, A detrimental reaction at the molybdenum back contact in $Cu_2ZnSn(S,Se)_4$ thin film solar cells, J. Am. Chem. Soc. 134 (2012) 19330–19333.

[43] X. Yin, C. Tang, L. Sun, Z. Shen, H. Gong, Study on phase formation mechanism of non- and near-stoichiometric $Cu_2ZnSn(S,Se)_4$ film prepared by selenization of $Cu-Sn-Zn-S$ precursors, Chem. Mater. 26 (2014) 2005–2014.

[44] K. Wang, B. Shin, K.B. Reuter, T. Todorov, D.B. Mitzi, S. Guha, Structural and elemental characterization of high efficiency Cu_2ZnSnS_4 solar cells, Appl. Phys. Lett. 98 (2011) 051912.

[45] T. Schwarz, O. Cojocaru-Mirédin, P. Choi, M. Mousel, A. Redinger, S. Siebentritt, D. Raabe, Atom probe study of $Cu_2ZnSnSe_4$ thin-films prepared by co-evaporation and post-deposition annealing, Appl. Phys. Lett. 102 (2013) 042101.

[46] K. Muska, M. Kauk-Kuusik, M. Grossberg, M. Altosaar, M. Pilvet, T. Varema, K. Timmo, O. Volobujeva, A. Mere, Impact of $Cu_2ZnSn(Se_xS_{1-x})_4$ $(x=0.3)$ compositional ratios on the monograin powder properties and solar cells, Thin Solid Films 535 (2013) 35–38.

[47] T. Gokmen, O. Gunawan, T.K. Todorov, D.B. Mitzi, Band tailing and efficiency limitation in kesterite solar cells, Appl. Phys. Lett. 103 (2013) 103506.

[48] A. Redinger, M. Mousel, M.H. Wolter, N. Valle, S. Siebentritt, Influence of S/Se ratio on series resistance and on dominant recombination pathway in $Cu_2ZnSn(SSe)_4$ thin film solar cells, Thin Solid Films 535 (2013) 291–295.

[49] V. Chawla, B. Clemens, Effect of composition on high efficiency CZTSSe devices fabricated using co-sputtering of compound targets, in: Proceedings of the 38th IEEE Photovoltaic Specialists Conference (PVSC), 2012, pp. 002990–002992.

[50] S.S. Hegedus, W.N. Shafarman, Thin-film solar cells: device measurements and analysis, Prog. Photovolt.: Res. Appl. 12 (2004) 155–176.
[51] M.A. Contreras, K. Ramanathan, J. AbuShama, F. Hasoon, D.L. Young, B. Egaas, R. Noufi, Diode characteristics in state-of-the-art ZnO/CdS/Cu($In_{1-x}Ga_x$)Se_2 solar cells, Prog. Photovolt.: Res. Appl. 13 (2005) 209–216.
[52] T. Kato, N. Sakai, H. Sugimoto, Efficiency improvement of $Cu_2ZnSn(S,Se)_4$ submodule with graded bandgap and reduced backside ZnS segregation, in: Proceedings of the 40th IEEE Photovoltaic Specialists Conference (PVSC), 2014, pp. 0844–0846.
[53] A. Chirilă, S. Buecheler, F. Pianezzi, P. Bloesch, C. Gretener, A.R. Uhl, C. Fella, L. Kranz, J. Perrenoud, S. Seyrling, R. Verma, S. Nishiwaki, Y.E. Romanyuk, G. Bilger, A.N. Tiwari, Highly efficient Cu(In,Ga)Se_2 solar cells grown on flexible polymer films, Nat. Mater. 10 (2011) 857–861.
[54] M. Neuschitzer, Y. Sanchez, S. López-Marino, H. Xie, A. Fairbrother, M. Placidi, S. Haass, V. Izquierdo-Roca, A. Perez-Rodriguez, E. Saucedo, Optimization of CdS buffer layer for high performance $Cu_2ZnSnSe_4$ solar cells and the effects of light soaking: elimination of crossover and red kink, Photovolt.: Res. Appl. (2015), http://dx.doi.org/10.1002/pip.2589.
[55] R. S., H. Schock, Chalcogenide Photovoltaics: Physics, Technologies, and Thin Film Devices, first ed., Wiley-VCH Verlag & Co. KGaA, Weinheim, 2011.

Supporting Information

Formation and impact of secondary phases in Cu-poor Zn-rich $Cu_2ZnSn(S_{1-y}Se_y)_4$ ($0 \leq y \leq 1$) based solar cells

Haibing Xie[a*], Mirjana Dimitrievska[a], Xavier Fontané[a], Yudania Sánchez[a], Simon López-Marino[a], Victor Izquierdo-Roca[a], Verónica Bermúdez[b], Alejandro Pérez-Rodríguez[a,c], Edgardo Saucedo[a]

[a]Catalonia Institute for Energy Research, IREC. Jardins de les Dones de Negre 1, 08930 Sant Adrià de Besòs, (Barcelona), Spain
[b]EDF R&D, 6, Quai Watier, 78401 Chatou, France
[c]IN^{2}UB, Departament d'Electrònica, Universitat de Barcelona, C. Martí i Franquès 1, 08028 Barcelona, Spain
[*]E-mail: xhaibing@irec.cat

Part 1: Determination of the S/(S+Se) ratios and evaluation of the in-depth S/(S+Se) ratios uniformity in CZTSSe thin films

1.1 Summary of different methods for obtaining the S/(S+Se) ratio in kesterite thin films

Methods for obtaining S/(S+Se) of kesterite thin films (<3μm)		Detection depth	Total composition (kesterite and secondary phases)	Kesterite composition	Accuracy	Corresponding theory
Direct methods	ICP	The whole bulk	YES	-	High accuracy	Calculation of each element´s concentration
	XRF	>>2μm, The whole bulk	YES	-	Higher than the real value (Mo Lα (5.41 KeV) and S Kα (5.37 KeV) lines overlap)	
	EDS	1-2μm (5-20 kV applied voltage)	YES	-		
Indirect methods	XRD	>>2μm, The whole bulk	-	YES	Rough estimation	Vegard´s law of lattice constants
	EQE	Normally <500nm (depending on the minority carrier diffusion length)	-	YES		Vegard´s law of band gap (E_g)
	Raman	<100nm (325nm-532nm)	-	YES		Quasi-linear correlation between S/(S+Se) and $A_{270\text{-}380cm^{-1}}/(A_{150\text{-}260cm^{-1}}+A_{270\text{-}380cm^{-1}})$

Table S1. Summary of different methods for obtaining the S/(S+Se) ratio in kesterite thin films.

1.2 Estimation of S/(S+Se) from XRD

According to the Vegard´s law and some experimental works [supp1], there is a quasi-linear relationship between S/(S+Se) and lattice constant, thus it is possible to use XRD patterns of CZTSSe thin films to estimate the S/(S+Se) ratio. The equation is as follows:

$S/(S+Se) = (d_{(112)CZTSe\ ref} - d_{(112)\ CZTSSe\ sample})/(d_{(112)CZTSe\ ref} - d_{(112)CZTS\ ref}) = (3.2804 - d_{(112)\ CZTSSe\ sample})/0.1442$

Reference XRD patterns for Cu_2ZnSnS_4 (CZTS) and $Cu_2ZnSnSe_4$ (CZTSe) samples are taken from ICDD # 01-075-4122 and ICDD # 01-070-8930, respectively. The lattice distance *d* has a linear relationship with the lattice constant *a*, thus using *d* to substitute the lattice constant is reasonable (see equation (1) and (2) below for explanation). Here the lattice distance *d* of the most intense peak (112) of kesterites is used for the calculation. Kesterites usually presents a tetragonal crystalline structure, with lattice constant $c \approx 2a$, then for the calculation of *d* the equation (1) can be used:

$$d = \frac{1}{\sqrt{\frac{h^2+k^2}{a^2} + \frac{l^2}{c^2}}} \qquad (1)$$

Where *h, k, l* are indices of crystal planes.
When c = 2a：

$$a = \frac{d\sqrt{4(k^2+h^2)+l^2}}{2} \qquad (2)$$

The equation (2) shows clearly the linear correlation between the lattice constant *a* and the lattice distance *d.*

1.3 Estimation of S/(S+Se) from EQE

When using EQE to estimate S/(S+Se), a quasi-linear relationship between band gap (E_g) and S/(S+Se) can be applied [supp 1,2]. The first step is to extract E_g from EQE curves. In general, there are three ways for obtaining E_g from EQE curves in the literature:

(1) **Linear way:** ideally the absorption edge of the spectral response should present a step decrease because of the band gap. By using the tangent line at the absorption edge, from the horizontal intercept it is possible to obtain E_g from the equation below:

$E_g = 1239.7/horizontal\ intercept.$

(2) **Equation way:** by plotting $(h\nu*\ln(1-EQE))^2$ vs $h\nu$, and using the tangent line at the absorption edge, E_g can be obtained directly from the horizontal intercept value.

(3) **Derivative way:** in theory there should be a deep change of the EQE at the position of the band gap. Most of the photons with energy higher than the band gap will be absorbed by the material, thereby at the band gap position the change rate of EQE should be the largest. Thus, by differentiating the EQE curve, and fitting the corresponding valley with a Gaussian plot it is possible to obtain the inflection point, X_c (see Fig. S1(c)). Finally the following equation to calculate E_g can be used:

$E_g = 1239.7/X_c$

Fig. S1 shows the E_g for one CZTS absorber extracted from the three different ways.

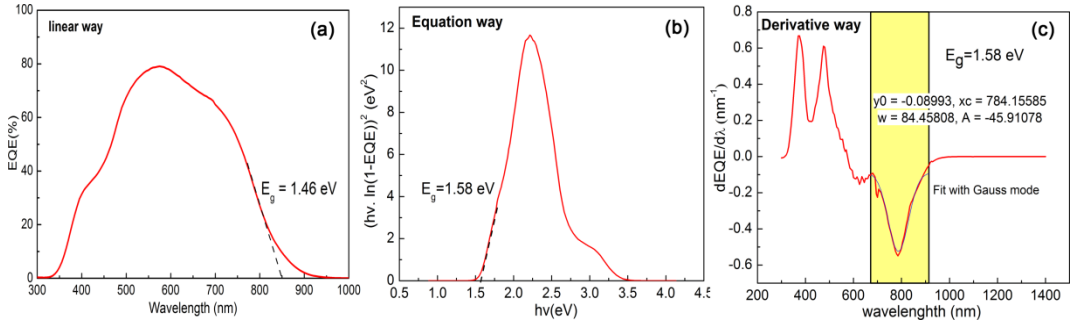

Fig. S1. E_g extracted from EQE data of one CZTS absorber using linear (a), equation (b) and derivative way (c).

From Fig. S1 it can be seen that E_g from the equation way and the derivative way are more reliable, having the same value of E_g. However, the value obtained from the linear way is significantly different. Furthermore, the linear and the equation way have a strong dependency on the way the tangent line is plotted, which will inherently cause considerable errors. In conclusion, the derivative way has less systematic errors than the other two ways, thus in this work the derivative way is employed to extract E_g from EQE data. It has to be noted that this method is also employed to obtain E_g for the world record CZTSSe and CZTSe samples by IBM [supp 3, 4].

Additionally, it is important to take into account that reference samples of pure CZTS and CZTSe with a similar thermal history of the CZTSSe sample were prepared, in order to determine the band gap of these solid solution CZTSSe samples using the derivative way. The reason is that the thermal history has a strong impact on the band gap of the materials, i.e. the cooling rate can induce an ordered/disordered transition on the kesterite phase and thus vary the band gap [supp 5, 6]. Finally, the S/(S+Se) ratios of the CZTSSe sample can be calculated via the following equation:

$$S/(S+Se) = (E_{g(CZTSSe)} - E_{g(CZTSe\ ref)})/(E_{g(CZTS\ ref)} - E_{g(CZTSe\ ref)})$$

Part 2: Influence of the Ar pressure and S/(S+Se) ratios on the presence of secondary phases in CZTSSe thin films

Table S2. Summary of the thermal treatment conditions, composition, and secondary phases of CZTSSe absorbers annealed under 1bar and 1mbar Ar pressure at 550 ℃ for 30 min with various added S/(S+Se) weight ratios.

Added S/(S+Se) (weight ratio)	Annealing Conditions	Precursor		Absorber					
		Cu/(Zn+Sn)	Zn/Sn	Cu/(Zn+Sn)	Zn/Sn	S/(S+Se) by XRD (atom ratio)	S/(S+Se) by EQE (atom ratio)	Sn(S,Se)	$Sn(S,Se)_2$
0.8	550℃-30min-1bar	0.83	1.21	0.87	1.14	0.91	0.95	NO	YES
0.4				0.87	1.11	0.85	0.82	NO	YES
0.04				0.85	1.08	0.39	0.35	NO	YES
0.8	550℃-30min-1mbar			0.87	1.13	0.8	0.82	YES	NO
0.4				0.86	1.06	0.77	0.77	YES	NO
0.2				0.83	1.04	0.73	0.77	YES	NO
0.04				0.84	1.03	0.58	0.55	YES	NO

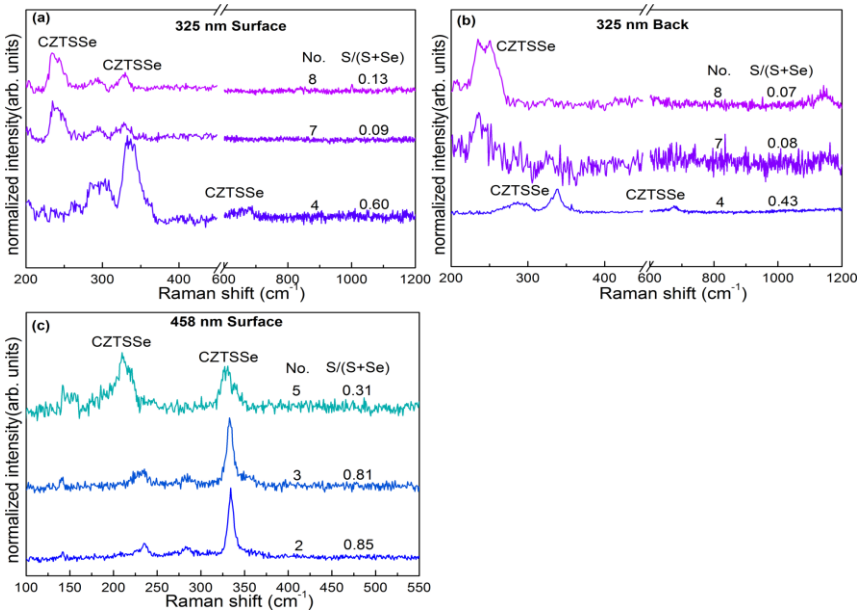

Fig. S2. Raman spectra with 325nm excitation light of the surface (a) and the back region (b), and 458nm excitation light of the surface(c) of CZTSSe samples with different S/(S+Se) ratios. The number and S/(S+Se) ratio in the figure correspond to the information shown in Table 2 of the manuscript.

Part 3: Influence of the S/(S+Se) ratios on the optoelectronic properties of CZTSSe thin film solar cells and their efficiency limitation problems

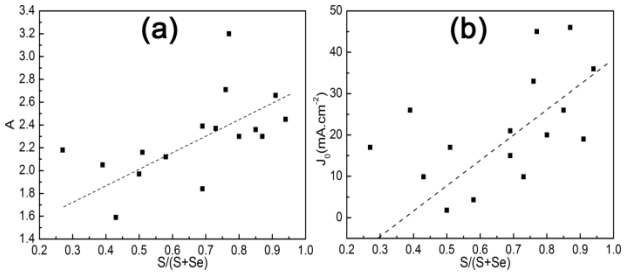

Fig. S3. Ideality factor A (a) and diode saturation current density J_0 (b) as a function of S/(S+Se).

Additional References

[supp1] J. He, L. Sun, S.Y. Chen, Y. Chen, P. X. Yang, J. H. Chu, Composition dependence of structure and optical properties of $Cu_2ZnSn(S, Se)_4$ solid solutions: an experimental study, J. Alloys Compd. 511 (2012) 129 – 132 .

[supp2] S. Chen, A. Walsh, J. Yang, X. G. Gong, L. Sun, P. Yang, J. Chu, S. Wei, Compositional dependence of structural and electronic properties of $Cu_2ZnSn(S, Se)_4$ alloys for thin film solar cells, Phys. Rev. B 83 (2011) 125201.

[supp3] W. Wang, M. T. Winkler, O. Gunawan, T. Gokmen, T. K. Todorov, Y. Zhu, D. B. Mitzi, Device characteristics of CZTSSe thin-film solar cells with 12.6% efficiency, Adv. Energy Mater. 4 (2014) 1301465.

[supp4] Y. S. Lee, T. Gershon, O. Gunawan, T. K. Todorov, T. Gokmen , Y. Virgus, S. Guha, $Cu_2ZnSnSe_4$ thin-film solar cells by thermal co-evaporation with 11.6% efficiency and improved minority carrier diffusion length, Adv. Energy Mater. (2014) 1401372, DOI: 10.1002/aenm.201401372.

[supp 5] M. Grossberg, J. Krustok , T. Raadik , M. Kauk-Kuusik , J. Raudoja, Photoluminescence study of disordering in the cation sublattice of Cu_2ZnSnS_4, Curr. Appl. Phys. 14 (2014) 1424 – 1427.

[supp 6] G. Rey, A. Redinger, J. Sendler, T. P. Weiss, M. Thevenin, M. Guennou, B. El Adib, S. Siebentritt, The band gap of $Cu_2ZnSnSe_4$: effect of order-disorder, Appl. Phys. Lett. 105 (2014) 112106.

ACS APPLIED MATERIALS & INTERFACES

Research Article

www.acsami.org

Impact of Sn(S,Se) Secondary Phases in $Cu_2ZnSn(S,Se)_4$ Solar Cells: a Chemical Route for Their Selective Removal and Absorber Surface Passivation

Haibing Xie,[†] Yudania Sánchez,[†] Simón López-Marino,[†] Moisés Espíndola-Rodríguez,[†] Markus Neuschitzer,[†] Diouldé Sylla,[†] Andrew Fairbrother,[†] Victor Izquierdo-Roca,[†] Alejandro Pérez-Rodríguez,[†,‡] and Edgardo Saucedo*,[†]

[†]IREC, Catalonia Institute for Energy Research, Jardins de les Dones de Negre 1, 2a, 08930 Sant Adrià del Besòs, Spain

[‡]IN2UB, Departament d'Electrònica, Universitat de Barcelona, Martí i Franquès 1-11, 08028 Barcelona, Spain

Supporting Information

ABSTRACT: The control and removal of secondary phases is one of the major challenges for the development of $Cu_2ZnSn(S,Se)_4$ (CZTSSe)-based solar cells. Although etching processes have been developed for Cu(S,Se), Zn(S,Se), and CuSn(S,Se) secondary phases, so far very little attention has been given to the role of Sn(S,Se). In this paper, we report a chemical route using a yellow $(NH_4)_2S$ solution to effectively remove Sn(S,Se). We found that Sn(S,Se) can form on the surface either because of stoichiometric deviation or by condensation. After etching, the efficiency of devices typically increases between 20 and 65% relative to the before etch efficiencies. We achieved a maximum 5.9% efficiency in Se-rich CZTSSe-based devices. It is confirmed that this feature is related not only to the removal of Sn(S,Se) but also to the unexpected passivation of the surface. We propose a phenomenological model for this passivation, which may open new perspectives for the development of CZTSSe-based solar cells.

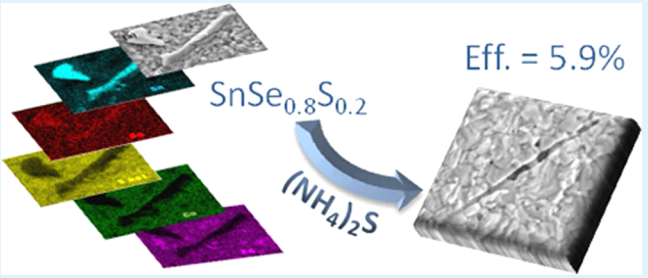

KEYWORDS: *thin films, solar cells, kesterites, $Cu_2ZnSn(S,Se)_4$, secondary phases, Sn(S,Se), chemical etching*

INTRODUCTION

As an ideal candidate for substituting $CuIn_{1-x}Ga_x(S,Se)_2$ (CIGSSe) solar cells due to its earth-abundant and low-toxic constituent elements, $Cu_2ZnSn(S,Se)_4$ (CZTSSe) solar cells are developing very quickly, recently achieving a record efficiency that exceeds 12%.[1] The technological applications of this family of materials range from solar cells to counter electrodes for dye-sensitized solar cells, photoelectrochemical hydrogen production, etc.,[2−4] because of its capability of covering a wide range of band gaps depending on the ratio of S/Se. However, this fascinating as well as complex material exhibits intrinsic properties that complicate its future development. Among these properties, it is important to mention the extremely narrow single-phase existence zone in the phase diagram, the off-stoichiometry conditions used for the preparation of high-efficiency devices (Zn-rich and Cu-poor composition), and the nonequilibrium conditions used during thermal treatments.[5−7] Because of these peculiarities, secondary phases like ternary CuSn(S,Se) and binary Zn(S,Se), Cu(S,Se), and Sn(S,Se) are prone to appearing in the as-prepared absorbers and have already been detected in several works.[1,7−10] If present, these secondary phases can potentially degrade the performance of solar cells, as has been recently observed.[10−12] They may be present either at the interfaces (surface and back contact) or in the bulk, and in fact there are several reports confirming their possible presence along the whole thickness of the films (see, for example, refs 11 and 12 for S and Se compounds, respectively).

When present in the back region or in the bulk,[11] the detrimental effects of secondary phases cannot be avoided, and in fact prevention is probably the only solution, by choosing idealized synthesis conditions: precursors, composition, process parameters, post-treatments, etc. Conversely, when present on the surface, one of the solutions is to remove them by etching. KCN etching is now a daily routine for CIGSSe processing, which can effectively remove Cu(S,Se) also for kesterites.[13−15] Br_2/MeOH was reported to remove Cu−Sn−Se-related secondary phases.[16,17] For ZnS, a 5−10% (75 °C) hot HCl solution is a useful way of selectively removing it.[18] For ZnSe removal, an oxidation route using $KMnO_4/H_2SO_4$ followed by a Na_2S solution rinse was developed, and its effectiveness was shown.[19] Table 1 shows the summary of the most interesting etching routes developed up to now for CIGSSe and CZTSSe solar cells.

Received: May 5, 2014
Accepted: July 17, 2014
Published: July 17, 2014

Table 1. Summary of the Etching Procedures for CIGSSe and CZTSSe Solar Cells

secondary phases	band gap (eV)	potential detriment	etching routes	etching reactions	ref
$Cu_x(S,Se)$ $(1 \le x \le 2)$	1.2–2.2	shunted devices	5–10% (w/v) KCN, RT, 0.5–30 min	$2CuS(Se)(s) + 5KCN(aq) + 2KOH(aq) = 2KCu(CN)_2(aq) + 2K_2S(Se)(aq) + KCNO(aq) + H_2O(l)$	13–15
ZnS	3.7	decrease J_{sc}, increase R_s	5–10% (v/v) HCl, 75 °C, 5–10 min	$2HCl(aq) + ZnS(s) = ZnCl_2(aq) + H_2S(g)$	18
ZnSe	2.7	decrease J_{sc}, increase R_s	$KMnO_4$(0.01 M)/H_2SO_4 (1 M), 30–40 s, and then Na_2S (1 M), 1 min, RT	$8H_2SO_4(aq) + 2KMnO_4(aq) + 5ZnSe(s) = 5Se(s) + 5ZnSO_4(aq) + 2MnSO_4(aq) + K_2SO_4(aq) + 8H_2O(l)$ and $6NaOH(aq) + 3Se(s) = Na_2SeO_3(aq) + 2Na_2Se(aq) + 3H_2O(l)$	19
Cu–Sn–Se (Cu_2SnSe_3, Cu_3SnSe_4)	0.8–1.0	reduce V_{oc}	0.02 M Br_2/MeOH, RT		16 and 17

However, the development of a method for the removal of Sn(S,Se) secondary phases is still a pending task presumably because this secondary phase occurs to a lesser extent than Cu(S,Se) in CIGSSe and Zn(S,Se) in CZTSSe absorbers. Nevertheless, its presence has been noticed in other literature cases.[20,21]

Sn(S,Se) is a low-band-gap phase with E_g approximately equal to 1 eV (this value was reported for a 1:1 stoichiometry compound; other stoichiometries typically exhibit band gaps between 1.1 and 2.5 eV).[22] If this phase is located in the CZTSSe/CdS interface, some subenergy levels will form and thus V_{oc} of the devices will be pulled down, although, in fact, the impact of Sn(S,Se) on the solar cell properties has not been thoroughly investigated yet. In addition, because it is common now to use Sn or Sn(S,Se) to suppress Sn loss during thermal treatment,[23] it is possible that an excess of Sn(S,Se) in the atmosphere may condense onto the surface of as-prepared absorbers during the cooling process. Then the occurrence of this secondary phase may happen by both composition- and/or process-related issues.

During the synthesis of CZTSSe absorbers with the methodology used in this paper and published elsewhere,[24] it was found that there are no Zn(S,Se) phases on the surface of Se-rich CZTSSe films, while Sn(S,Se) may be detected. In consideration of this problem, in this paper a chemical route to selectively remove Sn(S,Se) with a $(NH_4)_2S$ etching solution is presented, and optoelectronic properties before and after etching are discussed. We will demonstrate that the etching is highly effective at removing Sn(S,Se) secondary phases and also, as an additional novel feature, the solution is very useful in effectively passivating the CZTSSe surface.

EXPERIMENTAL SECTION

Metallic Precursor Preparation. Cu/Sn/Cu/Zn precursor stacks were deposited by direct-current (dc) magnetron sputtering (Ac450 Alliance Concepts) onto Mo-coated soda-lime glass (10 × 10 cm^2; 800 nm thickness; $R\square$ = 0.25 Ω/□). The conditions for the deposition of each metal can be found elsewhere.[18,19] Moreover, before metallic precursor deposition, the i-ZnO (10 nm) layer was deposited onto the Mo surface to minimize detrimental reactions between Mo and CZTSSe absorbers during high-temperature annealing.[12] Determined by X-ray fluorescence (XRF; Fisherscope XVD), the metallic stacks were approximately 600 nm thick, with composition ratios of Cu/(Zn + Sn) ≈ 0.8 and Zn/Sn ≈ 1.2.

Absorber Preparation. For solid solution CZTSSe absorbers, metallic precursors were reactively annealed in a graphite box at 550 °C, 1 mbar argon atmosphere for 30 min, and using two crucibles, one with a mixture of selenium (48 mg, Alfa-Aesar, 99.999%) and sulfur powder (2 mg, Alfa-Aesar, 99.995%) and the other with tin powder (5 mg, Alfa-Aesar, 99.999%). The ratio of S/(S + Se) in solid solution CZTSSe absorbers used in this paper was 0.45–0.55, as estimated by X-ray diffraction (XRD), which corresponds to a band gap of 1.22–1.27 eV. Varying the cooling down step of the annealing process, we have produced two types of samples: with low (CZTSSe1) and high (CZTSSe2) quantities of Sn(S,Se) on the surface. Using a natural cooling down step under relatively high vacuum (1×10^{-3} bar), we produced CZTSSe1 samples with little Sn(S,Se) on the surface, whereas using a fast cooling down process under ambient pressure, we obtained CZTSSe2-type samples, with a high quantity of the Sn(S,Se) secondary phase on the surface.

Etching Treatments. Etching of the absorbers was performed at room temperature using a $(NH_4)_2S$ [4–22% (w/w), Alfa-Aesar] aqueous solution or KCN [2% (w/v)] or Na_2S (1 M) solutions for 1 min in all cases. The solutions were stirred during the whole etching process.

Solar Cell Fabrication. Solar cells were assembled by depositing CdS (50−60 nm) by chemical bath deposition onto CZTSSe absorbers, followed by the pulsed dc magnetron sputtering deposition of intrinsic ZnO (50 nm) and ZnO:Al (450 nm, 25 Ω/□; CT100 Alliance Concepts).

Characterization. Inspection of the surface using Raman spectroscopy with three excitation wavelengths (532, 458, and 325 nm) allows us to confirm the absence of Cu(S,Se) and Zn(S,Se) secondary phases on the surface of both types of samples. In all cases, a Horiba Jobin−Yvon T64000 spectrometer at a backscattering configuration was used, and the excitation power density was kept below 100 kW/cm^2 to minimize the presence of thermal effects in the spectra. The scanning electron microscopy (SEM) images were obtained through a Zeiss series Auriga microscope using an accelerating voltage of 10 kV. Energy-dispersive X-ray spectroscopy (EDS; Oxford Instruments, X-Max) was performed using 10 and 20 kV in the working distance 5−8 mm. XRD measurements were performed using a Siemens D500 diffractometer in a 2θ configuration ranging from 10° to 80°. For the optoelectronic characterization, cells (3 × 3 mm^2) were scribed, and the illuminated $I-V$ curves were obtained using an ABET Technologies Sun 3000 Class AAA solar simulator. The external quantum efficiency (EQE) of the devices was performed on a Bentham PVE300 system without a bias voltage or with a bias voltage of −1 V.

RESULTS AND DISCUSSION

Secondary Phases on the Surface of CZTSSe Absorbers. Parts a and b of Figure 1 show the SEM images and EDS mappings of two different types of features observed on the surface of the typical as-annealed CZTSSe films, including the quantification of Cu, Zn, Sn, S, and Se. In particular, Figure 1a shows the typical phase with a rodlike shape, integrated into the surface of the CZTSSe film (type 1), whereas Figure 1b shows the typical phase with approximately round or semicircular shape, which probably originates from Sn(S,Se) condensation from the annealing atmosphere (type 2), as we will show later. EDS mappings performed in the surrounding area that includes these morphologies clearly demonstrate that these two kinds of phases are formed by Sn, Se, and S, suggesting that they are Sn(S,Se) and/or Sn−Se and Sn−S mixed secondary phases. Quantification with EDS shows that the atomic ratio is approximately Sn:Se:S ≈ 50:40:10 in both cases [see also the Supporting Information (SI), part 1], suggesting that these two phases are probably $SnSe_{0.8}S_{0.2}$. This agrees with the phase diagram of both systems (Sn−S and Sn−Se), where under the conditions used in this work, SnS and SnSe are the stable phases.[25,26] The same analysis performed at several points on the CZTSSe layer (excluding these features) allows us to quantify the average kesterite composition: Cu/(Zn + Sn) = 1.03, Zn/Sn = 1.02, and S/(S + Se) = 0.58 (the last ratio is in good agreement with the values obtained by XRD). It is important to remark that both types of Sn(S,Se) features are present in all absorbers used in this paper and that the composition of these absorbers is approximately the same. As we will show in the next section, the removal of both types of Sn(S,Se) features from the CZTSSe surface leads to different consequences on the etched surface.

Figure 2 shows the XRD and Raman spectra of typical as-annealed CZTSSe absorbers. The XRD pattern (Figure 2a) shows that the as-annealed films contain Sn(S,Se) as the secondary phase. In fact, the peak labeled as 3 in the figure presents a slight shift toward high angles with respect to the (400) diffraction peak of SnSe (PDF 00-048-1224), confirming

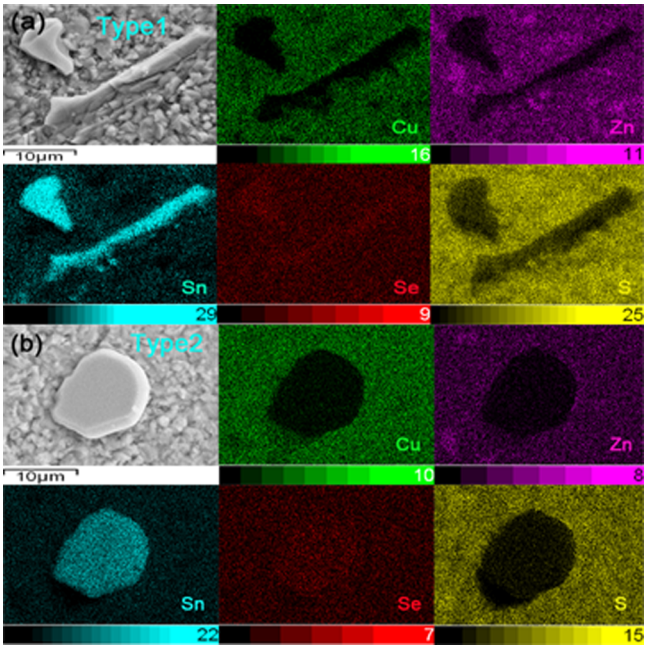

Figure 1. SEM images and EDS mappings of features with different morphologies observed on the surface of CZTSSe absorbers: (a) type 1, encrusted Sn(S,Se); (b) type 2, overgrowth originating from the condensation of Sn(S,Se) from the annealing atmosphere. Different color codes for the intensity of each element are included (Cu in green, Zn in violet, Sn in light blue, Se in red, and S in yellow), from black (no presence of the element) to full color scale (presence of the element).

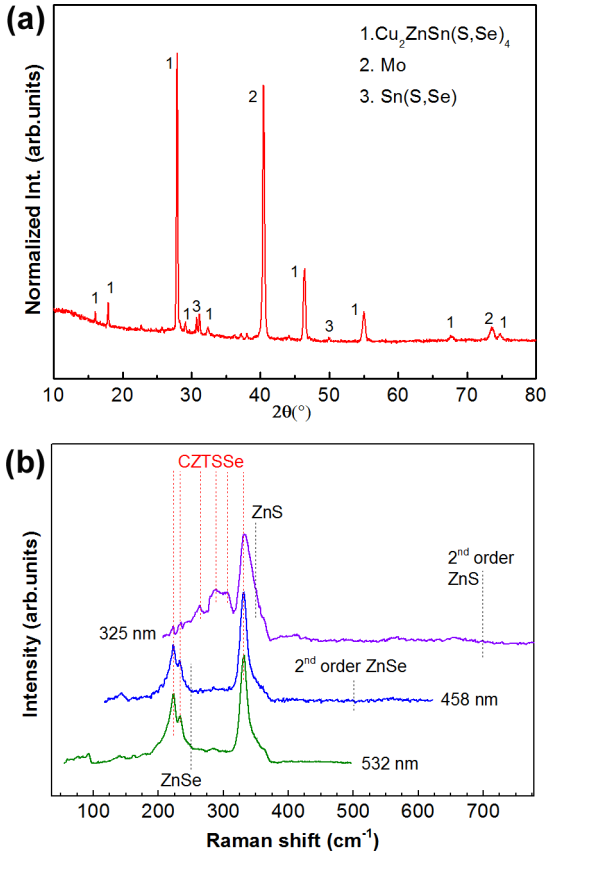

Figure 2. (a) XRD pattern of typical CZTSSe absorbers. (b) Raman spectra of typical CZTSSe absorbers with 532, 458, and 325 nm excitation light.

the presence of some S in this secondary phase. Additionally, this is in agreement with the SEM and EDS results that show the formation of Se-rich Sn(S,Se) together with the main kesterite phase. To unambiguously demonstrate the absence of secondary phases other than Sn(S,Se) on the surface, Raman spectra (Figure 2b) were obtained using three different wavelengths: 532, 458, and 325 nm. Raman with 532 nm is useful for detecting kesterites and Cu(S,Se) secondary phases, while 458 and 325 nm are highly sensitive to detection of ZnSe and ZnS, respectively.[27−30] As is shown in the literature, even tiny ZnSe or ZnS quantities on the surface can be detected using these resonant Raman conditions (peaks at 249 and 500 cm^{-1} correspond to ZnSe, and those at 348 and 697 cm^{-1} correspond to ZnS).[31] From Figure 2b, we can conclude that the CZTSSe surface of the samples under study in this work is free of Cu_xS, Cu_xSe ($x < 1.8$), ZnSe, and ZnS. In particular, the absence of the characteristic 260 cm^{-1} peak in the spectrum acquired using a 532 nm excitation wavelength confirms that a Cu_xSe secondary phase is not present on the surface (green spectrum in Figure 2b).[27] Additionally, the absence of the first-order (249 cm^{-1}) and second-order (500 cm^{-1}) peaks of ZnSe using a 458 nm excitation wavelength (blue spectrum in Figure 2b), as well as the first-order (348 cm^{-1}) and second-order (697 cm^{-1}) peaks of ZnS using a 325 nm excitation wavelength (violet spectrum in Figure 2b), allows us to discard the presence of these two secondary phases on the CZTSSe surface. The presence of ternary CuSn(S,Se) phases cannot be discarded, but considering the imposed Zn-rich and Cu-poor compositional conditions, their formation is highly unexpected. Thus, in these types of samples, Sn binaries are the only secondary phase on the surface, namely, Sn(S,Se), being ideal for the study of the etching process and the influence of Sn(S,Se) on CZTSSe solar cell parameters. This phase has already been observed in the literature by other authors, indicating that its formation can occur during different standard processes (see, for example, refs 20 and 21).

Removal of Sn(S,Se) Secondary Phases. To demonstrate the effectiveness of the $(NH_4)_2S$ etching, as-annealed layers were submitted to processes with different etchant solutions. Figure 3 shows the XRD diffractogram of CZTSSe absorbers before and after etching with different solutions [KCN, Na_2S, and $(NH_4)_2S$], as described in the Experimental Section. From Figure 3, it is clear that KCN and Na_2S etchings are not effective at removing Sn(S,Se), while after etching in a 22% (w/w) $(NH_4)_2S$ solution for 1 min, Sn(S,Se) is removed from the surface. The results show that the peak intensities of CZTSSe barely change before and after $(NH_4)_2S$ etching, which indicates the selective removal of Sn(S,Se), suggesting that the main kesterite phase is slightly or even not affected.

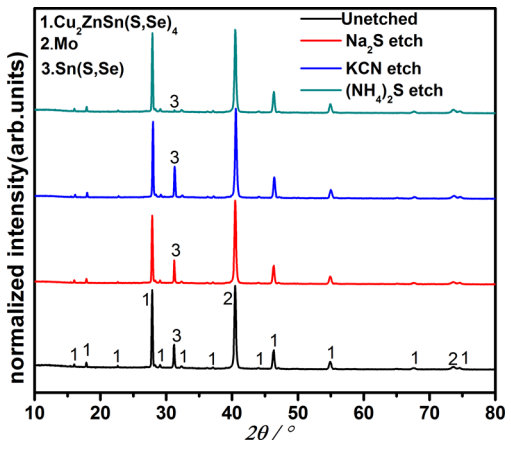

Figure 3. XRD of CZTSSe absorbers before and after etching. The concentrations of the solutions are 2% (w/v) KCN, 1 M Na_2S, and 22% (w/w) $(NH_4)_2S$. We use different units to express the concentrations in order to facilitate the preparation of each of them. In particular, the molarity of KCN and $(NH_4)_2S$ is not presented because the exact density of these solutions is unknown.

To demonstrate the selectivity of this process, the etching rate of different Sn binaries as well as CZTSSe is present in Table 2. The etching rate was determined using films prepared on glass (see the SI, part 2, for a detailed description of the methodology employed for the etch rate estimation) and measuring the thickness of these layers after different etching times by XRF. From Table 2, it is clear that the etching is very effective for the removal of SnS and SnSe [under the analyzed conditions: 22% (w/w) solution and room temperature], whereas it seems to be less effective for the SnS_2 and $SnSe_2$ phases. However, increasing the concentration of a $(NH_4)_2S$ solution or reaction temperature should be helpful for the improvement of the etching rate on SnS_2 and $SnSe_2$.[32] The kesterite phase is apparently not or very slightly etched, confirming the selectivity of the chemical process. It is important to remark that solubility tests were performed with powders of different secondary phases (ZnS, ZnSe, Cu_2Se, Cu_2S, SnSe, and SnS) and show that the solubility of the Zn and Cu binary compounds is negligible in this solution (see part 2.1 of the SI for a detailed description of the experiment).

Table 2. Etching Rate of 22% (w/w) $(NH_4)_2S$ on Sn−S, Sn−Se, and CZTSSe Thin Films

thin film	etching rate (nm/s)	thin film	etching rate (nm/s)
CZTSSe	<0.13	SnS	1.1
SnSe[a]	1.2	SnS_2[a]	0.5
$SnSe_2$	0.2		

[a]SnSe mixes with a little $SnSe_2$, and SnS_2 mixes with a little SnS. However, the conclusion is not affected. See the SI, part 2.

However, the process presented here also has effects on the morphology of the films (see Figure 4). Type 2 Sn binary phases are easily removed from the surface and do not have any apparent impact on the surface morphology. This is expected, taking into account that this type of secondary phase is a surface overgrowth. Nevertheless, the situation is different for the type 1 Sn binary secondary phases. After etching, there are some long trenches along the surface (see Figure 4b,c), which is the outline of the Sn(S,Se) rods after removal by yellow $(NH_4)_2S$. Note that these elongated trenches are shallow, and after removal, it is expected to have an impact only on the surface. However, no trace of the Sn(S,Se) phase with round shape (type 2) can be found (those corresponding to Figure 4a). This demonstrates that these two kinds of phases originated from different sources. The phases with elongated shape are most probably formed during the synthesis process, explaining why they are encrusted on the surface, while the other one may come from the condensation of Sn(S,Se) during the cooling process, explaining why it is on the surface of the films. When the annealing furnace is cooled down under vacuum, there are less type 2 secondary phases on the surface, which also supports this conclusion.

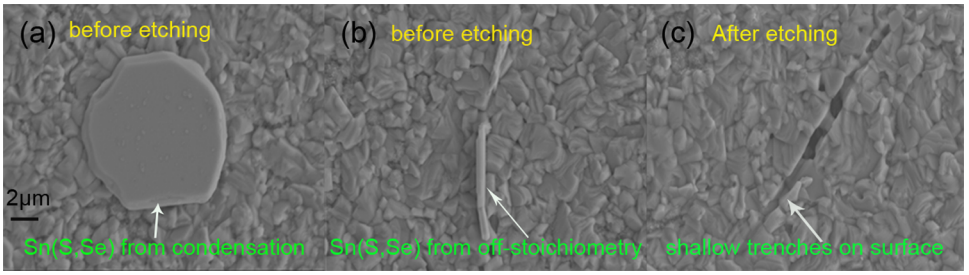

Figure 4. SEM images of type 2 (a) and type 1 (b) Sn(S,Se) secondary phases before etching on CZTSSe absorbers. (c) Surface image after removal of the type 1 Sn(S,Se) secondary phase with 22% $(NH_4)_2S$ chemical etching, showing the formation of shallow trenches.

The effectiveness of the etching process can be evaluated also with its impact on the global composition of the layers. Table 3

Table 3. Compositions of CZTSSe Absorbers before and after 22% (w/w) $(NH_4)_2S$ Etching by XRF

sample	Cu/(Zn + Sn)	Zn/Sn	thickness (μm)
unetched	0.86	1.22	1.73
$(NH_4)_2S$ etched	0.89	1.28	1.56

shows the composition of the absorbers before and after $(NH_4)_2S$ etching. After etching, both Cu/(Zn + Sn) and Zn/Sn increase, which is consistent with the removal of Sn(S,Se), i.e., with the diminution of the Sn concentration. The S/(S + Se) ratio seems to be unaffected by the etching, whereas the thickness slightly decreases, probably because of removal of the thin $SnSe_{0.8}S_{0.2}$ secondary phases on top of the layer. Similar changes in the thickness have been observed after etching of the ZnS and ZnSe phases on the surface and have been attributed to the removal of these phases.[17,19]

Note that the composition of the absorbers before etching measured by XRF differs from that obtained by EDS as mentioned before. This may be because XRF has a greater penetration depth than EDS, and Zn(S,Se) usually accumulates in the back, thus leading to lower Cu/(Zn + Sn) and higer Zn/Sn ratios in XRF measurements.[33]

To better understand the effect of etching in the CZTSSe-Sn(S,Se) system, it is important to analyze the route for the selective removal of Sn binaries. It was reported that yellow $(NH_4)_2S$ (namely, containing some S^0 traces) can dissolve SnS and SnS_2 via the formation of complexes.[34,35] Although not reported, considering the similar properties of S- and Se-based compounds, it is reasonable to suppose that SnSe [or Sn(S,Se)] behaves similarly. Tin(II) sulfide, selenide, or sulfoselenide will react with yellow ammonium sulfide, being oxidized to the tin(IV) state, forming the soluble ammonium thiostannate(IV) species (reaction I), and after with ammonia (reaction II), by means of the following reactions (the reactions are illustrated for the pure Se compounds but are analogues for the sulfide and sulfoselenide ones):

$$SnSe + S^{2-}{}_2S = SnSeS_2^{2-} \quad (I)$$

$$2NH_4^+ + SnSeS_2^{2-} = (NH_4)_2SnSeS_2(\text{soluble}) \quad (II)$$

Thus, using yellow $(NH_4)_2S$, the formation of soluble tin–ammonium chalcogenide complexes is the most probable chemical path for etching of the Sn binaries. Conversely, Cu and Zn complexes are not formed in the conditions studied in this work, probably because of the lower solubility of these compounds in an ammonia medium. It is important to remark that the use of colorless $(NH_4)_2S$ (without the presence of S^0) has a very limited impact on the solubility of tin chalcogenides and is considerably less effective for the removal of these secondary phases.

Improvements in the Optoelectronic Properties and Mechanism Discussion. To further investigate the role of Sn(S,Se) on the optoelectronic properties of CZTSSe solar cells, two different CZTSSe absorbers were prepared. CZTSSe1 has a little Sn(S,Se) content on the surface (check with SEM), while CZTSSe2 has a lot of Sn(S,Se) on the surface, as is described in the corresponding Experimental Section. With these two types of absorbers, devices were prepared with and without $(NH_4)_2S$ etching and $J-V$ curves were measured (see Figure 5a).

From Table 4, we can see that, after $(NH_4)_2S$ etching, the V_{oc}, J_{sc}, FF, and efficiency for CZTSSe1 devices increase

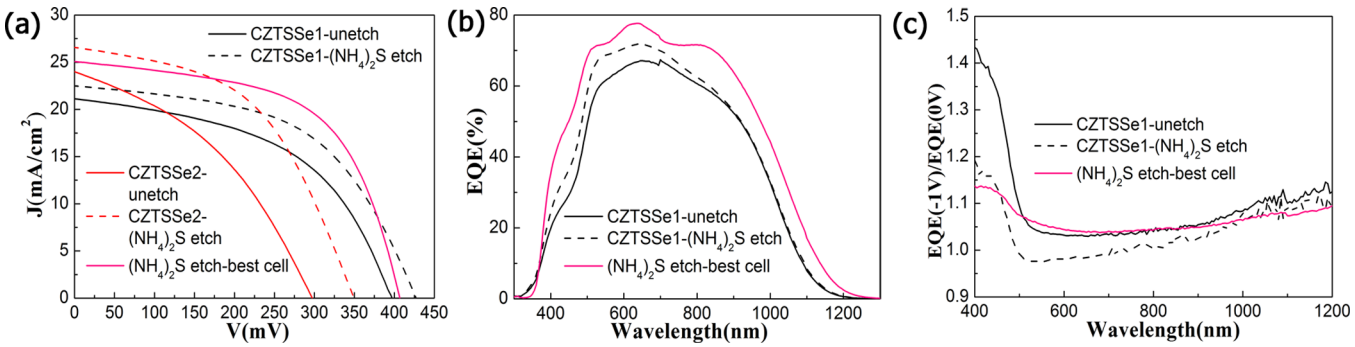

Figure 5. Illuminated $J-V$ curves of CZTSSe1 and CZTSSe2 solar cells before and after 22% (w/w) $(NH_4)_2S$ etching and the best solar cell obtained with the optimized process, producing a 5.9% efficiency device (a). EQE curves of CZTSSe1 and the best cell (b) and EQE(−1 V)/EQE(0 V) curves for CZTSSe1 and the best cell (c).

Table 4. Optoelectronic Properties of Devices before and after 22% (w/w) $(NH_4)_2S$ Etching

type	absorber	etching	J_{sc} (mA/cm^2)	V_{oc} (mV)	FF (%)	EFF (%)	R_s (Ω/cm^2)	R_{sh} (Ω/cm^2)	A	J_0 (mA/cm^2)
CZTSSe1	low Sn(S,Se) content on the surface	unetched	21.1	397	49.8	4.2	1.5	91	2.0	1.2×10^{-2}
		$(NH_4)_2S$ etched	22.4	427	52.9	5.1	2.6	142	1.7	2.1×10^{-3}
CZTSSe2	high Sn(S,Se) content on the surface	unetched	23.9	296	39.3	2.8				
		$(NH_4)_2S$ etched	26.5	349	49.5	4.6				
best cell		$(NH_4)_2S$ etched	25.1	406	57.6	5.9	0.7	109	1.7	1.4×10^{-3}

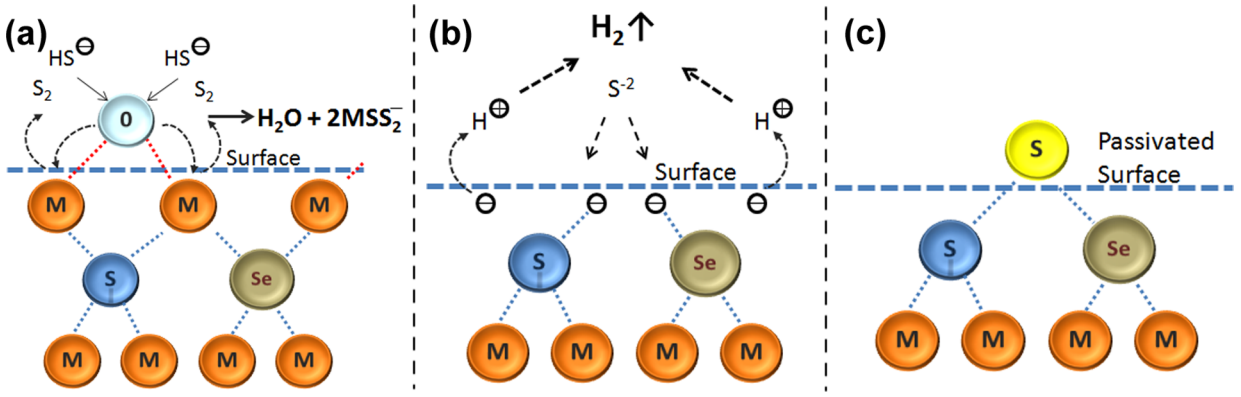

Figure 6. Schematic representation of passivation of the CZTSSe surface using yellow $(NH_4)_2S$ solutions: removal of the native oxides with the HS^- ions (a); electron transfer from the semiconductor toward the H^+ ions of the solution and production of H_2 (b); formation of the bond between the S and the dissolved chalcogen (c).

relatively by 7.6%, 6.2%, 6.2%, and 21.4%, respectively, while those for CZTSSe2 increase by 17.9%, 10.9%, 26%, and 64.2%, respectively. This shows that after etching all parameters were improved. Comparing the optoelectronic parameters of CZTSSe1 devices with those of CZTSSe2, we conclude that the higher the Sn(S,Se) quantity on the surface, the higher the V_{oc}, J_{sc}, and FF relative increase after etching. Nevertheless, the impact of the etching on J_{sc} is considerably less pronounced than that on V_{oc} and FF. This indicates that Sn(S,Se) mainly degrades V_{oc}, somehow also affecting FF of the devices because of, among others, the low band gap of this secondary phase. Additionally, R_s slightly changes, while R_{sh} markedly increases in the CZTSSe1 sample. Aside from the effect of Sn(S,Se) removal, the pronounced FF and R_{sh} increases could also be related to passivation effects of a $(NH_4)_2S$ solution on the surface of absorbers, as we will discuss below. After optimization of all processes, we obtain a cell with a maximum conversion efficiency of 5.9% (see the optoelectronic parameters in Table 4 and related curves in Figure 5), which is, to our knowledge, one of the highest values reported for a CZTSSe-based solar cell prepared from dc-sputtered metallic precursors. This efficiency, although still relatively low in comparison with the highest efficiencies reported in the literature for the CZTSSe solid solution based solar cells, is very encouraging, taking into account that the methodology presented here for the synthesis of CZTSSe absorbers is quite innovative. In ref 1, a 12.6% efficiency device was reported but using precursors containing S and a methodology involving the use of a highly toxic and explosive hydrazine compound. Additionally, other approaches using precursors containing S[2] and/or S−Se[8] compounds as precursors have reported efficiencies in the range of 6−9%. In our approach, we are using only metallic stacks as precursors, incorporating S and Se in a controlled manner using a one-step sulfoselenization process. In this sense, this methodology is suitable for the future industrial application of CZTSSe-based technologies and the obtained efficiencies are very encouraging for the future competitiveness of this technology. We have tested this etching with about 12 groups of devices, showing that the efficiency of all of the devices after etching increases by 20−65% relative to unetched values and depending on the quantity of Sn(S,Se) on the surface (the average increased value for the efficiency is 43% relative). In addition, the influence of the $(NH_4)_2S$ solution concentration on the optoelectronic properties of CZTSSe solar cells was also investigated, which shows that a 22% (w/w) $(NH_4)_2S$ solution is more effective than those with lower concentrations (see the SI, part 3.1).

To understand the improvements of the illuminated $J-V$ characteristics after $(NH_4)_2S$ etching, CZTSSe1 was analyzed to measure EQE with and without bias voltage. Parts b and c of Figure 5 show EQE and EQE(−1 V)/EQE(0 V) curves of CZTSSe1-based solar cells before and after $(NH_4)_2S$ etching. EQE shows that in the range 500−900 nm there are significant increases in EQE, which is consistent with the improvements of the p−n junction. From this EQE curve, we calculate the J_{sc} values, which are in very good agreement with those obtained from the $J-V$ illuminated curves (see the SI, part 3.2), indicating that there is a small influence of light-induced defects. Moreover, from Figure 5c, we know that after etching the EQE(−1 V)/EQE(0 V) curve is below that before etching, which means EQE is less dependent on the bias voltage, indicating that the device has better carrier collection efficiency. Note that EQE(−1 V)/EQE(0 V) curves increase considerably in the short-wavelength range for both samples, which is often associated with a low electron lifetime, or low field strength at the p−n interface, allowing electron back-diffusion into the p layer.[36] This problem is relatively well solved in the case of the best cell. In addition, ideality factor A and diode current density

J_0 were also extracted from the illuminated $J-V$ curves of the CZTSSe1 sample by Sites' method[37] and are shown in Table 4. After etching, A decreased from 2.0 to 1.7 and J_0 reduced almost one order of magnitude, which demonstrates better junction quality and less interface recombination in the device.

These results demonstrate that etching based in yellow $(NH_4)_2S$ has two beneficial effects on kesterites: (i) the selective removal of Sn binary secondary phases on the surface and (ii) the possible passivation of the surface. This passivation effect promoted by sulfide compounds has already been observed in III–V semiconductors[38−40] and very recently reported for CZTSe solar cells treated with Na_2S.[19] We propose a route for this passivation in the case of kesterites and using $(NH_4)_2S$ as a passivating agent, which implies the elimination of surface oxides and the formation of S passivated species. The mechanism is based on a three-step process, as shown in Figure 6. In the first step, the S ions (preferentially HS^- due to the pH of the solution) react with the surface metallic oxides, breaking the bond between the chalcogen and the metals as presented in Figure 6a, forming soluble metal chalcogenide species, and leaving H^+ ions in the solution. This process produces free bonds at the surface for subsequent bond formation with S ions from the $(NH_4)_2S$ solution. After dissolution of the native oxides, in a second step, the electrons from the conduction band of the semiconductor are transferred to the solution to neutralize the H^+ ions created in the previous step (Figure 6b), with the concomitant formation of $H_2(g)$, the formation of which is already observed during the etching process (formation of bubbles in the solution). This electron transfer allows the formation of chemical bonds between the S^{2-} free in the solution and the chalcogen atoms of the semiconductor (Figure 6c), explaining passivation of the surface. This mechanism explains the passivation effect of $(NH_4)_2S$ observed here and also reported previously for CZTSe with a Na_2S solution and is the key effect for the improvement of R_{sh} and FF presented in this work. A similar mechanism was proposed for III–V semiconductors.[41] However, it is the first time that we use the updated mechanism to explain the passivation effects of $(NH_4)_2S$ or Na_2S on chalcogenide-based solar cells. This opens a perspective for improvement of the CZTSSe/CdS heterojunction properties by elimination of the tail states in the kesterite surface before junction formation using yellow $(NH_4)_2S$ as a passivating agent.

CONCLUSIONS

In summary, in this paper we present a very effective chemical route using a yellow $(NH_4)_2S$ solution for the highly selective removal of Sn(S,Se) on the CZTSSe absorber surface. We find that Sn(S,Se) can form either from stoichiometric deviation or by condensation from the annealing atmosphere, which usually contains Sn and the chalcogens. We have shown that the presence of this detrimental secondary phase clearly degrades the performance of devices mainly because of the reduction of V_{oc}. Additionally, we report that the yellow $(NH_4)_2S$ solution not only is effective for the selective removal of Sn(S,Se) but also can passivate the surface, decrease interface recombination, and ultimately improve the p–n junction quality and the conversion efficiency of CZTSSe-based solar cells. We propose a surface passivation mechanism of CZTSSe with this type of solution, which can open new perspectives toward the preparation of high-efficiency devices with these kinds of earth-abundant absorbers.

ASSOCIATED CONTENT

Supporting Information

EDS measurements with 10 and 20 kV, powder solubility tests, XRD and etching curves of Sn–S, Sn–Se, and CZTSSe thin films, SEM and optoelectronic properties of CZTSSe etched with different concentrations of $(NH_4)_2S$, and comparison of J_{sc} from EQE and $J-V$ curves. This material is available free of charge via the Internet at http://pubs.acs.org.

AUTHOR INFORMATION

Corresponding Author

*E-mail: esaucedo@irec.cat.

Author Contributions

The manuscript was written through contributions of all authors. All authors have given approval to the final version of the manuscript.

Notes

The authors declare no competing financial interest.

ACKNOWLEDGMENTS

The research leading to these results has received funding from the People Program (Marie Curie Actions) of the European Union's Seventh Framework Program FP7/2007-2013/under REA Grant Agreement 316488 (KESTCELLS) and by European Regional Development Funds (ERDF; FEDER Programa Competitivitat de Catalunya 2007–2013). Authors from IREC and IN2UB belong to the M-2E (Electronic Materials for Energy) Consolidated Research Group and the XaRMAE Network of Excellence on Materials for Energy of the "Generalitat Generalitat de Catalunya". H.X. is thankful for a "China Scholarship Council" fellowship (CSC 201206340113), M.E.-R. for FPI-MINECO support (BES-2011-045774), D.S. for a PTA fellowship (PTA2011-5985-I), A.F. for a FPU fellowship (FPU12/05508), V.I.-R. for a "Juan de la Cierva" fellowship (JCI-2011-10782), and E.S. for a "Ramon y Cajal" fellowship (RYC-2011-09212).

REFERENCES

(1) Wang, W.; Winkler, M. T.; Gunawan, O.; Gokmen, T.; Todorov, T. K.; Zhu, Y.; Mitzi, D. B. Device Characteristics of CZTSSe Thin-Film Solar Cells with 12.6% Efficiency. *Adv. Energy Mater.* **2013**, *4*, 1301465.

(2) Wang, G.; Zhao, W.; Cui, Y.; Tian, Q.; Gao, S.; Huang, L.; Pan, D. Fabrication of a $Cu_2ZnSn(S,Se)_4$ Photovoltaic Device by a Low-Toxicity Ethanol Solution Process. *ACS Appl. Mater. Interfaces* **2013**, *5*, 10042–10047.

(3) He, J.; Lee, L.; Yang, S.; Li, Q.; Xiao, X.; Chen, T. Printable Highly Catalytic Pt- and TCO-Free Counter Electrode for Dye-Sensitized Solar Cells. *ACS Appl. Mater. Interfaces* **2014**, *6*, 2224–2229.

(4) Ma, G.; Minegishi, T.; Yokoyama, D.; Kubota, J.; Domen, K. Photoelectrochemical Hydrogen Production on Cu_2ZnSnS_4/Mo-mesh Thin-film Electrodes Prepared by Electroplating. *Chem. Phys. Lett.* **2011**, *501*, 619–622.

(5) Dudchak, I. V.; Piskach, L. V. Phase Equilibria in the CuSnSe–SnSe–ZnSe System. *J. Alloys Compd.* **2003**, *351*, 145–150.

(6) Olekseyuk, I. D.; Dudchak, I. V.; Piskach, L. V. Phase Equilibria in the Cu_2S–ZnS–SnS_2 System. *J. Alloys Compd.* **2004**, *368*, 135–143.

(7) Muska, K.; Kauk, M.; Altosaar, M.; Pilvet, M.; Grossberg, M.; Volobujeva, O. Synthesis of Cu_2ZnSnS_4 Monograin Powders with Different Compositions. *Energy Procedia* **2011**, *10*, 203–207.

(8) Chawla, V.; Clemens, B. Effect of Composition on High Efficiency CZTSSe Devices Fabricated Using Co-sputtering of Compound Targets. *IEEE Photovoltaic Spec. Conf.* **2012**, 002990–002992.

(9) Hsu, W.; Repins, I.; Beall, C.; DeHart, C.; Teeter, G.; To, B.; Yang, Y.; Noufi, R. The Effect of Zn Excess on Kesterite Solar Cells. *Sol. Energy Mater. Sol. Cells* **2013**, *113*, 160−164.
(10) Tanaka, T.; Sueishi, T.; Saito, K.; Guo, Q.; Nishio, M. Existence and Removal of Cu_2Se Second Phase in Coevaporated $Cu_2ZnSnSe_4$ Thin Films. *J. Appl. Phys.* **2012**, *111*, 053522.
(11) Fairbrother, A.; Fontané, X.; Izquierdo-Roca, V.; Espíndola-Rodríguez, M.; López, S.; Placidi, M.; Calvo-Barrio, L.; Pérez-Rodríguez, A.; Saucedo, E. On the Formation Mechanisms of Zn-rich Cu_2ZnSnS_4 Films Prepared by Sulfurization of Metallic Stacks. *Sol. Energy Mater. Sol. Cells* **2013**, *112*, 97−105.
(12) Lopez-Marino, S.; Placidi, M.; Perez-Tomas, A.; Llobet, J.; Izquierdo-Roca, V.; Fontane, X.; Fairbrother, A.; Espindola-Rodriguez, M.; Sylla, D.; Perez-Rodriguez, A.; Saucedo, E. Inhibiting the Absorber/Mo-back Contact Decomposition Reaction in $Cu_2ZnSnSe_4$ Solar Cells: the Role of a ZnO Intermediate Nanolayer. *J. Mater. Chem. A* **2013**, *1*, 8338−8343.
(13) Niki, S.; Fons, P. J.; Yamada, A.; Lacroix, Y.; Shibata, H.; Oyanagi, H.; Nishitani, M.; Negami, T.; Wada, T. Effects of the Surface $Cu_{2-x}Se$ Phase on the Growth and Properties of $CuInSe_2$ Films. *Appl. Phys. Lett.* **1999**, *74*, 1630.
(14) Schubert, B.; Marsen, B.; Cinque, S.; Unold, T.; Klenk, R.; Schorr, S.; Schock, H. W. Cu_2ZnSnS_4 Thin Film Solar Cells by Fast Coevaporation. *Prog. Photovoltaics* **2011**, *19*, 93−96.
(15) Weinhardt, L.; Fuchs, O.; Grob, D.; Umbach, E. Surface Modifications of $Cu(In,Ga)S_2$ Thin Film Solar Cell Absorbers by KCN and H_2O_2/H_2SO_4 Treatments. *J. Appl. Phys.* **2006**, *100*, 024907.
(16) Mousel, M.; Redinger, A.; Djemour, R.; Arasimowicz, M.; Valle, N.; Dale, P.; Siebentritt, S. HCl and Br_2-MeOH etching of $Cu_2ZnSnSe_4$ polycrystalline absorbers. *Thin Solid Films* **2013**, *535*, 83−87.
(17) Timmo, K.; Altosaar, M.; Raudoja, J.; Grossberg, M.; Danilson, M.; Volobujeva, O.; Mellikov, E. Chemical Etching of $Cu_2ZnSn(S,Se)_4$ Monograin Powder. *IEEE Photovoltaic Spec. Conf.* **2010**, 001982−001985.
(18) Fairbrother, A.; García-Hemme, E.; Izquierdo-Roca, V.; Fontané, X.; Pulgarín-Agudelo, F. A.; Vigil-Galán, O.; Peérez-Rodríguez, A.; Saucedo, E. Development of a Selective Chemical Etch to Improve the Conversion Efficiency of Zn-Rich Cu_2ZnSnS_4 Solar Cells. *J. Am. Chem. Soc.* **2012**, *134*, 8018−8021.
(19) López-Marino, S.; Sánchez, Y.; Placidi, M.; Fairbrother, A.; Espindola-Rodríguez, M.; Fontané, X.; Izquierdo-Roca, V.; López-García, J.; Calvo-Barrio, L.; Pérez-Rodríguez, A.; Saucedo, E. ZnSe Etching of Zn-Rich $Cu_2ZnSnSe_4$: An Oxidation Route for Improved Solar-Cell Efficiency. *Chem.—Eur. J.* **2013**, *19*, 14814−14822.
(20) Shin, S. W.; Pawar, S. M.; Park, C. Y.; Yun, J. H.; Moon, J.; Kim, J. H.; Lee, J. Y. Studies on Cu_2ZnSnS_4 (CZTS) Absorber Layer Using Different Stacking Orders in Precursor Thin Films. *Sol. Energy Mater. Sol. Cells* **2011**, *95*, 3202−3206.
(21) Xie, M.; Zhao, M.; Li, B.; Cao, M.; Song, J. Fabrication of Cu_2ZnSnS_4 Thin Films Using a Ceramic Quaternary Target. *Vacuum* **2014**, *101*, 146−150.
(22) Siebentritt, S. Why Are Kesterite Solar Cells Not 20% Efficient? *Thin Solid Films* **2013**, *535*, 1−4.
(23) Redinger, A.; Berg, D. M.; Dale, P. J.; Siebentritt, S. The Consequences of Kesterite Equilibria for Efficient Solar Cells. *J. Am. Chem. Soc.* **2011**, *133*, 3320−3323.
(24) Fairbrother, A.; Fontané, X.; Izquierdo-Roca, V.; Espindola-Rodriguez, M.; López- Marino, S.; Placidi, M.; López-García, J.; Pérez-Rodríguez, A.; Saucedo, E. Single-Step Sulfo-Selenization Method to Synthesize $Cu_2ZnSn(S_ySe_{1-y})_4$ Absorbers from Metallic Stack Precursors. *ChemPhysChem* **2013**, *14*, 1836−1843.
(25) Sharma, R. C.; Chang, Y. A. The S−Sn (Sulfur−Tin) System. *Bull. Alloy Phase Diagrams* **1986**, *7*, 269−273.
(26) Sharma, R. C.; Chang, Y. A. The Se−Sn (Selenium−Tin) System. *Bull. Alloy Phase Diagrams* **1986**, *7*, 68−72.
(27) Saucedo, E.; Izquierdo-Roca, V.; Ruiz, C. M.; Parissi, L.; Broussillou, C.; Grand, P. P.; Jaime-Ferrer, J. S.; Pérez-Rodríguez, A.; Morante, J. R.; Bermúdez, V. Key Role of Cu−Se Binary Phases in Electrodeposited $CuInSe_2$ Precursors on Final Distribution of Cu−S Phases in $CuIn(S,Se)_2$ Absorbers. *Thin Solid Films* **2009**, *517*, 2268−2271.
(28) Fontané, X.; Calvo-Barrio, L.; Izquierdo-Roca, V.; Saucedo, E.; Pérez-Rodriguez, A.; Morante, J. R.; Berg, D. M.; Dale, P. J.; Siebentritt, S. In-depth Resolved Raman scattering Analysis for the Identification of Secondary Phases: Characterization of Cu_2ZnSnS_4 Layers for Solar Cell Applications. *Appl. Phys. Lett.* **2011**, *98*, 181905.
(29) Redinger, A.; Hones, K.; Fontané, X.; Izquierdo-Roca, V.; Saucedo, E.; Valle, N.; Pérez- Rodríguez, A.; Siebentritt, S. Detection of a ZnSe Secondary Phase in Coevaporated $Cu_2ZnSnSe_4$ Thin Films. *Appl. Phys. Lett.* **2011**, *98*, 101907.
(30) Fairbrother, A.; Izquierdo, V.; Fontané, X.; Ibáñez, M.; Cabot, A.; Saucedo, E.; Pérez- Rodríguez, A. ZnS Grain Size Effects on Near-resonant Raman Scattering: Optical Non-Destructive Grain Size Estimation. *CrystEngComm* **2014**, *16*, 4120−4125.
(31) Fontané, X.; Izquierdo-Roca, V.; Fairbrother, A.; Espíndola-Rodríguez, M.; López-Marino, S.; Placidi, M.; Jawhari, T.; Saucedo, E.; Pérez-Rodríguez, A. Selective Detection of Secondary Phases in $Cu_2ZnSn(S,Se)_4$ Based Absorbers by Pre-resonant Raman Spectroscopy. *IEEE Photovoltaic Spec. Conf.* **2013**, 2581−2584.
(32) Seo, J.; Koker, T.; Agarwala, S.; Adesida, I. Etching Characteristics of $Al_xGa_{1-x}As$ in $(NH_4)_2S_x$ Solutions. *Appl. Phys. Lett.* **1992**, *60*, 1114−1116.
(33) Klenk, M.; Schenker, O.; Alberts, V.; Bucher, E. Control of Two-step Growth Processes of Chalcopyrite Thin Films by X-ray Fluorescence Spectroscopy. *Appl. Surf. Sci.* **2001**, *173*, 62−68.
(34) Raj, G. In *Advanced Inorganic Chemistry*, 31st ed.; Chatwal, M., Ed.; Krishna Prakashan Media: Meerut, Uttar Pradesh, India, 2008; Chapter 12, pp 506−601.
(35) Arora, A. *Text Book of Inorganic Chemistry*, 1st ed.; Discovery Publishing House: New Delhi, India, 2005; Chapter 14, pp 391−459.
(36) Hegedus, S. S.; Shafarman, W. N. Thin-Film Solar Cells: Device Measurements and Analysis. *Prog. Photovoltaics* **2004**, *12*, 155−176.
(37) Sites, J. R.; Mauk, P. H. Diode Quality Factor Determination for Thin-film Solar Cells. *Sol. Cells* **1989**, *27*, 411−417.
(38) Tseng, C.; Lee, C. Mechanisms of $(NH_4)_2S_x$-treated III−V Compound Triple-junction Solar Cells Incorporating with Hybrid Electrode. *Appl. Phys. Lett.* **2012**, *101*, 033902.
(39) Mariani, G.; Laghumavarapu, R. B.; Villers, B. T.; Shapiro, J.; Senanayake, P.; Lin, A.; Schwartz, B. J.; Huffaker, D. L. Hybrid Conjugated Polymer Solar Cells Using Patterned GaAs Nanopillars. *Appl. Phys. Lett.* **2010**, *97*, 013107.
(40) Lai, L.; Chen, J.; Lou, L.; Wu, C.; Lee, C. Performance Improvement of $(NH_4)_2S_x$-Treated III−V Compounds Multijunction Solar Cell Using Surface Treatment. *J. Electrochem. Soc.* **2008**, *155*, B1270−B1273.
(41) Bessolov, V. N.; Lebedev, M. Chalcogenide Passivation of III−V Semiconductor Surfaces. *Semiconductors* **1998**, *32*, 1141−1156.

Supporting information

Impact of Sn-(S,Se) Secondary Phases in $Cu_2ZnSn(S,Se)_4$ Solar Cells: a Chemical Route for Their Selective Removal and Absorber Surface Passivation

Haibing Xie[a], Yudania Sánchez[a], Simón López-Marino[a], Moisés Espíndola-Rodríguez[a], Markus Neuschitzer[a], Diouldé Sylla[a], Andrew Fairbrother[a], Victor Izquierdo-Roca[a], Alejandro Pérez-Rodríguez[a,b], and Edgardo Saucedo*[a]

[a] IREC, Catalonia Institute for Energy Research, Jardins de les Dones de Negre 1, 2ª, 08930 Sant Adrià del Besòs, Spain.

[b] IN2UB, Departament d'Electrònica, Universitat de Barcelona, Martí i Franquès, 1-11, 08028 Barcelona, Spain.

*Corresponding author e-mail: esaucedo@irec.cat

Part 1 Detection of Sn(S,Se) on the surface of $Cu_2ZnSn(S,Se)_4$ samples

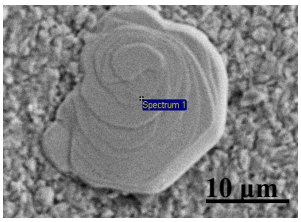

Acceleration Voltage	Cu (atom.%)	Sn (atom.%)	S (atom.%)	Se (atom.%)
10 kV	0	53.15	8.96	37.89
20 kV	0.89	51.75	9.49	37.87

Figure S1. Sn(S,Se) on the surface of CZTSSe and EDS measurements with 10kV and 20kV.

The Mo Lα (5.41 KeV) and S Kα (5.37 KeV) lines overlap in EDS spectrum, and this may disturb the measurement of S content. 10 kV and 20 kV was employed in EDS measurements to confirm the existence of S in the Sn(S,Se) secondary phases avoiding possible Mo interferences. According to previous research performed onto pure kesterite, EDS signal can reach Mo layer when acceleration voltage is 20kV, while 10kV not. From Figure S1 we can see that EDS measurement with 20kV indeed obtain slightly higher S content than with 10kV. We can discard the possible interference of Mo in the S quantification, because at 10 kV we do not detect neither Cu, nor Zn. This means that we are not detecting kesterite, and in conclusion the penetration depth of the electron beam with 10 kV is not collecting signal from Mo. This indicates that this secondary phase is Se-rich Sn(S,Se) with an average S/Se ratio close to 0.25 (S:Se = 1:4).

Part 2 Removal of Sn(S,Se) secondary phases

2.1 Powder solubility tests with 22% w/w $(NH_4)_2S$

Cu_2S SnSe

Figure S2. Change of color for SnSe after $(NH_4)_2S$ solubility test

For the solubility tests, 10mg of SnS, SnSe, ZnSe, ZnS, Cu_2Se and Cu_2S powders were immerged in 20mL of $(NH_4)_2S$ solution, 22% w/w in concentration, and stirring the solutions during 20min at room temperature. After this process, ZnSe, ZnS, Cu_2Se and Cu_2S powders remained at the bottom of the beakers, indicating a very low solubility of these secondary phases in $(NH_4)_2S$ solution. However, for SnSe the solution color changed from yellow to dark yellow or brown as is clearly observed in Figure S2 when comparing with Cu_2S case, indicating some solubility of SnSe in $(NH_4)_2S$. For SnS, color change is not so apparent as that of SnSe, but the powder quantity is clearly reduced in the beaker, suggesting that $(NH_4)_2S$ solution also could be useful for the etching of the tin sulfide compound.

2.2 Preparation of Sn-S and Sn-Se thin films by reactive thermal annealing of sputtered Sn on glass

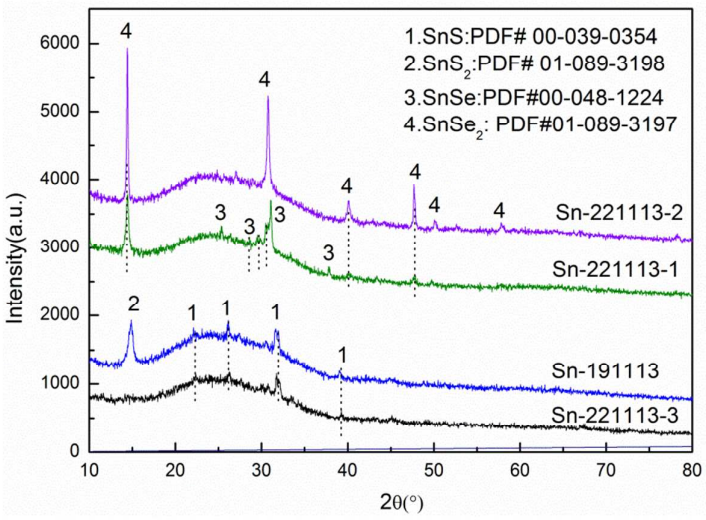

Figure S3. XRD spectra of as-prepared Sn-S and Sn-Se thin films.

Table S1. Summary of phases and thermal annealing conditions of as-prepared Sn-S and S-Se thin films

Thin films	Phases determined by XRD	Thermal annealing conditions
Sn-221113-2	$SnSe_2$	300℃, 1bar, 20min
Sn-221113-1	SnSe+ $SnSe_2$	300℃,1bar,10min
Sn-191113	SnS_2+ SnS	250℃,1bar,2h
Sn-221113-3	SnS	250℃,1bar,10min

Sn-S and Sn-Se thin films were prepared by thermal anealing of Sn precursors sputtered on glass. Figure S3 shows the XRD spectra of as-prepared Sn-S and Sn-Se thin films and Table S1 shows the summary of the phases and thermal annealing conditions of as-prepared thin films. According to the phase diagrams of Sn-Se [Supp1] and Sn-S [Supp2], 300℃ was chosen for SnSe and $SnSe_2$, and 250℃ was chosen to grow SnS and SnS_2, aiming to minimize evaporation of Sn-S and Sn-Se films from the substrate. In the used conditions, we found that Sn-221113-1 is composed of SnSe and $SnSe_2$, while Sn-191113 is composed of SnS_2 and SnS.

2.3 Etching of Sn-S, Sn-Se and solid solution CZTSSe thin films with 22% w/w $(NH_4)_2S$

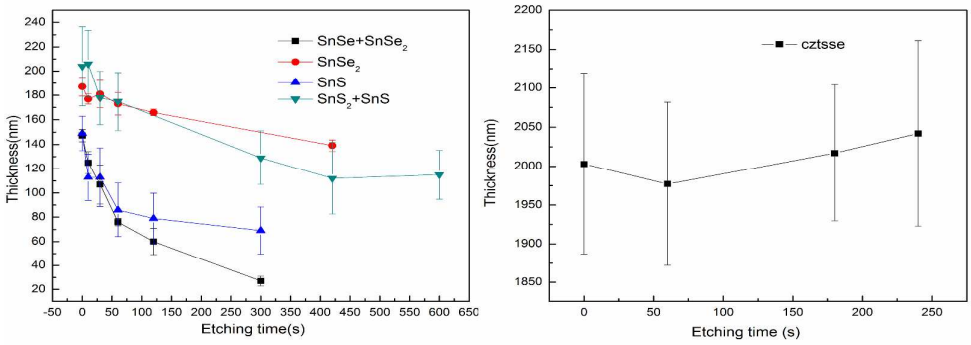

Figure S4. Etching curves of Sn-S, Sn-Se and CZTSSe(S/(S+Se)=0.43) thin films using $(NH_4)_2S$ solution.

Figure S4 shows the etching curves of Sn-S, Sn-Se and CZTSSe thin films on 22% w/w $(NH_4)_2S$. The thickness was measured by XRF. From the left figure we can see that for all the Sn-S and Sn-Se thin films, the etching rate is higher in the first 1 min and then decrease when etching time increase. Using this figure, the etching rate of Sn-S and Sn-Se by $(NH_4)_2S$ were

estimated during the first 1 min, and is presented in the paper. Also, we use in this manuscript, 1 min as the typical etching time. In addition, SnS, SnSe+$SnSe_2$ have higher etching rate than SnS_2+SnS and $SnSe_2$ thin films. This may indicate that it is easier to etch SnS and SnSe than SnS_2 and $SnSe_2$. In the right picture it is shown that the CZTSSe thickness is unaffected by the etching process, among the error of the XRF measurements. This experiment, clearly show that yellow $(NH_4)_2S$ etching is very selective to remove Sn-S and Sn-Se secondary phases, especially for SnS and SnSe phases on CZTSSe thin films.

Part 3 Improvements in optoelectronic properties and mechanism discussion

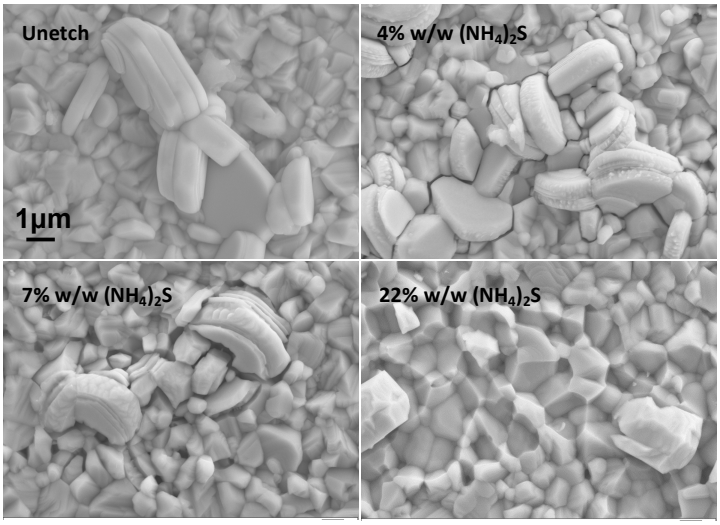

Figure S5. SEM pictures of etched solid solution CZTSSe(S/(S+Se)=0.5) with different concentrations of $(NH_4)_2S$ aqueous solutions

Figure S5 shows the SEM pictures of etched CZTSSe with different concentrations of $(NH_4)_2S$ aqueous solutions. From the picture we can see that before etch, there are some plate-like secondary phases on top. EDS measurements confirm that they are Sn(S,Se). If looking carefully we can find that these plate-like secondary phases have some layered structure, which is consistent with the fact that SnSe and SnS are layered structure compounds [Supp3]. After 4% w/w $(NH_4)_2S$ etch for 1 min, Sn(S,Se) seems to be only slightly dissolved. When the concentration of $(NH_4)_2S$ is increased to 7% w/w, it seems that more Sn(S,Se) was dissolved. However, after 22% w/w $(NH_4)_2S$ etch for 1 min, almost all the Sn(S,Se) disappeared from the surface. This experiment clearly shows that 22% w/w yellow $(NH_4)_2S$ is more efficient to etch Sn(S,Se) than other low concentrations. This is also supported by optoelectronic properties shown in Table S2. From Table S2 we can see that after 4% or 7% w/w $(NH_4)_2S$ etch, the efficiency does not change significantly. However, after 22% $(NH_4)_2S$ etch, J_{sc}, V_{oc} and FF all increase and in consequence, the efficiency increases from 3.3% to 4.4%.

Table S2. Optoelectronic properties of etched CZTSSe with different concentrations of yellow $(NH_4)_2S$ aqueous solutions.

Name	**Etching process**	**J_{sc} (mA/cm^2)**	**V_{oc} (mV)**	**FF(%)**	**EFF.(%)**
DPK150713-3	unetched	20.6	365	44.3	3.3
	4% w/w $(NH_4)_2S$	21.2	360	40.9	3.1
	7% w/w $(NH_4)_2S$	20.2	361	42	3.1
	22% w/w $(NH_4)_2S$	22.8	393	49.3	4.4

Finally, from the IPCE data we estimate the J_{sc} values for the different cells, comparing them with the values obtained from the analysis of the illuminated JV curves. Table S3 shows the comparison of J_{sc} from J-V curves with that estimated from EQE for CZTSSe1 solar cell and best cell before and after $(NH_4)_2S$ etching. We can see that the differences of J_{sc} from J-V and EQE are rather small, indicating that the influence of light induced defects are limited in these devices and the J-V and EQE measurements are reliable.

Table S3. Comparison of J_{sc} obtained from external quantum efficiency (EQE) and J-V curves

Sample	**J_{sc} from EQE (mA/cm^2)**	**J_{sc} from JV (mA/cm^2)**	**J_{sc} difference (mA/cm^2)**
CZTSSe1-unetch	21.8	21.1	0.7
CZTSSe1-$(NH_4)_2S$ etch	23.3	22.4	0.9
$(NH_4)_2S$ etch-best cell	27	25.1	1.9

Additional References

[Supp 1] Sharma R.C. ; Chang Y.A. The S− Sn (Sulfur-Tin) System. *Bull. Alloy Phase Diagrams* **1986**, *7*, 269-273.

[Supp 2] Sharma R.C. ; Chang Y.A. The Se− Sn (Selenium-Tin) System. *Bull. Alloy Phase Diagrams* **1986**, *7*, 68-72.

[Supp 3] Valiukonis G.; Guseinova D. A.; Krivaitb G.; Sileika A. Optical Spectra and Energy Band Structure of Layer-type $A^{IV}B^{VI}$ Compounds**.** *Phys. Status Solidi B* **1986**, *135*, 299-307.

ACS APPLIED MATERIALS & INTERFACES

Research Article

www.acsami.org

Impact of Na Dynamics at the $Cu_2ZnSn(S,Se)_4$/CdS Interface During Post Low Temperature Treatment of Absorbers

Haibing Xie,*[,†] Simon López-Marino,[†] Tetiana Olar,[‡] Yudania Sánchez,[†] Markus Neuschitzer,[†] Florian Oliva,[†] Sergio Giraldo,[†] Victor Izquierdo-Roca,[†] Iver Lauermann,[‡] Alejandro Pérez-Rodríguez,[†,§] and Edgardo Saucedo[†]

[†]Catalonia Institute for Energy Research (IREC), Jardins de les Dones de Negre 1, 08930 Sant Adrià del Besòs, Barcelona, Spain

[‡]Institute Heterogenerous Material Systems, Helmholtz-Zentrum Berlin für Materialien und Energie GmbH, Albert-Einstein-Strasse 15, 12489 Berlin, Germany

[§]IN2UB, Departament d'Electrònica, Universitat de Barcelona, Martí i Franquès, 1-11, 08028 Barcelona, Spain

Supporting Information

ABSTRACT: $Cu_2SnZn(S,Se)_4$ (CZTSSe) solar cells based on earth abundant and nontoxic elements currently achieve efficiencies exceeding 12%. It has been reported that, to obtain high efficiency devices, a post thermal treatment of absorbers or devices at temperatures ranging between 150 and 400 °C (post low temperature treatment, PLTT) is advisable. Recent findings point toward a beneficial passivation of grain boundaries with SnO_x or Cu-depleted surface and grain boundaries during the PLTT process, but no investigation regarding alkali doping is available, even though alkali dynamics, especially Na, are systematically reported to be crucial within the field. In this work, CZTSSe absorbers were subjected to the PLTT process under different temperatures, and solar cells were completed. We found surprisingly behavior in which efficiency decreased to nearly 0% at 200 °C during the PLTT process, being recovered or even improved at temperatures above 300 °C. This unusual behavior correlates well with the Na dynamics in the devices, especially with the in-depth distribution of Na in the active CZTSSe/CdS interface region, indicating the key importance of Na spatial distribution on device properties. We present an innovative model for Na dynamics supported by theoretical calculations and additional specially designed experiments to explain this behavior. After optimization of the PLTT process, a Se-rich CZTSSe solar cell with 8.3% efficiency was achieved.

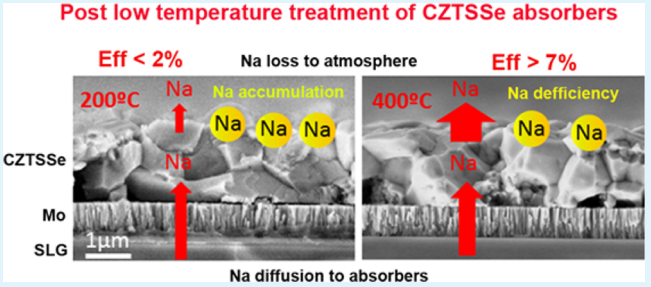

KEYWORDS: *kesterite, $Cu_2ZnSn(S,Se)_4$, thin film, solar cell, sodium, post low temperature treatment (PLTT)*

INTRODUCTION

$Cu_2SnZn(S,Se)_4$ (CZTSSe) solar cells have promising potential as a substitute for the more mature $Cu(In,Ga)Se_2$ (CIGS) solar cells in the mid- or long-term due to their earth abundant and nontoxic constituents. In the last five years, CZTSSe solar cells have developed quickly, starting at 6.8% efficiency in 2009[1] and recently achieving efficiencies exceeding 12%.[2] However, the efficiency is still far below their counterpart CIGS solar cells (21.7%),[3] mainly due to a large V_{oc} deficit (around 600 mV), which is linked to nonoptimized grain boundaries and interfaces.[4] Recently, IBM reported the introduction of a post low temperature treatment (PLTT) of CZTSSe absorbers at 375 °C in air before buffer layer deposition as a key step for high efficiency solar cells exceeding 10%.[5] The efficiency enhancement was ascribed to Cu-depleted and SnO_x-rich grain boundaries. Moreover, an air PLTT of pure selenide $Cu_2SnZnSe_4$ (CZTSe) solar cells at 200 °C for large improvement of performance was reported as well,[6] which correlates the efficiency increase primarily with a Cu-poorer Zn-richer surface and grain boundaries. Additionally, PLTT of pure sulfide Cu_2ZnSnS_4 (CZTS) solar cells or CZTS/CdS was proven to improve efficiency through changing ITO resistivity or forming a heterophase epitaxial junction at the CZTS/CdS interface, respectively.[7,8] Furthermore, another work showed that PLTT of CZTSSe absorbers under inert atmosphere at 200 °C can improve the efficiency considerably due to the increase of Na concentration in the bulk.[9] All this suggests that, independently of the S/Se content, the processes employed, and the characteristics of the solar cell architecture, the absorbers seem to respond distinctly to the PLTT process.

On the other hand, as is well-known, Na is paramount for high efficiency CIGS and CZTSSe solar cells due to passivation of defects in the grain boundaries and interfaces.[10−12] The impact of Na concentration on device properties is frequently reported, and the optimal concentration is considered to be around 0.1 atom %.[13,14] However, the role of Na spatial

Received: December 15, 2015
Accepted: February 2, 2016

DOI: 10.1021/acsami.5b12243
ACS Appl. Mater. Interfaces XXXX, XXX, XXX−XXX

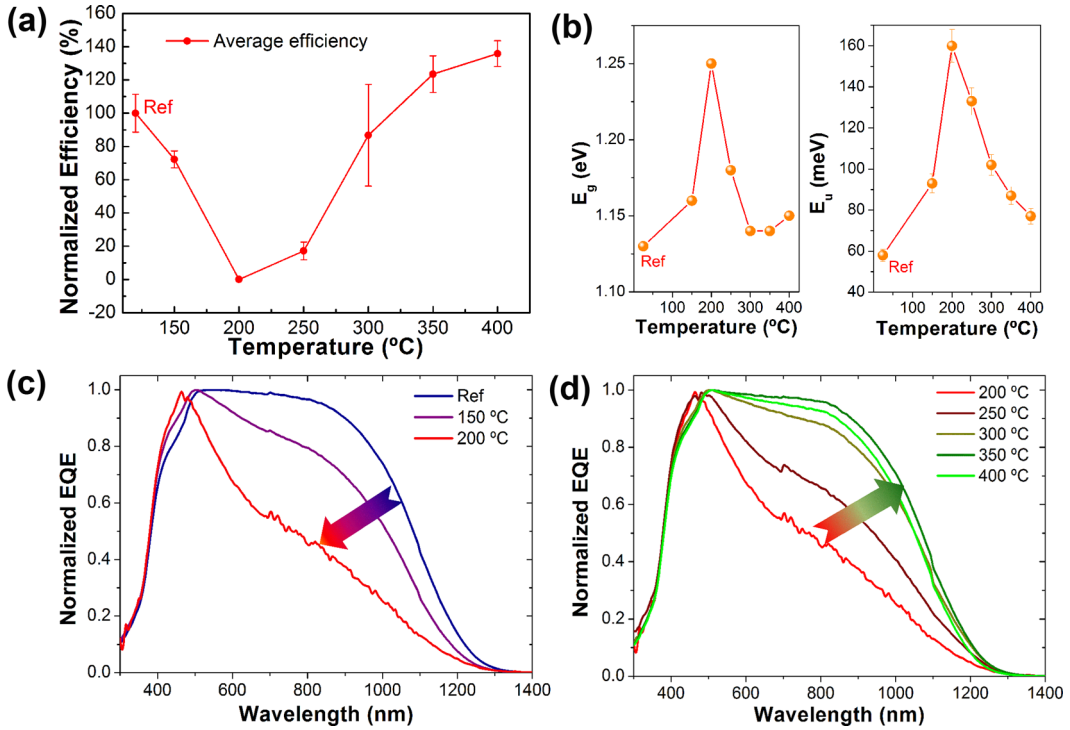

Figure 1. Normalized efficiency evolution with the PLTT temperature, including the standard deviation determined from 9 different cells (a), band gap (E_g) and Urbach energy (E_u) extracted from the EQE curves as a function of the PLTT temperature (b), EQE plots showing the degradation of the devices when submitted to a PLTT process in the range of 150−200 °C (c), and EQE plots showing the recovery of the device properties when submitted to a PLTT process in the range of 200−400 °C (d). Conversion efficiencies are normalized to the reference solar cell (without PLTT process), and EQE is normalized to the highest value of each spectrum, aiming to obtain a better comparison.

distribution, i.e., Na in-depth distribution in absorbers, interfaces, and buffer/window layer, is rarely investigated. Recently, Fjallstrom et al. reported the important role of Na distribution in an active CIGS/CdS interface region during the potential-induced degradation (PID) process,[15] which gives insight into the impact of Na spatial distribution on CIGS solar cell performance.

Na out-diffusion from soda-lime glass (SLG) to absorbers is common during thermal treatment. However, in those PLTT processes mentioned above, although SLG substrates were employed, the influence of Na is either not mentioned or is lacking deeper investigation. Thus, for illustrating the impact of Na during the PLTT process and obtaining insights into Na dynamics, CZTSSe absorbers (Cu/(Zn + Sn) = 0.77−0.83, Zn/Sn = 1.13−1.18, S/(S + Se) = 0.25−0.30) were prepared by a single-step sulfo-selenization process[16] and were then reannealed at temperatures from 150 to 400 °C under 1 bar N_2 atmosphere for 1 h. Solar cells were completed by etching the absorbers in $(NH_4)_2S$ solution[17] following deposition of CdS and the i-ZnO/ITO window layer. The impact of different temperatures during PLTT on the optoelectronic properties, external quantum efficiency (EQE), CZTSSe surface composition, and Na concentration is analyzed. On the basis of the results, an innovative model of Na dynamics is developed to illustrate the performance variation during the PLTT process, showing the key importance of Na spatial distribution control other than Na concentration in this technology.

EXPERIMENTAL SECTION

Preparation of Metallic Precursors. Cu/Sn/Cu/Zn metallic stack precursors were deposited by DC-magnetron sputtering (Ac450 Alliance Concepts) onto Mo-coated soda-lime glass substrates. Precursor films were approximately 600 nm thick with compositional ratios of Cu/(Zn + Sn) around 0.75−0.8 and Zn/Sn around 1.18−1.22. Some precursors were prepared using a nanometric Ge layer on top (10 nm thick) that has been shown to improve the efficiency of the devices[18] to confirm the PLTT effect in this type of absorber.

Preparation of $Cu_2ZnSn(S,Se)_4$ Absorbers. CZTSSe thin films were prepared through a single-step sulfo-selenization of metallic precursors. The singe-step sulfo-selenization was conducted in a graphite box at 550 °C for 30 min under a S + Se + Sn atmosphere with an Ar flow maintained at 1 mbar. To supply the S + Se + Sn atmosphere, two small containers were included inside the graphite box: one with 48 mg of Se plus 2 mg of S mixed powder and the other with 5 mg of Sn.

Post Low Temperature Treatment (PLTT) of Absorbers. A 4.2 × 3.3 cm^2 as-fabricated CZTSSe absorber was immediately cut into 7 pieces equally with 1 as a reference without the PLTT process and the other 6 for PLTT in a quartz boat at temperatures ranging from 150 to 400 °C under 1 bar N_2 atmosphere for 1 h.

Fabrication of Solar Cells. Solar cells were completed by etching the absorbers in 22% w/w $(NH_4)_2S$ solution for 1 min, following chemical bath deposition of 50 nm CdS and DC sputtering (Alliance CT100) of a 350 nm i-ZnO/ITO window layer.

Characterizations. Solar cells with 3 × 3 mm^2 area were scribed. Then illuminated and dark $J-V$ curves (ABET3000 Solar Simulator) and external quantum efficiency (EQE) spectra (B entham PV E300 characterization system) were measured. X-ray diffraction (XRD) (Siemens D500 diffractometer), Raman spectroscopy (532 nm, LabRam HR800-UV Horiba-Jobin Yvon spectrometer), and a scanning electron microscope (SEM) (ZEISS Series Auriga microscope) were employed to investigate the structure and morphology of CZTSSe absorbers. The integral composition of CZTSSe absorbers was checked by X-ray fluorescence (XRF) (Fischerschope XVD). For in-depth composition, especially Na distribution, time-off-flight secondary ion mass spectrometry (TOF-SIMS) was performed on full devices. TOF-SIMS measurements were performed in ION-TOF

DOI: 10.1021/acsami.5b12243
ACS Appl. Mater. Interfaces XXXX, XXX, XXX−XXX

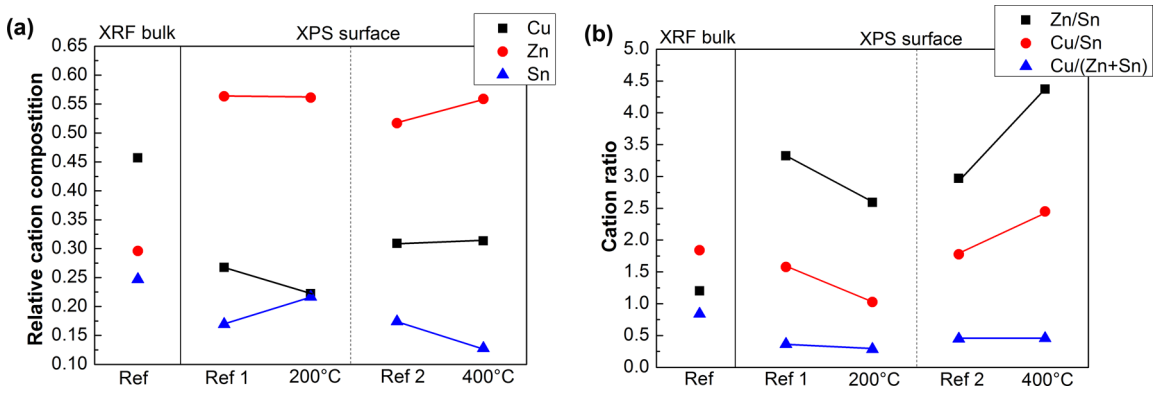

Figure 2. Relative cation composition (a) and cation ratio (b) of CZTSSe samples before and after the 200 and 400 °C PLTT process extracted from XPS data and in comparison with XRF bulk composition data. The reference sample was cut into ref 1 and ref 2 and then annealed at 200 and 400 °C inside the XPS chamber, respectively. XPS was measured before and after annealing for both samples.

IV equipment equipped with a 25 kV Bi cluster primary ion gun for analysis, and O_2 and Cs ion guns for sputtering in-depth profiling modes. The analyzed area was 50 × 50 μm^2 with a cycle time of 100 μs and a time to digital converter (TDC) resolution of 200 ps. For absorber surface composition, high energy X-ray photoelectron spectroscopy (XPS) measurements were performed at the KMC-1 beamline at the electron storage ring BESSY II Berlin (Germany). The high kinetic energy end station (HIKE) allows for tuning the excitation energy (E_{ex}) of the X-ray beam from 2.01 keV up to 12 keV and therefore to increase the information depth from roughly 5 nm up to 25 nm (where information depth is define as three times the mean free path of the excited photoelectrons). All measurements were performed in ultrahigh vacuum (<8.5 × 10^{-9} mbar) using an excitation energy E_{ex} = 3000 eV. Capacitance−voltage ($C-V$) measurements were performed in the dark at room temperature with a frequency of 15 kHz and a modulation voltage of 50 mV using an impedance analyzer from Novocontrol Technologies. From $C-V$ measurements, charge carrier concentration profiles were calculated assuming a relative dielectric permittivity of ε = 8 for CZTSSe.

RESULTS AND DISCUSSION

Figure 1 shows the normalized conversion efficiency, the band gap (E_g), the Urbach energy (E_u), and the normalized EQE spectra as a function of the temperature employed during the PLTT process of CZTSSe absorbers. Device performances are degraded considerably when reannealing temperatures are in the range of 150−200 °C, then recover in the range of 250−300 °C, and finally overpass the reference cell at higher temperatures between 350 and 400 °C (see Figure 1a). Other optoelectronic properties like J_{sc}, V_{oc}, and FF follow almost the same behavior and are shown in the Supporting Information Figure S1. The 500−1200 nm EQE range (related to the CZTSSe/CdS interface and CZTSSe absorber properties) decreases quickly during the PLTT process performed at 150−200 °C; then, the EQE goes back to almost the same level steadily as the as-fabricated cell at 250−400 °C (see Figure 1c and d), which can be considered consistent with the behavior of J_{sc} (see Figure S1). With a deeper analysis of the EQE curves, we can extract two important parameters to further understand the degradation and subsequent recovery of the solar cell performance, the E_g and E_u[19] (see Figure 1b and Figure S2 for the calculation of E_u). The E_g increases from 1.13 eV (ref) to 1.25 eV (200 °C) and then decreases and becomes almost stable at approximately 1.14 eV at higher temperatures. The E_u largely increases from 60 meV for reference sample, reaching a value as high as 160 meV at 200 °C, indicating the creation of a high degree of tail states. This energy is clearly reduced with higher PLTT temperatures, suggesting a strong reduction of the density of recombinative tail states below the band gap, perfectly correlating with the observed improvement of the general device properties. In summary, at 200 °C, the devices efficiency is drastically deteriorated, and the band gap increases together with the formation of a large amount of tail states, whereas at 400 °C, the devices properties recover and even get better than the as-fabricated solar cells. The results show that 200 °C seems to be the critical temperature during PLTT of the CZTSSe samples under the conditions employed for this study. For confirmation of this phenomenon, experiments were repeated to rule out errors or possible accidents during the process. Results of these complementary experiments confirm that PLTT of CZTSSe absorbers under 200 °C degrades the efficiency considerably, whereas at 400 °C, usually 0.8−1.5% absolute higher efficiency could be achieved compared with the reference cells (see Table S1).

For the unusual behavior of CZTSSe solar cell performance during the PLTT process to be understood, the bulk composition, crystalline structure, and morphology of these samples under different PLTT temperatures were analyzed by XRF, XRD, Raman, and SEM. However, no remarkable changes were observed (see Figures S3−S5). Therefore, the variations of the performance could be related to cationic composition change (Cu redistribution) on the surface or in the grain boundaries[5,6] or defect modifications induced by post thermal treatments, i.e., order−disorder, extrinsic doping, and so forth.

The observed E_g variations could be related to Cu−Zn order−disorder of kesterites.[20] However, the effect of order−disorder on optoelectronic properties is controversial. Rey et al. suggest that Zn_{Cu} and Cu_{Zn} defects might not be currently limiting the solar cell efficiency.[21] In contrast, according to Krämmer et al., a decrease in disorder leads to an increased band gap, V_{oc}, and ultimately the efficiency,[22] but the V_{oc} deficit remains unaltered. Nevertheless, here, the performance seems to have a negative relation with the band gap, with the highest band gap correlating with the lowest efficiency at 200 °C, and the V_{oc} deficit increases considerably. Therefore, the order−disorder effect is not likely responsible for the dramatic change in the performance of this work.

To check the composition variations on the surface of CZTSSe absorbers during PLTT process, we conducted XPS measurements. Figure 2 shows the relative cation composition and ratio of CZTSSe samples before and after the 200 and 400

DOI: 10.1021/acsami.5b12243
ACS Appl. Mater. Interfaces XXXX, XXX, XXX−XXX

°C PLTT process extracted from XPS data and in comparison with XRF bulk composition. The anion compositions are almost constant, although they are not shown here (see Figure S6). From Figure 2a, compared with bulk, it is clear that the CZTSSe absorber surface has higher Zn content and lower Cu and Sn content. During the PLTT process, Zn is almost constant up to 200 °C and then increases at 400 °C. In contrast, Cu decreases at 200 °C and then increases at 400 °C. Sn has an opposite behavior with Cu, increasing at 200 °C and then decreasing at 400 °C. These variations in the cation concentration result in a decrease at 200 °C and in an increase at 400 °C for both the Zn/Sn and Cu/Sn ratios (see Figure 2b). The Cu/(Zn + Sn) ratio remains almost unchanged. Cu/(Zn + Sn) around 0.5 and Zn/Sn above 2.5 indicates a very Cu-depleted and Zn-rich surface, which is beneficial for the kesterite solar cell performance due to reduced surface defects and higher V_{oc}.[5,6,23] Nevertheless, the variations of Zn/Sn and Cu/Sn ratios might not necessarily explain the drastic efficiency change, especially for the nearly zero efficiency at 200 °C for Zn/Sn ranging 0.6−3.3, and Cu/Sn ranging 0.7−1.9 on the surface were reported for high efficiency kesterite solar cells,[5,6,23] showing quite different results.

The use of SLG substrates without any chemical barrier layer implies that substrates act as an extrinsic alkali doping source for CZTSSe absorbers. Figure 3 shows the 3D (Figure 3a) and

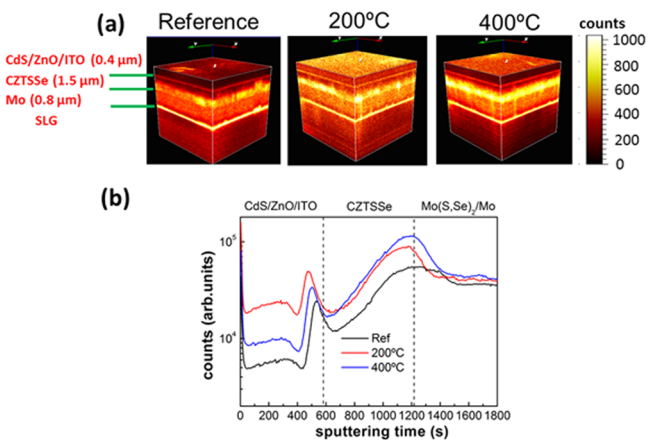

Figure 3. TOF-SIMS of Na concentration in the reference solar cell without PLTT and solar cells with 200 and 400 °C PLTT: (a) 3D TOF-SIMS and (b) 2D TOF-SIMS. Note that the thicknesses corresponding to each layer in the 3D TOF-SIMS pictures are inconsistent with the lengths added in the pictures due to the rough thickness estimation of the TOF-SIMS measurements.

2D TOF-SIMS (Figure 3b) of Na concentration profiles for the as-fabricated solar cells as well as those with 200 and 400 °C PLTT processes. The in-depth distribution of other elements (Cu, Zn, Sn, S, and Se) is not shown here, but no changes are observed among the in-depth resolution of the technique (see Figure S7), which is in agreement with the XRF and Raman results. From the 3D TOF-SIMS images, it is clear that, before the PLTT process, Na mainly accumulates in the interface of Mo/SLG and CZTSSe/Mo. After the PLTT process under 200 °C, Na apparently diffuses from SLG to the absorber to the CZTSSe/CdS interface and even to the buffer and window layer during subsequent device fabrication. Under the 400 °C PLTT process, more Na diffuses to the absorber, whereas less Na can be found in the buffer/window layer compared with that of the 200 °C PLTT. 2D TOF-SIMS profiles show more details regarding the Na profiles. At 200 °C, higher Na concentration in the absorber surface, CZTSSe/CdS interface, and window layer but lower Na concentration in the back of the absorber is observed. In contrast, at 400 °C, lower Na concentration in the upper layer but higher Na concentration in the back of the absorbers is detected. This could correlate with the Cu trends observed by XPS because Na naturally tends to substitute Cu positions in the kesterite structure.[24]

For these results to be understood, it seems reasonable to assume that Na diffuses from the glass to the absorber and is released from the surface to the atmosphere during the PLTT process. Figure 4 shows the schematic of Na dynamics in

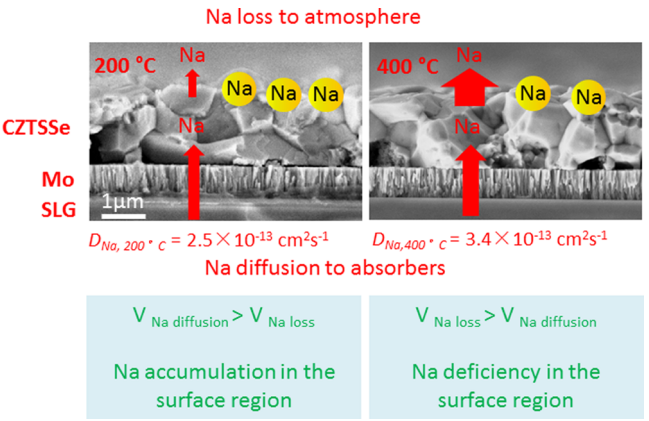

Figure 4. Schematic of Na dynamics during the PLTT process of CZTSSe absorbers.

CZTSSe absorbers during the PLTT process. At 200 °C, the diffusion rate of Na ($V_{Na\ diffusion}$) from the SLG to the absorber is higher than the loss rate of Na ($V_{Na\ loss}$) from the absorber surface to the atmosphere, leading to the accumulation of Na in the surface region. On the other hand, at 400 °C, higher temperature accelerates both $V_{Na\ diffusion}$ and $V_{Na\ loss}$, but it seems that $V_{Na\ loss}$ is more enhanced than $V_{Na\ diffusion}$, thus leading to the relative deficiency of Na in the surface region compared with that at 200 °C. It is important to note that the $(NH_4)_2S$ etching performed on CZTSSe absorbers after the PLTT to complete solar cells could remove Na and related oxides in the first tens of nm on the absorber surface. However, because the Na accumulation or deficiency region is approximately a 300 nm top surface layer (estimated from Figure 3b), the model of Na dynamics should be still valid for illustrating the Na in-depth profiles in the devices.

The empirical model presented above can be supported with additional theoretical calculations using the available experimental data. Considering that Na concentration gradient changes with time, we can estimate the Na diffusion coefficient by applying the second Fick's law. In our theoretical approach, we assume that (1) Na flux diffuses from the region of higher concentration (the substrate) toward the region with lower concentration (the CZTSSe layer) when the PLTT temperature rises, (2) the starting state (i.e., the initial Na concentration gradient) corresponds to the reference sample, and the final state (i.e., the final Na concentration gradient) corresponds to the one related to the PLTT process at a given temperature. Then, the change in concentration corresponding to the PLTT time is equal to the difference between the Na concentration profiles of the reference sample with respect to the samples treated at 200 and 400 °C. In such conditions, as is

DOI: 10.1021/acsami.5b12243
ACS Appl. Mater. Interfaces XXXX, XXX, XXX−XXX

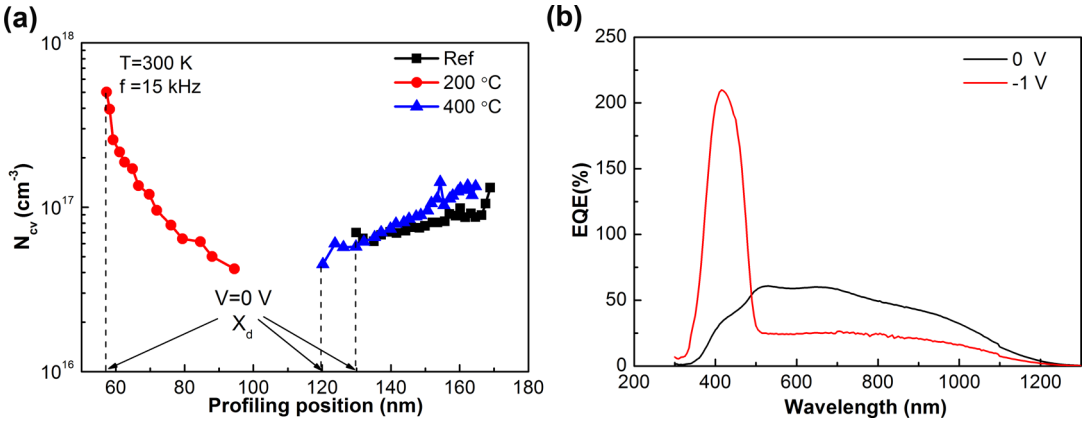

Figure 5. Hole concentration profiles obtained from C−V measurements of reference device and devices treated under 200 and 400 °C PLTT processes (a), and EQE of one representative device under 200 °C PLTT at 0 and −1 V (b).

explained in the Supporting Information, and supposing that the diffusion took place homogeneously by lattice diffusion (due to big grains of the thin films), the concentration of Na across the interfaces can be calculated as

$$c = \frac{c_0}{2(\pi D_t t)^{1/2}} e^{(-x^2/4D_t t)} \quad (1)$$

where c is Na concentration at a distance x from the interface, c_0 is Na concentration in the reference sample, and t is PLTT time. In this case, D_t is the Na diffusion coefficient. Following eq 1 and by plotting lnc vs x^2, we can obtain the following values: $D_{Na,200°C} = 2.5 \times 10^{-13}$ cm^2 s^{-1} and $D_{Na,400°C} = 3.4 \times 10^{-13}$ cm^2 s^{-1} (see Figure 4 and Figure S8). These values are on the same order of the Na diffusion coefficient recently reported for CIGS.[25] This confirms that the Na flux from the substrate is increased with temperature, as is proposed in our phenomenological model. Nevertheless, as was stated, the Na concentration at the surface is unexpectedly lower for the sample treated at 400 °C. Consequently, if theoretical calculations point toward a higher Na flux at higher temperatures, the only plausible cause is that Na is lost from the surface at high temperatures in a large extent due to a higher vapor pressure of possible Na-containing species like Na_2CO_3, Na_2O, $Na_2Se(S)$, $Na_2Se(S)O_3$, and so forth.[26] Unfortunately, vapor pressure data of these compounds are not available in the literature, although it is reasonable to assume that the higher the temperature, the higher the vapor pressure of the Na containing species, and the lower their concentration at the surface. This would explain our findings, confirming the complex Na dynamics in this system.

Figure 5a shows the hole concentration profiles obtained from C−V measurements of the reference device and devices treated under 200 and 400 °C PLTT processes. The hole concentrations of both the reference device and the device under the 400 °C PLTT process present similar values of 5−7 $\times 10^{16}$ cm^{-3}, whereas under the 200 °C PLTT process, the hole concentration of the device increases drastically by one order up to around 5×10^{17} cm^{-3}. Accordingly, the depletion widths (X_d, at zero bias voltage) of the reference and 400 °C-treated device are around 120−130 nm, whereas at 200 °C, the depletion width of the device sharply decreases to approximately 60 nm. This again shows behavior of considerable change of device properties at 200 °C and recovery at 400 °C. The results are consistent with the Na concentration variations obtained by TOF-SIMS shown above.

The efficiency variations during the PLTT process could be correlated with the Na redistribution. As is shown above, device efficiencies are degraded considerably at 200 °C correlating with the increase of tail state density and high level of Na in the absorber surface layer, CZTSSe/CdS interface, and buffer/window layer and then recover and reach even higher values at 400 °C with decreased Na concentration. The top surface of the absorbers (approximately 300 nm top layer), CZTSSe/CdS interface, and buffer/window layer are part of the active region for the formation of the p−n junction. The effect of PLTT on the performance of CZTSSe solar cells in this work is mainly from the change of V_{oc} and FF and partially from the change of J_{sc} (see Table S1). At 200 °C, a high level of Na concentration in the active region could cause severe recombination in the CZTSSe/CdS interface and in the n-type buffer/window layer and change the n-type doping of the layer because Na acts as an acceptor in the CdS and ZnO buffer/window layer.[27,28] Thus, according to the well-known diffusion-drift equilibrium in the p−n junction region, the built-in voltage could be weakened drastically, leading to severe degradation of V_{oc} in CZTSSe solar cells. At 400 °C, less Na in the active region compared with that at 200 °C leads to the recovery of the p−n junction quality and V_{oc}. The V_{oc} increase compared with the reference cells cannot only be related to doping concentration because the devices have similar values as those of the reference cells, although higher Na content was observed in the 400 °C case. Similar carrier concentrations were also reported when different thicknesses of NaF layers were introduced to CZTSe solar cells, being related to a change of intrinsic defects caused by Na.[29] Therefore, the V_{oc} increase could be, among other factors, associated with the passivation of nonradiative defects in the bulk or CZTSSe/CdS interface through an appropriate content of Na.[14,30−33] Furthermore, 400 °C PLTT devices have a Zn-richer surface than the reference devices (see Figure 2), which can decrease the interface recombination and increase V_{oc}.[23,34]

In addition, devices under the 200 °C PLTT process are heavily shunted (see Figure S9). Bias EQE measurements at −1 V for 200 °C PLTT devices show a large EQE increase in the range of 300−500 nm, which implies a drastic change of photoconductivity in the buffer/window layer (see Figure 5b). According to Hsu et al., this sharp increase of EQE in the short wavelength region could be related to shunt paths through the CZTSSe/CdS interface caused by lateral distributed defects induced by an excessive amount of Zn.[35] However, in this work, Zn remains almost constant during PLTT at 200 °C as shown

DOI: 10.1021/acsami.5b12243
ACS Appl. Mater. Interfaces XXXX, XXX, XXX−XXX

by XPS above; thus, an excess of Na in the CZTSSe/CdS interface region could be a possible explanation, leading to the severe degradation of FF. Furthermore, Na could also influence the sub-band gap states in the active region of CZTSSe solar cells,[29] which may be partially responsible for the E_u variations and ultimately have an impact on V_{oc} to a certain extent. The J_{sc} change can be explained by the depletion width and band gap variations as shown by $C-V$ and EQE measurements (see Figures 1 and 5a). In summary, the severe degradation of performance at 200 °C is mainly because of the degradation of V_{oc} and FF due to a possible weakening of built-in voltage and shunting in the interface as well as higher E_u caused by a high concentration of Na in the active CZTSSe/CdS interface region. Note that the 400 °C PLTT devices have the best performance but with medium Na concentration in the active region among these three devices, which indicates the importance of appropriate Na distribution in the CZTSSe/CdS p−n junction region. This also could be explained by the need for an appropriate absorber/emitter doping ratio for highly efficient solar cells.[36]

The crucial role of Na distribution in the active region can be supported by the results of the potential-induced degradation effect on CIGS solar cells.[15,37] The efficiency of CIGS solar cells decreases from more than 15% to nearly zero with an increased Na concentration in the CdS buffer layer and top third of the CIGS absorbers and recovers to the same level of the devices before degradation with a decreased Na concentration. On the basis of the dramatic change of depletion width and the results of replacing the buffer layer, it is speculated that the degraded CIGS solar cells are mainly due to the degradation of CdS and CdS/CIGS interface to the degree that the p−n junction is destroyed and partially by lowering the effective doping in the CIGS absorber because of Na. Another work reported by Sutter-Fella et al. also shows a considerable increase in Na concentration in the active CZTSSe/CdS interface region of CZTSSe solar cells and degraded efficiency when 200 nm NaF was introduced,[38] which is consistent with the results of the 200 °C PLTT process in this work.

Two specially designed experiments further support the model of Na dynamics and its important role on the performance of CZTSSe solar cells: (1) When 10 nm ZnO was introduced onto the Mo surface before metallic precursor deposition and an absorber was completed, the performance of the device was less deteriorated compared with the one without a ZnO barrier layer in the control group under the 200 °C PLTT process. (2) Samples annealed in 1 bar atmosphere degraded considerably, whereas those annealed in 1×10^{-6} bar were nearly unaffected at 200 °C (see Table S2 for details). These results can possibly be explained by the decrease of $V_{Na\ diffusion}$ and increase of $V_{Na\ loss}$ in experiments 1 and 2, respectively, which ultimately leads to less Na accumulation in the active region. It should be noted that the PLTT results in this work are inconsistent with the work reported by Hironiwa et al.,[9] which could be due to the different Na dynamics during reannealing caused by different fabrication processes. Although the present work focuses on Na dynamics during PLTT under inert atmosphere, so far the best efficiency results for CZTSSe solar cells in the literature rely on air PLTT. This would again point toward the relevance of Na dynamics because Na diffusion is enhanced in oxidation processes.[10,30]

On the basis of the better understanding of Na dynamics, after optimization of the single-step sulfo-selenization process, introduction of the optimized PLTT processes, and use of a Ge-doping technology that has been shown to be beneficial for increasing the devices efficiency,[18,39−41] the best conversion efficiencies of 7.1 and 8.3% for Se-rich CZTSSe solar cells were obtained after PLTT of absorbers in N_2 at 400 °C and air atmosphere at 300 °C, respectively (see Figure 6 for $J-V$ curves). The parameters of the 8.3% solar cell are as follows: J_{sc} = 27.4 mA/cm^2, V_{oc} = 466 mV, FF = 64.7%, and E_g = 1.11 eV. Further work is needed to improve the short circuit current by optimizing the window layer and using an antireflective coating.

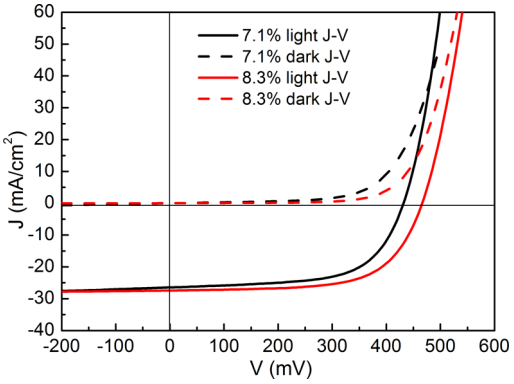

Figure 6. $J-V$ curves of the two champion Se-rich CZTSSe solar cells with conversion efficiencies of 7.1 and 8.3% after PLTT processes of absorbers under N_2 and air atmosphere, respectively.

CONCLUSIONS

In summary, we showed that large variations of device properties of CZTSSe solar cells during the PLTT process can be correlated with different Na concentrations in the active CZTSSe/CdS p−n junction region. Na diffusion from the SLG substrate via the PLTT process seems to largely affect the doping level, but in contrast, it does not exhibit a remarkable impact on the morphology, composition, secondary phases, or grain size of the absorbers. A model of Na dynamics is developed featuring two Na fluxes, including Na diffusion from the SLG to the absorbers and Na loss from the surface to the atmosphere. Depending on the rate of these two fluxes at a given temperature, namely, $V_{Na\ diffusion}$ and $V_{Na\ loss}$, different Na in-depth profiles could be obtained. This model is validated by theoretical calculations, which allows for estimating the Na diffusion coefficient at two key PLTT temperatures: $D_{Na,200°C}$ = 2.5×10^{-13} cm^2 s^{-1} and $D_{Na,400°C}$ = 3.4×10^{-13} cm^2 s^{-1}. Results show that appropriate content of Na doping, especially in the active CZTSSe/CdS interface region of the solar cells, could be critical for device performance, and the PLTT process can be a way to optimize Na in-depth profiles. This may provide new perspectives for the development of high efficiency CZTSSe solar cells.

ASSOCIATED CONTENT

Supporting Information

The Supporting Information is available free of charge on the ACS Publications website at DOI: 10.1021/acsami.5b12243.

Additional characterizations by XRF, XRD, Raman, SEM, XPS, and TOF-SIMS, optoelectronic properties of CZTSSe solar cells in related experiments, and the method for determining the Urbach energy (E_u) and Na diffusion coefficient (D_{Na}) (PDF)

DOI: 10.1021/acsami.5b12243
ACS Appl. Mater. Interfaces XXXX, XXX, XXX−XXX

AUTHOR INFORMATION

Corresponding Author

*E-mail: xhaibing@irec.cat.

Notes

The authors declare no competing financial interest.

ACKNOWLEDGMENTS

The research leading to these results has received funding from MINECO (Ministerio de Economía y Competitividad de España) under the NASCENT project (ENE2014-56237-C4-1-R), funding from the Framework 7 program under the project KESTCELLS (FP7-PEOPLE-2012-ITN-316488), and European Regional Development Founds (ERDF, FEDER Programa Competitivitat de Catalunya 2007−2013). Authors from IREC and IN2UB belong to the M-2E (Electronic Materials for Energy) Consolidated Research Group and the XaRMAE Network of Excellence on Materials for Energy of the "Generalitat de Catalunya". H.X. thanks the "China Scholarship Council" fellowship (CSC No. 201206340113); Y.S. thanks MINECO for the PTA fellowship (PTA2012-7852-A). S.G. is thankful for the FPI fellowship (BES-2014-068533), and E.S. is thankful for the "Ramon y Cajal" fellowship (RYC-2011-09212).

REFERENCES

(1) Katagiri, H.; Jimbo, K.; Maw, W. S.; Oishi, K.; Yamazaki, M.; Araki, H.; Takeuchi, A. Development of CZTS-Based Thin Film Solar Cells. *Thin Solid Films* **2009**, *517*, 2455−2460.

(2) Wang, W.; Winkler, M. T.; Gunawan, O.; Gokmen, T.; Todorov, T. K.; Zhu, Y.; Mitzi, D. B. Device Characteristics of CZTSSe Thin-Film Solar Cells with 12.6% Efficiency. *Adv. Energy Mater.* **2014**, *4*, 1301465.

(3) Jackson, P.; Hariskos, D.; Wuerz, R.; Kiowski, O.; Bauer, A.; Friedlmeier, T. M.; Powalla, M. Properties of $Cu(In,Ga)Se_2$ Solar Cells with New Record Efficiencies up to 21.7%. *Phys. Status Solidi RRL* **2015**, *9*, 28−31.

(4) Kanevce, A.; Repins, I.; Wei, S.-H. Impact of Bulk Properties and Local Secondary Phases on the $Cu_2(Zn,Sn)Se_4$ Solar Cells Open-circuit Voltage. *Sol. Energy Mater. Sol. Cells* **2015**, *133*, 119−125.

(5) Sardashti, K.; Haight, R.; Gokmen, T.; Wang, W.; Chang, L.-Y.; Mitzi, D. B.; Kummel, A. C. Impact of Nanoscale Elemental Distribution in High-Performance Kesterite Solar Cells. *Adv. Energy Mater.* **2015**, *5*, 1402180.

(6) Neuschitzer, M.; Sanchez, Y.; Olar, T.; Thersleff, T.; Lopez-Marino, S.; Oliva, F.; Espindola-Rodriguez, M.; Xie, H.; Placidi, M.; Izquierdo-Roca, V.; Lauermann, I.; Leifer, K.; Pérez-Rodriguez, A.; Saucedo, E. Complex Surface Chemistry of Kesterites: Cu/Zn Reordering after Low Temperature Postdeposition Annealing and Its Role in High Performance Devices. *Chem. Mater.* **2015**, *27*, 5279−5287.

(7) Wang, K.; Gunawan, O.; Todorov, T.; Shin, B.; Chey, S. J.; Bojarczuk, N. A.; Mitzi, D.; Guha, S. Thermally evaporated Cu_2ZnSnS_4 Solar Cells. *Appl. Phys. Lett.* **2010**, *97*, 143508.

(8) Tajima, S.; Asahi, R.; Isheim, D.; Seidman, D. N.; Itoh, T.; Hasegawa, M.; Ohishi, K. Atom-Probe Tomographic Study of Interfaces of Cu_2ZnSnS_4 Photovoltaic Cells. *Appl. Phys. Lett.* **2014**, *105*, 093901.

(9) Hironiwa, D.; Sakai, N.; Kato, T.; Sugimoto, H.; Tang, Z.; Chantana, J.; Minemoto, T. Impact of Annealing Ttreatment before Buffer Layer Deposition on $Cu_2ZnSn(S,Se)_4$ Solar Cells. *Thin Solid Films* **2015**, *582*, 151−153.

(10) Kronik, L.; Cahen, D.; Schock, H. W. Effects of Sodium on Polycrystalline $Cu(In,Ga)Se_2$ and Its Solar Cell Performance. *Adv. Mater.* **1998**, *10*, 31−36.

(11) Urbaniak, A.; Igalson, M.; Pianezzi, F.; Bücheler, S.; Chirilă, A.; Reinhard, P.; Tiwari, A. N. Effects of Na Incorporation on Electrical Properties of $Cu(In,Ga)Se_2$-Based Photovoltaic Devices on Polyimide Substrates. *Sol. Energy Mater. Sol. Cells* **2014**, *128*, 52−56.

(12) Zhou, H.; Song, T.-B.; Hsu, W.-C.; Luo, S.; Ye, S.; Duan, H.-S.; Hsu, C.-J.; Yang, W.; Yang, Y. Rational Defect Passivation of $Cu_2ZnSn(S,Se)_4$ Photovoltaics with Solution-Processed Cu_2ZnSnS_4:Na Nanocrystals. *J. Am. Chem. Soc.* **2013**, *135*, 15998−16001.

(13) Granata, J. E.; Sites, J. R.; Asher, S.; Matson, R. Quantitative Incorporation of Sodium in $CuInSe_2$ and $Cu(In,Ga)Se_2$ Photovoltaic Devices. *IEEE Photovoltaic Spec. Conf., 26th* **1997**, 387−390.

(14) Pianezzi, F.; Reinhard, P.; Chirila, A.; Bissig, B.; Nishiwaki, S.; Buecheler, S.; Tiwari, A. N. Unveiling the Effects of Post-Deposition Treatment with Different Alkaline Elements on the Electronic Properties of CIGS Thin Film Solar Cells. *Phys. Chem. Chem. Phys.* **2014**, *16*, 8843−8851.

(15) Fjallstrom, V.; Szaniawski, P.; Vermang, B.; Salome, P. M. P.; Rostvall, F.; Zimmermann, U.; Edoff, M. Recovery After Potential-Induced Degradation of $CuIn_{1-x}$ Ga_xSe_2 Solar Cells with CdS and Zn(O,S) Buffer Layers. *IEEE J. Photovoltaics* **2015**, *5*, 664−669.

(16) Xie, H.; Dimitrievska, M.; Fontané, X.; Sánchez, Y.; López-Marino, S.; Izquierdo-Roca, V.; Bermúdez, V.; Pérez-Rodríguez, A.; Saucedo, E. Formation and Impact of Secondary Phases in Cu-poor Zn-rich $Cu_2ZnSn(S_{1-y}Se_y)_4$ ($0 \leq y \leq 1$) based solar cells. *Sol. Energy Mater. Sol. Cells* **2015**, *140*, 289−298.

(17) Xie, H.; Sánchez, Y.; López-Marino, S.; Espíndola-Rodríguez, M.; Neuschitzer, M.; Sylla, D.; Fairbrother, A.; Izquierdo-Roca, V.; Pérez-Rodríguez, A.; Saucedo, E. Impact of Sn(S,Se) Secondary Phases in $Cu_2ZnSn(S,Se)_4$ Solar Cells: a Chemical Route for Their Selective Removal and Absorber Surface Passivation. *ACS Appl. Mater. Interfaces* **2014**, *6*, 12744−12751.

(18) Giraldo, S.; Neuschitzer, M.; Thersleff, T.; López-Marino, S.; Sánchez, Y.; Xie, H.; Colina, M.; Placidi, M.; Pistor, P.; Izquierdo-Roca, V.; Leifer, K.; Pérez-Rodríguez, A.; Saucedo, E. Large Efficiency Improvement in $Cu_2ZnSnSe_4$ Solar Cells by Introducing a Superficial Ge Nanolayer. *Adv. Energy Mater.* **2015**, *5*, 1501070.

(19) López-Marino, S.; Sánchez, Y.; Placidi, M.; Fairbrother, A.; Espindola-Rodríguez, M.; Fontané, X.; Izquierdo-Roca, V.; López-García, J.; Calvo-Barrio, L.; Pérez-Rodríguez, A.; Saucedo, E. ZnSe Etching of Zn-Rich $Cu_2ZnSnSe_4$: An Oxidation Route for Improved Solar-Cell Efficiency. *Chem. - Eur. J.* **2013**, *19*, 14814−14822.

(20) Krämmer, C.; Huber, C.; Zimmermann, C.; Lang, M.; Schnabel, T.; Abzieher, T.; Ahlswede, E.; Kalt, H.; Hetterich, M. Reversible Order-Disorder Related Band Gap Changes in $Cu_2ZnSn(S,Se)_4$ via Post-Annealing of Solar Cells Measured by Electroreflectance. *Appl. Phys. Lett.* **2014**, *105*, 262104.

(21) Rey, G.; Redinger, A.; Sendler, J.; Weiss, T. P.; Thevenin, M.; Guennou, M.; El Adib, B.; Siebentritt, S. The Band Gap of $Cu_2ZnSnSe_4$: Effect of Order-Disorder. *Appl. Phys. Lett.* **2014**, *105*, 112106.

(22) Krämmer, C.; Huber, C.; Schnabel, T.; Zimmermann, C.; Lang, M.; Ahlswede, E.; Kalt, H.; Hetterich, M. Order-Disorder Related Band Gap Changes in $Cu_2ZnSn(S,Se)_4$: Impact on Solar Cell Performance. *IEEE Photovoltaic Spec. Conf.* **2015**, 1−4.

(23) Repins, I. L.; Li, J. V.; Kanevce, A.; Perkins, C. L.; Steirer, K. X.; Pankow, J.; Teeter, G.; Kuciauskas, D.; Beall, C.; Dehart, C.; Carapella, J.; Bob, B.; Park, J. S.; Wei, S. H. Effects of Deposition Termination on $Cu_2ZnSnSe_4$ Device Characteristics. *Thin Solid Films* **2015**, *582*, 184−187.

(24) Maeda, T.; Kawabata, A.; Wada, T. First-Principles Study on Alkali-Metal Effect of Li, Na, and K in Cu_2ZnSnS_4 and $Cu_2ZnSnSe_4$. *Phys. Status Solidi C* **2015**, *12*, 631−637.

(25) Laemmle, A.; Wuerz, R.; Schwarz, T.; Cojocaru-Mirédin, O.; Choi, P.-P.; Powalla, M. Investigation of the Diffusion Behavior of Sodium in $Cu(In,Ga)Se_2$ Layers. *J. Appl. Phys.* **2014**, *115*, 154501.

(26) Granath, K.; Bodegård, M.; Stolt, L. The Effect of NaF on $Cu(In, Ga)Se_2$ Thin Film Solar Cells. *Sol. Energy Mater. Sol. Cells* **2000**, *60*, 279−293.

(27) Tell, B. Properties of the Alkalis in CdS. *J. Appl. Phys.* **1971**, *42*, 2919−2924.

DOI: 10.1021/acsami.5b12243
ACS Appl. Mater. Interfaces XXXX, XXX, XXX−XXX

(28) Lin, S. S.; Lu, J. G.; Ye, Z. Z.; He, H. P.; Gu, X. Q.; Chen, L. X.; Huang, J. Y.; Zhao, B. H. P-Type Behavior in Na-Doped ZnO Films and ZnO Homojunction Light-Emitting Diodes. *Solid State Commun.* **2008**, *148*, 25−28.
(29) Gershon, B. T.; Lee, Y. S.; Mankad, R.; Gunawan, O.; Gokmen, T.; Bishop, D.; McCandless, B.; Guha, S. The Impact of Sodium on the Sub-Bandgap States in CZTSe and CZTS. *Appl. Phys. Lett.* **2015**, *106*, 123905.
(30) Gershon, T.; Shin, B.; Bojarczuk, N.; Hopstaken, M.; Mitzi, D. B.; Guha, S. The Role of Sodium as a Surfactant and Suppressor of Non-Radiative Recombination at Internal Surfaces in Cu_2ZnSnS_4. *Adv. Energy Mater.* **2015**, *5*, 1400849.
(31) Lopez-Marino, S.; Sanchez, Y.; Espindola-Rodriguez, M.; Alcobe, X.; Xie, H.; Neuschitzer, M.; Becerril, I.; Giraldo, S.; Dimitrievska, M.; Placidi, M.; Fourdrinier, L.; Izquierdo-Roca, V.; Perez-Rodriguez, A.; Saucedo, E. Alkali Doping Strategies for Flexible and Light-Weight $Cu_2ZnSnSe_4$ Solar Cells. *J. Mater. Chem. A* **2016**, *4*, 1895−1907.
(32) Li, J. V.; Kuciauskas, D.; Young, M. R.; Repins, I. L. Effects of Sodium Incorporation in Co-Evaporated $Cu_2ZnSnSe_4$ Thin-Film Solar Cells. *Appl. Phys. Lett.* **2013**, *102*, 163905.
(33) Yang, K.-J.; Sim, J.-H.; Jeon, B.; Son, D.-H.; Kim, D.-H.; Sung, S.-J.; Hwang, D.-K.; Song, S.; Khadka, D. B.; Kim, J.; Kang, J.-K. Effects of Na and MoS_2 on Cu_2ZnSnS_4 thin-film Solar Cell. *Prog. Photovoltaics* **2015**, *23*, 862−873.
(34) Hsu, W.-C.; Zhou, H.; Luo, S.; Song, T.-B.; Hsieh, Y.-T.; Duan, H.-S.; Ye, S.; Yang, W.; Hsu, C.-J.; Jiang, C.; Bob, B.; Yang, Y. Spatial Element Distribution Control in a Fully Solution-Processed Nanocrystals-Based 8.6% $Cu_2ZnSn(S,Se)_4$ Device. *ACS Nano* **2014**, *8*, 9164−9172.
(35) Hsu, W.-C.; Repins, I.; Beall, C.; DeHart, C.; Teeter, G.; To, B.; Yang, Y.; Noufi, R. The Effect of Zn Excess on Kesterite Solar Cells. *Sol. Energy Mater. Sol. Cells* **2013**, *113*, 160−164.
(36) Scheer, R.; Schock, H. W. *Chalcogenide Photovoltaics: Physics, Technologies, and Thin Film Devices*, 1st ed; WILEY-VCH Verlag & Co. KGaA: Weinheim, 2011.
(37) Vermang, B.; Rostvall, F.; Fjällström, V.; Edoff, M. Potential-Induced Optimization of Ultra-Thin Rear Surface Passivated CIGS Solar Cells. *Phys. Status Solidi RRL* **2014**, *8*, 908−911.
(38) Sutter-Fella, C. M.; Stückelberger, J. A.; Hagendorfer, H.; La Mattina, F.; Kranz, L.; Nishiwaki, S.; Uhl, A. R.; Romanyuk, Y. E.; Tiwari, A. N. Sodium Assisted Sintering of Chalcogenides and Its Application to Solution Processed $Cu_2ZnSn(S,Se)_4$ Thin Film Solar Cells. *Chem. Mater.* **2014**, *26*, 1420−1425.
(39) Bag, S.; Gunawan, O.; Gokmen, T.; Zhu, Y.; Mitzi, D. B. Hydrazine-Processed Ge-Substituted CZTSe Solar Cells. *Chem. Mater.* **2012**, *24*, 4588−4593.
(40) Hages, C. J.; Levcenco, S.; Miskin, C. K.; Alsmeier, J. H.; Abou-Ras, D.; Wilks, R. G.; Bär, M.; Unold, T.; Agrawal, R. Improved Performance of Ge-alloyed CZTGeSSe Thin-Film Solar Cells Through Control of Elemental Losses. *Prog. Photovoltaics* **2015**, *23*, 376−384.
(41) Kim, S.; Kim, K. M.; Tampo, H.; Shibata, H.; Matsubara, K.; Niki, S. Ge-Incorporated $Cu_2ZnSnSe_4$ Thin-Film Solar Cells with Efficiency Greater than 10%. *Sol. Energy Mater. Sol. Cells* **2016**, *144*, 488−492.

DOI: 10.1021/acsami.5b12243
ACS Appl. Mater. Interfaces XXXX, XXX, XXX−XXX

Supporting Information

Impact of Na Dynamics at the $Cu_2ZnSn(S,Se)_4$/CdS Interface During Post Low Temperature Treatment of Absorbers

Haibing Xie[†], Simon López-Marino[†], Tetiana Olar[‡], Yudania Sánchez[†], Markus Neuschitzer[†], Florian Oliva[†], Sergio Giraldo[†], Victor Izquierdo-Roca[†], Iver Lauermann[‡], Alejandro Pérez-Rodríguez[†, §] and Edgardo Saucedo[†]*

[†] Catalonia Institute for Energy Research (IREC), Jardins de les Dones de Negre 1, 08930 Sant Adrià del Besòs,Barcelona, Spain.

[‡] Institute HeterogenerousMaterial Systems, Helmholtz-Zentrum Berlin für Materialien und Energie GmbH, Albert-Einstein-Str. 15, 12489 Berlin, Germany.

[§]IN2UB, Departament d'Electrònica, Universitat de Barcelona, Martí i Franquès, 1-11, 08028 Barcelona, Spain.

**Corresponding author e-mail: xhaibing@irec.cat*

1. **Additional supporting characterization**

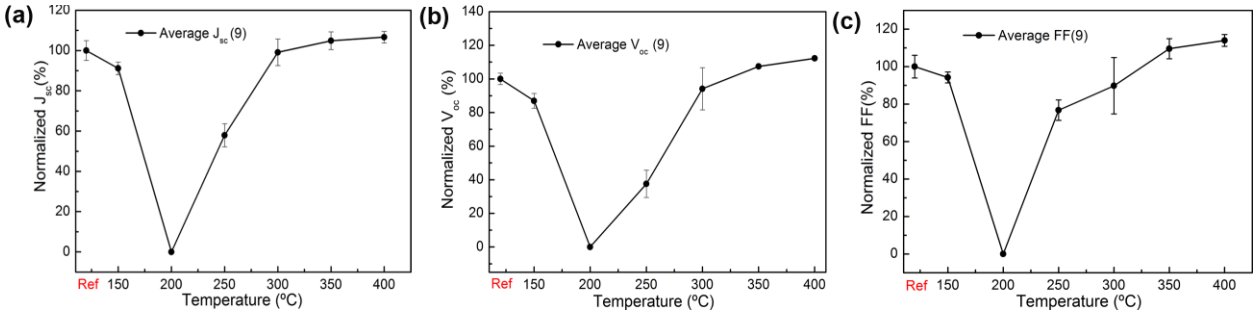

Figure S1. J_{sc} (a), V_{oc} (b) and FF (c) as a function of re-annealing temperature during PLTT process. J_{sc}, V_{oc} and FF are normalized to the values of the reference solar cell, respectively.

Figure S1 shows the evolution of the different optoelectronic parameters complementing the information presented in Figure 1 of the manuscript. Clearly, the devices are almost destroyed at 200 ºC, being recovered at higher temperatures. The J_{sc} seems to be improved around 10% in average, whiles the V_{oc} and FF are improved around 20% in average at 400 ºC. Here J_{sc} is almost zero at 200 ºC while EQE in Figure 1c still suggests some carrier collection at the visible region of the light spectrum. Actually, the sample annealed at 200 ºC was practically a non performing sample, except that only one of the 9 small cells had some photocurrent response under J-V illuminated measurement. To illustrate EQE evolution with PLTT temperature this photo-active small cell was selected, while for J_{sc} comparison the average value of the 9 small cells was employed.

Table S1 shows complementary experiments performed onto different devices, to show the reproducibility of the optoelectronic parameters presented in this manuscript. As a general trend, the results presented here were confirmed in 3 different and independent experiments observing

always a general decrease of the device efficiencies at 200 ºC, and their recovery at higher temperatures.

Table S1. Optoelectronic properties of CZTSSe solar cells without PLTT process (reference cells) and with PLTT of CZTSSe absorbers at 200 and 400 ºC under 1bar N_2 atmosphere.

Batch of experiments	Temperature	J_{sc} (mA/cm^2)	V_{oc} (mV)	FF (%)	Eff. (%)	Average Eff. (9) (%)
1	Ref	23.4	348	44.9	3.7	3.3
	200ºC	0	0	0	0	0
	400ºC	24.5	389	52.1	5.0	4.5
2	Ref	25.1	361	53.3	4.8	4.6
	200ºC	21.0	198	38.0	1.6	1.5
	400ºC	24.3	441	57.2	6.1	6.0
3	Ref	24.2	359	53.2	4.6	4.3
	200ºC	18.1	72.6	32.3	0.4	0.3
	400ºC	23.2	432	58.2	5.8	5.1

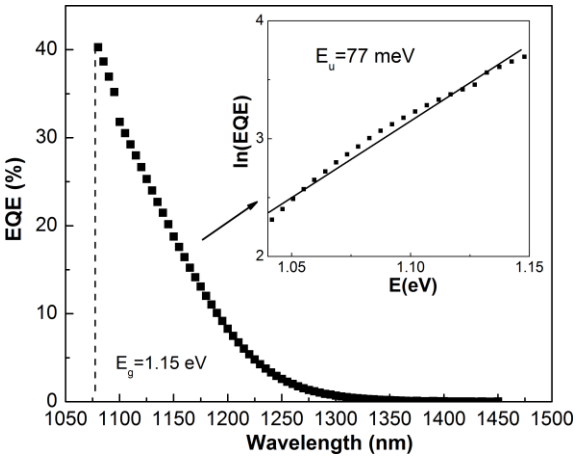

Figure S2. Determination of E_u from EQE spectrum of a CZTSSe device under 400 ºC PLTT process.

Figure S2 shows an example to obtain E_u from EQE spectrum. The device was treated under 400 ºC PLTT process. Urbach energy E_u can be roughly estimated via EQE because the photocurrent generated at photon energy lower than the fundamental band gap can be associated to the carrier excitation from the tail states, which is based on the following equations [supp1,2]:

$$\alpha = \alpha_0 \exp(\frac{E-E_g}{E_u}) \qquad \text{Eq.S1}$$

$$EQE = 1-\exp(-\alpha W) \qquad \text{Eq.S2}$$

Where α is the absorption coefficient, E_g the band gap, E the photon energy, E_u the Urbach energy and W the space charge region width. α_0 is a constant. Applying logarithm in both sides of the equations S1 and S2, we can get:

$$\ln \alpha = \ln\alpha_0 + \frac{E-E_g}{E_u} \qquad \text{Eq.S3}$$

$$\ln(1-EQE) = -\alpha W \qquad \text{Eq.S4}$$

As $0 < EQE < 0.5$, by mathematical approximations we can get:

$$\ln(1-EQE) \approx -EQE \qquad \text{Eq.S5}$$

Thus we have:

$$\ln(EQE) = \ln(\alpha_0 W) + \frac{E-E_g}{E_u} \qquad \text{Eq.S6}$$

By ploting ln(EQE) *vs* E and applying linear fitting, from the slope we can get E_u:

E_u=1/slope Eq.S7

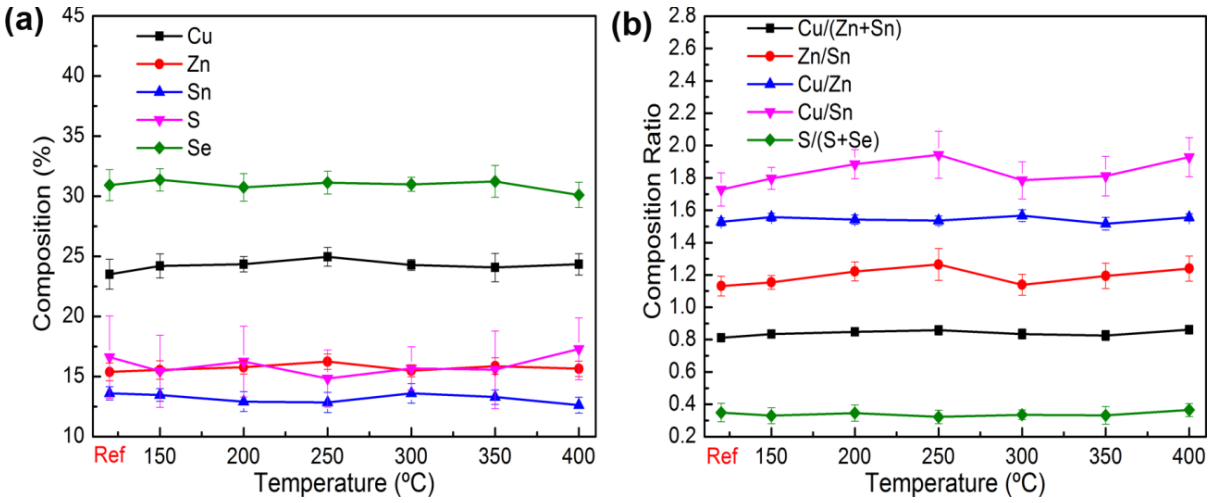

Figure S3. Compositions (a) and ratios (b) of CZTSSe absorbers as a function of re-annealing temperature during PLTT process measured by XRF (the same samples present in Figure 1).

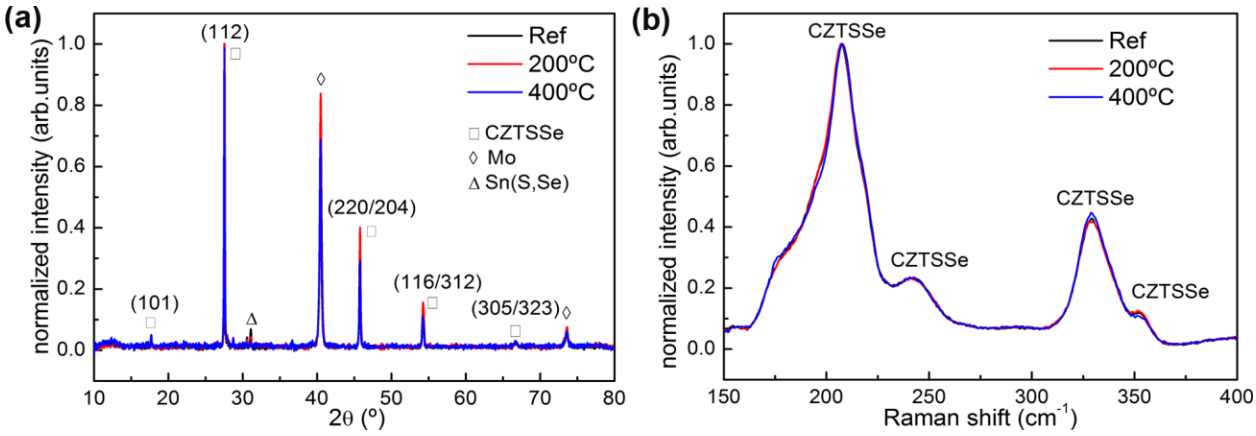

Figure S4. XRD patterns (a) and Raman spectra (532nm) (b) of CZTSSe absorbers without PLTT(reference) and with 200 and 400 ºC PLTT processes**.**

Figure S3 shows the evolution of the concentration of different elements as a function of the PLTT temperatures (average value of 9 positions scattered on the absorber surface of each temperature). Clearly, there are no remarkable changes on the composition, with the probable

exception of Sn concentration that seems to slightly decrease at the highest temperature. This could be related to the well-known Sn loss. Figure S4 shows the XRD patterns and the Raman spectra of three representative samples. These characterizations confirm rather small or even no changes in the layers composition with the PLTT process, and very slight structural changes.

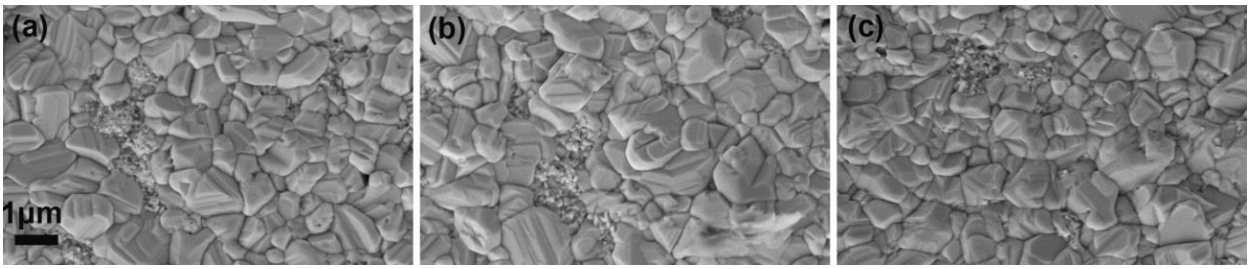

Figure S5. SEM pictures of CZTSSe absorbers without PLTT (a) and with 200 (b) and 400 ºC (c) PLTT process.

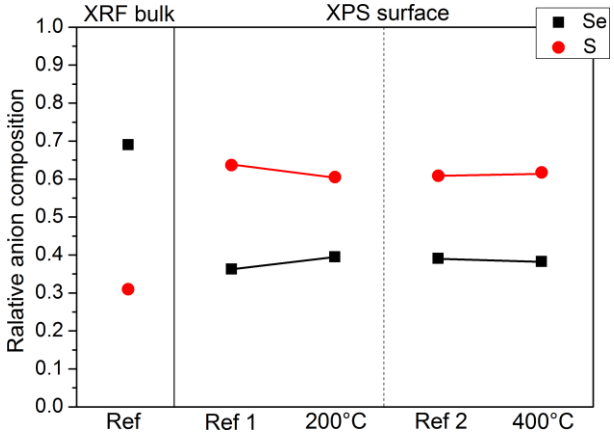

Figure S6. Relative anion composition of CZTSSe samples before PLTT process and after 200 and 400 ºC PLTT process extracted from XPS data and in comparison with XRF bulk composition. The reference sample was cut into ref 1 and ref 2 and then annealed at 200 and 400 ºC inside XPS chamber, respectively. XPS were measured before and after annealing for both samples.

Figure S5 additionally shows that the morphology is almost unaffected by the thermal treatment. Figure S6 shows no remarkable change of S and Se concentration on the surface of CZTSSe absorbers during PLTT processes, which is consistent with the results of Raman spectra.

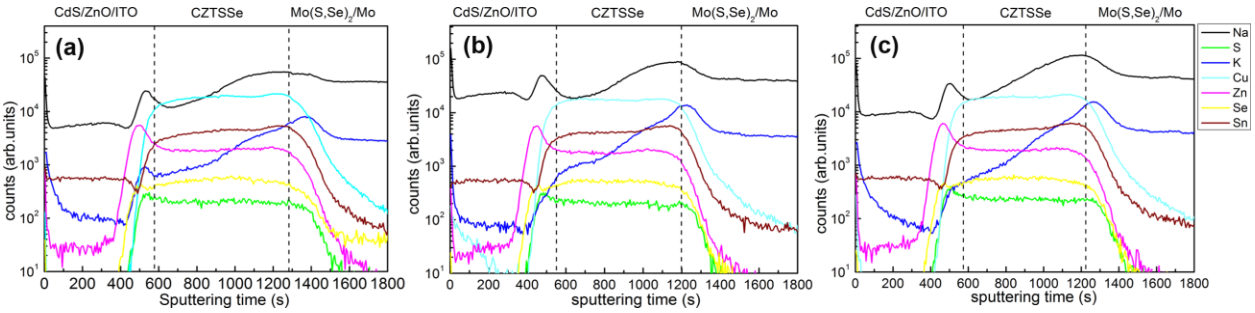

Figure S7. 2D TOF-SIMS profiles of the reference solar cell without PLTT (a) and solar cells with 200 (b) and 400 ºC PLTT processes(c).

Table S2. Optoelectronic properties of CZTSSe solar cells without PLTT process (reference cells) or with PLTT of CZTSSe absorbers under 200ºC, using 10nm ZnO under layer or 1×10^{-6} bar pressure.

Experiments		Samples	J_{sc} (mA/cm^2)	V_{oc} (mV)	FF (%)	Eff.(%)
Control group	1bar	Ref	27.1	334	52.6	4.5
		200 ºC	0.0	0	0.0	0.0
Experiment 1	ZnO under layer	Ref	24.7	362	48	4.3
		200 ºC	20.7	307	41.7	2.6
Experiment 2	1×10^{-6} bar	Ref	23.8	359	49.9	4.3
		200 ºC	21.7	373	48.8	4.0

Figure S7 presents the TOF-SIMS in depth profiles of three representative samples, confirming the rather small variation of Cu, Sn, Zn, Se and S concentrations in agreement with XRF, XRD and Raman results. This suggests that not only the global composition is almost unaffected, but also the in-depth distribution of the main elements does not change in large extent after the PLTT process. The exception is that Na seems to be affected by this thermal process as shown in the manuscript.

2. Determination of Na diffusion coefficient (D_{Na})

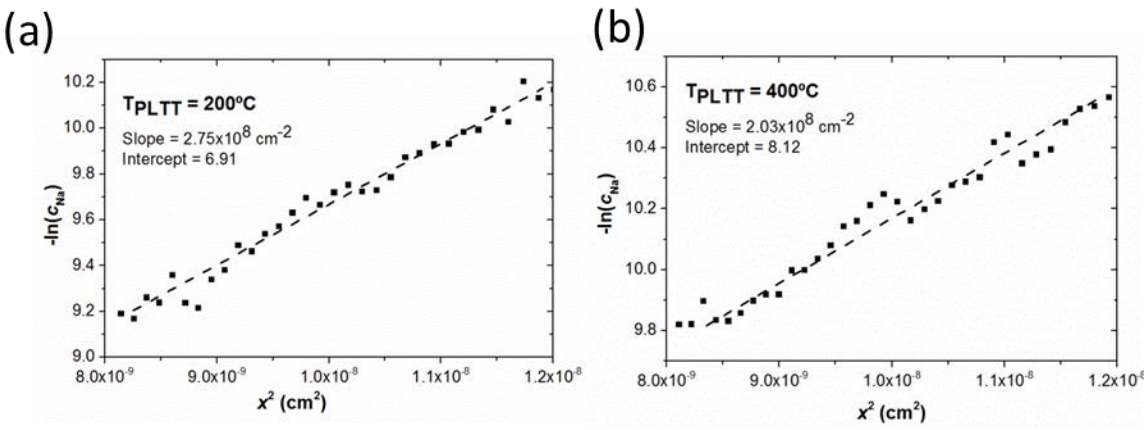

Figure S8. lnc *vs* x^2 curves for the determination of the Na diffusion coefficient at the back region of layers annealed at 200 (a) and 400 ºC (b**).**

For the determination of the Na diffusion coefficient, we assume that Na concentration changes with time during the PLTT process, i.e., that the system is described by the second Fick's law, but that at any given time, the first Fick's law is also applicable. In this work, our background state corresponds to the Na concentration of the reference sample. In consequence, when the PLTT temperature rises (200 or 400 ºC), during the thermal treatment lapse, Na flux diffuses

from the region of higher concentration (the substrate, being the flux j_1), towards the region with lower concentration (the CZTSSe layer, being the flux j_2), across a distance dx. The change in concentration per unit time is proportional to the gradient in the flux at a given position at any time, and can be represented as:

$$\frac{\partial c}{\partial t} = -\frac{\partial j}{\partial x} \quad \text{Eq. S8}$$

Where c is the Na concentration and t *is* the time. Although Na concentration and their corresponding gradient changes with time, we can assume that the first Fick's law is valid at any given time, then combining this law with Eq. S8 we obtain:

$$\frac{\partial c}{\partial t} = -\frac{\partial j}{\partial x} = \frac{\partial}{\partial x}\left(D\frac{\partial c}{\partial x}\right) \quad \text{Eq. S9}$$

Where D is the Na diffusion coefficient. Assuming that D is independent on the Na concentration, then the last equation can be summarized as:

$$\frac{\partial c}{\partial t} = -\frac{\partial j}{\partial x} = D\frac{\partial^2 c}{\partial x^2} \quad \text{Eq. S10}$$

Assuming as well CZTSSe layer as semi-infinite with respect to the Na diffusion zone (we are only considering the first nanometers at the interface of the samples, where the samples thickness is around 1.5 µm), and diffusion as homogeneous, implying that the Na diffusion is mainly controlled by lattice diffusion (grains of Cu-poor layers are very large, i.e. Na diffuses mainly by the Cu vacancies), then Na concentration normal to the interfaces can be expressed by solving Eq. S10 with the corresponding boundary conditions, resulting in:

$$c = \frac{c_0}{2(\pi D_{Na} t)^{1/2}} e^{\left(-x^2/4D_{Na}t\right)} \quad \text{Eq. S11}$$

Where c is Na concentration at a distance x from the interface, c_0 is Na concentration in the reference sample and t is PLTT time. In this case, D_{Na} is the Na diffusion coefficient. Following Eq.S11 and by plotting lnc *vs* x^2, we can determine D_{Na} through the slope of the curve:

$$Slope = -\frac{1}{4D_{Na}\,t} \quad \text{Eq. S12}$$

Then, to determine D_{Na} at both, 200 and 400 ºC, we subtract the Na concentration obtained by TOF-SIMS from the reference sample. This corresponds to the concentration c, i.e., the concentration that has changed due to the Na flux. Using the distance obtained in the TOF-SIMS profiles, it is possible to plot the curves corresponding to the $lnc_{200ºC}$ and $lnc_{400ºC}$, as shown in Figure S8. Using the slope obtained after a linear fitting, D_{Na} can be estimated and is presented in the manuscript.

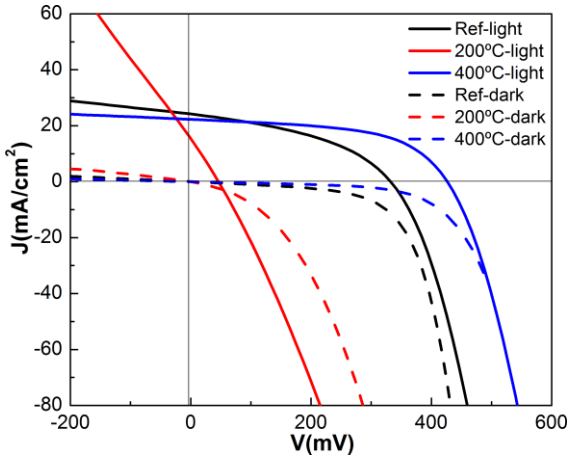

Figure S9. Light and dark J-V curves of the reference solar cells without PLTT and solar cells with 200 and 400 ºC PLTT processes.

Figure S9 shows that solar cells under 200 ºC PLTT are heavily shunted probably due to a high concentration of Na in the active region.

Additional references

[supp1] Sa-Yakanit, V.; Glyde, H.R. Urbach Tails and Disorder. *Comments Condens. Matter Phys.* **1987**, *13*, 35-48.

[supp2] Scragg, J.J.; Dale, P.J.; Peter, L.M.; Zoppi, G.; Forbes, I. New Routes to Sustainable Photovoltaics: Evaluation of Cu_2ZnSnS_4 as an Alternative Absorber Material, *Phys. Status Solidi B* **2008**, *245*, 1772-1778.

Solar Energy Materials & Solar Cells ∎ (∎∎∎∎) ∎∎∎–∎∎∎

Contents lists available at ScienceDirect

Solar Energy Materials & Solar Cells

journal homepage: www.elsevier.com/locate/solmat

Ultra-thin CdS for highly performing chalcogenides thin film based solar cells

Y. Sánchez [a,*], M. Espíndola-Rodríguez [a], H. Xie [a], S. López-Marino [a], M. Neuschitzer [a], S. Giraldo [a], M. Dimitrievska [a], M. Placidi [a], V. Izquierdo-Roca [a], F.A. Pulgarín-Agudelo [b], O. Vigil-Galán [b], E. Saucedo [a]

[a] Catalonia Institute for Energy Research (IREC), Jardin de les Dones de Negre 1, 08930 Sant Adrià de Besòs, Barcelona, Spain
[b] Escuela Superior de Física y Matemáticas-Instituto Politécnico Nacional (IPN), C.P. 07738 México DF, México

ARTICLE INFO

Article history:
Received 31 July 2015
Received in revised form
11 November 2015
Accepted 28 December 2015

Keywords:
CdS:Cu doping
$Cu(In,Ga)Se_2$
$Cu_2ZnSn(S,Se)_4$
Thin film solar cells
MIS structure

ABSTRACT

Ultra-thin CdS layers non intentionally doped and doped with Cu were grown by chemical bath deposition and applied as buffer layers for chalcogenide $CuIn_{1-x}Ga_xSe_2$ and $Cu_2ZnSnSe_4$ (CZTSe) based solar cells. We demonstrate that the use of Cu as dopant allows to reduce the CdS thickness below 30 nm while keeping the same efficiency levels as those obtained with conventional 70 nm in thickness undoped CdS. This is mainly explained by the improved V_{OC} values when Cu-doped CdS is employed, obtaining voltages among the highest reported values, especially for CZTSe devices. We propose the formation of a metal–insulator–semiconductor (MIS) type device for explaining the observed experimental behavior based in indirect optoelectronic characterization of the layers and devices. This opens the possibility to use ultra-thin buffer layers for high efficiency chalcogenide based solar cells, reducing the environmental impact of the CdS buffer deposition, without detrimental impact on the optoelectronic properties of the devices.

1. Introduction

Thin films photovoltaic (PV) technologies, especially those based in chalcogenide compounds (sulfides, selenides and tellurides) are very well positioned to become a real alternative to conventional crystalline and multi-crystalline Si technologies. The excellent absorbing properties of these materials allow for the implementation of photovoltaic devices with absorbers thicknesses below 2 μm, saving materials and reducing the environmental impact of these technologies. Among them, $CuIn_{1-x}Ga_xSe_2$ (CIGS) still holds the highest efficiency (21.7%) [1] in thin-film PV based technologies, achieving efficiencies comparable or even higher than those reported for Si thin film solar cells. Additionally, due to the predicted problems of In and Ga scarcity in CIGS, the interest of the photovoltaic community in $Cu_2ZnSn(S_{1-y}Se_y)_4$ (CZTSSe) absorbers has increased in last years. With a record efficiency of 12.6% [2], this material has already demonstrated a high potential. Nevertheless, this value is still far from those reached with more mature technologies like CIGS and CdTe [3], and is mainly related to the V_{OC} deficit.

Notably, CIGSe and CZTSSe absorbers have several similarities, mainly in device architecture that has led to an effective technological transfer from the know-how developed for CIGSe to the development of CZTSSe. Among these similarities, CdS has shown to have the best properties acting as n-type layer in p–n heterojunction thin films solar cells with both, CIGSe and CZTSSe. There are many scientific papers reporting the CdS production by different physical and chemical techniques. For example, physical vapor deposition (PVD) [4], RF sputtering [5], ion-layer gas reaction (ILGAR) [6], and chemical bath deposition (CBD) [7]. Nevertheless, all the certified world record efficiency for CIGS and CZTSSe were obtained using CdS grown by CBD as buffer layer [3].

In contrast with its excellent properties, CdS has the disadvantage of containing Cd, a very toxic and contaminant element. For this reason, in the last decade, several efforts have been made in the development of cadmium-free buffer layer such as In_2S_3, ZnS, Zn(O,OH)S, $Zn_{1-x}Mg_xO$ and their derivatives [7,8]. However, the obtained efficiencies and the corresponding reproducibility are still far from that of CdS, showing long-term stability problems. Also, these buffers usually require additional activation steps: soft thermal annealing typically at temperatures about 200 °C with the combination of the so-called light soaking (consisting in the exposition of the solar cells to the solar simulator light during long

* Corresponding author.
E-mail address: ysanchez@irec.cat (Y. Sánchez).

http://dx.doi.org/10.1016/j.solmat.2015.12.037
0927-0248/

Table 1
Comparison of some of the best reported efficiencies using different buffer layers for CIGS and CZTSSe solar cells. Here CZTSe, CZTS and CZTSSe denote pure selenide, sulfide and solid solution $Cu_2ZnSn(S,Se)_4$, respectively.

Absorber	Buffer Layer	Efficiency [%]	FF [%]	J_{sc} [mA/cm^2]	V_{oc} [mV]	Reference
CIGS	CdS (CBD)	21.7	79.3	36.6	746	[1]
	CdS (CBD)	20.8	79.1	34.8	757	[9]
	Zn(O,S) (CBD)	19.7	77.8	37.1	683	[10]
	In_xS_y (evaporation)	17.1	74.9	34.8	655	[11]
	$Zn_{1-x}Sn_xO_y$ (ALD)	18.2	75.3	35.1	688.7	[12]
	ZnSe (MOCVD)	11	62.2	36.3	488	[13]
	ZnS(O,OH) (CBD)	18.6	78.2	36.1	660.7	[14]
CZTSSe	CdS (CBD on CZTSe)	11.6	67.3	40.6	423	[15]
	CdS (CBD on CZTSSe)	12.6*	69.8	35.2	513.4	[2]
	CdS(CBD on CZTSe)	8.2	64.4	32.4	392	[16]
	CdS (CBD on CZTS)	9.19	60.0	21.6	708	[17]
	In_2S_3 (CBD on CZTSSe)	7.59	55.0	32.3	424	[18]
	ZnS (CBD on CZTS)	5.85	50.2	19.6	593	[19]
	Zn(O,S) (ALD on CZTS)	4.6	55.5	17.2	482	[20]
	ZnS(O,OH) (CBD on CZTSSe)	5.8	52.0	29.0	389	[21]
	ZnO (USP on CZTS)	4.29	48.0	13.8	650	[22]
	In_2S_3/CdS (CBD on CZTSSe)	12.7	69.8	38.9	466	[23]
	(Zn,Mg)O/CdS (sputtering/CBD on CZTSSe)	10.9	63.7	36.2	470	[24]

* Certificated record efficiency.

Table 2
Optical and structural properties of the two series of CdS layers deposited in this work: varying the growth time and the Cu doping concentration. RMS of the different layers was obtained from the AFM images (see Fig. S2 of the Supporting information).

Buffer	Sample name	Growth time (s)	$[Cu]_{NOM}$ (M)	$[Cu]_{ICP}$ (ppb)	Thickness (nm)	E_g (eV)	RMS (nm)	Pin holes
Undoped CdS	–	20	0	ND	19	2.65	–	YES
	–	30	0	ND	22	2.66	2.05	YES
	–	50	0	ND	26	2.63	2.04	YES
	–	60	0	ND	33	2.64	4.62	YES
	–	180	0	ND	40	2.58	7.65	YES
	–	300	0	ND	49	2.53	19.12	YES
	Ref	420	0	ND	70	2.54	16.69	YES
CdS:Cu	Cu1	420	1×10^{-4}	ND	50	2.49	16.97	NO
	Cu2	420	4×10^{-4}	6	39	2.50	16.79	NO
	Cu3	420	8×10^{-4}	7	37	2.50	17.12	NO
	Cu4	420	1.2×10^{-3}	18	34	2.51	15.63	NO
	Cu5	420	2×10^{-3}	11	27	2.51	18.17	NO
	Cu6	420	5×10^{-3}	9	21	2.52	5.02	FEW

periods of time). Table 1 shows a comparison of some of the best reported cells using different buffer layers for both, CIGS and CZTSSe.

Having in mind that till now CdS has demonstrated unique properties as buffer layer, and its replacement at medium term is not foreseen, one strategy to minimize the Cd content on the final devices could be to go towards extremely thin CdS layers while keeping similar devices performance level. Currently, 50–80 nm thick CdS layers can be considered as a good standard for the CIGS and CZTSSe technologies [25–28]. These thicknesses seem to be the lowest acceptable limit to allow for a good match between performance and good surface coverage without pin holes. Until very recently, a thickness reduction of CdS was coupled to a dramatic decrease of device performance, due to homogeneity problems and pin holes formation when CBD is used in the preparation of extremely thin layers [29]. Nevertheless, recent advances in CIGS surface modification via potassium post deposition treatment (PDT) has allowed for a considerable thickness reduction [30], open the possibility to dramatically reduce the environmental impact of this layer.

In this paper, we present an approach based on the use of Cu as doping agent on the chemical bath during the deposition of CdS, which allows a reduction of the buffer layer thickness, keeping its quality and improving the surface coverage of the absorber. We study the morphological, optical and structural properties of the CdS:Cu layers deposited by CBD showing that, by means of the doping, higher quality layers with reduced pin holes density can be obtained. This allows to effectively reducing the CdS thicknesses from 70 nm to less than 30 nm, in both CIGS and CZTSe technologies, keeping the same highly performing efficiency level. We propose a MIS type structure of the devices for explaining the optoelectronic characteristic of the devices. This proposal is based on two important aspects: (a) the MIS structure model can explain the properties of the cells better than the conventional model based on p–n junction [31–34], and (b) this model is based on the introduction of a very thin insulator layer between a metal and a semiconductor. In our case we assume that the insulating layer is CdS and therefore the model fits the requirement stated above, although further deep investigation of the devices is required.

2. Materials and methods

CIGSe and $Cu_2ZnSnSe_4$ (CZTSe) absorbers were prepared onto Mo coated soda lime glass substrates (SLG/Mo, the thickness of Mo was 800 nm with a resistivity of $R=0.5\ \Omega$/sq) via sequential DC magnetron sputtering deposition (AC450 Alliance Concepts) using Cu, Cu–Ga (50–50%) and In; and Cu, Zn and Sn targets respectively

Please cite this article as: Y. Sánchez, et al., Ultra-thin CdS for highly performing chalcogenides thin film based solar cells, Solar Energy Materials and Solar Cells (2016), http://dx.doi.org/10.1016/j.solmat.2015.12.037

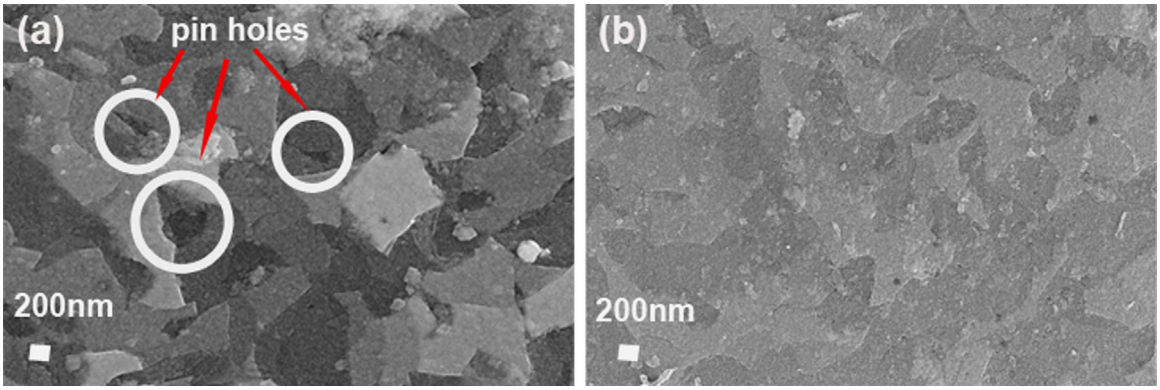

Fig. 1. SEM images of the CdS layers grown onto glass. Undoped CdS (a) and Cu6 (b). For both layers the deposition time was 420 s. Big pin holes are marked with white circles in the undoped CdS layer. Those pin holes are not observed at all when the layer is intentionally doped with Cu.

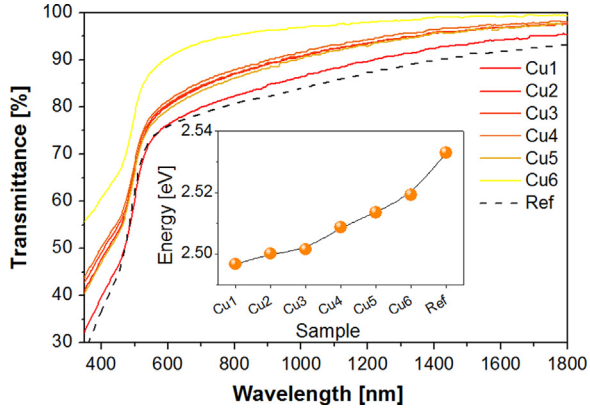

Fig. 2. Transmittance of the different Cu-doped CdS layers, and evolution of the band-gap as a function of the nominal Cu concentration in the bath (inset). The same figure for the deposition time series layers is presented in the Supporting information for comparison.

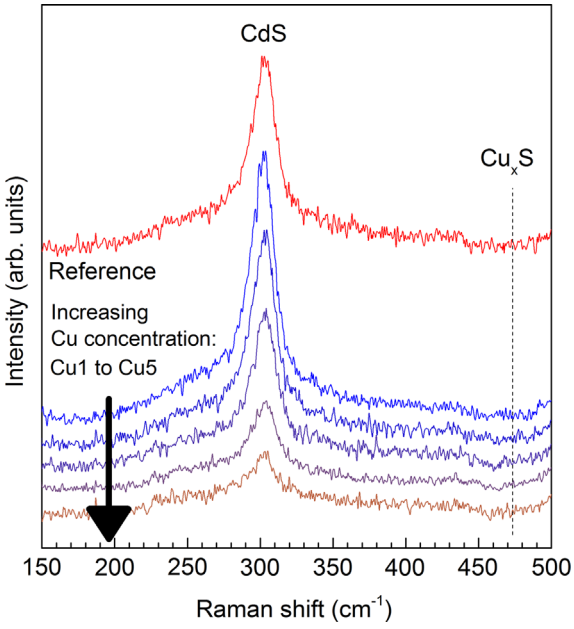

Fig. 3. Raman spectra of CdS:Cu samples with different Cu concentrations grown onto soda lime glass (SLG) substrates.

(99.99% purity for all of them). Reactive annealing under Se atmosphere for CIGSe and Se+Sn atmospheres for CZTSe of the sputtered metallic stacks (see Ref. 16 for experimental details) was used to produce the absorbers. The final compositions were: Cu/(In+Ga)=0.90 and Ga/(In+Ga)=0.28 for CIGSe; and Cu/(Zn+Sn)=0.76 and Zn/Sn=1.15 for CZTSe, which were kept constant in this study. After the thermal annealing, the CIGSe absorbers were etched by the classical KCN route (aqueous solution 2% m/V, 25 °C, 120 s) [35] and the CZTSe absorbers were etched using $KMnO_4/Na_2S$ oxidizing etching as was reported elsewhere [36].

CdS and CdS:Cu layers were grown by chemical bath deposition (CBD) in vertical configuration. The chemical bath was composed by: $[CdSO_4]=0.1$ M, $[CH_4N_2S]=0.3$ M, $[NH_4OH]=1.6$ M, pH=9.5 and $T=70$ °C. For the undoped CdS, the thicknesses of the films were varied between 20 nm to 70 nm approximately, by changing the deposition time (from 20 s to 7 min). For the Cu doped samples, $CuSO_4 \cdot 5H_2O$ was added to the solution using six different concentrations: Cu1 = 1×10^{-4} M, Cu2 = 4×10^{-4} M, Cu3 = 8×10^{-4} M, Cu4 = 1.2×10^{-3} M, Cu5 = 2×10^{-3} M and Cu6 = 5×10^{-3} M; whiles keeping the deposition time constant (7 min) (see also Table 2). The CdS layers were grown onto SLG, SLG/Mo/CIGSe and SLG/Mo/CZTSe substrates. The introduction of Cu into the bath seems to accelerate the CdS precipitation, by affecting the deposition kinetic (see Supporting information Fig. S1).

Surface morphology of samples grown onto SLG substrates were analyzed by scanning electron microscopy (SEM, FEI NovaTM NanoSEM 230) using a work distance of 5 mm and an operating voltage of 5 kV and atomic force microscopy (AFM) in tapping and non-contact modes (Park Systems XE-100). Transmission spectra where recorded in the 400–1800 nm wavelength range, using a Perkin Elmer Lambda 950 UV/VIS Spectrometer. The value of the band gap energy gap of the different CdS layers was estimated from the first derivative of the transmittance. Composition and thicknesses were measured with X-ray fluorescence equipment (XRF, Fisherscope XVD). Cu concentration was determined in the as-grown CdS layers using inductively coupled plasma optical emission spectroscopy (ICP-OES) with a Perkin Elmer Optima 3200 RL spectrometer. The obtained films were also characterized by Raman spectroscopy in backscattering configuration using a Raman probe developed at IREC, coupled with an optical fiber to an iHR320 Horiba Jobin Yvon spectrometer. A 532 nm in wavelength diode laser was used as excitation source, studying previously the optimal excitation power density in order to avoid thermal effect in the measurements. All measurements have been calibrated fixing the 520 cm^{-1} Raman shift for the main mode of the Si single crystal spectrum.

Solar cells were fabricated with both CIGSe and CZTSe absorbers, combined with the different undoped and Cu-doped CdS. To complete the solar cells, intrinsic ZnO and SnO_2–In_2O_3 (ITO) films were grown by pulsed DC magnetron sputtering deposition (CT100 Alliance

Please cite this article as: Y. Sánchez, et al., Ultra-thin CdS for highly performing chalcogenides thin film based solar cells, Solar Energy Materials and Solar Cells (2016), http://dx.doi.org/10.1016/j.solmat.2015.12.037

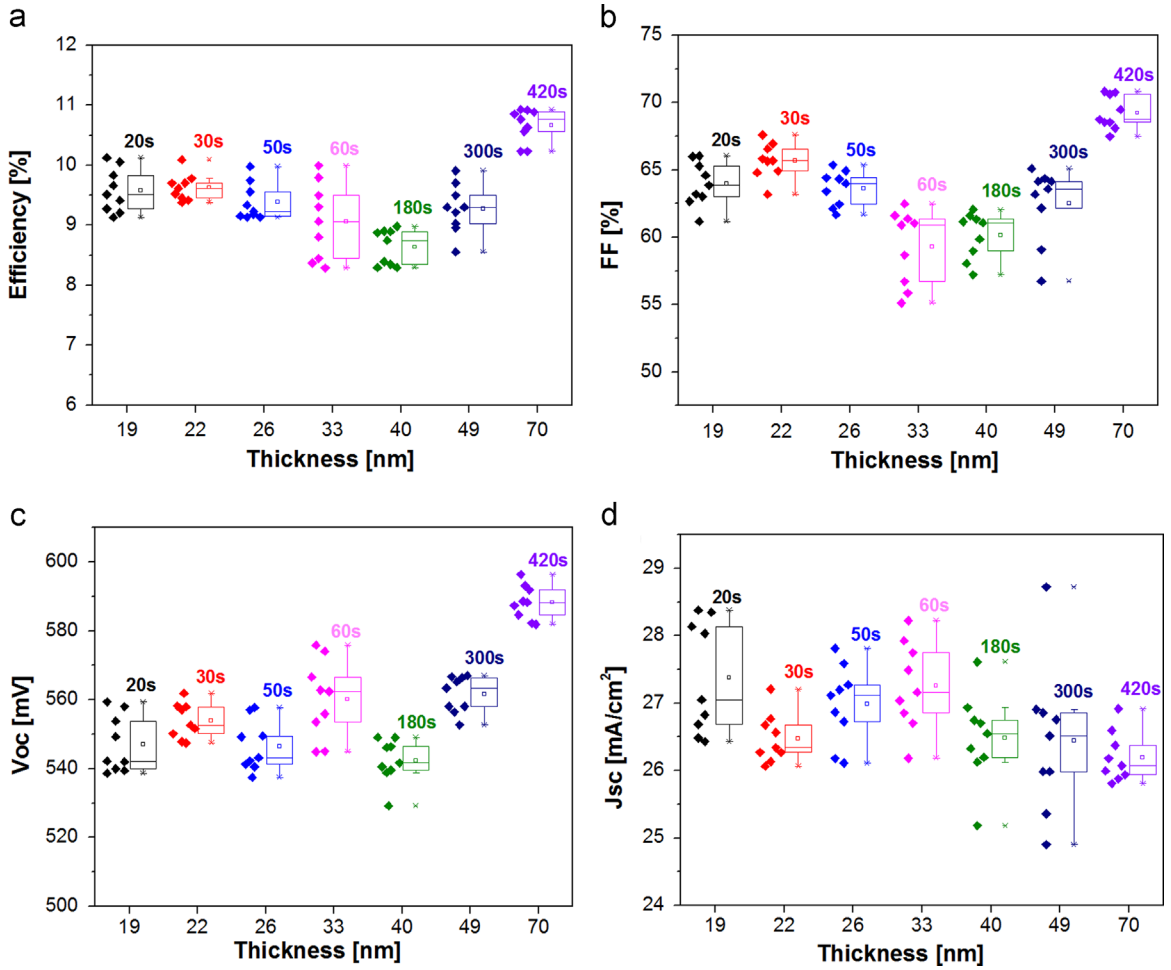

Fig. 4. Optoelectronic parameters of CIGS solar cells with different CdS deposition time: efficiency (a), FF (b), V_{OC} (c) and J_{SC} (d).

Concepts). For the optoelectronic characterization, 3×3 mm^2 cells were scribed using a micro-diamond scriber (MR200 OEG). Measurement of the optoelectronic properties was carried out using a Sun 3000 Class AAA solar simulator from Abet Technologies (uniform illumination area of 15×15 cm^2, AM 1.5 filter) with the previous calibration of the system using a reference Si solar cell, fixing the temperature of the samples to 298 K. The external quantum efficiency (EQE) of the devices was also measured, using a Bentham PVE300 system in the 300–1600 nm wavelength range, and calibrated by using Si and Ge photodiodes.

3. Results and discussion

Table 2 summarizes the main optical and structural properties of the two series of CdS layers deposited in this work: varying the growth time and doping with Cu. As is expected, the deposition time has a strong impact on the CdS layer thicknesses, varying from 70 nm for the standard one (420 s) to 19 nm for the shorter time used in this work (20 s). Similar effect is observed when Cu concentration is increased in the CBD bath, while keeping the deposition time constant at 420 s. By varying the [Cu] in one and half orders of magnitude, it is possible to change the thickness from 50 nm ($[Cu]=1 \times 10^{-4}$ M) to 21 nm ($[Cu]=5 \times 10^{-3}$ M), similarly to the deposition time series.

Unexpectedly, the [Cu] in the layers (measured by ICP-OES) does not follow the nominal concentration of Cu in the CBD bath. First of all, it is important to remark that in all the layers grown without intentionally Cu doping, this element was not detected with the sensitivity of this methodology for Cu (1 ppb approximately). Secondly, whiles the Cu concentration is increased in the bath, their quantity in the layer increases and saturates for a nominal Cu concentration of 1.2×10^{-3} M. Further increments in the solution lead to a saturation of the dopant. Note that, in all cases the doping level is about ppb, i.e. a very low dopant concentration. This corresponds well with the observed changes in the deposition bath. As is shown in the Fig. S1 of the Supporting information, the higher the Cu concentration in the bath, the darker the solution color, suggesting an uncontrolled Cu_xS precipitation that limits the availability of this element for its incorporation in the buffer layer. Aside this, by using Raman spectroscopy, Cu_xS is not detected in the CdS layer (even for the highest Cu concentration in the solution), indicating that this phase precipitates in the bath and is not effectively incorporated in the buffer.

Additionally to the impact on the thicknesses, the Cu doping also has remarkable effects on the morphology of the layers. As is observed in Fig. 1, the undoped CdS layer (Fig. 1(a)) shows some pin holes on the surface typically observed in this material (those morphologies are marked with circles in the figure) [37,38], while CdS:Cu doped layer (Fig.1(b)) exhibits a remarkable improvement on the surface morphology homogeneity and smoother aspect, suggesting that these layers can have better conformal properties to effectively cover both, the CIGSe and CZTSe absorbers. Notably, when Cu is used as dopant, the pin holes density and sizes seem to be effectively removed, that is expected to have a positively impact

Please cite this article as: Y. Sánchez, et al., Ultra-thin CdS for highly performing chalcogenides thin film based solar cells, Solar Energy Materials and Solar Cells (2016), http://dx.doi.org/10.1016/j.solmat.2015.12.037

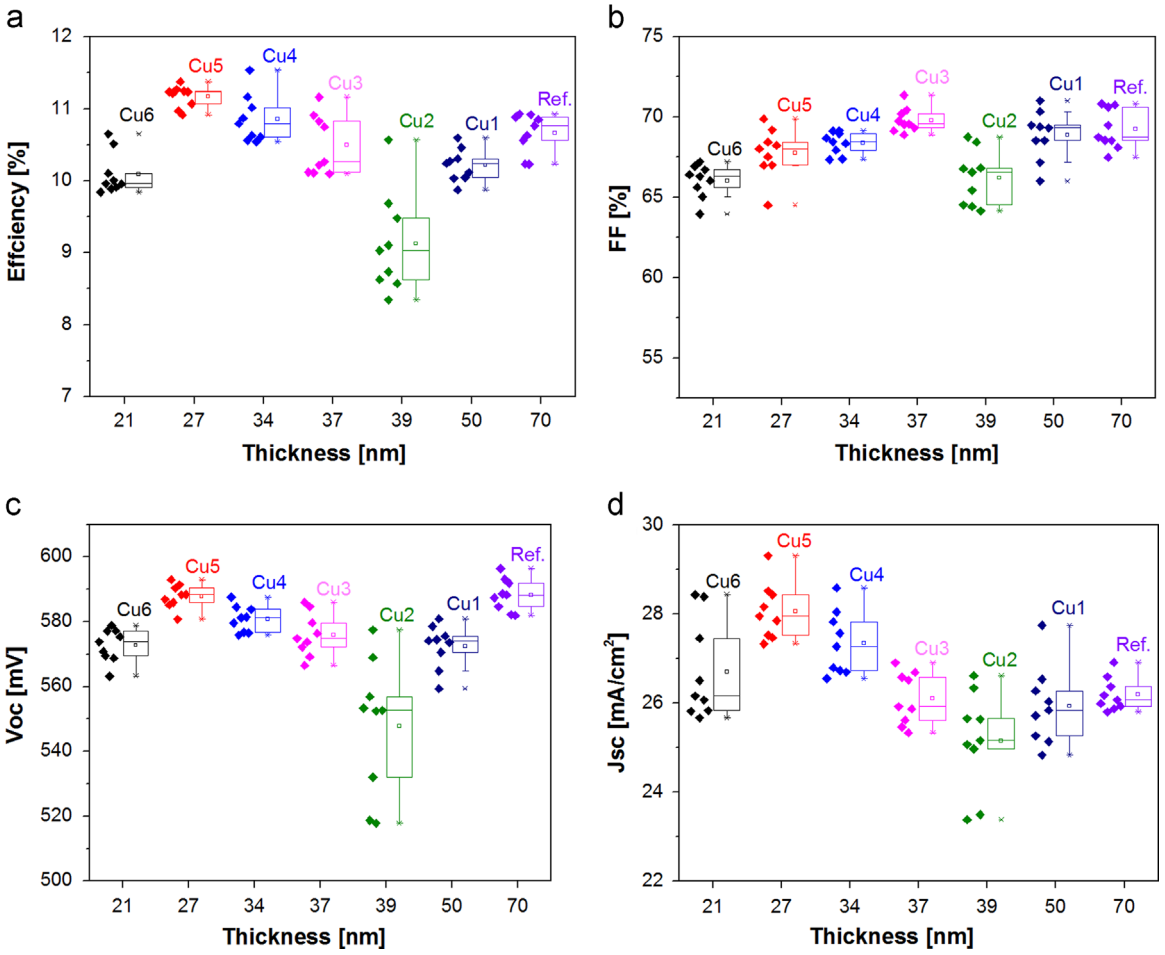

Fig. 5. Optoelectronic parameters of CIGS solar cells with different Cu doping concentration in CdS deposition.

on the properties of the CIGSe/CdS and CZTSe/CdS heterojunctions. Note that here Cu6 sample is selected as representative of the Cu series samples for comparison, since other Cu-doped CdS samples show similar well coverage, whiles undoped layers exhibit always pin holes (see Supporting information Fig. S3). This result is not necessarily transferable to the CdS layers grown onto the absorbers, but it is important to remark that the morphological analysis by SEM of the CdS layer in such case is almost impossible, due to the very thin nature of this layer and the high roughness of the absorber. Nevertheless, these results are quite indicative of the improved morphology of the CdS when Cu is used as dopant.

The deposition time and Cu concentration seem also to impact on the optical properties of the layers. Fig. 2 shows the evolution of the transmittance spectra for the Cu-doped series together with the plot of the corresponding extracted band-gap (inset of the figure). As is observed, the lower the Cu concentration in the bath deposition is, the lower the transmittance of the layer in the whole wavelength region under study is obtained (400–1800 nm). Notably, by increasing the Cu nominal concentration from Cu1 to Cu6, a better transmittance is obtained, with an average 10% higher value. This correlates well with the observed reduced thickness for highly doped buffer layers, but contrast with literature reported data, where higher Cu concentrations as dopant has shown to reduce the CdS transmittance [39]. To better support that the improved transmittance is related to the reduced thickness, a complementary study is presented in Fig. S4 of the Supporting information, which includes the transmission of the undoped layers with varied growth time. If we compare both plots (Figs. 2 and S4), the layers with comparable thicknesses exhibit very similar transmission (for example Cu6 and 30 s or Cu4 and 60 s), supporting our assumption that the transmittance increase is mainly related to the thickness reduction. Additionally, the reduction in the transmission reported in the literature for Cu doped CdS, was obtained with doping levels that are orders of magnitude higher than those reported here [39].

At the same time, for the Cu1 sample, the band gap is reduced (from 2.54 eV for the reference layer, to 2.49 eV). Subsequent increments of the Cu concentration lead to a monotonically minor increase of the band gap (see Table 2). This effect is not well understood yet, but it could be related to either: changes on layers composition (Cd/S ratio) that leads to changes on the fundamental optical parameters (n,k) of the different layers, and/or the grain size reduction as is observed in the AFM surface images of the Supporting information (Fig. S2). This trend is very similar to those previously reported by CdS doped with Ga [40], Sn [41] and Ag [42].

For the deposition time series (see Supporting information Fig. S4), trends of the optical properties are in agreement with the expected behavior. In particular, the lower the deposition time, the thinner the layer, and the higher the transparency of the as grown CdS. With respect to the band gap, a remarkable increase is observed when the deposition time is reduced (and concomitantly the thicknesses too) (see Table 2). Particularly, the band gap increases from 2.54 eV (for the standard 420 s deposition time CdS), towards 2.65 eV (for the thinnest CdS with 20 s of deposition time). This behavior is similar to those observed in the Cu-doped series, i.e. the thinner the layer, the smaller the grain size and the higher the band-gap. Nevertheless, the band-gap of the undoped series samples is about 100–200 meV higher than

Please cite this article as: Y. Sánchez, et al., Ultra-thin CdS for highly performing chalcogenides thin film based solar cells, Solar Energy Materials and Solar Cells (2016), http://dx.doi.org/10.1016/j.solmat.2015.12.037

the typical values reported in the literature (2.41–2.42 eV) [37–41], and the values obtained for the Cu series.

In summary, increasing the nominal Cu concentration in the CBD bath leads to a drastic reduction of the CdS thickness, a better coverage and homogeneity of the layers with few and very small pin holes, whiles the band gap is reduced with respect to the non-doped CdS standard layer. Conversely, the reduction of the deposition time leads to a decrease of the CdS layer thickness as was expected, whiles the band gap of the CdS is increased.

Fig. 3 shows the quasi-resonant Raman spectra obtained in Cu-doped CdS samples prepared onto soda lime glass (SLG) under 532 nm excitation wavelength (2.33 eV). As is observed, the Raman intensity is dominated for the S–S vibrational mode of CdS at 300 cm^{-1} approximately [43], and monotonically decreases with the increasing Cu-doping. This feature, cannot be associated with the increase of the band gap with Cu concentration, because the higher the Cu content, the more similar the band-gap to the reference layer. Presumably, the decrease of the Raman intensity is mainly related to the reduction of the thickness of the layer, more than other optical or structural features.

Cu doped CdS were also prepared onto CZTSe absorbers, and almost no changes of CZTSe A1 peak were observed in the Raman spectra after the CBD process (see Supporting information Fig. S5), confirming that further changes in the optoelectronic parameters are mainly related to the CdS layers, and not associated to changes in the absorber surface due to the slight differences between the bath compositions.

All the layers presented before were implemented in solar cells, using both absorbers: CIGSe and CZTSe. Fig. 4 shows the evolution of the optoelectronic parameters (V_{OC}, J_{SC}, FF and Eff.) for the CIGSe based solar cells obtained with different CdS deposition times, while Fig. 5 shows the same parameters for the solar cells obtained with different Cu doped CdS buffer layers. In the figure, a statistical analysis is presented based in the average and variation coefficient of 9 representative cells for each different CdS.

The reduction of the CdS thickness by decreasing the deposition time has a non-negligible impact on the performance of the CIGSe based solar cells as is clearly observed in Fig. 4. In average, the reduction of the CdS thickness leads to an increase in the J_{SC} of 1.5–2.0 mA/cm^2, in agreement with the better transmittance of the layers and the higher band gap. Nevertheless, the V_{OC} and FF of the devices remarkably decrease. About 50 mV are lost when the CdS thickness is reduced from 70 nm to 20 nm. Also, the FF is reduced 5% in absolute approximately. These two effects can be associated to the formation of pin-holes for the thinner layers, which will directly impact on the FF and V_{OC} [44]. This is also negatively impacting on the solar cells performance where, 1.0–1.5% efficiency in absolute is lost, implying that the strategy to reduce the CdS thickness by reducing the deposition time only, is not enable to keep the same efficiency levels with respect to the 70 nm standard CdS. Apparently, this is a useless strategy to reduce the environmental impact of Cd.

Nevertheless, the behavior is different when Cu-doped CdS is used as buffer layer. As is clearly observed in Fig. 5, by increasing the Cu nominal concentration in the CdS deposition bath (and consequently with the reduction of the CdS thickness), the J_{SC} increases in similar way as observed previously for the deposition time series: the increase is in average between 1.0–2.0 mA/cm^2. Once again, this correlates well with the reduced thickness and increased band gap presented before. But notably, the V_{OC}, FF and efficiency behave differently than the deposition time series. By increasing the Cu concentration (reducing thickness), the FF and V_{OC} seems to be only slightly affected, keeping in average very similar values as those reported for the standard CdS. In particular for the Cu5 CdS layer with a thickness of only 27 nm, the V_{OC} and FF are almost the same than those obtained for the standard non intentionally doped CdS with 70 nm in thickness, whiles the current is a bit higher, and consequently the efficiency of the devices is a bit higher in average (0.5–1.0% higher in absolute).

But, observing more in detail the evolution of the optoelectronic parameters with the Cu concentration, it is important to remark that the efficiency is reduced when a CdS:Cu buffer layer with about 40–50 nm in thickness is used, and after recovered or even improved for higher nominal Cu concentrations (and lower thickness). We propose that this behavior is an indication of the formation of a Metal–Insulator–Semiconductor (MIS) type device. Cu has been revealed as an acceptor dopant in CdS, affecting the resistivity and even changing their conductivity from n to p [45]. In this sense, the CdS:Cu layer with 50 nm in thickness has an increased resistivity (about 7.0×10^4 Ω cm) with respect to the non-doped one (see Table S1 of the Supporting information). This increase in resistivity can be attributed to two effects due to the polycrystalline character of the samples: (i) the compensation effect by donor levels within the CdS grains and (ii) the increase of the intergranular barrier potential due to Cu diffusion into the grain boundaries. In both cases this can create a kind of MIS structure, but this layer is thick enough to introduce a large resistance of the CdS layer and therefore large series resistance in the device that deteriorates the V_{OC} and FF as is observed in Fig. 5. When the thickness of the CdS:Cu layer is reduced to values lower than 30 nm, the resistance of this layer (with resistivity value about 6×10^4 Ω cm) decreases, supporting the model of a MIS structure of

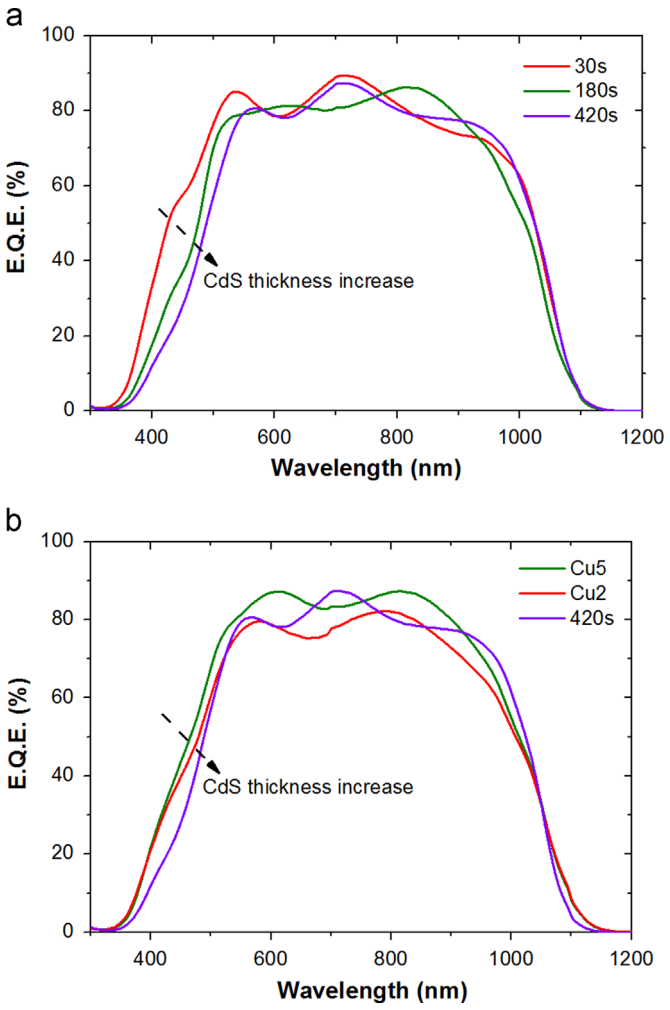

Fig. 6. E.Q.E. plots of the time (a) and Cu concentration (b) series, corresponding to selected cells presented in Figs. 4 and 5.

Please cite this article as: Y. Sánchez, et al., Ultra-thin CdS for highly performing chalcogenides thin film based solar cells, Solar Energy Materials and Solar Cells (2016), http://dx.doi.org/10.1016/j.solmat.2015.12.037

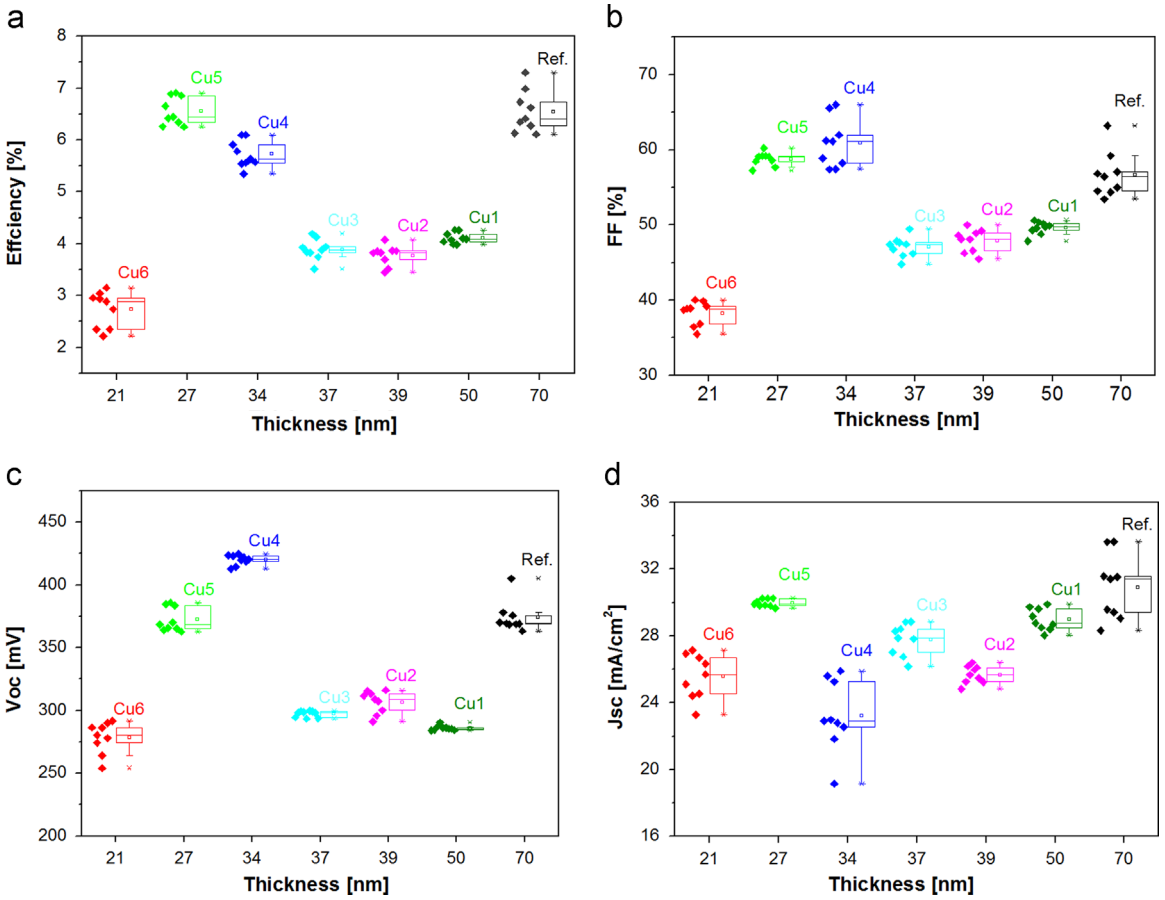

Fig. 7. Optoelectronic parameters for CZTSe solar cells with different Cu doping concentration in CdS deposition.

these devices, although due to the indirect evidences presented here, further analysis to confirm it is required.

This opens very interesting perspectives for this technology, because we demonstrate that it is possible to produce ultra-thin CdS buffer layers by doping with Cu with the concomitant formation of a MIS type device structure, without affecting or even improving the solar cells characteristics. Reducing the CdS thicknesses from 70 nm to 27 nm (or even 21 nm), will strongly affect the environmental foot print of this technology, very positively impacting in the reduction of costs of CIGSe based modules.

Fig. 6 shows the E.Q.E. plots of selected samples from the time (Fig. 6a) and Cu concentration (Fig. 6b) series. Considering that all the layers thicknesses were kept constant, with the exception of the CdS one, the different optical interference patterns observed could be tentatively assigned to the variation of the CdS thickness. As is observed, in the short wavelength region (300–600 nm), the thinner the CdS layer, the higher the E.Q.E. value for both, the time and the Cu concentration series, correlating with the results presented in Figs. 4d and 5d. In this sense, both strategies seem to be valuable for increasing the current of the devices by reducing the CdS thickness. Nevertheless, and as was shown before, the devices fabricated using CdS doped with Cu, exhibit the additional advantage that this current increase is neither affecting the V_{OC}, nor the FF.

The same Cu-doped CdS layers were tested in the incipient CZTSe technology. As is presented in Fig. 7, increasing the Cu concentration till Cu5 (and reducing the thicknesses from 70 nm to 27 nm), the trends of the V_{OC}, FF and J_{SC} is similar to those reported previously for CIGSe. Once again, in the 40–50 nm thickness range, a decrease of the V_{OC} and FF is observed, which are further recovered for lower CdS:Cu thicknesses. It is demonstrated then, that the Cu doping of CdS is a potential way to go towards ultra-thin buffers layers in both CZTSe and CIGSe technologies, that allows to keep very good performance of the solar cells, saving material, and reducing the environmental impact of Cd.

4. Conclusions

The doping of chemical bath deposited CdS with Cu is systematically studied, and the impact on the CIGS/CdS and CZTSe/CdS based devices is reported. The Cu doping seems to strongly affect the properties of CdS. In particular, with increasing the Cu concentration: (i) the thickness of the CdS layer is reduced, (ii) the homogeneity of the layer is improved and the presence of pin holes reduced, (iii) the current density of the solar cells slightly increases, while the V_{OC} and FF is first reduced and after increased, and (iv) the efficiency of the devices is also first reduced and after recovered when the CdS:Cu thickness is changed from 70 nm to 27 nm. This behavior may be associated with the formation of a MIS structure type device, due to the nature of Cu as acceptor dopant into the CdS grains or due to the diffusion of Cu into the grain boundaries, although this hypothesis requires further investigation. We propose the use of CdS doped with Cu, to keep the performance of the devices, allowing for a drastically reduction of the CdS thickness. This can have a remarkable positive impact on the environmental issues of these technologies, contributing to the better acceptance of the society and a reduction of the costs and risks associated to the CIGS and CZTSe devices production.

Acknowledgments

The research leading to these results has received funding from the People Program (Marie Curie Actions) of the European Union's

Seventh Framework Program FP7/2007–2013/ under REA Grant agreement no. 316488 (KESTCELLS) and by European Regional Development Funds (ERDF, FEDER Programa Competitivitat de Catalunya 2007–2013). Authors from IREC and IN2UB belong to the M-2E (Electronic Materials for Energy) Consolidated Research Group and the XaRMAE Network of Excellence on Materials for Energy of the "Generalitat Generalitat de Catalunya". Y.S. thanks the Government of Spain for the PTA fellowship (PTA2012-7852-A), M.E-R. for the FPI-MINECO (BES-2011-045774), S.G. for the FPI fellowship (BES-2014-068533), M.P. for the MINECO postdoctoral fellow (FPDI-2013-18968), and E.S. for the "Ramón y Cajal" fellowship (RYC-2011-09212). H.X. thanks the "China Scholarship Council" fellowship (CSC No. 201206340113). O. Vigil-Galán acknowledges support from COFAA and EDI of IPN and CeMIE-Sol-207450/P26 (SENER-Conacyt).

Appendix A. Supplementary material

Supplementary data associated with this article can be found in the online version at http://dx.doi.org/10.1016/j.solmat.2015.12.037.

References

[1] P. Jackson, D. Hariskos, R. Wuerz, O. Kiowski, A. Bauer, T.M. Friedlmeier, M. Powalla, Properties of Cu(In,Ga)Se_2 solar cells with new record efficiencies up to 21.7%, Phys. Status Solidi RRL 9 (2014) 28–31.

[2] W. Wang, M.T. Winkler, O. Gunawan, T. Gokmen, T.K. Todorov, Y. Zhu, D. B. Mitzi, Device characteristics of CZTSSe thin-film solar cells with 12.6% efficiency, Adv. Energy Mater. 4 (2014) 1301465.

[3] M.A. Green, K. Emery, Y. Hishikawa, W. Warta, E.D. Dunlop, Solar cell efficiency tables (Version 45), Prog. Photovolt.: Res. Appl. 23 (2015) 1–9.

[4] D. Abou-Ras, G. Kostorz, A. Romeo, D. Rudmann, A.N. Tiwari, Structural and chemical investigations of CBD- and PVD-CdS buffer layers and interfaces in Cu(In,Ga)Se_2-based thin film solar cells, Thin Solid Films 280–481 (2005) 118–123.

[5] B.S. Moon, J.H. Lee, H. Jung, Comparative studies of the properties of CdS films deposited on different substrates by R.F. sputtering, Thin Solid Films 511–512 (2006) 299–303.

[6] H.J. Muffler, C.H. Fischer, K. Diesner, M.C. Lux-Steiner, ILGAR – a novel thin-film technology for sulfides, Sol. Energy Mater. Sol. Cells, 67, (2001) 121–127.

[7] N. Naghavi, D. Abou-Ras, N. Allsop, N. Barreau, S. Bü cheler, A. Ennaoui, C.-H. Fischer, C. Guillen, D. Hariskos, J. Herrero, R. Klenk, K. Kushiya, D. Lincot, R. Menner, T. Nakada, C. Platzer-Bjö rkman, S. Spiering, A.N. Tiwari, T. Törndahl, Buffer layers and transparent conducting oxides for chalcopyrite Cu(In,Ga)(S,Se_2 based thin film photovoltaics: present status and current developments, Prog. Photovolt.: Res. Appl. 18 (2010) 411–433.

[8] B. Asenjo, C. Guillén, A.M. Chaparro, E. Saucedo, V. Bermudez, D. Lincot, J. Herrero, M.T. Gutiérrez, Properties of In_2S_3 thin films deposited onto ITO/glass substrates by chemical bath deposition, J. Phys. Chem. Solids 71 (2010) 1629–1633.

[9] P. Jackson, D. Hariskos, R. Wuerz, W. Wischmann, M. Powalla, Compositional investigation of potassium doped Cu(In,Ga)Se_2 solar cells with efficiencies up to 20.8%, Phys. Status Solidi RRL 8 (2014) 219–222.

[10] M. Nakamura, Y. Kouji, Y. Chiba, H. Hakuma, T. Kobayashi, T. Nakada, Achievement of 19.7% efficiency with small-sized Cu(InGa)$(SeS)_2$ solar cells prepared by sulfurization after selenization process with Zn-based buffer, In: Proceedings of the 39th IEEE Photovoltaic Specialists Conference (PVSC), 2013, pp. 0849–0852.

[11] M. Powalla, W. Witte, P. Jackson, S. Paetel, E. Lotter, R. Wuerz, F. Kessler, C. Tschamber, W. Hempel, D. Hariskos, R. Menner, A. Bauer, S. Spiering, E. Ahlswede, T.M. Friedlmeier, D. Blazquez-Sanchez, I. Klugius, W. Wischmann, CIGS cells and modules with high efficiency on glass and flexible substrates, IEEE J. Photovolt. 4 (2014) 440–446.

[12] J. Lindahl, U. Zimmermann, P. Szaniawski, T. Torndahl, A. Hultqvist, P. Salome, C. Platzer-Bjorkman, M. Edoff, Inline Cu(In,Ga)Se_2 co-evaporation for high-efficiency solar cells and modules, IEEE J. Photovolt. 3 (2013) 1100–1105.

[13] S. Siebentritt, T. Kampschulte, A. Bauknecht, U. Blieske, W. Harneit, U. Fiedeler, M. Lux-Steiner, Cd-free buffer layers for CIGS solar cells prepared by a dry process, Sol. Energy Mater. Sol. Cells 70 (2002) 447–457.

[14] M.A. Contreras, T. Nakada, M. Hongo, A.O. Pudov, J.R. Sites, ZnO/ZnS(O,OH)/Cu(In,Ga)Se_2/Mo solar cell with 18.6% efficiency, in: Proceedings of the 3rd World Conference Photovoltaic Energy Conversion (WCPEC), 2003, pp. 570–573.

[15] Y.S. Lee, T. Gershon, O. Gunawan, T.K. Todorov, T. Gokmen, Y. Virgus, S. Guha, $Cu_2ZnSnSe_4$ thin-film solar cells by thermal co-evaporation with 11.6% efficiency and improved minority carrier diffusion length, Adv. Energy Mater. (2015), http://dx.doi.org/10.1002/aenm.201401372.

[16] M. Neuschitzer, Y. Sánchez, S. López-Marino, H. Xie, A. Fairbrother, M. Placidi, S. Haass, V. Izquierdo-Roca, A. Perez-Rodriguez, E. Saucedo, Optimization of CdS buffer layer for high-performance $Cu_2ZnSnSe_4$ solar cells and the effects of light soaking: elimination of crossover and red kink, Prog. Photovolt.: Res. Appl. 23 (2015) 1660–1667, http://dx.doi.org/10.1002/pip.2589.

[17] T. Kato, H. Hiroi, N. Sakai, S. Muraoka, H. Sugimoto, Characterization of front and back interfaces on Cu_2ZnSnS_4 thin-film solar cells, in: Proceedings of the 27th European Photovoltaic Solar Energy Conference and Exhibition, 2012, pp. 2236–2239.

[18] D.A.R. Barkhouse, R. Haight, N. Sakai, H. Hiroi, H. Sugimoto, D.B. Mitzi, Cd-free buffer layer materials on $Cu_2ZnSn(S_xSe_{1-x})_4$: band alignments with ZnO, ZnS, and In_2S_3, Appl. Phys. Lett. 100 (2012) 193904.

[19] H. Hiroi, N. Sakai, S. Muraoka, T. Katou, H. Sugimoto, Development of high efficiency Cu_2ZnSnS_4 submodule with Cd-Free buffer layer, in: Proceedings of the 38th IEEE Photovoltaic Specialists Conference (PVSC), 2012, pp. 001811– 001814.

[20] T. Ericson, J.J. Scragg, A. Hultqvist, J.T. Wätjen, P. Szaniawski, T. Törndahl, C. Platzer-Björkman, Zn(O,S) buffer layers and thickness variation of CdS buffer for Cu_2ZnSnS_4 solar cells, IEEE J. Photovolt. 4 (2014) 465–469.

[21] W. Sun, Y. Deng, J. Liu, W. Liu, Y. Cheng, L. Wang, Y. Gu, Electrochemical behavior and voltammetric determination of p-methylaminophenol sulfate using $LiCoO_2$ nanosphere modified electrode, Thin Solid Films 564 (2014) 379–383.

[22] M.T. Htay, Y. Hashimoto, N. Momose, K. Sasaki, H. Ishiguchi, S. Igarashi, K. Sakurai, K. Ito, A cadmium-free Cu_2ZnSnS_4/ZnO hetrojunction solar cell prepared by practicable processes, Jpn. J. Appl. Phys. 50 (2011) 032301.

[23] J. Kim, H. Hiroi, T.K. Todorov, O. Gunawan, M. Kuwahara, T. Gokmen, D. Nair, M. Hopstaken, B. Shin, Y.S. Lee, W. Wang, H. Sugimoto, D.B. Mitzi, High efficiency $Cu_2ZnSn(S,Se)_4$ solar cells by applying a double In_2S_3/CdS emitter, Adv. Mater. 26 (2014) 7427–7431.

[24] D. Hironiwa, J. Chantana, N. Sakai, T. Kato, H. Sugimoto, T. Minemoto, Application of multi-buffer layer of (Zn,Mg)O/CdS in $Cu_2ZnSn(S,Se)_4$ solar cells, Curr. Appl. Phys. 15 (2015) 383–388.

[25] M.T. Winkler, W. Wang, O. Gunawan, H.J. Hovel, T.K. Todorov, D.B. Mitzi, Optical designs that improve the efficiency of $Cu_2ZnSn(S,Se)_4$ solar cells, Energy Environ. Sci. 7 (2014) 1029–1036.

[26] S. López-Marino, M. Placidi, A. Pérez-Tomás, J. Llobet, V. Izquierdo-Roca, X. Fontané, A. Fairbrother, M. Espíndola-Rodríguez, D. Sylla, A. Pérez-Rodríguez, E. Saucedo, Inhibiting the absorber/Mo-back contact decomposition reaction in $Cu_2ZnSnSe_4$ solar cells: the role of a ZnO intermediate nanolayer, J. Mater. Chem. A 1 (2013) 8338–8343.

[27] A. Bosio, D. Menossi, A. Romeo, N. Romeo, Chapter 4 - Polycrystalline Cu(InGa)Se_2/CdS thin film solar cells made by new precursors, Arturo Morales-Acevedo (Ed.), Solar Cells - Research and Application Perspectives, p. 79, ISBN 978-953-51-1003-3.

[28] K. Orgassa, U. Rau, Q. Nguyen, H.W. Schock, J.H. Werner, Role of the CdS buffer layer as an active optical element in Cu(In,Ga)Se_2 thin-film solar cells, Prog. Photovolt. Res. Appl. 10 (2002) 457–463.

[29] M.A. Contreras, M.J. Romero, B. To, F. Hasoon, R. Noufi, S. Ward, K. Ramanathan, Optimization of CBD CdS process in high-efficiency Cu(In,Ga)Se_2-based solar cells, Thin Solid Films 403–404 (2002) 204–211.

[30] A. Chirilă, P. Reinhard, F. Pianezzi, P. Bloesch, A.R. Uhl, C. Fella, Potassium-induced surface modification of Cu(In,Ga)Se_2 thin films for high-efficiency solar cell, Nat. Mater. 12 (2013) 1107–1111.

[31] M. Courel, J.A. Andrade-Arvizu, O. Vigil-Galán, Loss mechanisms influence on Cu_2ZnSnS_4/CdS-based thin film solar cell performance, Solid-State Electron. 111 (2015) 243–250.

[32] V.G. Karpov, D. Shvydka, Y. Roussillon, Physics of CdTe photovoltaics: from front to back, Mater. Res. Soc. Symp. Proc. 865 (2005) F10.1.1–F10.1.12.

[33] O. Vigil-Galán, A. Arias-Carbajal, R. Mendoza-Pérez, G. Santana-Rodríguez, J. Sastre-Hernández, J.C. Alonso, E. Moreno-García, G. Contreras-Puente, A. Morales-Acevedo, Improving the efficiency of CdS/CdTe solar cells by varying the thiourea/$CdCl_2$ ratio in the CdS chemical bath, Semicond. Sci. Technol. 20 (2005) 819–822.

[34] M. Courel, J.A. Andrade-Arvizu, O. Vigil-Galán, Towards a CdS/Cu_2ZnSnS_4 solar cell efficiency improvement: a theoretical approach, Appl. Phys. Lett. 105 (2014) 2335011–12335014.

[35] B. Canava, O. Roussel, J.F. Guillemoles, D. Lincot, A. Etcheberry, Increasing solar cell efficiencies based on Cu(In,Ga)Se_2 after a specific chemical and oxidant treatment, Phys. Status Solidi C 3 (2006) 2551–2554.

[36] S. López-Marino, Y. Sanchez, M. Placidi, A. Fairbrother, M. Espindola-Rodriguez, X. Fontane, V. Izquierdo-Roca, J. López-García, L. Calvo-Barrio, A. Perez-Rodriguez, E. Saucedo, ZnSe etching of Zn-rich $Cu_2ZnSnSe_4$: an oxidation route for improved solar-cell efficiency, Chem. Eur. J. 19 (2013) 14814–14822.

[37] N.M. Megahid, M.M. Wakkad, E.K. Shokr, N.M. Abass, Microstructure and electrical conductivity of In-doped CdS thin films, Phys. B: Condens. Matter 353 (2004) 150–163.

[38] N.A. Shah, A. Nazir, W. Mahmood, W.A.A. Syed, S. Butt, Z. Ali, A. Maqsood, Physical properties and characterization of Ag doped CdS thin films, J. Alloy. Compd. 512 (2012) 27–32.

[39] N.A. Shah, R.R. Sagar, W. Mahmood, W.A.A. Syed, Cu-doping effects on the physical properties of cadmium sulfide thin films, J. Alloy. Compd. 512 (2012) 185–189.

[40] H. Khallaf, G. Chai, O. Lupan, L. Chow, S. Park, A. Schulte, Characterization of gallium-doped CdS thin films grown by chemical bath deposition, Appl. Surf. Sci. 255 (2009) 4129–4134.

Please cite this article as: Y. Sánchez, et al., Ultra-thin CdS for highly performing chalcogenides thin film based solar cells, Solar Energy Materials and Solar Cells (2016), http://dx.doi.org/10.1016/j.solmat.2015.12.037

[41] A. Jafari, A. Zakaria, Z. Rizwan, M.S. Mohd Ghazali, Effect of low concentration Sn doping on optical properties of CdS films grown by CBD technique, Int. J. Mol. Sci. 12 (2011) 6320–6328.
[42] S.R. Ferrá-González, D. Berman-Mendoza, R. García-Gutiérrez, S.J. Castillo, R. Ramírez-Bon, B.E. Gnade, M.A. Quevedo-López, Optical and structural properties of CdS thin films grown by chemical bath deposition doped with Ag by ion exchange, Optik 125 (2014) 1533–1536.
[43] C. Insignares-Cuello, C. Broussillou, V. Bermúdez, E. Saucedo, A. Pérez-Rodríguez, V. Izquierdo-Roca, Raman scattering analysis of electrodeposited $Cu(In,Ga)Se_2$ solar cells: impact of ordered vacancy compounds on cell efficiency, Appl. Phys. Lett. 105 (2014) 021905.
[44] F. Lisco, P.M. Kaminski, A. Abbas, J.W. Bowers, G. Claudio, M. Losurdo, J. M. Walls, High rate deposition of thin film cadmium sulphide by pulsed direct current magnetron sputtering, Thin Solid Films 574 (2015) 43–51.
[45] Y. Kashiwaba, K. Isojima, K. Ohta, Improvement in the efficiency of Cu-doped CdS/non-doped CdS photovoltaic cells fabricated by an all-vacuum process, Sol. Energy Mater. Sol. Cells 75 (2003) 253–259.

Please cite this article as: Y. Sánchez, et al., Ultra-thin CdS for highly performing chalcogenides thin film based solar cells, Solar Energy Materials and Solar Cells (2016), http://dx.doi.org/10.1016/j.solmat.2015.12.037

Supporting Information

Ultra-thin CdS for highly performing chalcogenides thin film based solar cells

Y. Sánchez[a*], M. Espíndola-Rodríguez[a], H. Xie[a] , S. López-Marino[a], M. Neuschitzer[a], S. Giraldo[a], M. Dimitrievska[a], M. Placidi[a], V. Izquierdo-Roca[a], F.A. Pulgarín-Agudelo[b], O. Vigil-Galán[b], E. Saucedo[a]

[a]*Catalonia Institute for Energy Research (IREC), Jardin de les Dones de Negre 1, 08930 Sant Adrià del Besòs, Barcelona, Spain*
[b]*Escuela Superior de Física y Matemáticas-Instituto Politécnico Nacional (IPN), C.P. 07738, México DF, México*

Email: ysanchez@irec.cat

Figure S1 shows the aspect of both baths, without (undoped CdS, left hand side) and with Cu (CdS:Cu, sample Cu6, right hand side). The pictures were taken after the same reaction time (1 min), highlighting the large differences between the two processes. The introduction of Cu seems to accelerate the precipitation of CdS together with the appearance of a dark brown color powder that we associate with the formation of a Cu_xS precipitate.

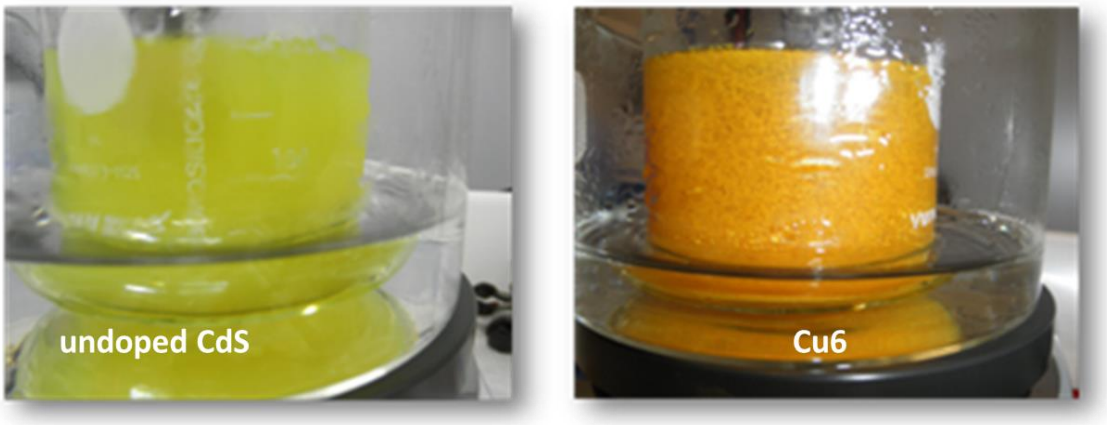

Fig. S1. The introduction of Cu into the bath accelerates the deposition kinetic.

Figure S2 shows the AFM surface images of the different CdS layers deposited onto glass, including the time (upper figures) and Cu (lower figures) series. Analyzing these images we obtain the RMS values presented in the Table 2 of the manuscript. The roughness values are determined from areas of 3×3 μm². As is clear, the lower the deposition time or the higher the Cu concentration, the smaller the grain size of the CdS layer. The thickness is also reduced with the same tendency.

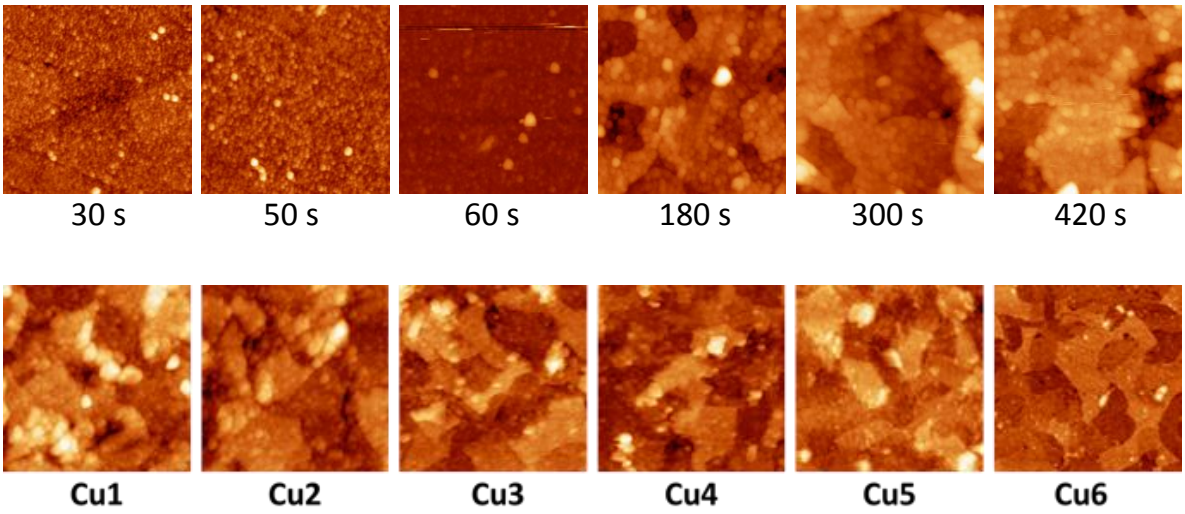

Fig. S2. AFM picture of CdS thin films on SLG with different deposition time (upper) and Cu doping concentration (under).

Figure S3 presents two additional top view SEM images for undoped CdS samples grown onto glass, with 60 s and 300 s of deposition time. Both layers show several pin holes of different size randomly distributed in the whole surface area.

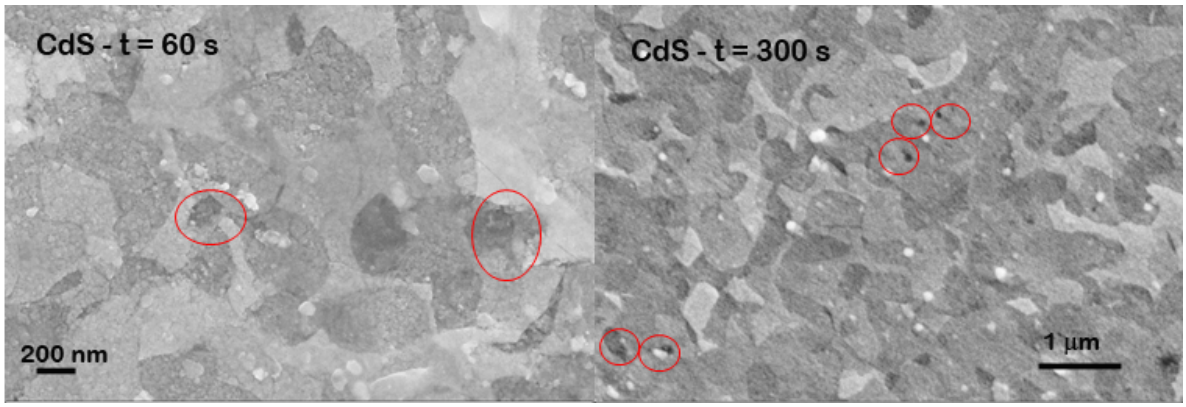

Fig. S3. Top view SEM images of undoped CdS samples with a deposition time of 60s and 300s.

Figure S4 shows the transmittance of the undoped CdS layers deposited with different times. The transmission behaves in the expected way, i.e. the thinner the layer, the higher the transmission in the whole wavelength region. Additionally, the thinner the layer is, the higher the band-gap. As is explained in the manuscript, this can be related to the reduction of the grain size of the CdS.

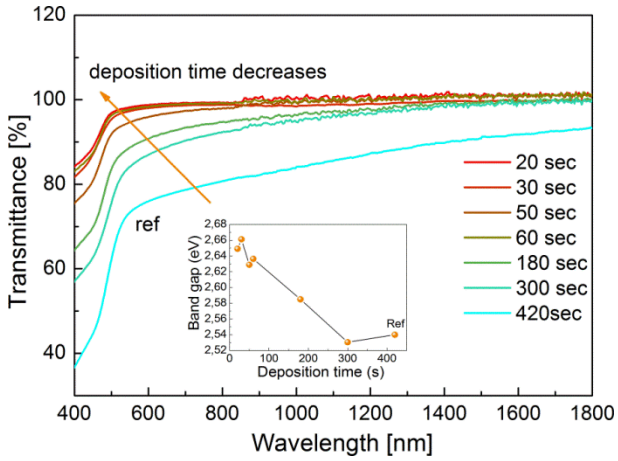

Fig. S4. Transmittance of the CdS layers with different deposition time, and evolution of the band gap as a function of the deposition time in the bath (inset).

Complementary Raman analysis is presented in Fig. S5. Raman spectroscopy is a surface sensitive technique, and this study demonstrates that the Cu-doping has a negligible impact on the CZTSe surface. This implies that we are not modifying the absorber by introducing Cu onto the CdS growth bath.

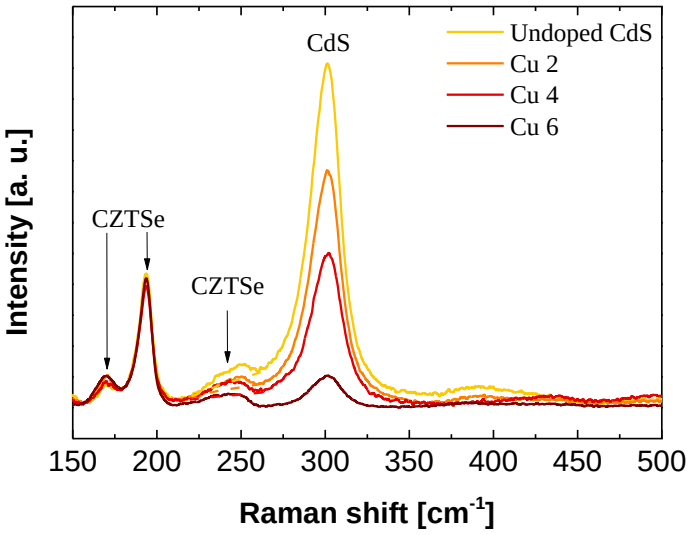

Fig. S5. Raman spectra of CdS/CZTSe with different Cu doping concentration. The excitation wavelength is 514.5 nm.

A summary of the electrical resistivity of the different Cu layers together with the series resistance of the devices reported in Figure 5 is presented in Table S1. The resistivity of the layers increases with the increasing Cu content until Cu4 sample and then decreases, in very good correlation with the values presented in Table 2 of the manuscript. The series resistance of the devices seems to slowly increase.

Table S1. Resistivity of the different Cu doped layers including the reference one, and comparison with the series resistance of the devices reported in Figure 5.

Buffer	**ρ_{dark} (Ω.cm)**	**Espesor (nm)**	**Rs ($\Omega.cm^2$)**
Ref	$1{,}1x10^4$	70	0.2
Cu1	$7{,}0x10^4$	50	0.2
Cu2	$6{,}0x10^4$	39	0.3
Cu3	$9{,}0x10^4$	37	0.3
Cu4	$2{,}3x10^5$	34	0.3
Cu5	$1.1x10^5$	27	0.5
Cu6	$9{,}3x10^4$	21	0.5